POLITECNICO DI TORINO

Corso di Laurea Magistrale
in Ingegneria Meccanica

Tesi di Laurea Magistrale

Study and modular CFD modeling of the ENEA CIRCE ICE experiment.

Relatore
prof. Pietro Asinari
firma del relatore
....

Candidato
Stefano Lampis
firma del candidato
....

A.A.2017/2018

Abstract

The research illustrated in the present thesis focuses on the study and numerical CFD modeling of the ICE experiment conducted in the CIRCE facility, located at the ENEA research center of Brasimone (Bologna, Italy). Such experiment plays a pivotal role in the research process involving the use of HLM (heavy liquid metals) as coolants in the primary circuit of the future 4th generation LFR reactors. The present study describes the generation process of a "modular" CFD model of the CIRCE ICE experiment (created by means of the Siemens STAR-CCM+ software), with the main aim to investigate and appropriately simulate the fluid-dynamic behaviour of molten lead-bismuth eutectic under the typical circumstances required by a modern LFR reactor. In the first chapter, the study focuses on the most important components of the real CIRCE facility, also illustrating how their geometries have been imported in the CFD simulation environment. In a second phase, the procedures followed to generate the meshes for the CFD model are described. The third chapter of the research accurately analyses the numerical modeling approaches followed in order to simulate the "regime condition" phase of the CIRCE ICE experiment, providing results and validating them by comparison with the experimental data. The last section of the thesis focuses on the analysis of the simulation of the "SCRAM transient" phase of the experiment. The concluding chapter demonstrates the relevance of the present CFD model, its current and future applications, and its contribution to the progress of the research on the CIRCE experiments.

Table of contents

List of Tables

List of Figures

List of Abbreviations

CAD	Computer aided design
CFD	Computational fluid dynamics
CIRCE	Circulation eutectic experiment
DHR	Decay heat removal system
FPS	Fuel pin simulator
FVM	Finite volume method
HERO	Heavy liquid mEtal pRessurized water cOoled tubes
HLM	Heavy liquid metal
HX	Heat exchanger (steam generator)
ICE	Integral circulation experiment
LBE	Lead bismuth eutectic
LFR	Lead cooled fast reactor
RANS	Reynolds Averaged Navier Stokes equations (turbulence)
SCRAM	Safety control rod axe man (emergency reactor shutdown)
VoF	Volume of fluid model

Introduction

The constant struggle for the achievement of a cleaner and more efficient approach to energy production has always been one of the most critical challenges humanity has ever had to face. Through the last centuries, in parallel with the development of the industrial sector, the necessity for energetic resources has grown exponentially, and has heavily relied on the persistent employment of fossil fuels as primary raw material. Nowadays, the role of energy production is crucial for the society we live in, at the point that it permeates almost every aspect of our lives, and will become even more pivotal in the near future. Therefore, a resolute response to such a complex challenge is the cornerstone of a future healthy global energetic scenario, and embodies the true spirit of research in this sector.

Most importantly, the mandatory necessity to preserve and protect a clean environment will inevitably cause the gradual dismission of fossil fuel-based energy systems, which will need to be replaced by other (much cleaner) forms of production. At the present time, the research focus is thus mainly pointed on this issue, in the attempt to preliminarily study and design the future systems that should be at the centre of the energetic revolution of the next decades.

The large-scale introduction of renewable energy systems will obviously play the most important role in this process. In fact, the inevitable diffusion of high-efficiency systems such as the STE (solar thermal energy system) and various others will utterly transform the foundations of the global framework of energy production.

In parallel, the other systems that could additionally have a strong impact in this direction are the nuclear-based ones. The research on nuclear energy production has made huge progress over the last decades, and has been mainly focused on the improvement of the safety of such systems. Most importantly, the essential philosophy at the foundation of the new 4th generation reactors consists in the previous study and design of efficient emergency procedures (which must be mandatorily diverse and redundant), upon which the whole following reactor design phase is based.

One of the most important breakthroughs in the nuclear energy production field is represented by the new concept of the LFR reactors (Lead-cooled fast reactors), which are still under thorough study. The most important characteristic of these technology is the peculiar use of molten lead or lead-bismuth eutectic (LBE) in a “pool” configuration as the primary coolant. This choice allows for some crucial advantages, namely:

- Both molten lead and LBE do not chemically react violently with air or water. This essentially translates into the impossibility of generating fires or explosions in case of coolant leakage both towards the environment or towards the water in the secondary circuit (through the heat exchangers).
- The vaporization temperature of lead at ambient pressure is around 1750°C (1670°C for LBE), hence considerably higher than the maximum temperatures that it could reach through an ordinary LFR primary circuit. This essentially means that such core coolants

can be operated at ambient pressure without the risk of possible vaporization issues. Furthermore, an external guard vessel is designed in order to appropriately ensure the containment of the coolant in case of leakage (LOCA).

- LFR reactors allow for a way more efficient use of nuclear fuel comparatively to the older technologies, since they operate with a closed fuel cycle, and can also be employed to recycle residual resources contained in pre-existing spent fuel.
- In case of an accidental loss of coolant from the primary circuit (LOCA), the molten lead/LBE would almost instantly solidify at contact with the environmental air, impeding further large-scale leakages and diffusion of radioactive material.
- The high density of the molten lead/LBE very well shields the core from the environment.

These previous important advantages of the LFR technology have prompted a long series of studies and researches, and the future generation reactors of this type are currently under design phase.

Anyway, the biggest obstacle to the completion of this design phase is represented by the current lack of utter confidence in predicting and modeling the thermo-fluid dynamic behaviour of lead (or LBE) under the circumstances imposed by the LFR technology.

In the pursuit to acquire such desired level of knowledge, some experiments are currently being conducted. The intended aim of these experiments is focused on two key points:

1. Studying, monitoring and deeply understanding the behaviour of heavy liquid metal coolants (lead/LBE) under a wide range of different circumstances, especially in “pool” configurations as demanded by the LFR design.
2. Correctly predicting and modeling such behaviour via dedicated numerical CFD (Computational Fluid Dynamics) models.

Most notably, the real success of such experiments strongly depends on the interconnection between these previous points. In fact, the only condition that can actually prove the achievement of a satisfying degree of knowledge about the fluid dynamic phenomena involving heavy liquid metal coolants is the proper validation of the CFD models of the experiments. Such validation is reached when the CFD results show a good degree of accordance with the experimental data provided by the observation of the real experiment.

Currently, the most important experiments on LBE cooled reactors are performed in the CIRCE (CIRCulation Eutectic) facility, mainly in the framework of the SESAME European project, located in the ENEA research centre of Brasimone (BO, Italy). The CIRCE experiment fundamentally aims to simulate the behaviour of a common primary LBE loop of a generic LFR reactor in pool configuration, under both the regular regime operative condition and in case of accident (simulation of the core SCRAM and subsequent decay phase). Further details on the experiment are illustrated in the next paragraphs.

The fundamental objective of the research work presented in this thesis is the generation of an appropriate CFD model of the CIRCE (ICE) experiment, based on the official data provided by ENEA, and aiming to portray the behaviour of the facility in the most accurate way possible. This model is also meant to be versatile enough to be employed for future analyses, in order to predict the effects of possible modifications to the original structure of the facility; in order to reach this goal, a “modular” approach has been followed (described in paragraph 1.3.6).

Furthermore, many previous CFD models have attempted to depict the CIRCE regime working condition, but all of them have shown some important degree of detachment from the official experiment; this model tries to get inspiration from these previous attempts, learning from their successes and limits, and trying to apply the necessary modifications that will testify a progress in the knowledge of the ENEA/SESAME community about liquid metal cooled reactors.

Furthermore, obtaining a sufficiently accurate result would grant enough confidence to apply the gained knowledge to the other SESAME projects (MYRRHA, ALFRED etc.), allowing the research for the future LFR reactors to progress in a much faster and trustworthy way.

Introduction to the CIRCE facility and its experiments

CIRCE is one of the various experimental facilities hosted in the ENEA research center of Brasimone (BO, Italy), and is currently the world’s largest pool-type facility operating with heavy liquid metal (LBE). A detailed view of the ENEA Brasimone research center is displayed in the following Figure 1.

Figure 1. *External view of the ENEA research center of Brasimone (BO, Italy). Image courtesy of ENEA and Dr. Antoine Gerschenfeld, CEA.*

As mentioned in the previous introductive paragraph, the main purpose of this facility lies in the study of the global fluid-dynamic behaviour of LBE as a coolant for the primary circuit of the future pool-type LFR reactors. The CIRCE experiment has been intrinsically designed for this objective, and its constructive elements are thus recalling the ones that are typical of the

LFR nuclear reactors. Technically speaking, the CIRCE experiment is based on a LBE loop designed as illustrated in the scheme in the following Figure 2:

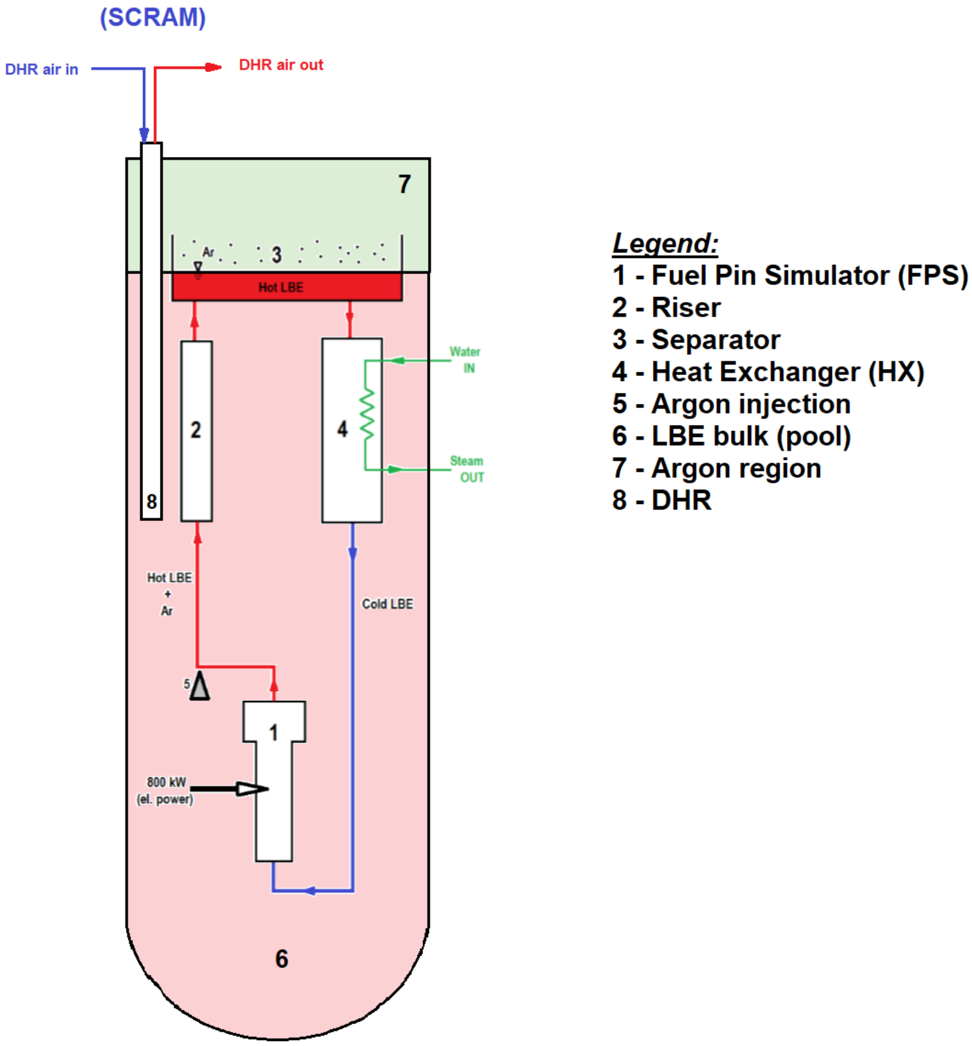

Figure 2. *Functional scheme of the ENEA CIRCE facility, highlighting its fundamental components.*

As can be noticed, all the various elements of the CIRCE facility are immersed in a pool of molten LBE, hereupon referred to as the "LBE bulk" region of the facility (element 6 in Figure 2), isolated from the external environment by means of a steel vessel (total height of about 8 m and diameter of 1.2 m) .

Figure 3 shows the real CIRCE facility (dismounted due to maintenance operations), highlighting the various components depicted in the previous functional scheme (Figure 2).

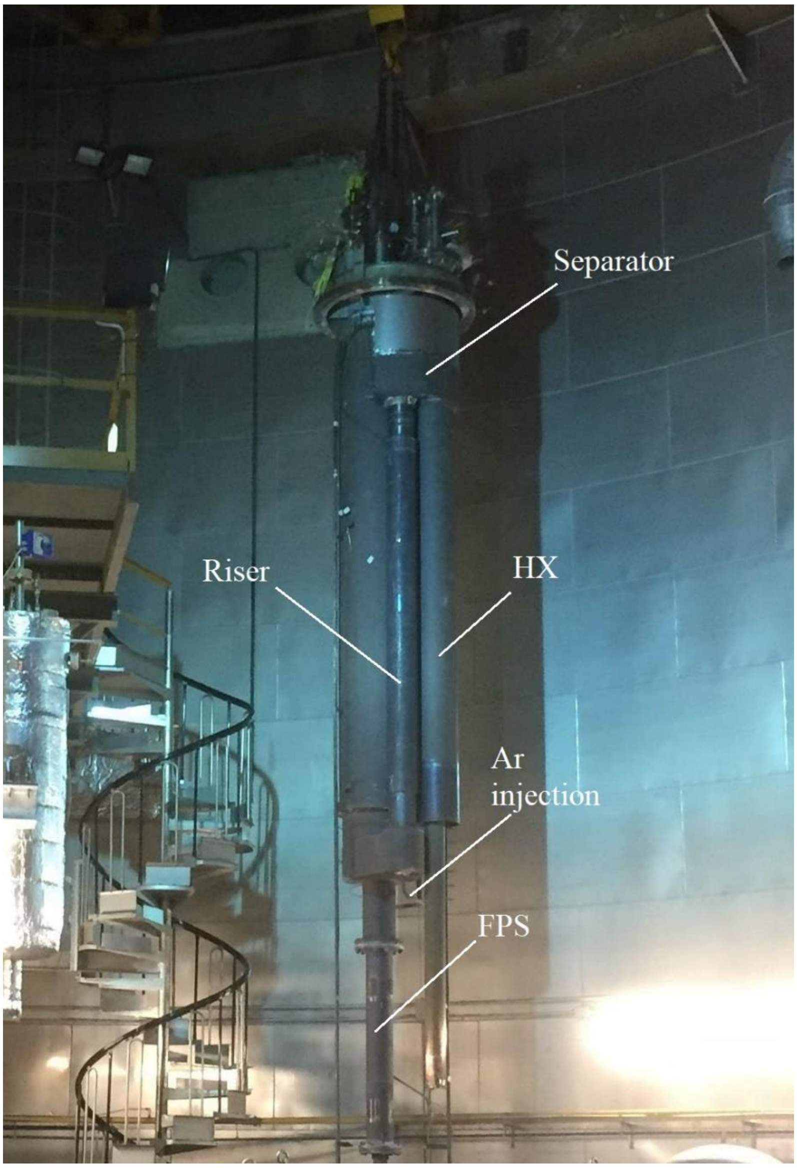

Figure 3. Internal structure of the CIRCE facility dismounted during maintenance operations. The most important components are highlighted. Image courtesy of ENEA and Dr. Ferry Roelofs, NRG.

The experiments conducted in this facility can be subdivided in two main phases:

Regime condition experiment:

During a standard regime condition experiment, the mass flow rate (values change between the different experiments) of cold LBE located in the bottom regions of the LBE bulk (~300 °C) enters the so called "Fuel Pin Simulator" (element 1 in Figure 2). This element is designed in order to simulate the physical configuration of a real nuclear fuel pin bundle, and is thus composed of a large number of electrified pins that are meant to provide the heat power to the cold LBE flow incoming from the bottom regions of the bulk. The actual geometry of this element will be discussed later, and is illustrated in detail in Figure 7. The maximum thermal duty of the CIRCE FPS is around 1 MW, but for the majority of the experiments here conducted, the total heat power supplied to the LBE is set around 800 kW. As a result, the LBE exits the FPS at a considerably higher temperature (~370 °C), and reaches the Conveyor element. Here, a particular “gas lift” system has been introduced in order to generate the LBE mass flow rate through the circuit. Such system works by means of a nozzle (element 5 in Figure 2) attached to the bottom of the conveyor, which injects a mass flow rate of argon into the LBE flow, thus creating an effective dual-phase flow condition. The resulting decrease in the density of the LBE+Ar mixture causes the generation of a vertical buoyancy thrust which is responsible for the movement of the LBE through the riser element (element 2 in Figure 2). As will be later discussed, such LBE+Ar mixture is characterised by a very complex and bubbly flow regime that will need to be greatly simplified in order to be concretely modeled. The LBE+Ar mixture then exits the riser and flows into the separator element (3 in Figure 2), located at the top region of the facility. Here, the argon component leaves the mixture, flowing upwards in the so called “Gas volume” (“argon region” element 7 in Figure 2), while the LBE mass flow rate proceeds further into the heat exchanger (HX) (element 4 in Figure 2). In the HX, the LBE mass flow rate flows through a bundle of cold water-fed double bayonet tubes, exchanging a total heat power of ~800 kW with them. As a result of this heat exchange, the water in the HX tubes vaporizes, while the LBE mass flow rate exits the HX at a lower temperature (~300 °C), and returns to the lowest regions of the bulk, completing the loop. As will be later illustrated in paragraph 3.4.2.1, the thermal stratification of the LBE bulk region is probably the most important object of study of the CIRCE experiment, and its behaviour will be thoroughly analysed. During the real experiment, the CIRCE facility operates in this “regime experiment” condition for a certain time span (around some hours, depending on the chosen experiment); later, the SCRAM simulation is initiated.

“SCRAM simulation” (PLOHS+LOF transient)

After completing the stable “regime condition” phase of the experiment, the operative conditions of the facility are abruptly changed in order to simulate a typical accident of a nuclear reactor and the following decay scenario. In a real situation of such kind, the SCRAM procedure is initiated, and the control rod safety system is activated in order to contain the nuclear core total heat power supply to the coolant. In this experimental facility, such result is simply obtained by reducing the electrical power supplied to the pins down to a typical value around 30 kW. In parallel, some other changes to the working conditions of the facility are applied at the start of the SCRAM experiment:

- **Deactivation of the HX:** the cooling water mass flow rate supplied to the HX element is rapidly interrupted.
- **Deactivation of the argon gas lift system:** The argon mass flow rate injected by the nozzle is suppressed.
- **Activation of the Decay Heat Removal (DHR) system:** The DHR element of the facility (element 8 in Figure 2) is essentially an air-fed heat exchanger (constituted of a single large double bayonet tube), which has been designed to simulate the natural, slow cooling process of the LBE inside the pool during the decay phase following the core SCRAM.

The molten LBE in the facility reacts violently to these changes, and enters a transient operative condition whose main parameters are constantly monitored over time, in order to evaluate the LBE response to a possible accidental scenario.

Different configurations of the CIRCE facility

It is extremely important to highlight that the CIRCE facility has undergone various changes from its original design, and will probably be updated again in the near future. More precisely, the two most recent configurations of the facility are the CIRCE ICE and the CIRCE HERO experiments, which essentially differ for the following aspects:

- **CIRCE ICE:** this experiment configuration features an HX design composed of 91 double bayonet tubes arranged in an hexagonal matrix bundle, and also presents the original DHR design of the facility. This version of the CIRCE experiment will be the one analysed in the present research.
- **CIRCE HERO:** this configuration represents the most recent update to the facility setup, and features an alternative version of the HX, composed of only 7 double bayonet tubes arranged in a hexagonal matrix bundle. These tubes are larger in diameter and way longer if compared to the previous ICE HX configuration. Furthermore, the DHR element has been simplified by removing some of the most external insulating regions, for reasons that will be furtherly explained in paragraph 1.3.7.

Employed computational resources:

All the activities inherent to the present research have been conducted employing the computational resources provided by the HPC for Energy & Environment team of the CRS4 research center (CA, Italy). These resources essentially consisted in:

- Access to a personal Siemens STAR-CCM+ software license, used to carry out all the CFD simulations necessary to complete the research.
- Access to the CRS4 main CPU clusters, whose computational power has allowed to complete the calculations associated to the CFD modeling.

The CRS4 research center[5]

The CRS4 (Center for advanced studies, research and development in Sardinia), is currently one of the most important research institutions in Italy, constantly operating across very diverse fields, from energy and visual computing to high performance computing and biosciences. The present research work has been guided by the HPC for energy and environment team (led by Dr. Ernesto Bonomi) and, more precisely, under the supervision of Dr. Vincent Moreau of the Smart Energy Systems group (program head: Dr. Luca Massidda). The HPC for energy and environment team is involved in a wide variety of research projects, all focused to provide satisfying answers to complex and diverse energetic problems by employing multi-disciplinary methods, mainly based on the numerical modeling of physical phenomena.

In the next chapter 1, the procedures followed to create a valid CAD geometry model for the CIRCE facility will be discussed. Later, this geometry will be employed as the foundation of the whole CFD model of the CIRCE facility.

1. Geometry of the CIRCE facility.

1.1 Official data

The very first step required to start the modeling process has obviously been the study of the geometry of the whole CIRCE facility.

All the available data related to the various components of the facility was gathered in the form of a large number of technical drawings and official ENEA documents; furthermore, since no official CAD model was provided, it has been compulsory to generate the CAD geometry completely from scratch, employing the CAD editor included in the STAR-CCM+ software.

Although the geometry of one of the previous CRS4 models of CIRCE has been used as simple orienting reference (especially considering the complexity of the facility), nothing has been imported, and all the parts of the geometry have been created following the information directly provided by the drawings, thus ensuring a much cleaner approach.

1.2 Issues and difficulties related to the creation of the geometry.

The practical procedure of transforming the ENEA official drawings of the CIRCE facility into a reliable and accurate CAD geometry model has not been devoid of various issues and difficulties, principally due to the large scale of the facility and the complexity of its components.

In order to set a solid base for the CAD geometry, the principal coordinate system of the whole model has been fixed considering an origin placed exactly at the centre of the active zone of the FPS (i.e. at the centre of the intermediate grid of the FPS, as illustrated in Figure 4), and the z axis oriented vertically towards greater heights; the origin of the abovementioned coordinate system has been the starting point for the construction of the geometry.

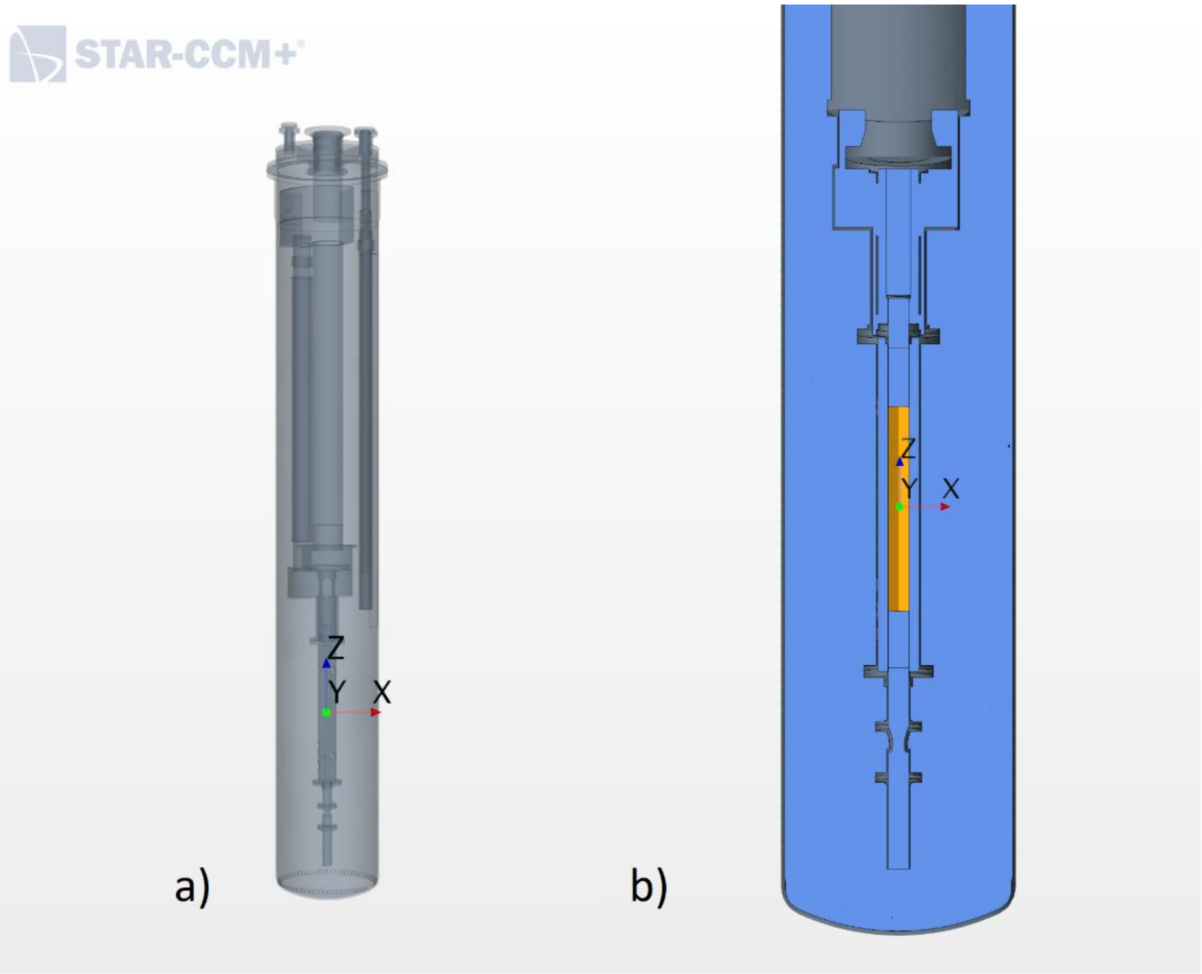

Figure 4. Main coordinate system of the CIRCE model. a) global position of the main coordinate system. b) detail: position of the origin of the main coordinate system at the central section of the FPS active region (highlighted in orange).

The very first region to be designed in the CAD editor has thus been the bottom part of the facility (suction pipe and FPS zone), then all the other regions were subsequently generated considering an order based on the effective path followed by the LBE.

Furthermore, the whole facility has been subdivided into a very large number of different geometry bodies, essentially due to three main reasons:

- **Meshing purposes:**

  each single body of the geometry has been created considering the later process of mesh generation, in order to take advantage of the most efficient meshing operation possible. For instance, almost every prismatic region has been isolated, thus allowing the later use of the directed mesh operation (described in paragraph 2.2).

- **Modeling purposes:**

  some zones of the geometry had to be necessarily separated in different bodies due to modeling reasons that would have been of paramount importance later (porous zones, volumetric energy source/sink zones etc.).

- **Analysis versatility:**

  one of the main objectives of this new model is to allow the user to perform a wide range of different reports and controls over single targeted portions of the facility, and this is only possible with a highly-subdivided structure of the geometry parts.

This process inevitably leads to a drastic increase in the total number of bodies of the CAD model. In order to efficiently manage such a high number of parts (not only at CAD level, but being mindful of the later possible issues occurring especially at simulation level) a very simple numbering system has been adopted. By doing so, each body of the geometry, whether it be a solid, liquid or gaseous component, has been permanently linked to a unique alpha-numerical reference code, making the whole process of recalling elements of the model both faster and "cleaner".

The choice of such a highly fragmented structure of the CAD geometry inevitably affects its total number of surfaces, which rises noticeably; this implies that, at simulation level, this large number of surfaces will transform into a wide and complex system of contact interfaces.

In order to have complete control of the surfaces of the geometry, every single body has been imprinted with the neighbouring ones, and then each resulting surface has been renamed following a particular convention based on the bodies numbering system.

Precisely, each surface has been renamed considering the contact between the body it belongs to and the adjacent one causing such contact; Figure 5 below clarifies the convention.

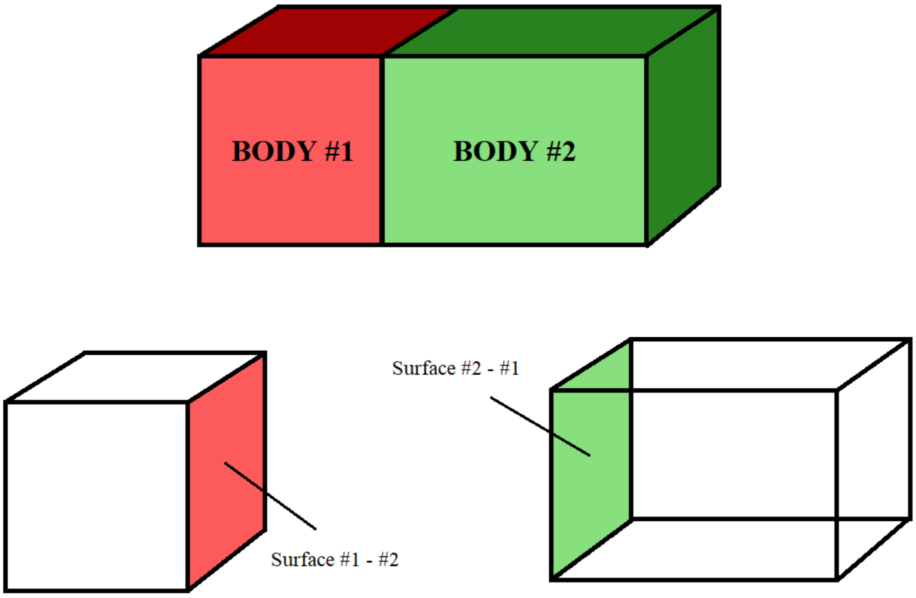

Figure 5. Scheme of the adopted surface naming convention.

The first alpha-numerical code in the surface name is related to the body to whom the surface belongs, while the second is the code of the adjacent contacting body. The only exceptions to this convention are the external surfaces of the geometry (vessel, top cover and few others) which obviously are not contacting with any other body.

This method offers two key advantages when later progressing to the simulation level:

- **Very simple interface check:**

  when assigning the parts of the geometry to regions of the model, the STAR-CCM+ software automatically searches for contacts between the various parts, and when it finds them creates a contact-mode interface named with the following pattern: “[name of surface A]/[name of surface B]” where surface A and surface B are the two surfaces responsible for the contact. Considering the abovementioned convention for the surface names, each **correct** interface will have a “symmetric” name, for instance “#1 - #2 / #2 - #1”, while a **wrong** interface, probably caused by errors in CAD modeling phase, will show an “asymmetric” name, rather easy to spot. Without an appropriate naming convention noticing an incorrect interface would have been much more difficult and slower.

- **Unambiguous surface recall:**

  when performing controls and reports it is often necessary to address one or more specific surfaces of the geometry; the adopted naming convention makes this procedure unambiguous, fast, and less susceptible to mistakes.

Please notice that this convention has been applied to every single body designed in the CAD geometry, independently from its physical nature (valid for solid regions, but also for liquid and gaseous ones).

Another issue of the CAD model generation is related to the desired level of accuracy. Generally, in the attempt of staying as truthful as possible to the original ENEA data, most of the details up to the coupling flange-level ones have been maintained and included in the CAD model. Conversely, the model does not include very small details like bolts, cables and slightly bigger ones like the bulk physical thermocouple lines (described in paragraph 3.4.2.1) and supporting structures.

1.3 Analysis of the single regions of the geometry

In the following paragraphs each single component of the geometry will be described alongside with its main characteristics. The various elements are presented in the same order by which they were generated in the STAR-CCM+ editor.

1.3.1 Suction pipe zone

This is the lowest region of the facility, whose main function is the suction of the cold LBE from the bottom of the S100 Vessel and its transport upwards to the FPS.

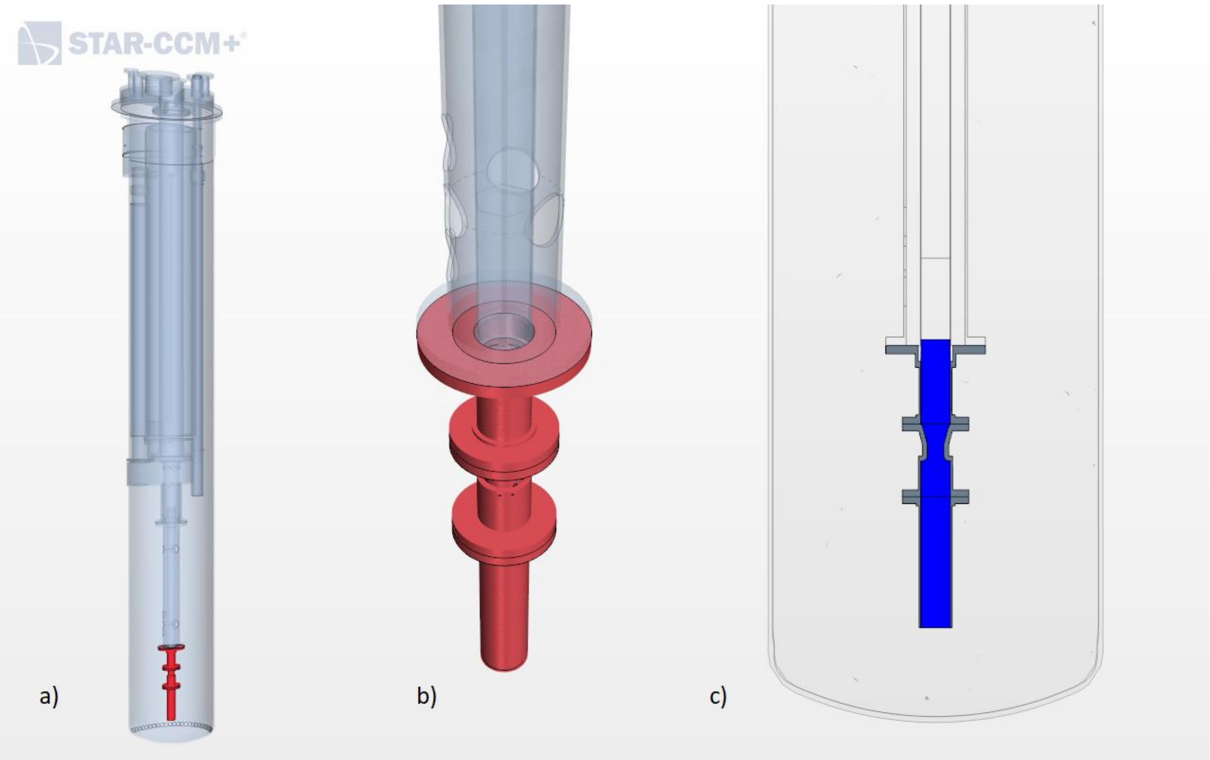

Figure 6. CAD geometry of the suction pipe zone. a) general location. b) detail. c) section highlighting the LBE zones (blue) and steel pipes (grey).

In the previous Figure 6 the single elements of the region are depicted. It is important to notice the presence of the Venturi flow meter, whose geometry has been roughly approximated based on the official data provided on the real component.

1.3.2 FPS region

The FPS region, whose main role is the supply of the heat power to the liquid LBE incoming from the suction pipe, is also one of the most geometrically complex parts of the whole facility.

The FPS assembly is composed of 37 electrified pins (Figure 7 below), engineered in order to simulate thermal behaviour of the real fuel pins of a common reactor; in this case the heat power is simply supplied via Joule effect.

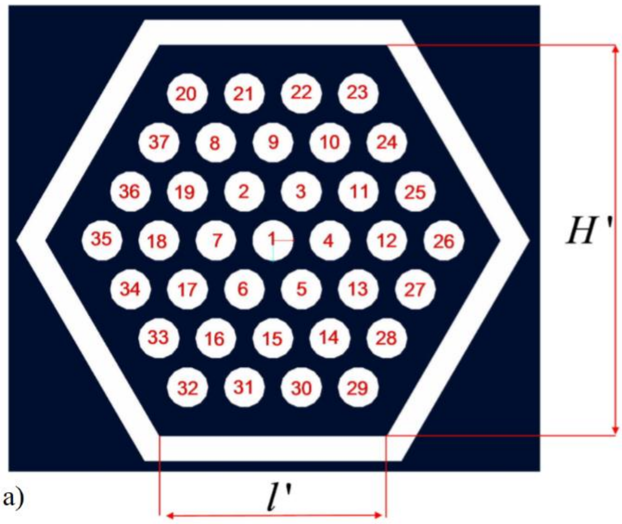

a)

b)

Parameter	***Value***
Number of pins *n*	37
Pin outer diameter ϕ	8.2 mm
Power of a pin	25 kW
Pin wall heat flux	1 MW/m^2
Pitch to diameter p/ϕ	1.8
Active Length	1 m
l'	55.4 mm
H'	96 mm

c)

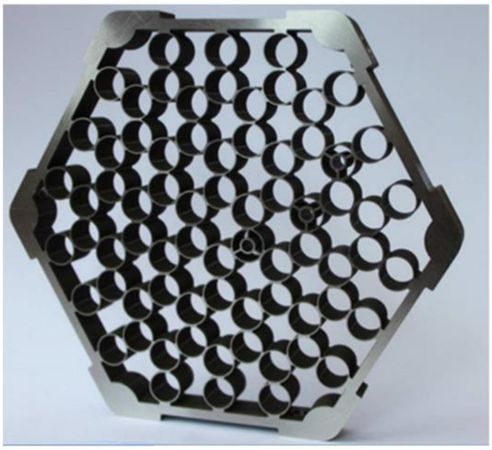

d)

Figure 7. *Details of the real FPS element. a) geometrical scheme of a perpendicular section of the FPS, depicting the external hexagonal wrapper, and the 37 pins. b) detailed view of the electrical pins of the real FPS; an FPS spacer grid is also visible. c) main characteristics and dimensions of the FPS element. d) detailed view of one of the three FPS spacer grids. Image and data reported in document [1], courtesy of ENEA.*

The pins are arranged in a hexagonal matrix, bound together by three spacer grids set respectively at the origin of the principal coordinate system of the model, 500mm above and 500mm below. Furthermore, they are surrounded by a thin hexagonal wrapper, and the whole assembly is enclosed into another more external steel pipe. Figure 8 shows the transition from the original ENEA drawing to the CAD model in the STAR-CCM+ editor.

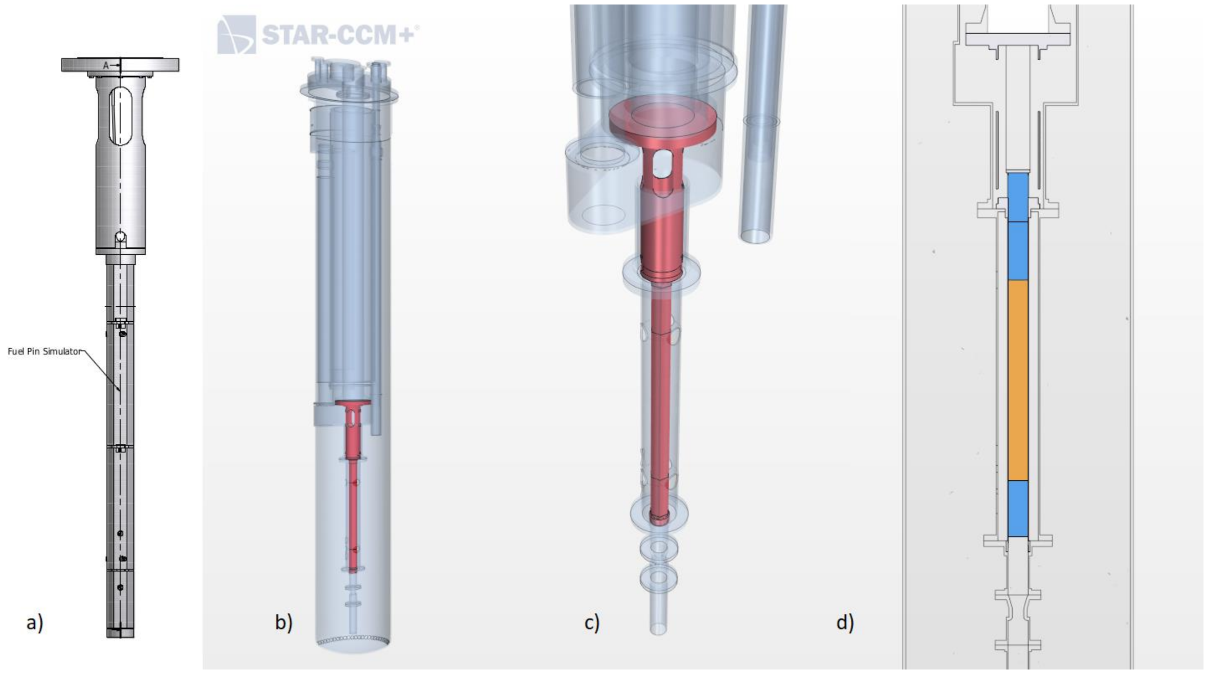

Figure 8. *CAD geometry of the FPS element. a) extract from an official CIRCE drawing, courtesy of ENEA. b) general location. c) detail. d) section highlighting the LBE zones (orange: active region, blue: inactive region) and steel pipes (grey).*

Some important details must be noticed:

- The pins have not been physically modeled in the geometry, due to excessive future complications in the meshing process; also, such level of accuracy would have drastically increased the computational cost of the simulation. Considering that the main aim of this model is the analysis of the global behaviour of the whole facility, such cost was deemed excessive, and the pin region has been modeled by means of an "equivalent porous medium". As can be seen in the previous Figure 8, three porous LBE bodies can be highlighted, all originally occupied by LBE flowing around the pins, but with some differences: the blue regions are designed to be inactive zones of the FPS, while the only portion of the FPS which actually supplies the heat power is modeled by the region highlighted in orange. The two interfaces between these bodies will be later employed as porous baffle interfaces in order to simulate the pressure losses induced by the grids.
- The external steel pipe surrounding the whole assembly presents several holes meant to host the instrumentation cables exiting the FPS assembly; these cables obviously cause an increase in the fluid-dynamic resistance felt by the LBE passing through the holes. In order to take into account this effect, the holes have been "filled", creating the "caps" depicted in Figure 9, which will be then modeled as porous LBE elements.

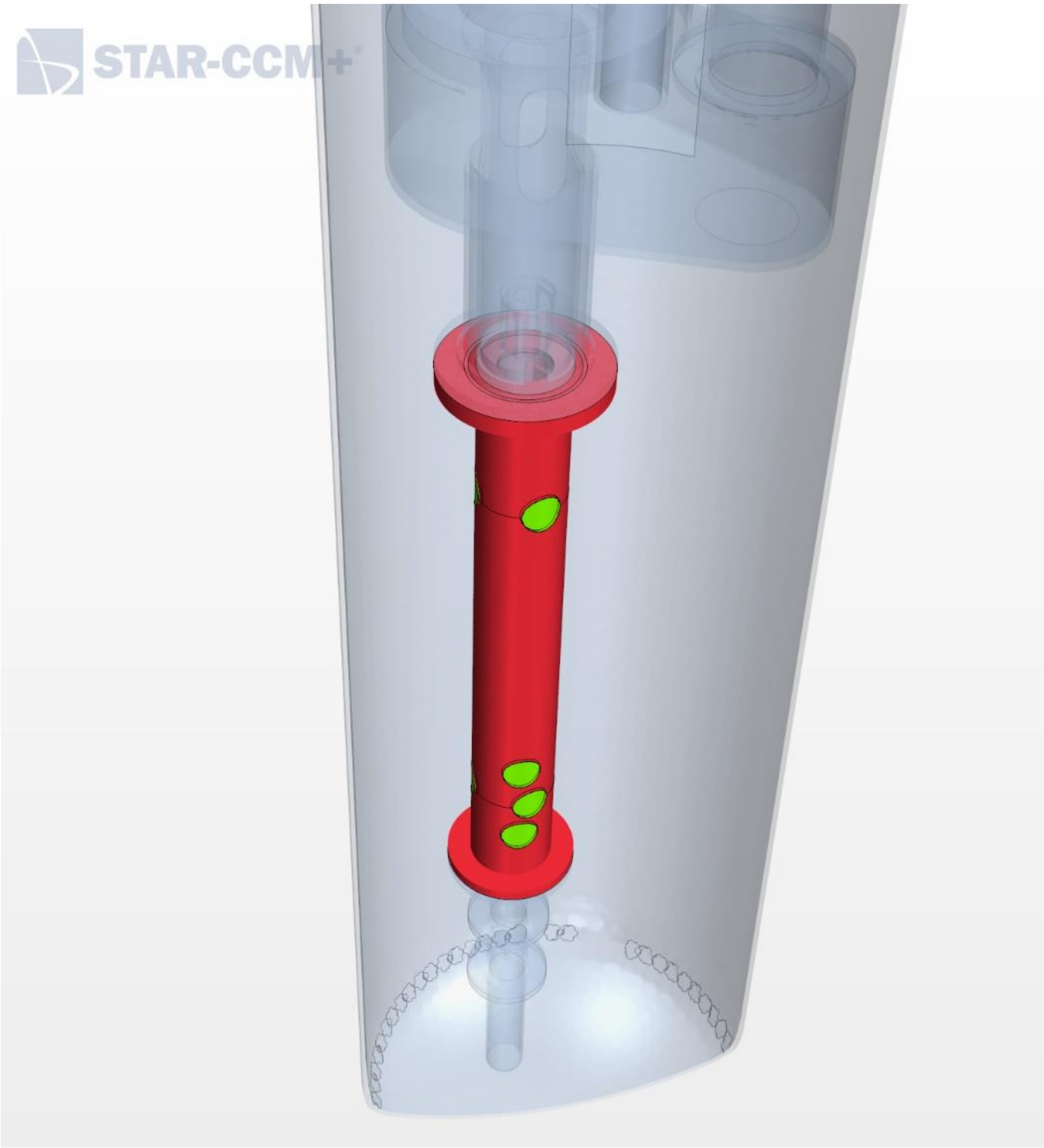

Figure 9. *Detailed view of the external steel element surrounding the FPS hexagonal wrapper (red). The "porous caps" simulating the presence of the FPS instrumentation cables through the holes are highlighted (green)*

1.3.3 Conveyor region

After passing through the FPS assembly, the LBE exits the hexagonal wrapper and passes through the release pipe, depicted in Figure 8, reaching the Conveyor. This element has two main functions:

- It allows the hot LBE flow coming from the FPS assembly to homogenize before accessing the Riser region. The Argon nozzle responsible for the whole generation of the LBE mass flow rate in the facility is also located here, at the bottom of the element just below the Riser inlet.
- It hosts the terminating part of the pins of the FPS, allowing them to exit the facility passing directly into the dead volume (which is in direct contact with the conveyor).

In Figure 10 below, each element of the Conveyor geometry is displayed:

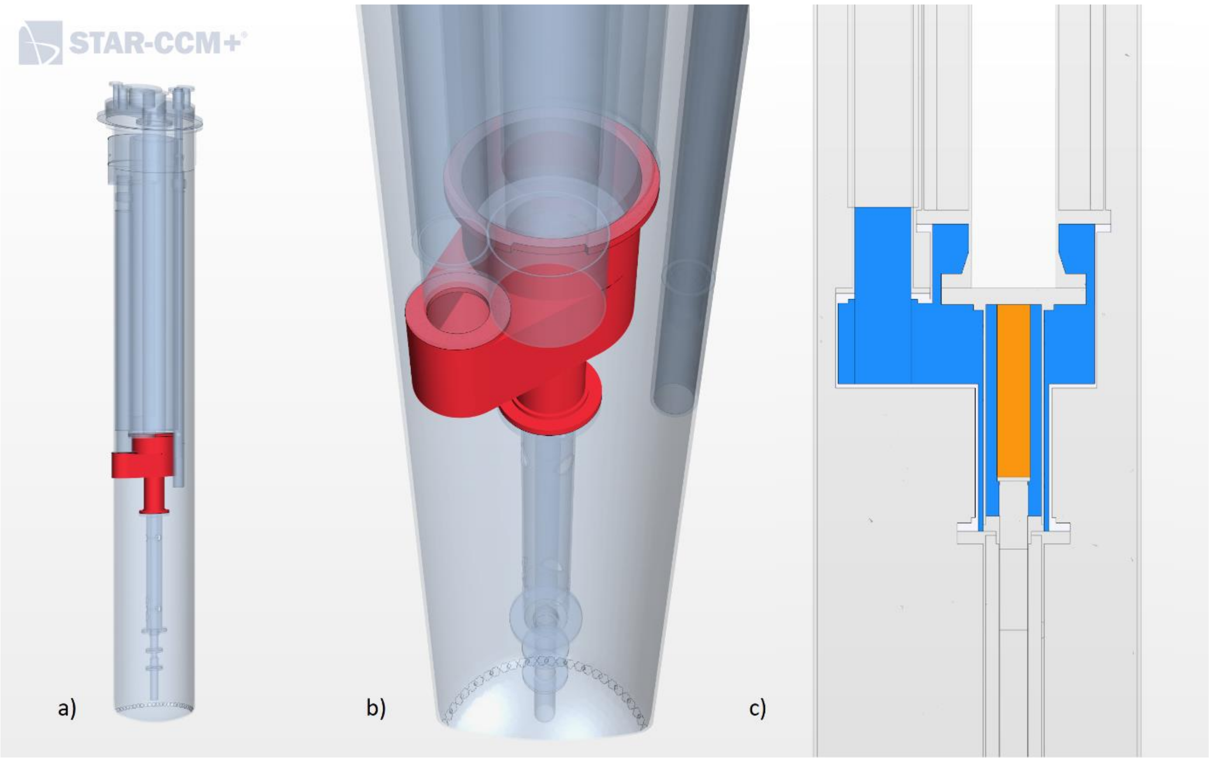

__Figure 10.__ CAD geometry of the conveyor zone. a) general location. b) detail. c) section highlighting the LBE zones (blue: non porous, orange: porous) and steel structural components.

Some observations have to be made:

- The LBE body highlighted in orange in Figure 10 (where the FPS exiting pins should have been located) has been isolated from the surrounding LBE inside the Conveyor, in order to be later able to assign a porous media condition there. This also allows possible future modifications of the geometry in that selected zone.
- With the same philosophy, the portion of LBE under the Riser inlet has also been isolated, thus allowing possible future modifications of the geometry there (e.g. adding the physical nozzle element).

1.3.4 Riser region

After being homogenized in the conveyor, the hot LBE flow is mixed with the argon injected by the nozzle, and flows upwards through the riser. This element of the facility shows a very complex fluid-dynamic behaviour, characterised by a chaotically bubbly and turbulent regime which is almost impossible to simulate efficiently with a high level of accuracy.

The riser geometry is essentially composed by the following elements depicted in Figure 11:

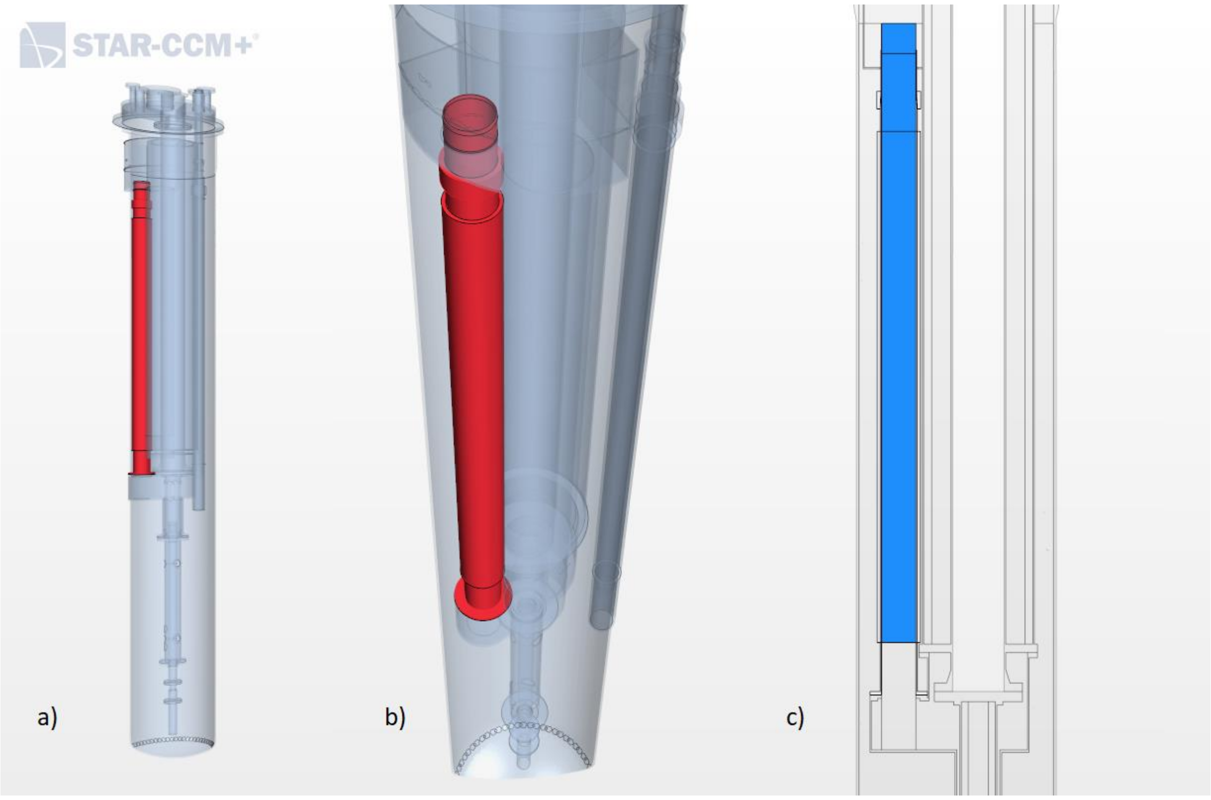

Figure 11. CAD geometry of the riser zone. a) general location. b) detail. c) section highlighting the LBE zones (blue) and the structural components.

Some important details:

- The LBE body inside the riser pipe has been isolated from the other contacting LBE bodies (separator and conveyor regions). This is due to the necessity to be later able to assign a momentum source option here, in order to simulate the thrust provided by the argon gas lift system.
- The insulation elements surrounding the riser pipe have been slightly modified for the sake of simplicity, and a single “riser insulation” body has been created; anyway, at simulation level, the physical properties of this part have been calculated still considering the effective layers by which it is composed (paragraph 3.3.3).
- The riser axial expansion joint has been roughly approximated from the original design, in order to simplify the later meshing process.

1.3.5 Separator region

The bubbly LBE-argon mixture exits the riser and reaches the separator region at the top of the facility, whose main function is the actual separation of the gas component from the hot LBE flow. Here, the LBE free surface shows a chaotic behaviour due to the influence of the highly turbulent flow exiting the riser.

The actual simulation of such a complex moving free surface would have required a highly demanding multiphase VoF model, and has thus not been considered viable in this situation (excessive computational cost considering the expected low benefits).

The LBE free surface has then been modeled as a very simple horizontal surface (respecting the data found in the official ENEA drawings. The following Figure 12 shows the various components of the geometry of this region.

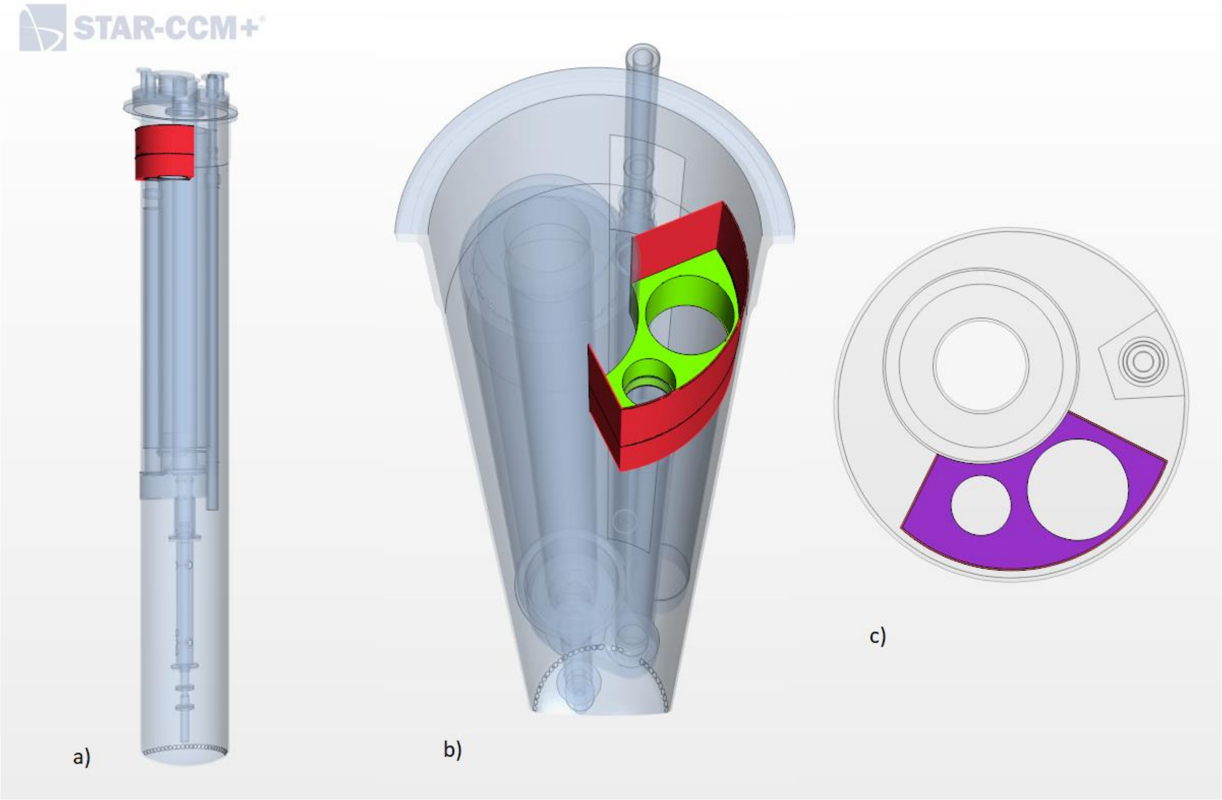

Figure 12. CAD geometry of the separator zone. a) general location. b) detailed view, highlighting the steel separator element (red) and a portion of the LBE contained in it (green). The average LBE free surface coincides with the top surface of the LBE zone here depicted. c) section of the element.

Some important elements must be pointed out:

- **Gas Volume:**

  The argon exiting the LBE flow tends to rise, occupying the top region of the facility, between the LBE free surface and the top cover of the vessel. As can be seen in Figure 13, this region has been designed as a single CAD body, and will be later modeled in an extremely approximated way, essentially considering it as "solid" component while still taking into account the actual thermodynamic properties of the gas (the thorough study of the argon behaviour and its flow properties is not of paramount importance in this model).

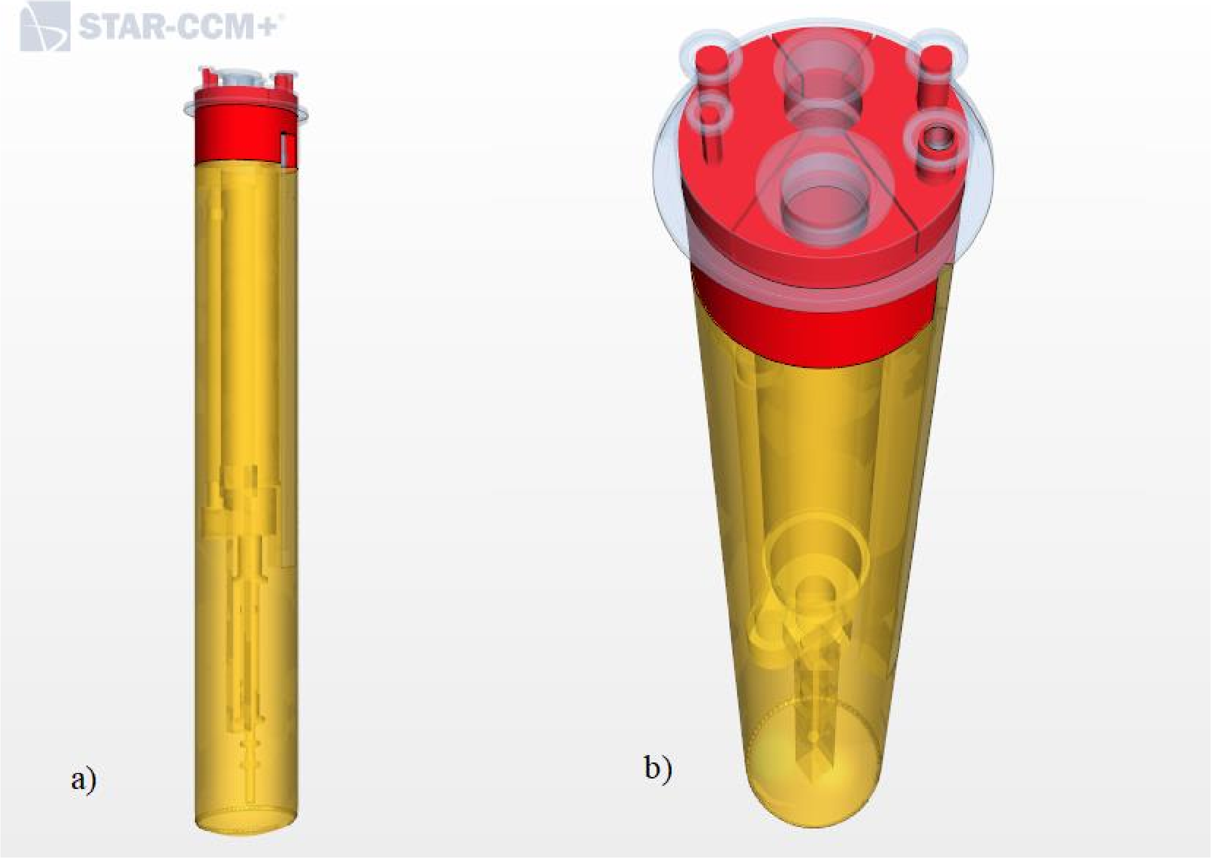

Figure 13. CAD geometry of the argon gas volume region (red), located above the LBE pool (bulk) region (yellow). a) general location. b) top detail.

Furthermore, isolating this gas region allows for future improvements of the model (for instance by adding hypothetic models for radiative heat transfer).

- **Separator Leakage Ring:**

  The outlet part of the riser pipe is welded to the bottom of the separator, generating the link between the two elements of the facility. Considering ENEA's reports and on-field experience on this particular element of the facility, the presence of a very small leakage zone (from the separator through the welding and into the LBE bulk) has often been hypothesized; in order to take this detail into account, a small "LBE leakage ring" body has been designed in the CAD editor (depicted in Figure 14). Later, this part will be modeled as a porous medium (with rather high porous inertial resistance) in order to allow a very small hot LBE mass flow rate to directly pass from the separator into the bulk region, thus modeling the abovementioned leakage phenomenon.

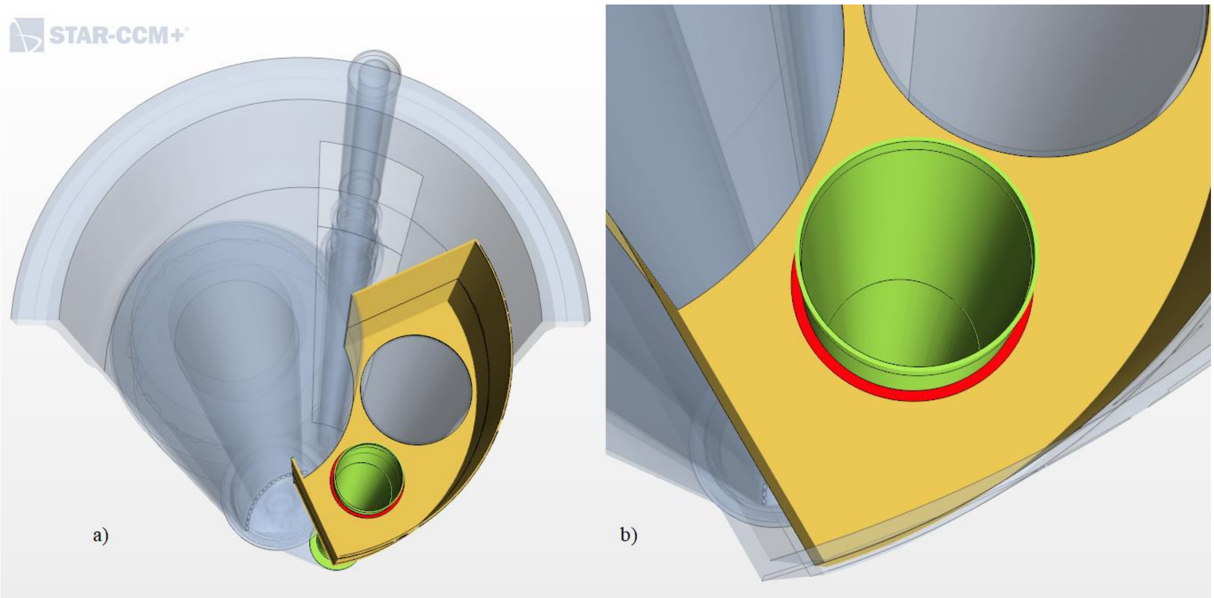

Figure 14. *Detailed view of the separator element (yellow). a) Top view. b) The riser outlet (green) and the separator "leakage ring" (red) are also highlighted.*

Figure 15. *Detailed view of the real separator element, also highlighting the presence of the HX double bayonet tubes and the riser outlet thermocouples. Image courtesy of ENEA, Ref. document [1].*

- The LBE inlet of the heat exchanger (the top zone of contact with the HX double bayonet tubes) is separated from the LBE inside the separator; this is due to various reasons that will be explained in the next paragraph.

1.3.6 HX region and philosophy of the modular approach.

The heat exchanger is one of the most complex parts of the whole facility, essentially due to its really dense double bayonet tubes structure (Figure 15), arranged in a hexagonal matrix, and directly contacting with the LBE contained in the separator.

As previously explained in the introductive chapter, CIRCE has hosted various experiment configurations through the years (ICE, HERO and other future possible ones); due to this reason, there is a strong need for a versatile model which can be easily adapted to any change in some selected zones of the facility (especially the HX and DHR elements).

In order to create such a flexible model, and pursuing the ideal objective of designing a substructure capable of simulating multiple HX configurations without the need to apply major later changes to the remaining geometry and mesh of the facility, a simple modular approach has been studied.

The general principle at the basis of this approach is the identification and isolation of a very precise region of the model (in this case the one that should include the HX), which has been designed directly in the CAD editor and is portrayed in the following Figure 16.

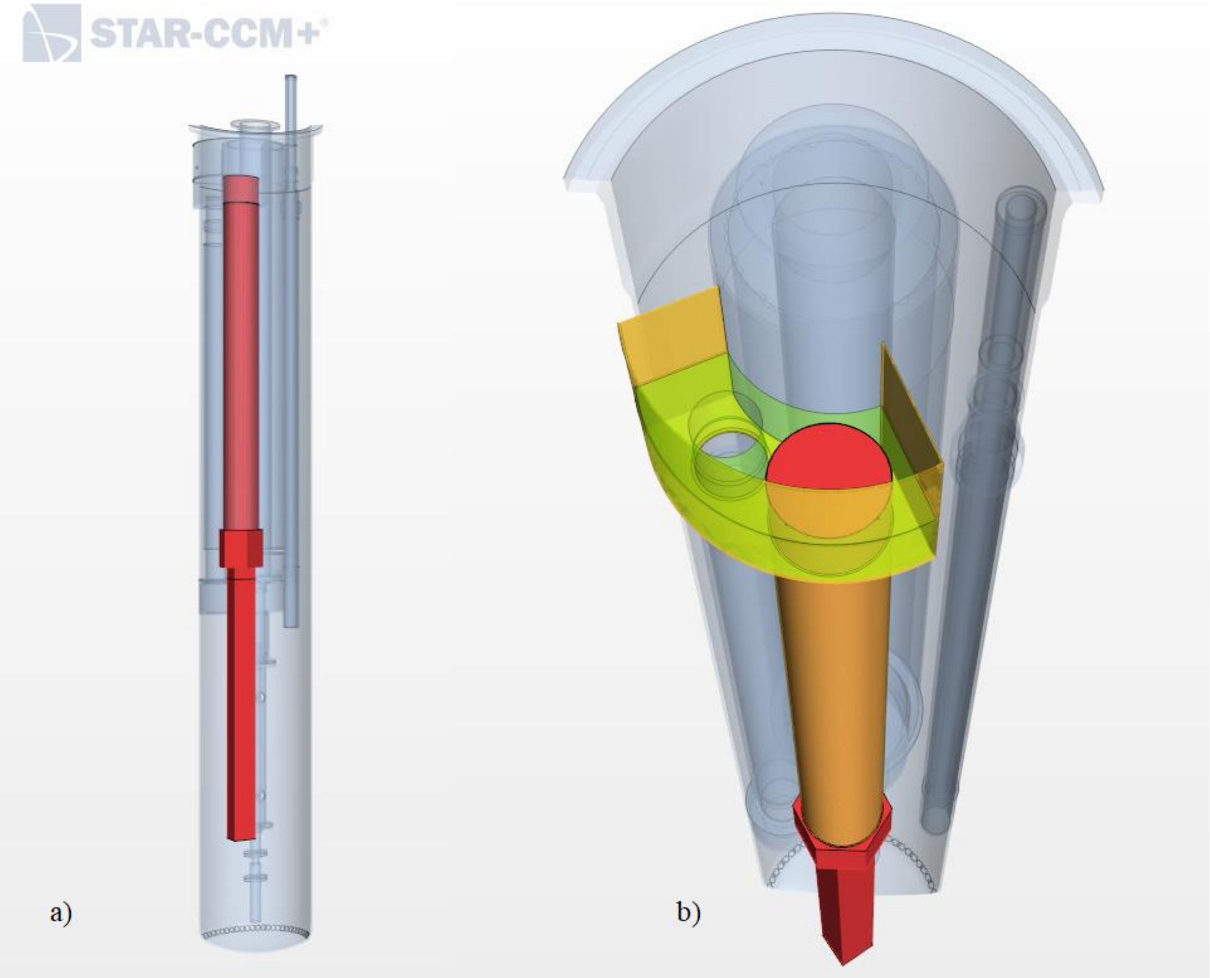

Figure 16. CAD representation of the HX control volume (red). a) general location. b) detailed view highlighting the position of the HX control volume relatively to the separator and HX shell elements (orange) and LBE contained in the separator (green).

This CAD geometry body, appropriately named “HX control volume”, encloses all the regions of the HX that might be subject to future changes/alterations, and is thus consisting of the double bayonet tubes region inside the HX shell, the solid HX skirt, and the bottom part of the LBE region near the outlet of the HX.

It is important to notice two crucial factors:

- The particular hexagonal/squared prismatic shape at the bottom of the volume has been preferred to a simpler cylindrical one in order to avoid later possible issues due to meshing and interface issues, which are much less common with polygonal shapes.
- The vertical length of this HX control volume has been chosen in order to be able to host the HERO configuration for the HX (much longer and thinner than the ICE HX).

N.B.: the HX shell is not included in the HX modular control volume, since it has been considered a stable part of the facility.

This HX control volume is not meant to actually contain the physical CAD bodies of the HX, but is more considered as an “empty module”; in fact, the philosophy behind its creation is based on the idea of copying it and translating such copy further away outside the domain of the facility, where it can be geometrically edited. In order to do this, a dedicated coordinate system has been created under the name of “HX translation system”, with the X axis intersecting both with the central vertical axis of the external S100 Vessel and with the central vertical axis of the empty HX control volume. By means of this coordinate system, the HX control volume has been duplicated and translated outside the facility. Here (x-coordinate=1 m along the X axis of the HX translation system), the HX control volume copy has been edited in order to create the CAD body configuration of the CIRCE ICE HX, as depicted in Figure 17, alongside a technical scheme of the actual element.

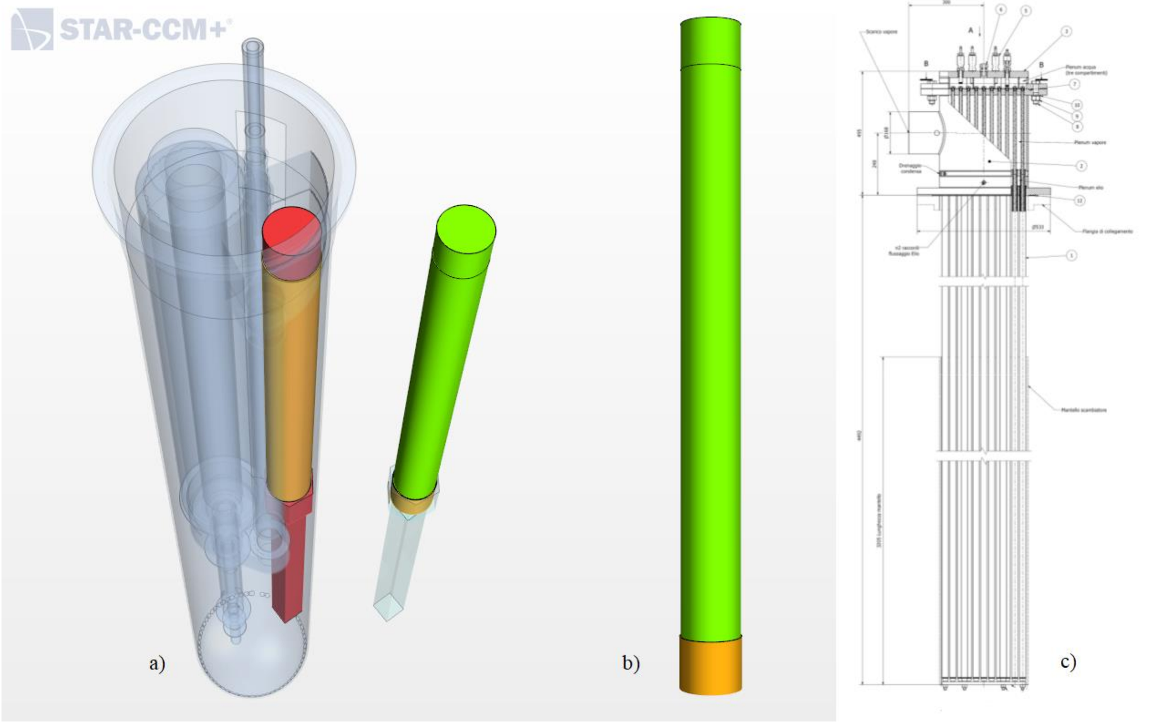

__Figure 17.__ CAD geometry for the ICE HX element. a) general view of the ICE HX in its “storing” position (right), compared to its “mounting” position represented by the HX control volume (red). b) detailed view of the active region of the ICE HX (green) and of its steel skirt (orange). c) technical scheme of the element, courtesy of ENEA, Ref. document [8].

The actual double bayonet tubes have not been included in the physical geometry of the HX due to the excessive computational cost required; the tubes zone has been modeled employing a porous medium approach, similarly to what has been done for the FPS region. The regions highlighted in green in the previous Figure 17 have thus been later set as porous, with particular conditions related to the hexagonal matrix of the tubes (analysed in paragraph 3.3.2). Furthermore, the spacer grid at the bottom of the HX has been modeled by means of an appropriate porous baffle interface.

Later, at simulation level, the parts related to the CIRCE ICE HX have been assigned to their respective regions, and have been meshed while still being outside the S100 main Vessel of the facility ("storing" position). Only then, by employing a region-translating function of STAR-CCM+, they have been moved back in the location of the original HX control volume ("mounting" position) still by means of the HX translation system, thus "filling" the empty HX module with the actual HX elements of the ICE experiment.

This procedure has the advantage to allow a wide possible number of configurations of the facility, simply by copying various times the HX empty control volume, translating it at different x-coordinates along the X axis of the HX translation system, creating the desired geometry configuration, and repeating the abovementioned meshing and back-translating procedure in order to "mount" it.

It is also important to notice that, whenever "mounting" a modular HX configuration from outside the facility into the HX empty control volume, the user needs to manually set all the interfaces between the external boundaries of the translated regions and the contacting "fixed" regions of the facility. This is essentially due to the fact that the STAR-CCM+ software does not recognize such contact interfaces when assigning parts to regions; this happens because before the region-translating operation, the facility regions and the modular HX configurations are obviously not contacting.

Such issue also affects the "un-mounting" operation, since whenever a change in the modular configuration is needed, it is mandatory for the user to delete the abovementioned contact interfaces first, being only later allowed to move back the undesired configuration from the HX "mounting" position to the "storing" position.

In the attempt of speeding up this "mounting" and "unmounting" procedures (for future applications), some macros have been created by recording the operations explained before. Precisely, the "ICE HX mounting" macro simply translates the ICE HX regions into the empty HX control volume and creates the interfaces, while the "unmounting" one deletes all the interfaces and moves the ICE HX back outside the facility in its "storing" position. The user is then able to mount and unmount the CIRCE ICE HX simply by playing the appropriate macro.

The following scheme in Figure 18 summarizes the global modular mounting procedure, which has also been applied for the DHR region.

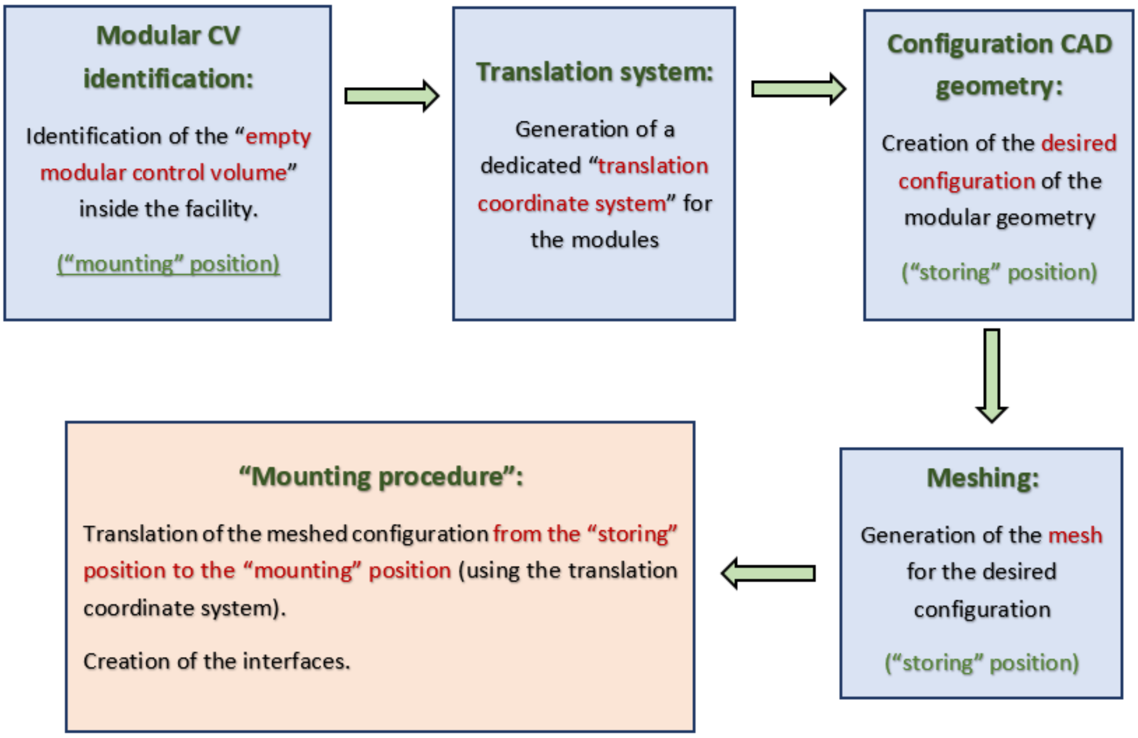

Figure 18. *Schematic summarization of the adopted modular procedure, valid for both the HX and DHR elements.*

1.3.7 DHR region

The DHR is the secondary heat-removal element installed in the facility, with the function of substituting the HX during the simulation of the SCRAM experiment. Its original geometry (ICE) is rather complex, and is essentially composed of a single large double bayonet tube (fed by the forced cooling air from the environment) surrounded by various other elements designed to guide the LBE flux around it, realizing a counter-flow LBE/air heat exchange.

This element of the facility has historically shown irregularities and problems in its behaviour and is thus a staple candidate for studies and/or modifications; for this reason, the same modular approach described for the HX in paragraph 1.3.6 has been applied also for the DHR. In this case, the empty module "DHR control volume" (depicted in Figure 19) includes the whole DHR (excluding the top inlet region of the double bayonet air-fed tube), together with the surrounding LBE and a portion of the gas volume.

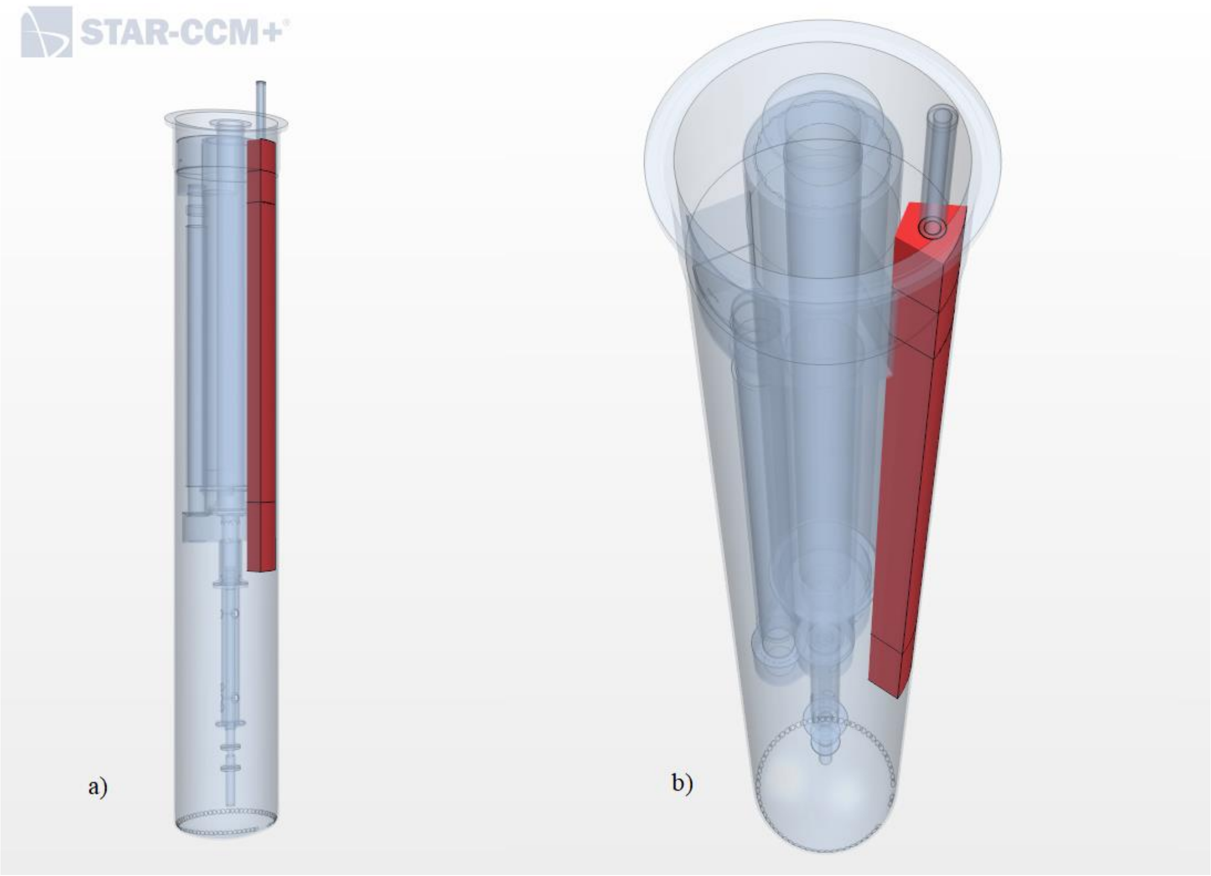

__Figure 19.__ CAD geometry of the DHR control volume. a) general location. b) top detail.

The same steps illustrated in paragraph 1.3.6 have then been followed, namely:

- Creation of a dedicated coordinate system for the DHR modular elements translation (DHR translation system).
- Duplication of the empty DHR control volume body.
- Translation of the DHR control volume copy alongside the X axis of the DHR translation system (x-coordinate=1 m, "storing" position).
- Modification of the DHR control volume copy into the actual original geometry of the CIRCE ICE DHR configuration.

This assembly has then been imported at simulation level, each of its parts have been assigned to an appropriate region, meshed, and then translated back as a whole inside the facility "filling" the empty region defined by the DHR control volume ("mounting" position). In the following Figure 20 the various elements of the ICE DHR are depicted.

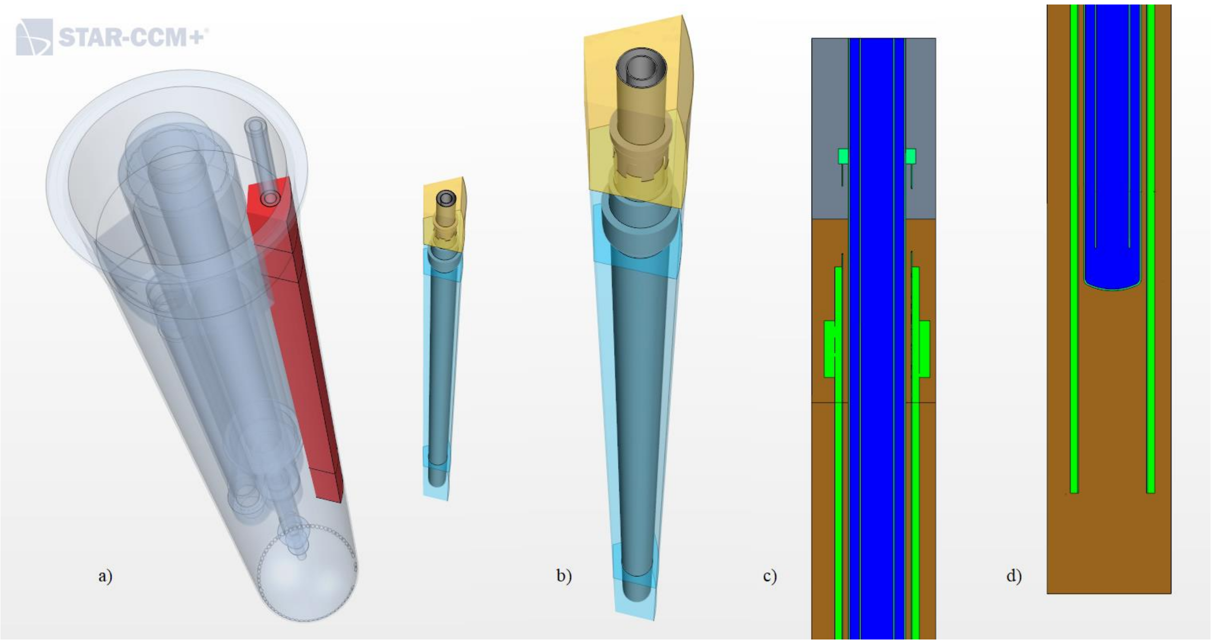

Figure 20. *CAD geometry of the ICE DHR element. a) representation of the ICE DHR configuration (right) alongside its "mounting" position inside the facility (DHR control volume, red). b) ICE DHR detailed view. The regions occupied by the argon gas (yellow) and LBE in the pool (cyan) are highlighted. c)/d) top and bottom sections of the ICE DHR element, with particular focus to the air region (blue) contained in the double bayonet pipe. The steel regions are highlighted in green.*

Due to the elongated shape of the element, a directed-meshing operation has been foreseen as very efficient, and the geometry has been constructed accordingly. This has led to a noticeable increase in the number of bodies generated.

This particular configuration of the DHR (ICE) has previously been affected by strong problems during the past experiments, essentially due to the tendency of solid metallic oxides to deposit near the bottom region of the double bayonet tube (where LBE temperatures tend to drop significantly), thus causing the malfunction of the whole DHR element. in the last experiments (CIRCE HERO) its structure has been greatly simplified by removing the external pipes and leaving exclusively the air-fed double bayonet tube at direct contact with the LBE bulk.

Anyway, in the present model the only DHR configuration that has actually been simulated has been the original CIRCE ICE one. Obviously, the DHR component will be activated only during the transient simulation of the facility, since at regime conditions this element is designed to be inactive.

1.3.8 Dead Volume region

This component of the facility has been engineered in order to allow the terminating ends of the electrified FPS pins (and other various instrumentation cables) to exit the CIRCE main vessel while being insulated from the surrounding LBE bulk (two layers: air + Cerablanket®) and refrigerated by a forced flow of cooling air. The CAD geometry of the element is depicted in the following Figure 21.

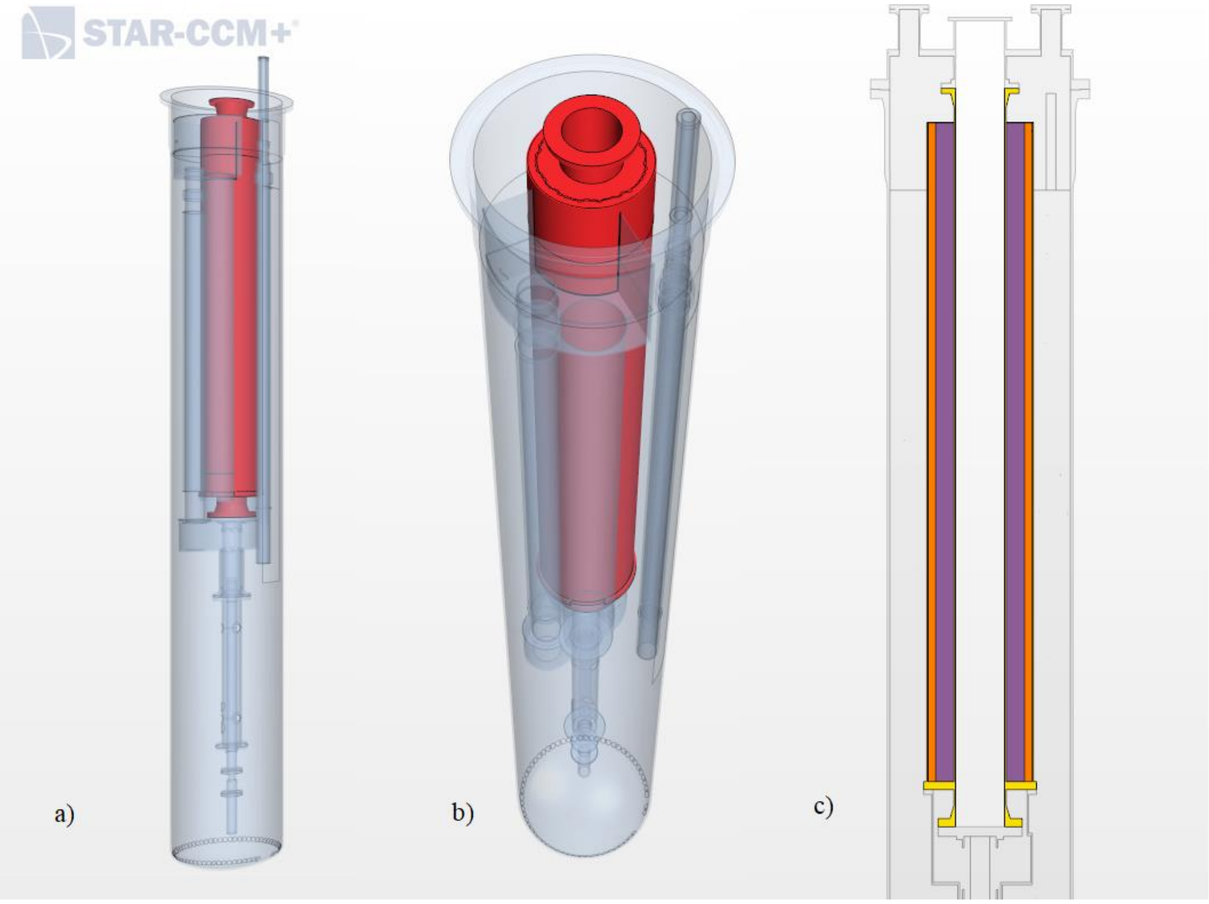

Figure 21. CAD geometry for the dead volume region. a) general location. b) top detail. c)vertical section, highlighting the steel parts (yellow), air (orange) and Cerablanket® (purple) insulating layers.

Most importantly, the insulating layer of air between the steel external layer of the dead volume and the internal Cerablanket® layer has been modeled as solid (thus neglecting the natural convection movements induced by the heat flux from the surrounding LBE bulk, in favour of a much reduced computational cost).

1.3.9 S100 vessel, top cover and LBE bulk

The most external elements of the facility are the S100 vessel and the top cover, which are connected together sealing the whole LBE bulk region and the gas volume (depicted in Figure 22). In the actual facility, the S100 Vessel is isolated from the surrounding environment by means of an insulating layer, which has not been represented in the current model CAD geometry, but its presence has been taken into account considering an appropriate boundary condition on the vessel external surface (illustrated in paragraph 3.3.6).

Figure 22. *CAD geometry for the S100 vessel and top cover regions. The terminating section of the DHR double bayonet tube (inlet/outlet zone) is highlighted in yellow.*

It is important to notice that the terminating regions of the DHR are contacting with the top cover of the facility. These parts of the DHR have been considered fixed, and are thus not included in the DHR modular control volume.

The LBE bulk has then been created (shown in Figure 23) starting from the LBE free surface previously identified in Figure 12 and considering the internal surface of the S100 vessel. All the previously created bodies have then been subtracted with a Boolean operation, and all the resulting surfaces have been appropriately renamed accordingly to the convention explained in paragraph 1.2.

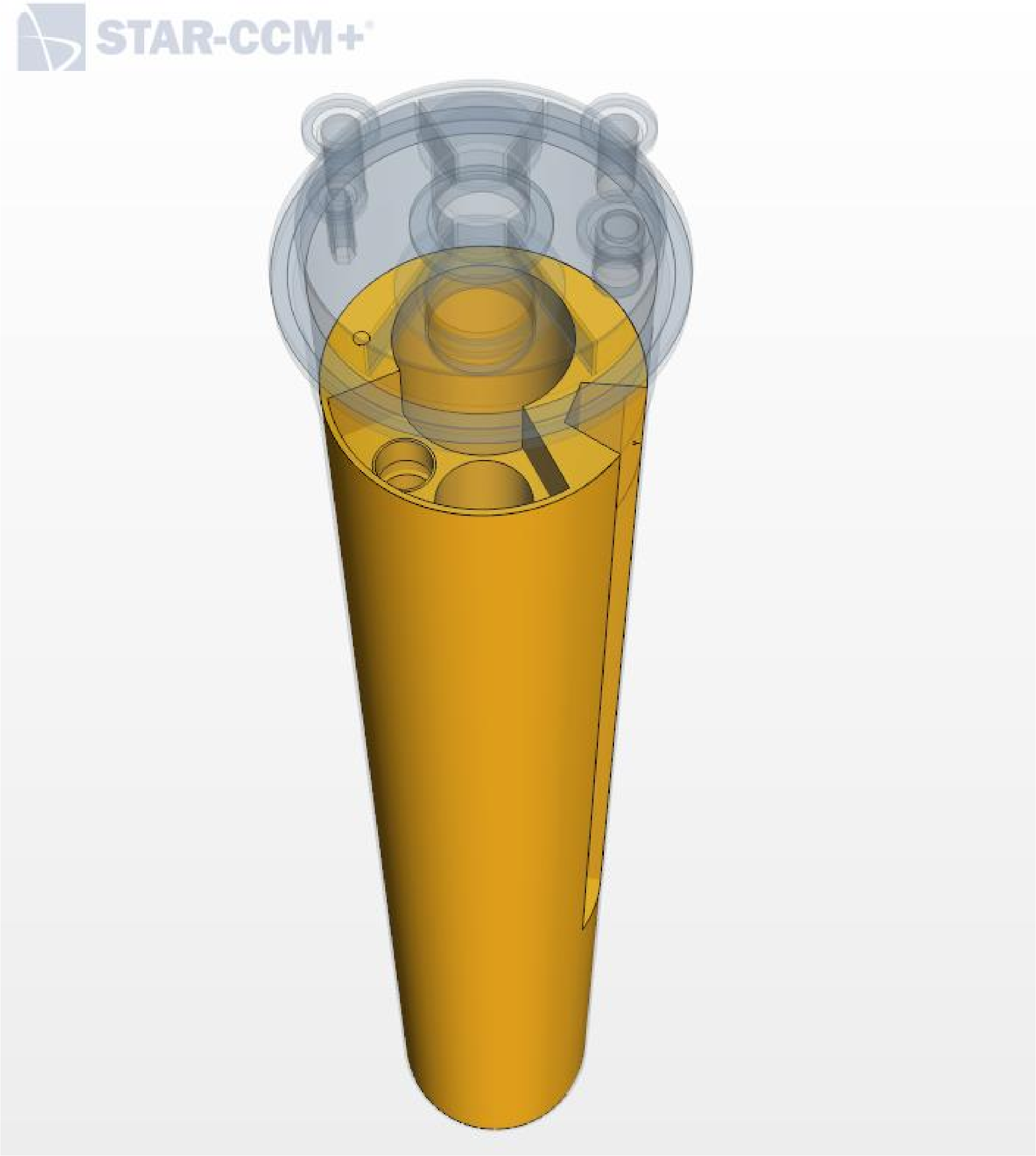

Figure 23. *CAD geometry for the LBE pool (bulk) region. The volume occupied by the LBE in the ICE DHR modular block (cyan region in Figure 20) is especially visible (right).*

In the next chapter all the meshing procedures adopted for the abovementioned CAD bodies will be discussed.

2. Mesh

2.1 A brief introduction to meshing for FVM CFD models.

In the previous chapter, the process of creating the CAD geometry for the CIRCE facility has been thoroughly analysed. Up to this point, such geometry is memorized by means of a very simple triangular tessellation system that completely defines the boundary surfaces of each different CAD body.

In order to be now able to make use of this CAD geometry in an ordinary tri-dimensional FVM (Finite Volume Method) CFD model, it is necessary to introduce a proper volumetric discretization for it, essentially subdividing the CAD bodies into a large number of polyhedral "cells", and thus generating the mesh of the model. The reason behind this is that the FVM modeling approach is based upon the concept of applying a set of discretized differential balance equations (continuity, momentum, energy, etc.) to a certain number of precisely defined and circumscribed control volumes (which are the actual cells of the mesh).

The solution to these equations will later be obtained by means of a series of iterative steps, and will provide as output an approximate value of each thermo-fluid dynamic greatness (temperature, velocity, pressure etc.) averaged within each different cell of the mesh. This, considering the mesh as a whole, translates into an approximate solution of the global velocity, temperature and pressure fields of the flow.

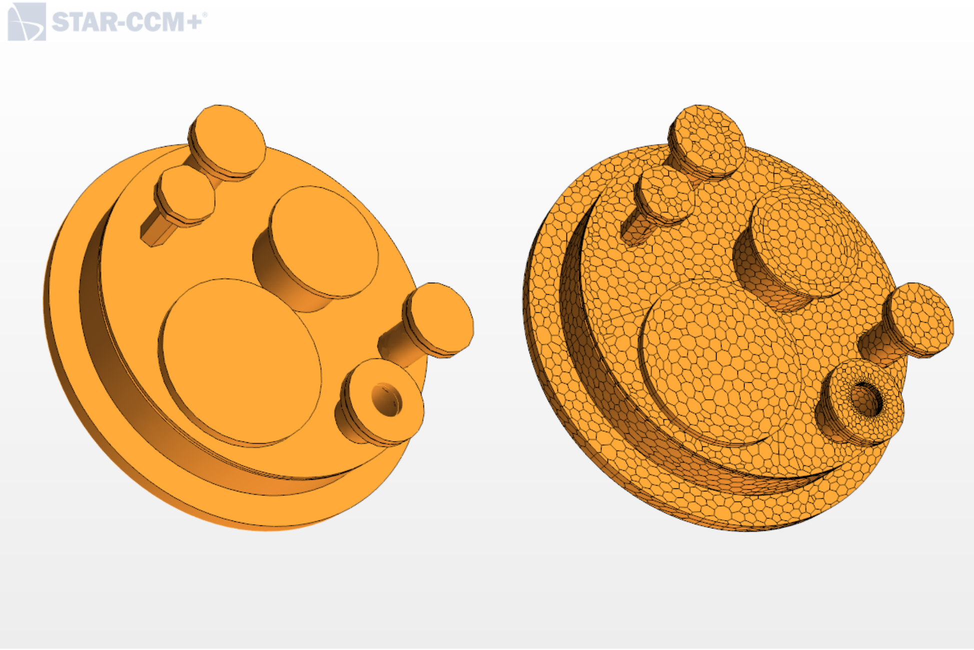

__Figure 24.__ Volumetric mesh discretization for a generic CAD body. In this case the top cover of the S100 vessel and its mesh are represented.

Some important issues related to the mesh generation have to be discussed:

- **Mesh size and global number of cells:**

  this parameter highly influences both the precision of the simulation and its computational cost. In fact, a very fine mesh will produce a much more realistic and precise approximation of the characteristics of the flow; on the other hand, considering that the solvers will have to compute a set of five equations for each cell (per single iteration), it is easily understandable that finer meshes will require much longer calculation times (considering the same computational architecture employed). It is thus very important to take these issues into account while trying to determine an adequate average dimension of the mesh cell, while pursuing an optimal balance between accuracy and computational cost.

- **Mesh quality and shape of the cells:**

  Another factor that plays a very important role in determining the accuracy and stability of the numerical solution is the global quality of the mesh. The most important parameter that influences the general quality of a mesh is the shape of its individual cells: generically speaking, all the cells that present high-skewness angles and very "elongated" aspect ratios have to be avoided, while more "regular" cell shapes have to be preferred. Having bad quality cells can cause instabilities of the solvers and inaccurate solutions, especially in gradient-heavy regions of the flow; the problems become even greater if such cells are not spatially "oriented" along the direction of the flow.

- **Mesh conformity:**

  creating a conformal mesh (each face of a cell is exactly coincident with the face of the neighbouring cell) grants a faster and more stable solution. With this idea, mesh conformity has been pursued wherever possible throughout the whole geometry of the model.

- **Boundary layer mesh:**

  correctly capturing the flow behaviour in proximity of the boundary layers requires some basic modifications of the mesh in those selected locations: typically, a prism layer mesher is employed in order to reach satisfying results.

The next paragraph will explain in detail how these basic principles have been applied to the real CIRCE model.

2.2 Meshing techniques in STAR-CCM+

The mesh generation process in the STAR-CCM+ environment has been conducted following the so-called “parts-based meshing” philosophy, which is the most modern one adopted by the software.

This meshing technique follows the following steps:

1) Importing the geometric bodies created in the CAD editor (discussed in chapter 1) directly into the simulation environment, by creating a geometry “part” for each one of them. These geometry parts retain all the properties (name of the body, names of the surfaces, curves etc.) that have been assigned to the corresponding CAD body during its design phase within the CAD editor.
2) Assigning each part to an appropriate “region” of the model. Each different region can be composed of one or more different geometry parts, all sharing the same physical continuum; it is also fundamental to point out that the “region” level plays a central role during the actual CFD numerical phase of the modeling process, since every single volumetric/boundary condition will be later assigned here.
3) Creating a meshing operation for the chosen part or group of parts, and appropriately setting the various parameters for the desired mesh (choosing the meshers, fixing the base, minimum and maximum cell sizes, setting volumetric and surface controls etc.).

   N.B.: although parts associated with different physical continuums can NOT be assigned to the same region, they can be meshed within the same mesh operation, in order to obtain mesh conformity between different continuums (e.g. solid and liquid regions etc.).
4) Executing the mesh operation and checking the result (with particular attention to possible “bad quality” cells (paragraph 2.1)
5) (Optional) finely adjusting the mesh parameters in order to reach the optimal result, and relaunching the mesh operation.

Once these passages are completed, the mesh for the chosen part is ready to be later employed for the calculation. Furthermore, as previously mentioned in paragraph 2.1, the choice of an appropriate combination of cells shape, size and distribution is crucial for the success of the whole simulation. Generally speaking, every single mesh created for the present CIRCE model has been realized employing one (or a combination) of the following meshers:

- **Polyhedral mesher:**

  very reliable and versatile mesher, used for nearly every “bulk” region of the different parts, due to its capability of realizing regular polyhedral cell structures in almost every situation. Furthermore, meshes created with this mesher guarantee a good degree of stability during the calculation phase (especially if compared with tetrahedral meshes).

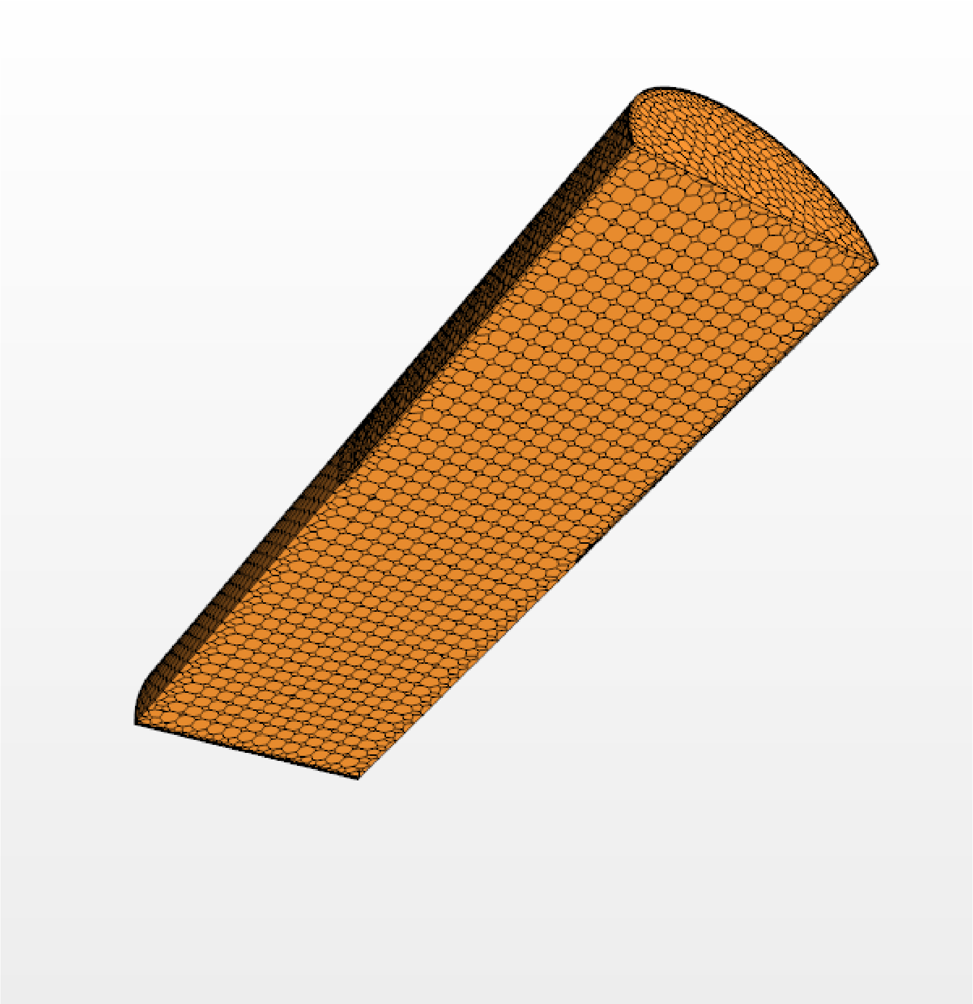

Figure 25. Example of a typical polyhedral volumetric mesh on a simple cylinder (section). The internal cell structure is usually very regular and homogeneous.

- **Thin layer mesher:**

  this particular mesher has the capability of automatically recognising thin layer structures (e.g. thin steel pipes, plates and so on), and creating a very regular prismatic structure that optimizes the computational cost. This mesher has often been used in combination with the polyhedral mesher in many different situations, most notably when meshing together liquid and steel regions within the same operation, in the attempt to obtain the mesh conformity between the two continua. An example of the use of this mesher is depicted in the following Figure 26.

  N.B.: the maximum thin layer thickness can be manually set, together with the total number of thin layers (usually set to 3 for the thin steel regions, in order to better capture the heat fluxes).

- **Prism layer mesher:**

  As mentioned in paragraph 2.1, the modeling of the properties of the flow in proximity of the boundary layers requires adequate meshing strategies. This is the actual function of the prism layer mesher, widely employed in conjunction with the polyhedral mesher whenever meshing fluid regions, in order to solve the boundary layers with much more precision. The mesher pursues this result by constructing a dense structure of prismatic cells in proximity of the boundary surfaces of the chosen part, as can be seen in Figure 26.

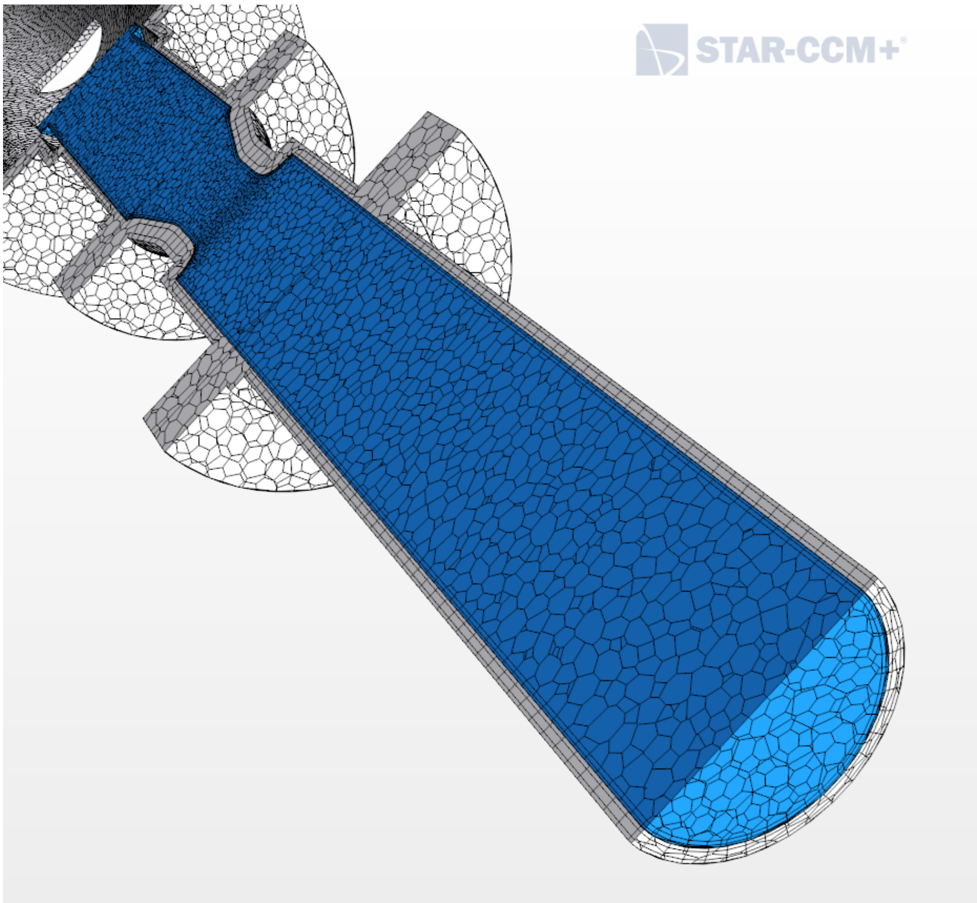

Figure 26. *Example of a combination of different meshers for the suction pipe region of the facility. The steel pipe structures (grey) have been meshed using a thin layer mesher (3 layers), while the use of a prism layer mesher can be observed in the LBE region (blue) proximity of the boundary layers.*

The total number of prism layers and their total thickness can be manually adjusted directly from the controls of the mesh operation.

N.B.: the prism layer mesher, in absence of any other prescription, generates the prismatic cells on every boundary of the part that is being meshed; this effect is typically undesired in all those boundary surfaces that do not physically host a boundary layer flow regime (e.g. fluid-fluid interfaces).

In these situations, the user needs to set up a dedicated surface control with the function of disabling the prism layer mesher wherever not needed.

- **Directed mesher:** This mesher is usually employed when dealing with very elongated and regular prismatic geometry parts. The volume mesh is essentially extruded starting from a certain source surface mesh and reaching a set target surface.
    1) Identify the source surface(s).
    2) Identify the target surface(s).
    3) Choose a surface mesh for the source surface (generally the surface mesh of the contacting part is employed).
    4) Choose the number of extruded volume layers and their volume distribution (constant or “stretched”).
    5) Execute directed mesh operation.

A typical result is depicted in Figure 27 below:

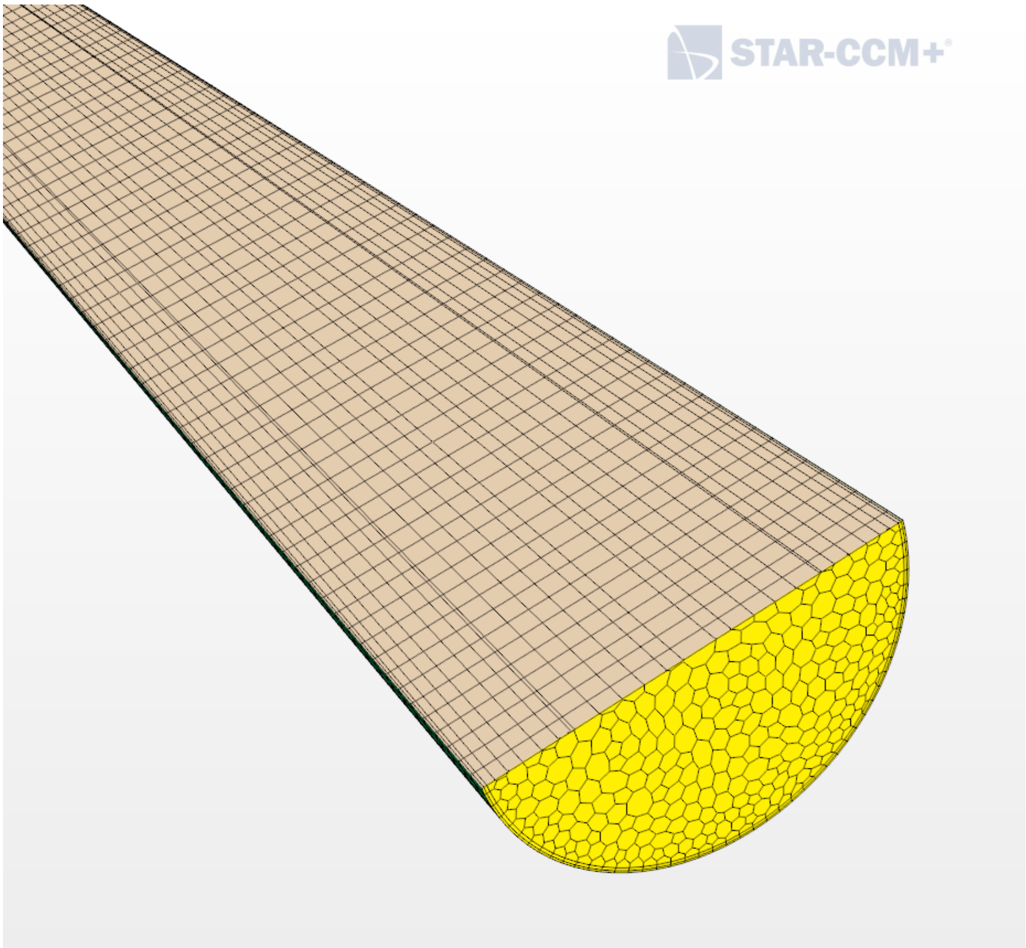

Figure 27. Example of a volumetric mesh generated by means of a directed mesher.

The meshes created with this procedure show their best behaviour in very regular flow conditions, especially when the cells are aligned alongside the main direction of the flow.

These different techniques have been combined in various ways in the attempt to obtain an adequate volume mesh for the whole CIRCE geometry; in the next paragraph, the mesh procedure adopted for each single region of the facility will be briefly illustrated and discussed.

2.3 Analysis of the mesh of the different portions of the CIRCE facility

The aim of these next paragraphs is to briefly highlight some of the most particular details of the mesh of the CIRCE model, giving some examples of how the techniques illustrated in the previous paragraphs 2.1 and 2.2 have been practically applied.

All the procedures hereupon illustrated have been pursued in the attempt to obtain a conformal mesh wherever possible.

2.3.1 Suction pipe region mesh

The mesh for this region is depicted in the following Figure 28.

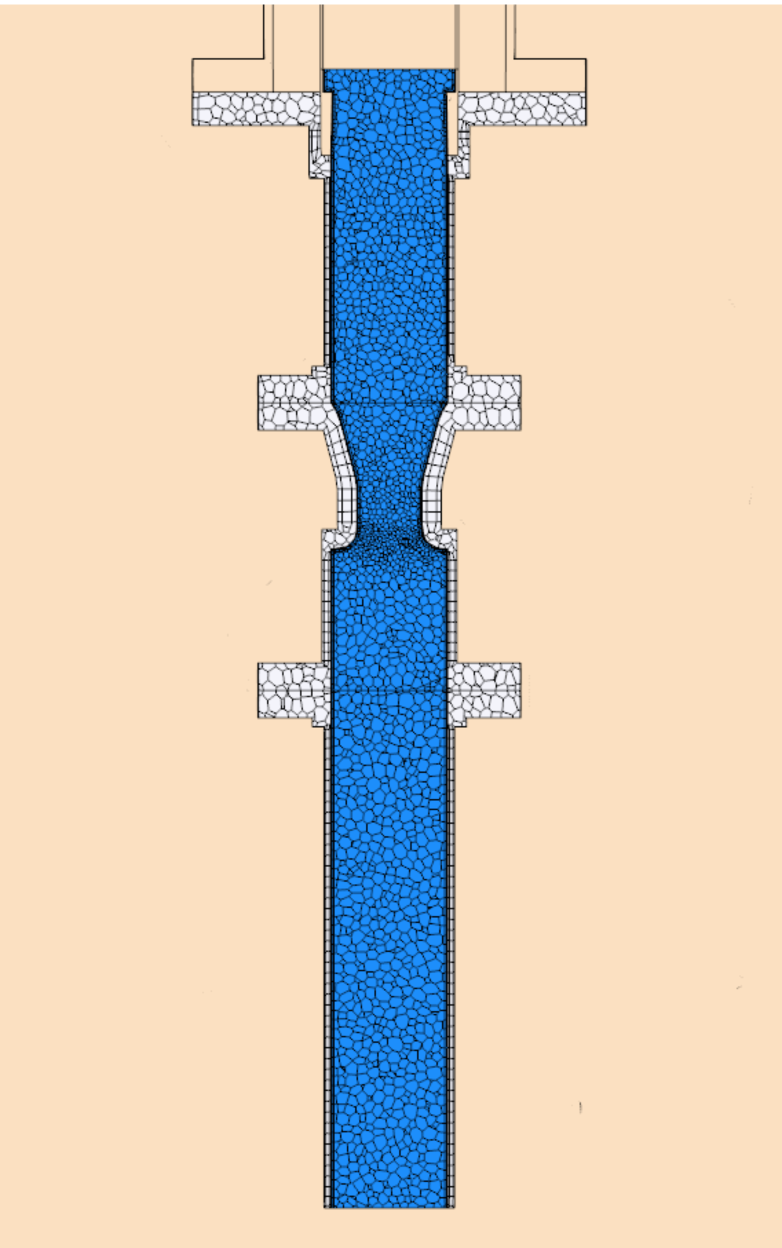

Figure 28. *Volumetric mesh for the suction pipe region.*

Important details:

- Chosen meshers: combination of polyhedral mesher (LBE regions and thick steel parts) in conjunction with a thin layer mesher (thin steel pipes) and a prism layer mesher (LBE boundary layers).
- Slight volumetric mesh refinement for the LBE in proximity of the throat of the Venturi flow meter.

2.3.2 FPS region mesh

Figure 29 illustrates the mesh for the FPS region.

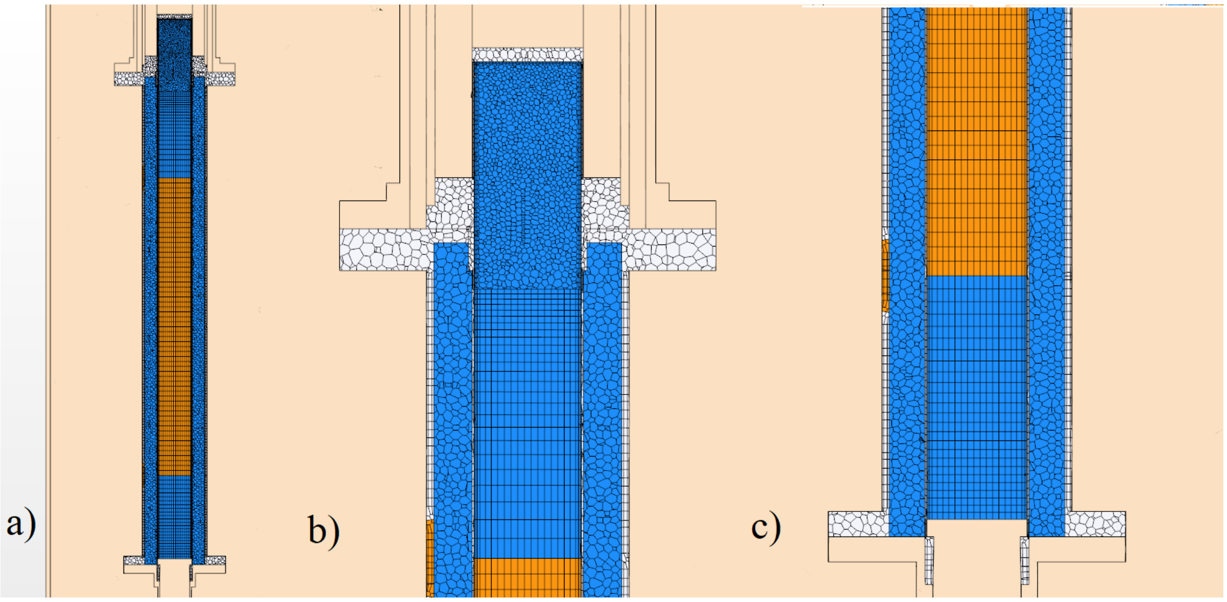

Figure 29. *Volumetric mesh for the FPS region. a) global view. b) detail of the top (outlet) region. c) detail of the bottom (inlet) region. The FPS active region is highlighted in orange.*

Important details:

- The top part of the LBE in the suction pipe has been meshed by employing a polyhedral mesher, thus allowing the use of a directed mesher for the remaining length of the LBE contained in the hexagonal wrapper (region modeled as a porous medium simulating the fluid dynamic resistance imposed by the pins).
- For all the remaining regions, a combination of polyhedral mesher (LBE "thick" bodies), prism layer mesher (boundary layers) and thin layer mesher (thin steel layers) has been employed.
- The mesh of the LBE recirculation region (around the FPS hexagonal wrapper) has been selectively made coarser in order to optimize the calculation efficiency.

2.3.3 Release pipe and conveyor region mesh

Figure 30 shows the meshes for this region.

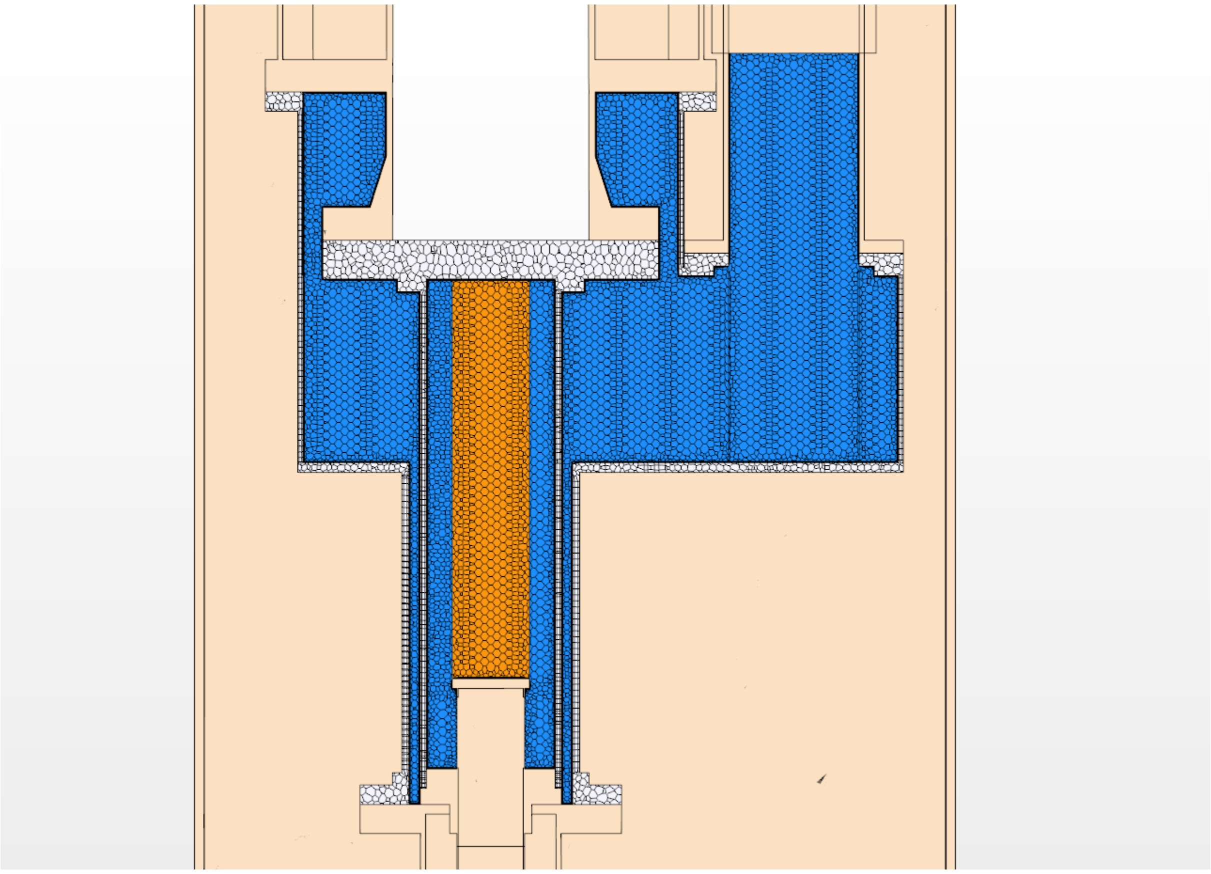

Figure 30. *Volumetric mesh for the conveyor region.*

- Chosen meshers: polyhedral mesher (LBE thick regions), prism layer mesher (boundary layers) and thin layer mesher (thin steel regions).
- The orange region highlighted in orange in the previous Figure 30 is meant to simulate the terminating part of the fuel pins, and has been later set as porous.

2.3.4 Riser region mesh

The mesh for the various components of the riser is portrayed here in Figure 31.

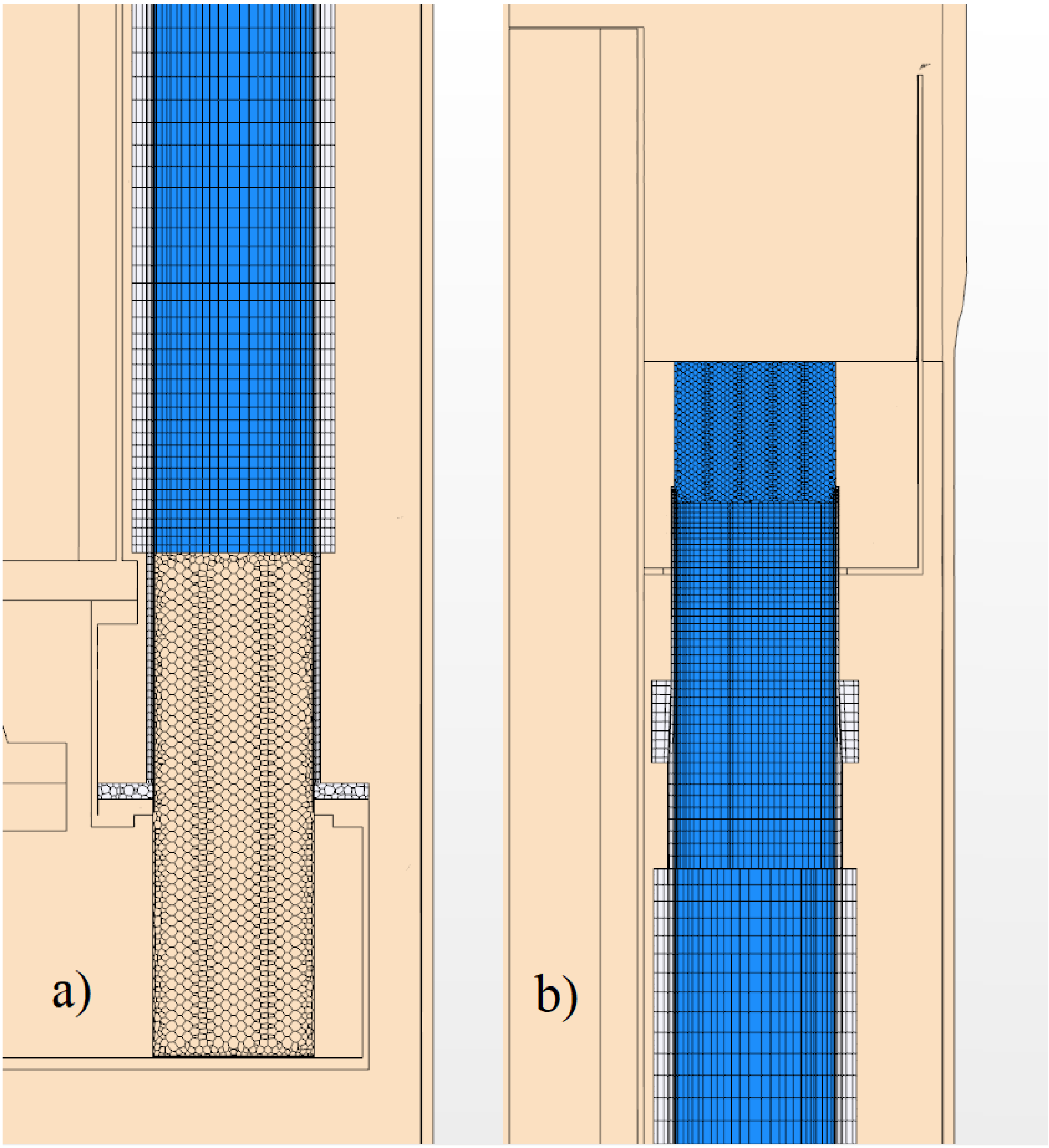

Figure 31. *Volumetric mesh for the riser region. a) bottom detail. b) top detail.*

The mesh for this region has been generated mainly by means of a directed mesher, due to the elongated shape of the element.

2.3.5 Separator region mesh

The mesh for this region is illustrated in the following Figure 32.

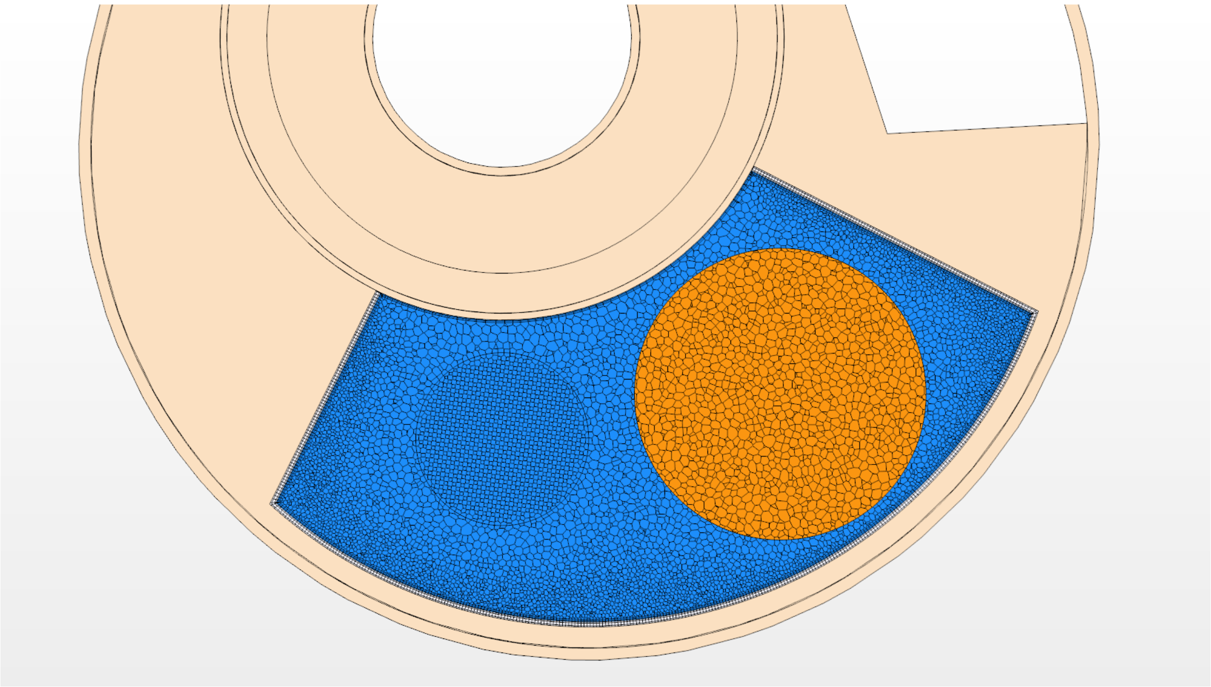

Figure 32. *Volumetric mesh for the separator region. The inlet section of the HX active region is highlighted in orange.*

Important details:

- Chosen meshers: polyhedral mesher (LBE thick regions), prism layer mesher (boundary layers) and thin layer mesher (thin steel regions)
- The separator element, the whole LBE contained in it and the "separator leakage ring" have all been meshed within the same operation, in order to ensure the desired mesh conformity.
- The upper part of the separator steel container (the portion extending above the LBE free surface and contacting with the Gas volume) presents a coarser mesh. This structure has been imposed by means of a dedicated volumetric control in order to optimize the calculation efficiency, since that portion of the separator is not particularly relevant for the simulation.

2.3.6 ICE HX region mesh

As can be noticed from the previous Figure 32, the inlet LBE region of the HX (where the double bayonet tubes should be located) is separated from the LBE contained in the separator; this is due to the modular approach adopted (previously described in paragraph 1.3.6). In fact, the mesh for the HX has been previously created from its "storing" position outside the facility, and then moved back to occupy the "empty modular" HX control volume. The mesh for the ICE HX component is portrayed in the following Figure 33.

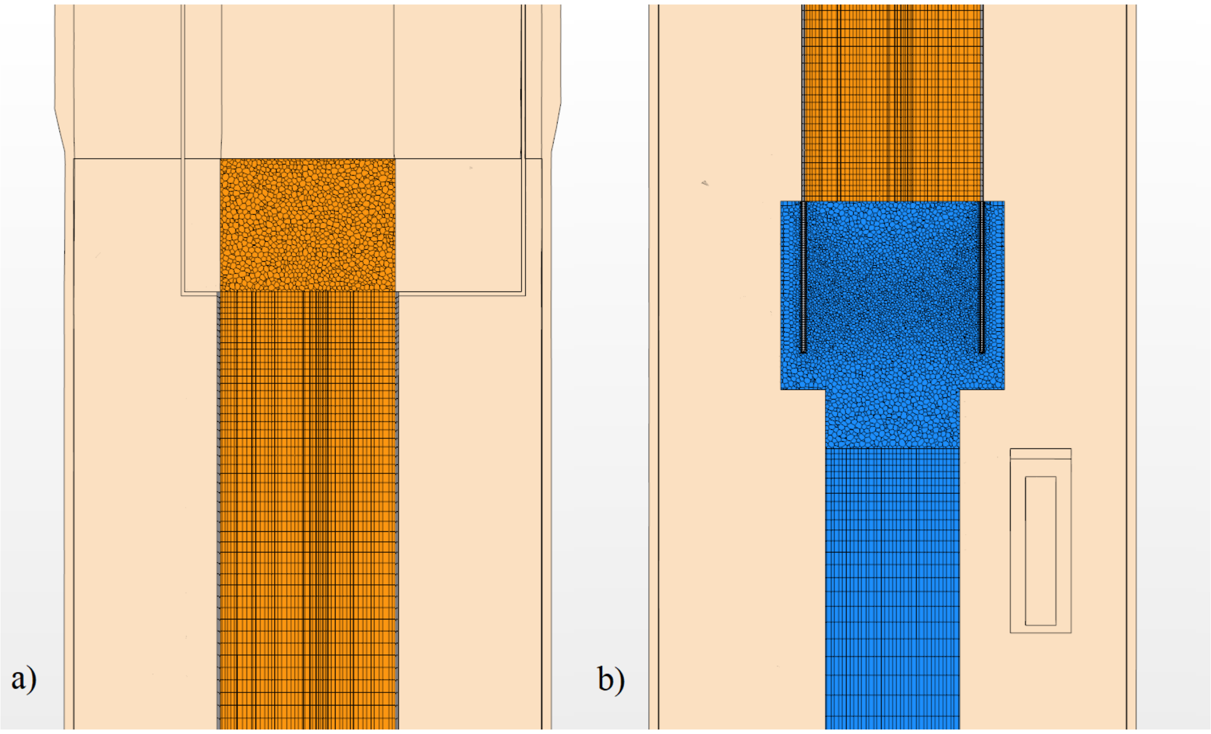

Figure 33. *Volumetric mesh for the ICE HX region. a) top detail. b) bottom detail, The HX active region (porous) has been highlighted in orange.*

The upper region of the LBE contained in the HX (contacting with the LBE in the separator) has been meshed employing a polyhedral mesher, using parameters similar to those used to mesh the LBE contained in the separator (in order to ensure some cell size homogeneity between the two meshes). The intermediate region (where the real 91 double bayonet tubes should have been located) has been meshed by means of a directed mesher, which simply extrudes downwards the contacting surface mesh of the upper region of the LBE in the HX.

2.3.7 Dead volume region mesh

The next Figure 34 illustrates the mesh for the Dead volume element of the facility.

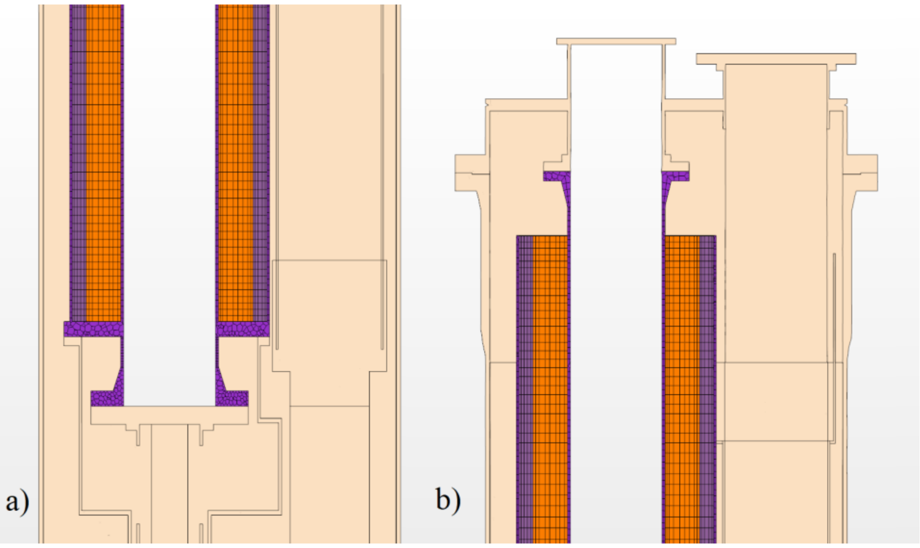

Figure 34. *Volumetric mesh for the dead volume region. a) bottom detail. b) top detail.*

Due to the rather extended shape of the component, an approach based on the usual combination of polyhedral/thin layer meshers (for the bottom and top parts) and directed mesher (for the long intermediate regions) has been pursued.

In the previous Figure 34 the meshes for the different layers of steel, air and Cerablanket® insulation are visible.

2.3.8 ICE DHR region mesh

The ICE DHR has been modeled following the same modular approach adopted for the HX, previously discussed in paragraph 1.3.7; due to this reason, its mesh has been created "outside" the facility, in the DHR "storing" position. Later, the DHR regions have been translated in order to occupy the empty modular "DHR control volume" inside the facility.

Figure 35 shows the meshes for the ICE DHR configuration.

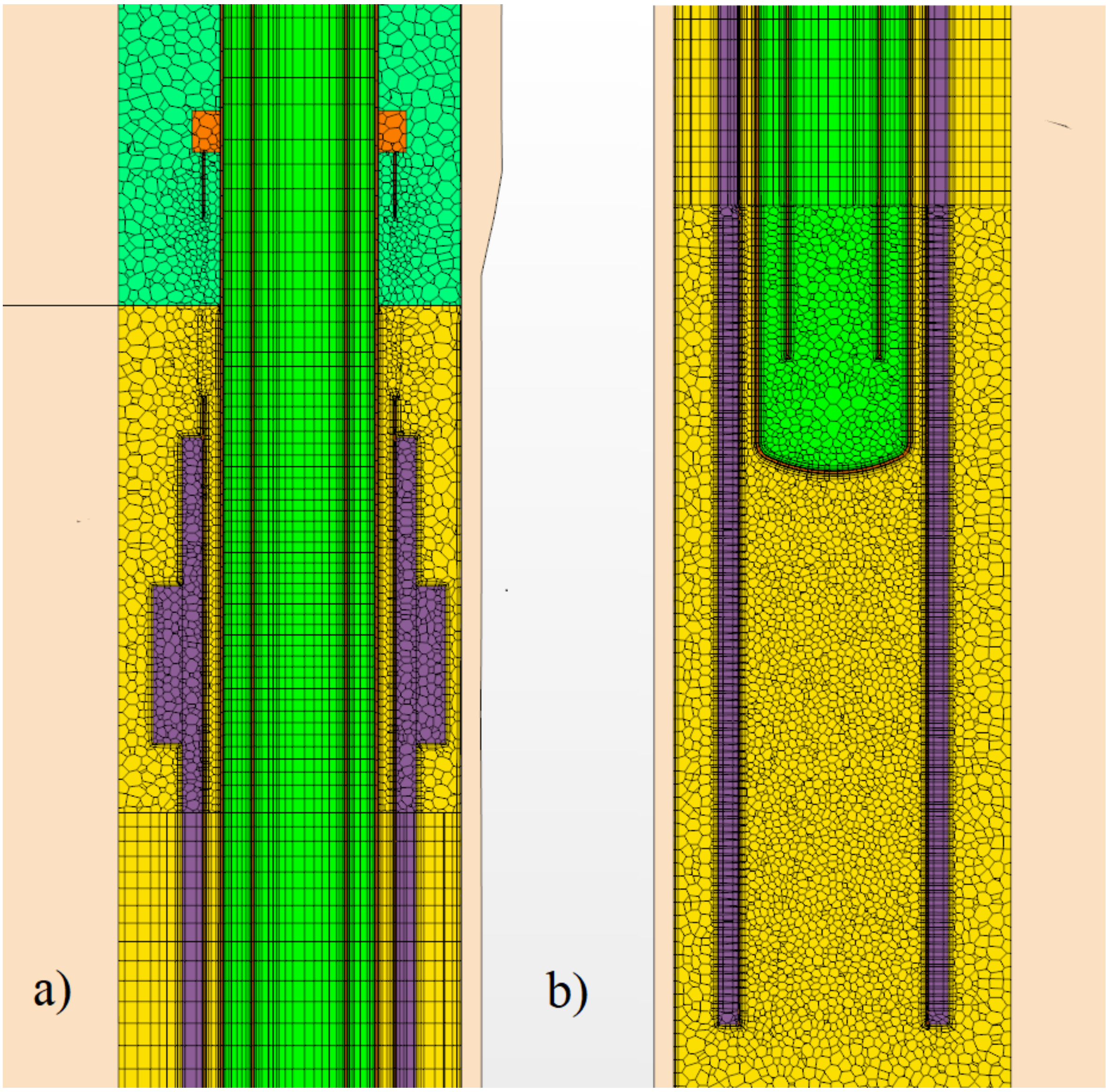

Figure 35. *Volumetric mesh for the ICE DHR region. a) top detail. b) bottom detail.*

As can be noticed, the geometry of the inlet region of the ICE DHR is very complex and has thus required a rather fine polyhedral mesh. The bottom part of the element has been meshed in the same fashion, while the intermediate regions have been processed by a directed mesher.

2.3.9 LBE bulk and Gas volume

The mesh for the LBE bulk region has been realized only by means of the polyhedral mesher, due to the strong irregularity of its shape. Furthermore, some volumetric controls have been defined in order to refine the mesh in selected zones of the bulk, especially where the accuracy of the simulation would be of primary importance, such as the LBE region between the DHR and the HX shell, due to the presence of the main LBE bulk thermocouple lines (discussed in paragraph 3.4.2.1).

The result is depicted in the following Figure 36.

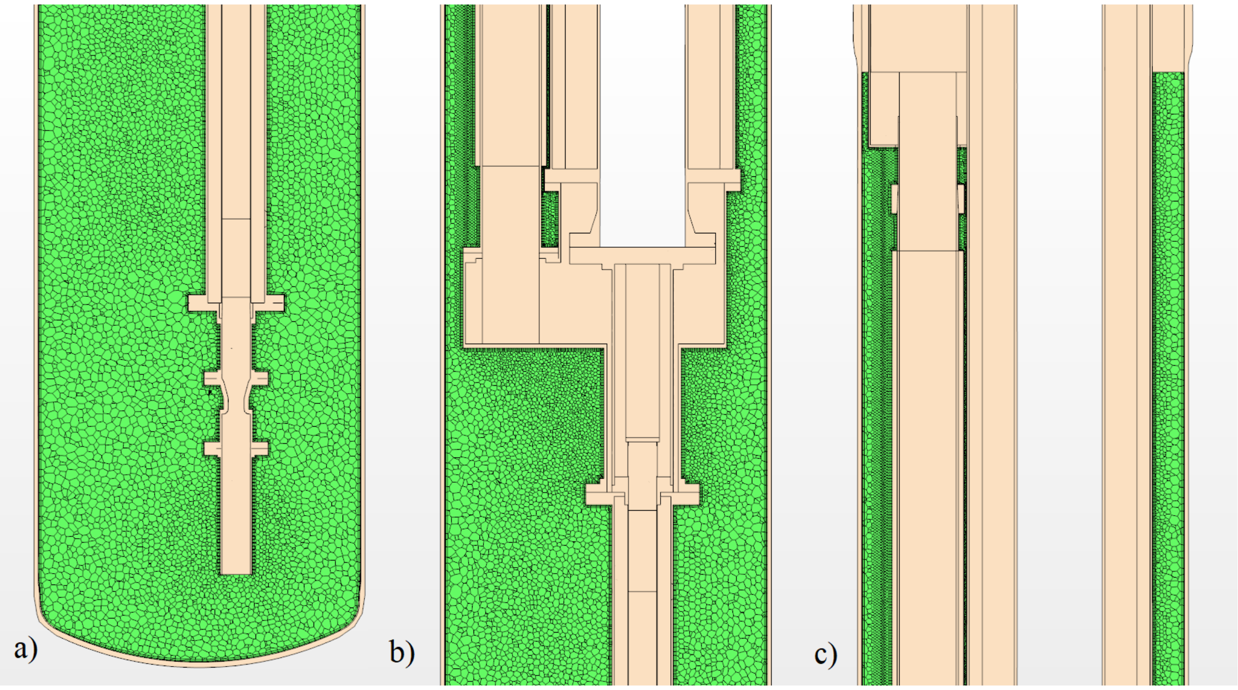

Figure 36. Volumetric mesh for the LBE bulk region. a) bottom detail. b) intermediate/conveyor detail. c) top detail.

The gas volume above the LBE free surface has been meshed in the exact same way, yet choosing a very large base cell size, since the accurate modeling of the argon in this region is not a primary objective of this present model. Figure 37 below shows the mesh for this element.

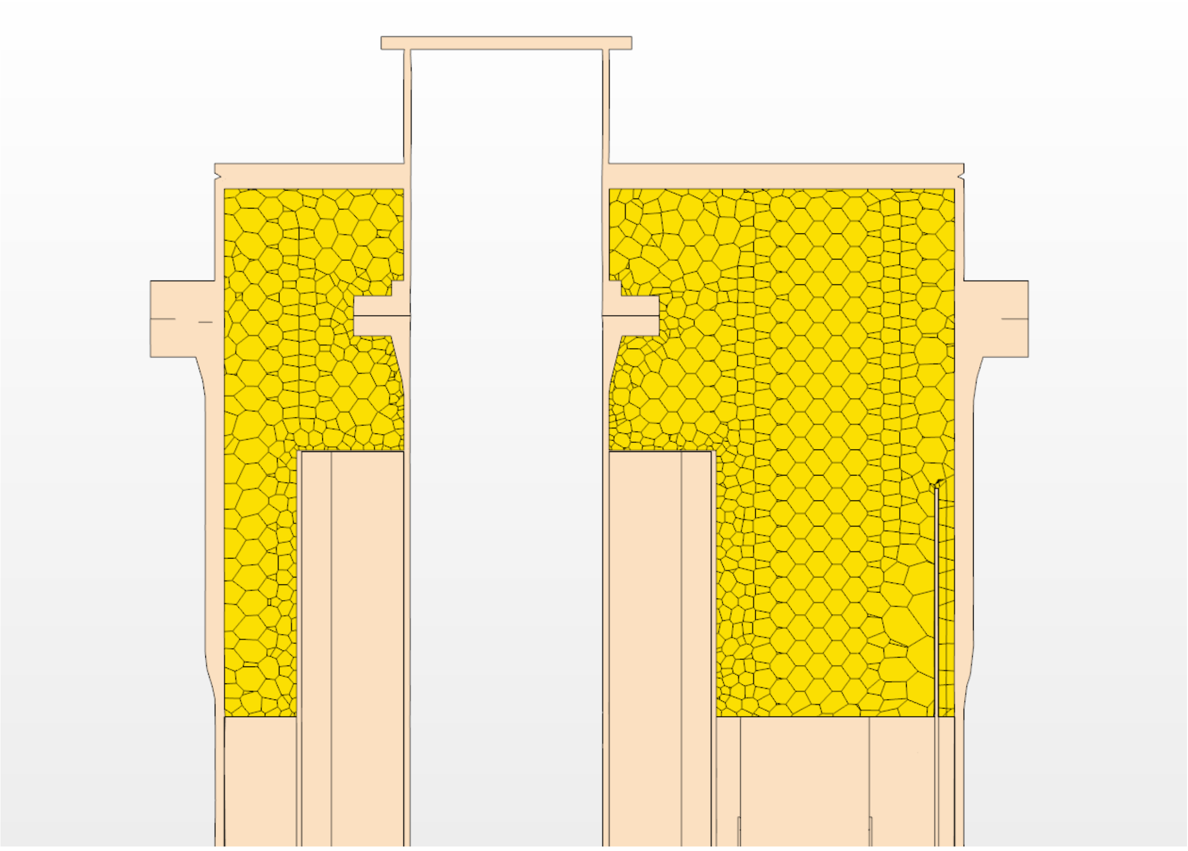

Figure 37. Volumetric mesh for the gas volume region.

The resulting volume mesh for the whole CIRCE facility (considering all regions) is characterised by a total number of cells $\sim 6{,}58 \cdot 10^6$. The next chapter will explain how these meshes have been employed in order to compute the steady state simulation for the CIRCE ICE experiment.

3. Stationary model of the CIRCE facility

3.1 Introduction

In the previous chapters 1 and 2 all the various issues related to the generation of a versatile CAD geometry for the CIRCE facility (based on the official ENEA data) and its meshing procedure have been discussed. The main aim of this chapter is to analyse in depth how these objects have later been employed in order to create a reliable steady state model, capable of portraying the regime working condition of the facility with a satisfying degree of accuracy. Such model must thus be adequately validated by the official ENEA experimental results, and should also be versatile enough to allow present and future users to perform a wide range of analyses and reports on the behaviour of the facility, highlighting possible modifications and enhancements to its real structure.

In the following paragraphs all the technical details of the generation of this steady state model will be explained.

3.1.1 The CIRCE ICE steady state model: reference experiment.

Before delving deeper into the details of the chosen modeling approach for the CIRCE facility, it is now fundamental to clearly assess which one of the various CIRCE experiments has been taken as a reference for the present CFD simulations; this is even more important considering that, through the years, the CIRCE facility has undergone a certain number of changes and enhancements that have marked noticeable differences between each experiment.

In the introductive paragraph, the two most recent standard configurations of the facility have been described, namely:

- **CIRCE ICE** (91 double-bayonet tubes HX, "original" DHR design)
- **CIRCE HERO** (7 double bayonet tubes HX, "simplified" DHR design)

This particular model will be based on the CIRCE ICE experiment configuration, due to the following reasons:

- **Previous HX study:**

  The heat exchanger of the CIRCE ICE primary loop has been the central object of study of a previous curricular internship; its regime condition has been thoroughly studied by creating a large number of steady state CFD simulations of growing complexity, in the attempt of highlighting the most important criticalities of the element (for a detailed analysis see document [5]) while a short recap can be found in paragraph 3.3.2.1). Furthermore, all the previous CIRCE ICE models have been created without such deep knowledge of the behaviour of the HX element, whose inappropriate modeling has often been suspected of being responsible for the low adherence between the CIRCE CFD simulations and the experimental results.

It thus seemed very useful to “bridge” the two different studies, and transfer the knowledge gained during the curricular internship into the bigger framework of the modeling of the entire CIRCE facility. This idea has been accomplished by adequately refining the HX portion of the CIRCE model accordingly to the results of the previous HX study.

- **Experimental data availability:**

  the amount of data available for the CIRCE ICE configuration is significantly larger than the one for CIRCE HERO, essentially due to the very recent establishment of the last one. This allowed for a more solid and data-supported approach to the modeling process.

After having chosen the CIRCE ICE configuration, the relative ICE HX and ICE DHR elements have been “mounted” into their correct positions by following the modular procedure illustrated in paragraph 1.3.6. This has been done by translating their meshes (at region level) directly from the “storing” location of each element (outside the facility along the dedicated translation axis) into the internal respective HX and DHR “empty control volumes”.
Once clarified which element configuration will be the object of the current steady state model, it is compulsory to define which moment of the real experiment will be simulated.
As previously explained in the introductive paragraph, the structure of the experiments conducted in the CIRCE facility is essentially composed of two main sections briefly summarized again in the points below:

1) **Regime condition experiment:**

   after a starting transient (~1 h), the facility reaches its regime condition: the FPS is supplying 800kW of thermal power to the LBE while the HX subtracts the same amount of power, theoretically realizing a stable steady-state loop (in the real experiment some slight time-dependant fluctuations of the parameters are inevitable, yet negligible). The riser argon pump is active and realizes a forced LBE mass flow rate through the loop (around 65 kg/s).

2) **“SCRAM experiment” (PLOHS+LOF transient):**

   After maintaining the regime condition for some hours (depending on the chosen test), the SCRAM experiment begins, aiming to simulate a typical nuclear reactor accident. In order to do so, the heat power supplied by the FPS is reduced from 800 kW to 30 kW, and both the riser gas lift system and the HX are disabled. On the other hand, the DHR is activated (air mass flow rate circulating) and removes a total heat power of around 40 kW.

Figure 38 illustrates the time-depending behaviour of the different elements of the facility throughout the whole duration of the experiment; it is possible to notice exactly how the various components are activated or deactivated in order to follow the previously illustrated steps. All data hereupon displayed refers to the CIRCE ICE “Test 1” reported in [6], whose main characteristics are summarized in the following Table 1.

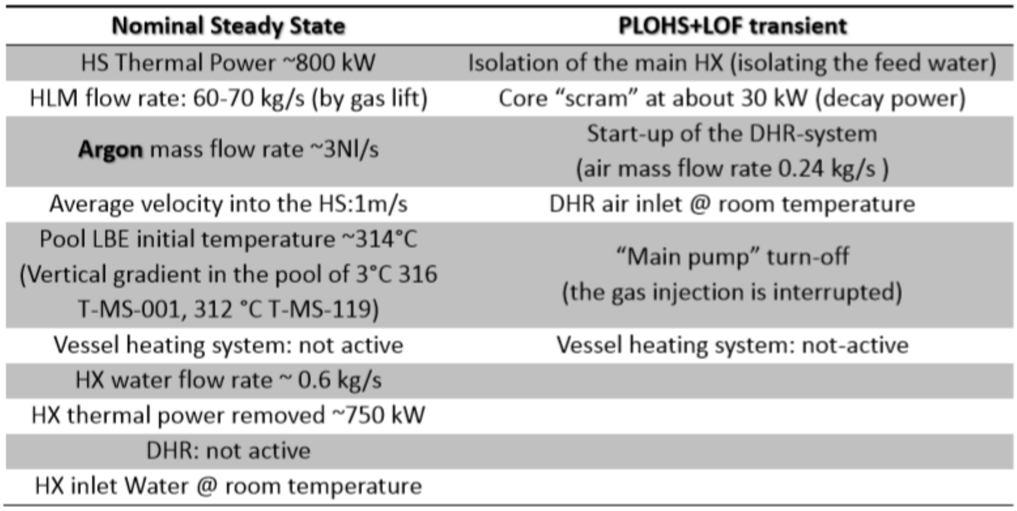

Nominal Steady State	PLOHS+LOF transient
HS Thermal Power ~800 kW	Isolation of the main HX (isolating the feed water)
HLM flow rate: 60-70 kg/s (by gas lift)	Core "scram" at about 30 kW (decay power)
Argon mass flow rate ~3Nl/s	Start-up of the DHR-system (air mass flow rate 0.24 kg/s)
Average velocity into the HS:1m/s	DHR air inlet @ room temperature
Pool LBE initial temperature ~314°C (Vertical gradient in the pool of 3°C 316 T-MS-001, 312 °C T-MS-119)	"Main pump" turn-off (the gas injection is interrupted)
Vessel heating system: not active	Vessel heating system: not-active
HX water flow rate ~ 0.6 kg/s	
HX thermal power removed ~750 kW	
DHR: not active	
HX inlet Water @ room temperature	

Table 1. *Main characteristics of the CIRCE ICE "Test 1" experiment, accordingly to ref. document [6] (p.8). Courtesy of ENEA.*

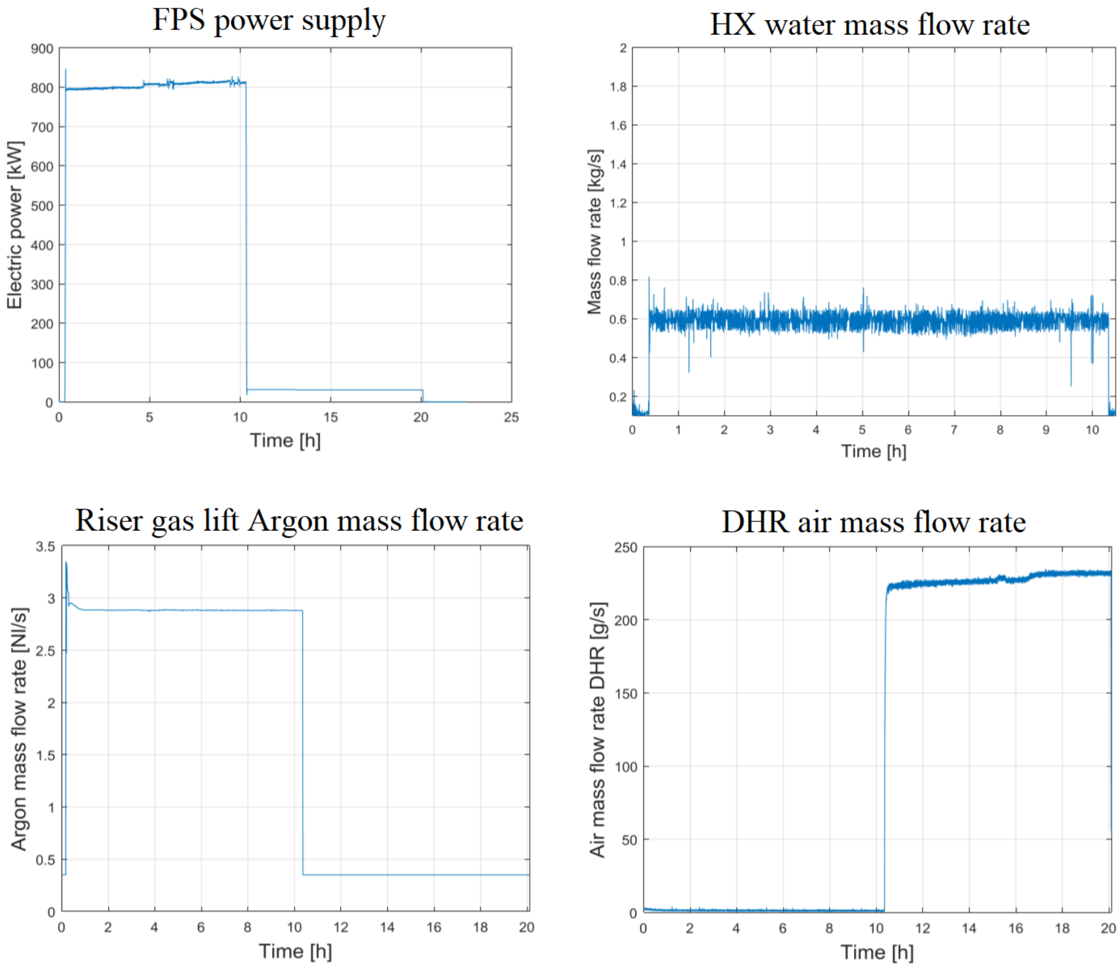

Figure 38. *Plots illustrating the behaviour of the various elements of the CIRCE facility throughout the whole duration of the CIRCE ICE "Test 1" experiment, reported in ref. document [6] (pp. 9-13). Courtesy of ENEA.*

The CFD steady state model that will be described in the next paragraphs aims to portray the "proper" stable regime condition of the CIRCE ICE experiment ("Test 1" in ref. document [6]), which begins right after the starting transient (time around ~1 h) and ends after around ~5 h. The SCRAM phase is initiated only after ~10 h from the beginning of the experiment.

This steady state result will then be processed and used as the initial condition for the transient simulation of the SCRAM phase of the same experiment (discussed in the next chapter 4).

3.2 <u>The regions of the CIRCE ICE model.</u>

3.2.1 Differences between geometry "parts" and "regions" of the model.

In the previous chapter 2, the techniques employed to generate the mesh for the various parts of the geometry of the CIRCE facility have been discussed. In order to be able to generate such meshes, the STAR-CCM+ software requires the assignment of the CAD geometry parts to the different "regions" of the model (parts-based meshing).

It has although not yet been completely clarified which is the concrete difference between the "part" level and the "region" level of the various components of the model. Essentially, a "part" object in STAR-CCM+ is simply a CAD element that has been imported from the CAD editor into the simulation environment, but is not yet representative of the actual physical nature of the element itself, nor of its modeling. In fact, the software simply treats the "part" object as a geometrical representation of some element of the model; for instance, for the STAR-CCM+ software there is no actual difference between a solid and fluid geometry "part" object.

This last assertion changes when a geometry "part", or more than one typically, are assigned to a certain "region" of the model.

A "region" object constitutes a homogeneous continuum within the simulation environment, being not only simply representative of the geometrical shape of an element, but portraying a wide series of characteristics of such element that are constant within the region itself, namely:

1. **Physical continuum properties:**

   all parts within a definite region of the model must share the same physical continuum characteristics. This essentially means that every single part associated to a certain region will be modeled following a unique set of material properties specified for the said region. In other words, this translates into the impossibility of defining a region of the model that is "constituted" of a multiple number of materials.

   This physical continuum can be defined upstream the assignment of the parts to a region, as described in the following point 2.

2. **Selected models and equations:**

   In order to define a physical continuum in the STAR-CCM+ software, the user needs not only to set the physical properties associated to it, but most importantly to define the numerical models meant to be used to perform the calculation. This translates into choosing the desired approaches to simulate the physical behaviour of a certain region of the model (e.g. segregated flow vs. coupled flow, k-epsilon turbulence vs. k-omega turbulence, energy equations etc.). Since there can only be a single physical continuum associated to a determinate region of the model, this means that the solvers will inevitably apply the same identical set of equations to all the part meshes contained in the same region. Furthermore, all the boundary conditions of the model must be specified only at "region" level.

In the next paragraph 3.2.2 the various regions of the model will be briefly depicted, summarizing their general characteristics.

3.2.2 The regions of the CIRCE ICE model: general characteristics and physical continuums

The regions of these models can be subdivided into the following categories, based on the nature of their physical continuum:

- **LBE regions** – (liquid state)
- **AISI304 Steel regions and Insulation layers** – (solid state)
- **Argon gas volume region** – (in gaseous state in the real facility, but here modeled as solid due to calculation efficiency reasons)
- **Proper gas regions** – (gaseous state)

Each single category of regions has been modeled following a different approach, mainly due to the very diverse characteristics of the materials constituting each one of them. These characteristics will now be analysed, and a basic description of the employed models will also be provided, together with a brief list of all the regions falling into each different category.

3.2.2.1 LBE regions and properties

These regions of the model are meant to simulate the liquid LBE flowing in the real CIRCE facility.

The large majority of these regions are non-porous, while some of them have been set as porous in order to simulate the presence of resistance-inducing elements (e.g. pipes in the HX and pins in the FPS). Apart from this particular difference, all these regions have been modeled in the same way, and obviously share the same material properties, illustrated in Table 2, accordingly to [2].

Property	SI unit	Correlation	Temp. range (K)	Estimated error
Melting point	K	$T_M = 398$	n/a	1
Latent heat of melting	kJ/kg	$L = 38.6$	n/a	0.3
Density	kg/m^3	$\rho = 11065 - 1.293T$	$T_M - 1300$	0.8%
Heat capacity at constant pressure	J/kg.K	$c_p = 164.8 - 3.94\times10^{-2}T + 1.25\times10^{-5}T^2 - 4.56\times10^{5}T^{-2}$	$T_M - 1100$	7%
Dynamic viscosity	Pa.s	$\mu = 4.94\times10^{-4}\exp(754.1/T)$	$T_M - 1200$	8%
Thermal conductivity	W/m.K	$k = 3.284 + 1.617\times10^{-2}T - 2.305\times10^{-6}T^2$	$T_M - 1200$	15%

***Table 2.** Temperature-dependent modeled expressions for the various properties of LBE, accordingly to [2].*

As can be noticed from the previous tables, all the most important properties of LBE have been modeled as temperature-dependent functions; these temperature dependencies are actually not negligible at all, and have an impressive impact on the general behaviour of the LBE flow through the facility. Most importantly, the density shows a rather strong decrease with temperature ($\rho = \rho(T)$). Considering that in the momentum equation the $\rho\vec{g}$ source term is present (where $\vec{g} = [0, 0, -9.81\ m/s^2]$ is the gravity acceleration vector) , this leads to a very strong coupling between the temperature and velocity fields of the flow (via the density field), causing really important buoyancy effects. In some situations, especially where the temperature gradients become relevant, these effects are capable of almost totally dictating the configuration of the velocity field.

Another important issue that needs to be highlighted about LBE is its tendency to solidify under certain circumstances. As can be seen in Table 2, the freezing point of LBE is relatively low ($\cong$125°C), but can sometimes be reached, most frequently when the fluid tends to recirculate at very low velocities in "cold" zones of the domain (e.g. interstices in proximity of the coldest regions of the heat exchangers). This effect has been neglected in this present model, but is currently a fundamental object of study of various other models.

Furthermore, the LBE is characterized by a very low Prandtl number, meaning that it tends to be much more sensible to the rate of thermal diffusion rather than to the momentum one in proximity of the boundaries of the domain (thermal boundary layer thicker than the viscous one).

In the attempt of simulating the behaviour of LBE while respecting all the abovementioned properties, a dedicated physical continuum "LBE" has been created within the STAR-CCM+ simulation environment, and the following models have been selected and associated to it:

- Steady, 3D model
- Liquid (polynomial density)
- RANS k-ε turbulence model
- Coupled flow
- Coupled energy
- Gravity

The material properties for this continuum have been set in accordance with Table 2. In conclusion, Figure 39 briefly displays the LBE regions of the simulation (the porous ones are also shown).

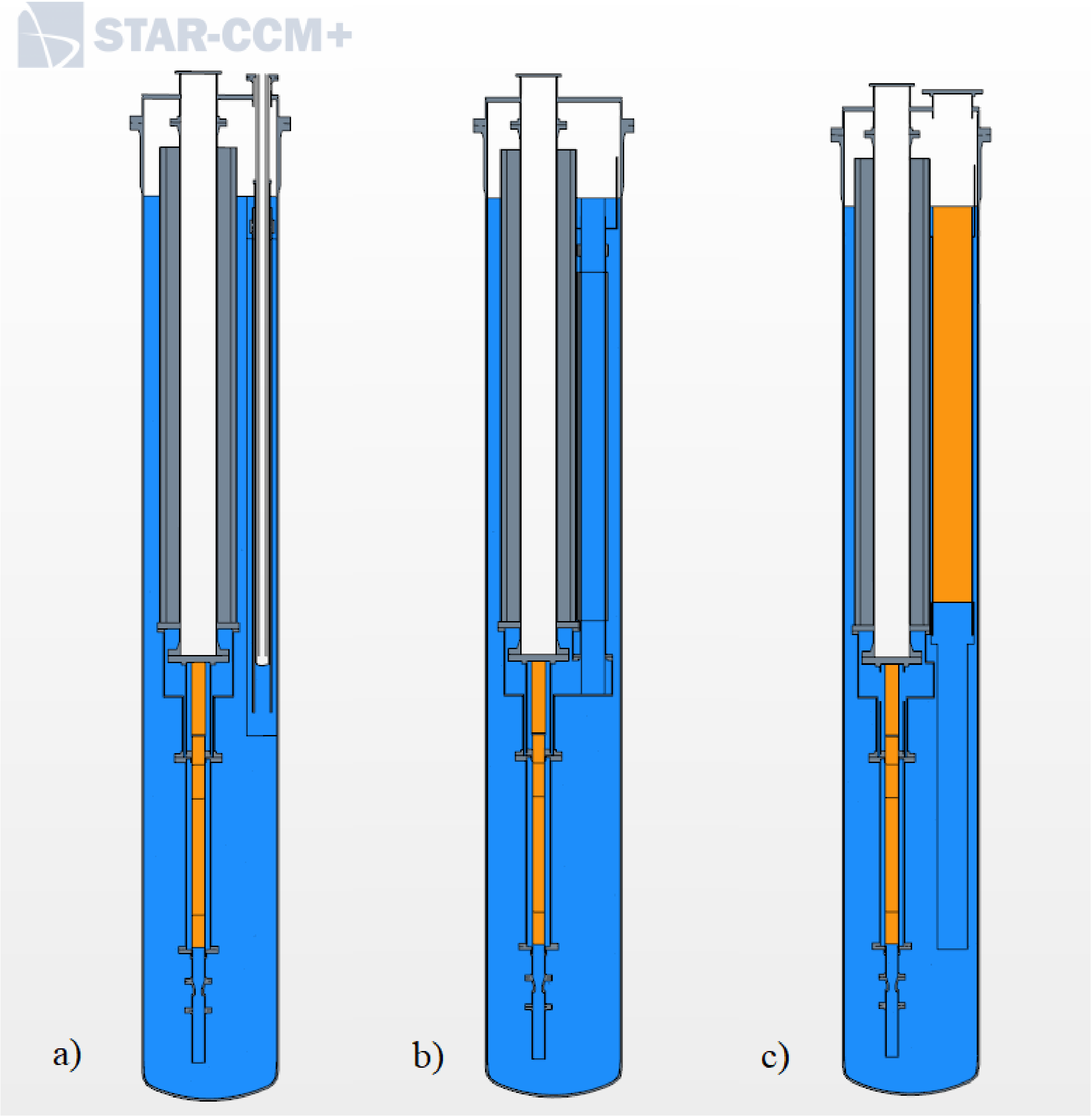

Figure 39. Overview of the LBE regions of the CIRCE facility. a), b) and c) are three different vertical sections that highlight the various components. The "regular" LBE regions are highlighted in blue, and the porous ones in orange.

N.B.: The porous properties of the highlighted regions in Figure 39 have been specified only later, directly from within the region settings; in fact, apart from this detail, the porous LBE regions are modeled by means of the same identical "LBE" physical continuum associated to all the other regular LBE regions

3.2.2.2 Solid regions: AISI304 steel regions and insulation layers

AISI 304 Steel regions

The vast majority of the internal solid elements constituting the CIRCE primary loop are made of AISI304 steel, whose main properties are listed in the following Table 3.

AISI 304 steel (avg. properties)	
Density [kg/m^3]	8000
Specific heat [J/kg*K]	502
Thermal conductivity [W/m*K]	16,2

Table 3. *Modeled average properties for the AISI 304 steel regions*

In order to appropriately simulate the behaviour of the solid metallic elements of the model, a dedicated physical continuum has been created, named "Steel regions". Its material properties have been set accordingly to the previous Table 3 (all properties considered approximately constant with the temperature variations), and the following models have been selected:

- Steady, 3D model
- Solid (constant density)
- Coupled solid energy

Later, this physical continuum has been associated to all the AISI 304 steel regions of the facility.

The other solid regions of the model that are not constituted of AISI304 steel are the insulation layers of the dead volume and riser elements.

Dead volume insulation regions

More precisely, the dead volume insulation is composed of two concentric layers, namely:

- External air insulation layer
- Internal Cerablanket® insulation layer

As previously mentioned in paragraph 1.3.8 the air insulation layer of the dead volume has been modeled as solid (strong approximation) for the sake of computational cost, since the evaluation of the natural convection movements of the gas in that region was not contemplated among the objectives of the model. The selected properties of the "solid equivalent air" are listed in Table 4 :

Dead volume air layer (avg. properties)	
Density [kg/m^3]	1
Specific heat [J/kg*K]	1000
Thermal conductivity [W/m*K]	0,026

Table 4. *Modeled average properties for the dead volume air region.*

A dedicated physical continuum for this insulation layer has been created, and its material properties have been set accordingly to Table 4. The numerical models selected for such "solid air" continuum are the same ones employed for the solid AISI304 steel regions, namely:

- Steady, 3D model

- Solid (constant density)
- Coupled solid energy

The more internal Cerablanket® layer of the Dead volume was modeled considering the available characteristics for the material, listed in Table 5 below.

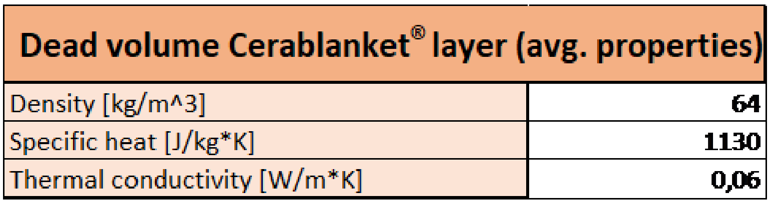

Dead volume Cerablanket® layer (avg. properties)	
Density [kg/m^3]	**64**
Specific heat [J/kg*K]	**1130**
Thermal conductivity [W/m*K]	**0,06**

Table 5. *Modeled average properties for the dead volume Cerablanket® layer (data from Morgan Advanced Materials, thermal ceramics).*

These material properties were used to define and generate the "Cerablanket®" physical continuum, which has then been associated to this region of the model. The selected models for this continuum are the usual ones employed for all the other solid regions:

- Steady, 3D model
- Solid (constant density)
- Coupled solid energy

The "solid equivalent air" and Cerablanket® insulation regions of the dead volume are thus shown in the next Figure 40.

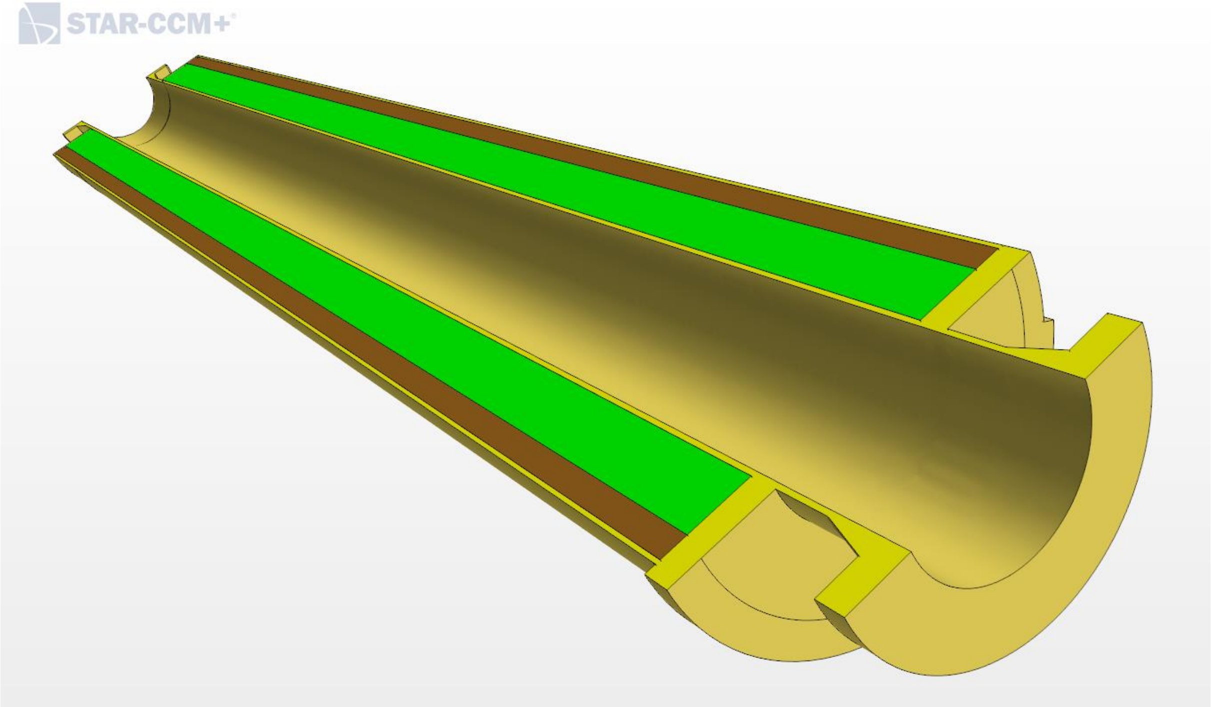

Figure 40. *Detailed section of the dead volume element, highlighting the steel regions (yellow), the air insulating region (brown) and the Cerablanket® layer (green).*

Riser insulation region

The insulation for the riser element is essentially composed of a relatively thick layer of air, enclosed in an external AISI 304 steel pipe. Furthermore, as previously illustrated in paragraph 1.3.4, a single CAD body has been created, incorporating both elements into a single geometry part. This has been done in order to later be able to manage a single "equivalent riser insulation" region within the STAR-CCM+ environment, capable of simulating the behaviour of the assembly of both the steel and air layers combined together. In Figure 41 below, a simple structural scheme of the real riser insulation geometry is portrayed, together with the abovementioned "equivalent riser insulation" region.

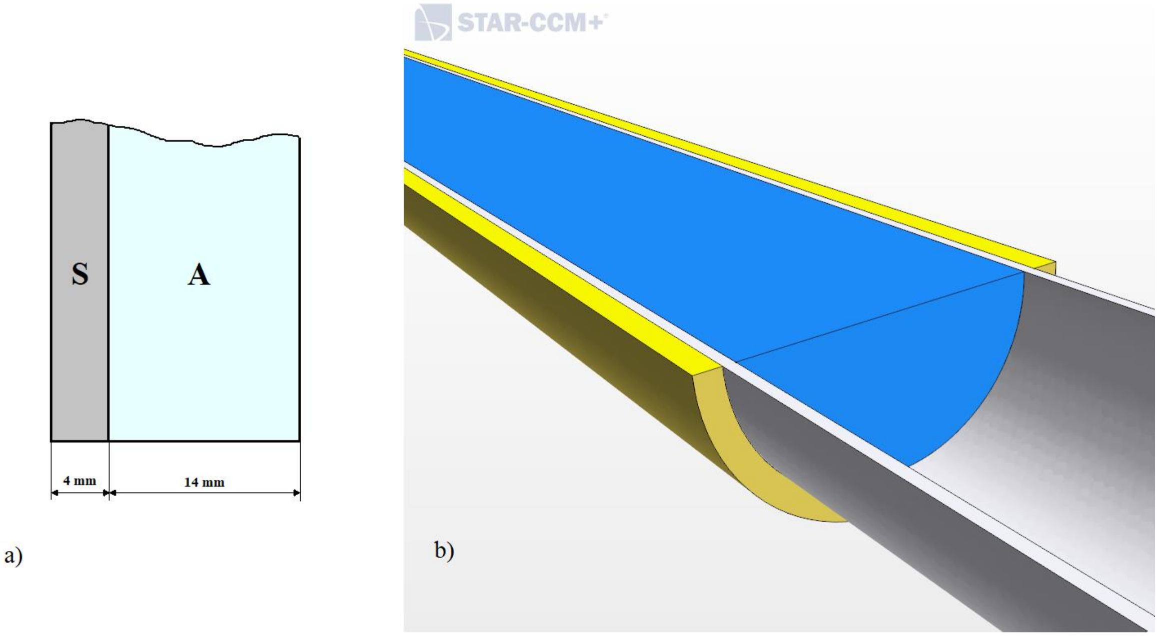

Figure 41.Detail of the Riser insulation region. a) scheme of the steel and air layers composing the real insulation structure of the riser element. b) detailed view of the "Equivalent riser insulation region" (yellow) simulating the behaviour of the air and steel layer in the present CFD model.

Consequently, a new "Riser insulation" physical continuum has been defined, in the attempt to appropriately model the physical behaviour of the "equivalent riser insulation" region. The properties of such continuum must be estimated still theoretically taking into account the internal subdivision between the two layers of steel and air, in order to determine some representative average values for the global assembly.

Equivalent conductivity of the riser insulation (k_{eq})

With reference to Figure 41 and to the properties for AISI304 steel and air listed in Table 3 and Table 4 respectively, an approximated value for the equivalent conductivity k_{eq} of the "riser insulation" region has been determined as follows:

$$k_{eq} = \frac{(S_s + S_a)}{\frac{S_s}{k_s} + \frac{S_a}{k_a}} \cong 3.3 \cdot 10^{-2} \frac{W}{mK} \qquad (1)$$

Where:

- S_s and S_a are the thicknesses of respectively the steel and air layers of the insulation
- k_s and k_a are the thermal conductivities of steel and air respectively
- k_{eq} is the desired thermal conductivity of the “equivalent” unique insulation layer (with thickness equal to $(S_s + S_a)$.

N.B.: Equation (1) provides a roughly approximated value of the equivalent conductivity of the riser insulation region, essentially due to the fact that it considers only the conductive heat transfer through the various layers.

This means that two important factors have been neglected:

- Convective heat transfer in the air gap
- Radiative heat transfer in the air gap

Most notably, the second factor is suspected to have an important influence on the equivalent conductivity of this region and will require further improvements in future models.

Equivalent density of the riser insulation (ρ_{eq})

The average density for this region has been determined considering a weighted average between the densities of the single layers, with the weights being the volumes of the two layers of steel and air, accordingly to Equation (2)

$$\rho_{eq} = \frac{\rho_a \cdot V_a + \rho_s \cdot V_s}{V_a + V_s} \cong 1779\ \frac{kg}{m^3} \qquad (2)$$

Where:

- V_s and V_a are the thicknesses of respectively the steel and air layers of the insulation
- ρ_s and ρ_a are the densities of steel and air respectively

Equivalent specific heat of the riser insulation ($c_{p_{eq}}$)

The average equivalent specific heat for the riser insulation region has been determined considering the conservation of the total heat capacity of the two layers of the real element: namely:

$$c_{p_{eq}} = \frac{c_{p_a}\rho_a V_a + c_{p_s}\rho_s V_s}{\rho_a V_a + \rho_s V_s} \qquad \left[\frac{J}{kgK}\right] \qquad (3)$$

Where:

- c_{p_a} and c_{p_s} are the specific heats of the air and steel layers respectively.
- $c_{p_a}\rho_a V_a$ and $c_{p_s}\rho_s V_s$ represent the total heat capacities ($[J/K]$) of the two layers of air and steel respectively.

These averaged properties have then been associated to the “riser insulation” physical continuum; the models selected for this region are:

- Steady, 3D model
- Solid (constant density)
- Coupled solid energy

3.2.2.3 Gaseous regions

Apart from the air layers inside the insulations of the various elements discussed in the previous paragraph, the most important gaseous regions of this present model are:

Argon gas volume region:

located at the top of the facility, just above the LBE bulk free surface (as illustrated in Figure 13); this gas volume is filled with the argon gas that has served its purpose of generating the LBE mass flow rate through the riser, and then leaves the LBE from the separator region.

As previously mentioned in several occasions, since the accurate modeling of the argon behaviour in this part of the facility is not a central objective of this model, this region has been modeled as “solid”. This allows to very approximately take into account the heat transfer phenomena relative to this element, while the actual modeling of the argon flow fields would have required a way finer mesh and a considerably higher computational cost.

The “Argon” physics continuum is characterized by the properties listed in Table 6.:

Argon gas volume (avg. properties)	
Density [kg/m^3]	1,784
Specific heat [J/kg*K]	523
Thermal conductivity [W/m*K]	0,0172

***Table 6.** . Modeled average properties for the argon gas volume region.*

The models employed for this region are the following:

- Steady, 3D model
- Solid (constant density)
- Coupled solid energy

<u>DHR air region:</u>

This region of the DHR represents the refrigerating air flowing inside the DHR double bayonet tube during the SCRAM experiment; this is the only region of the domain that has actually been modeled as a proper gaseous region, and is displayed in Figure 42:

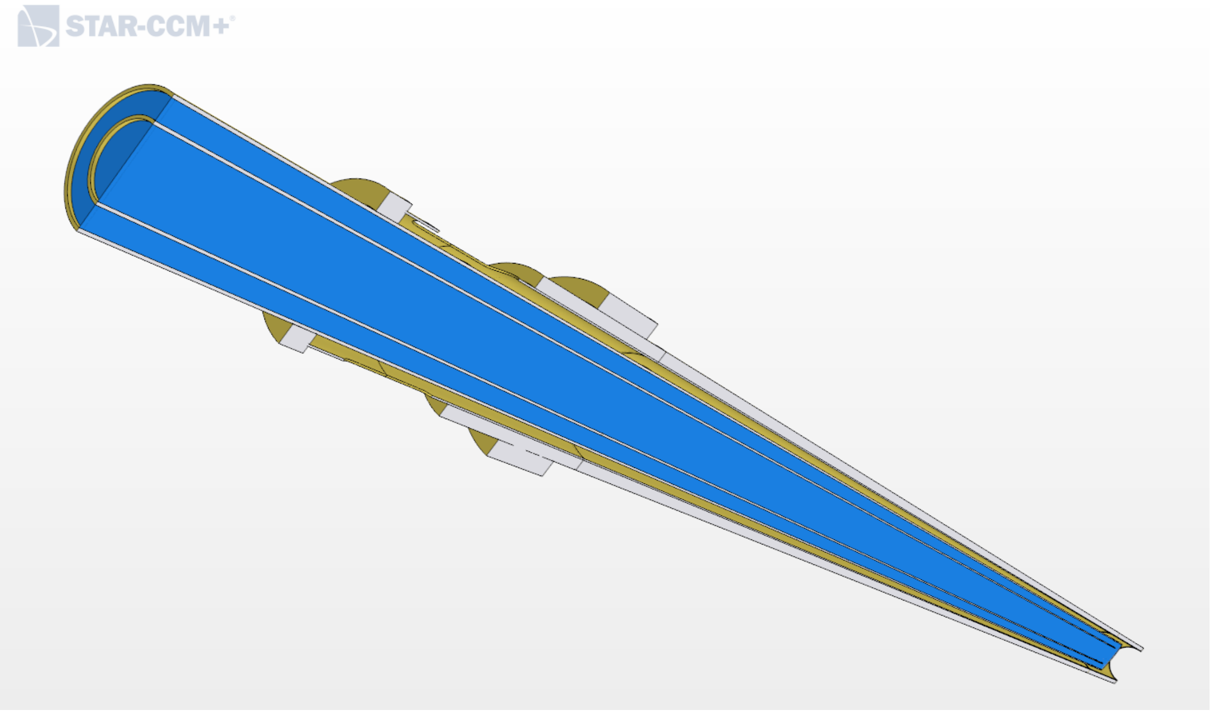

Figure 42. *Detailed section view of the DHR air region, here highlighted in blue.*

The "DHR air" physical continuum associated to this region is described by the material properties illustrated in the following Table 7.

DHR air (avg. Properties)	
Density [kg/m^3]	1,184
Specific heat [J/kg*K]	1003,6
Dynamic Viscosity [Pa*s]	1,85E-05
Thermal conductivity [W/m*K]	0,026

Table 7. *Modeled average properties for the DHR air region.*

Furthermore, the models that have been chosen to simulate the air flow behaviour in this element of the facility are the following ones:

- 3D, Implicit unsteady model (only during the transient simulation)
- Gas (constant density)
- RANS, k-ε turbulence model
- Coupled flow
- Coupled energy

3.3 Design of the single elements of the steady state model

After having analysed the various regions constituting the CIRCE ICE model and their physical properties, it is now time to technically illustrate how such regions have been processed within the STAR-CCM+ simulation environment in order to produce a valid CFD steady state model of the regime experiment; in fact, some elements of the facility have required a more customized approach than others, principally due to their peculiar constructive details and operative conditions.

3.3.1 FPS region design

During the CIRCE ICE regime experiment, the FPS is designed to supply a total heat power of 800 kW to the LBE mass flow rate incoming from the suction pipe, as illustrated in Figure 43 below (accordingly to [6]).

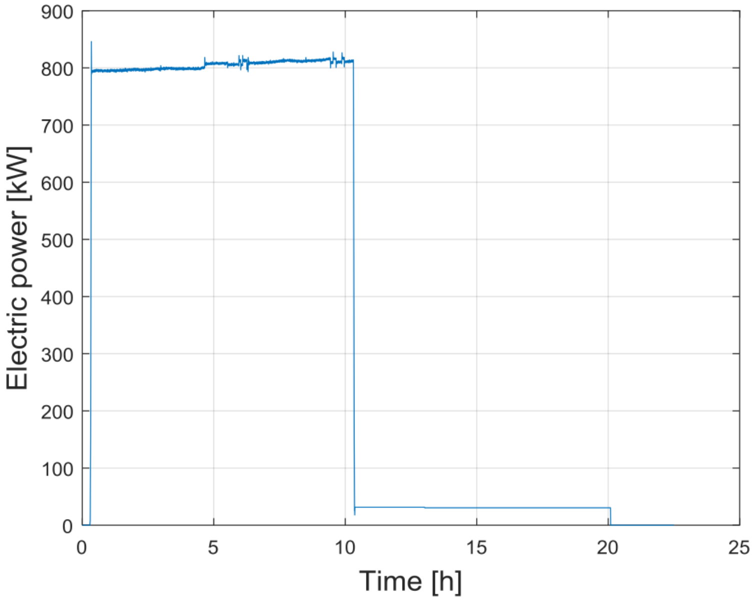

Figure 43. *Total electric power supplied to the FPS pins throughout the whole duration of the CIRCE ICE "Test 1" experiment reported in [6] (p. 9), which almost globally transforms into heat power supplied to the LBE via Joule effect. Courtesy of ENEA.*

Furthermore, some other issues relative to the real FPS must be taken into account:

1. The FPS pins are designed to supply the heat power only along a restricted portion of their total length, i.e. the so called "active region" of the FPS; such region extends vertically for 1 m, and its centre has been identified as the origin of the main coordinate system for the present model (described in paragraph 1.2). Since the actual pins are not geometrically present in the model, the heat power supplied in this region of the FPS has been simulated following a localized volumetric heat source approach (paragraph 3.3.1.1).

2. The presence of the FPS pins hinders the smooth circulation of the LBE flow, essentially due to the viscous irreversibilities localized in the boundary layers in proximity of the pins surfaces. Globally, this translates into a noticeable fluid-dynamic resistance of the element, acting not only along its active region, but throughout the whole length of the pins. This effect has been modeled by means of a porous media approach simulating the presence of the pins (paragraph 3.3.1.2).
3. The FPS pins are kept together and steadily held in place by means of three spacer grids, which interfere with the regular LBE flow causing concentrated fluid dynamic resistances. Such resistances have been kept into account considering some equivalent "porous baffle interfaces" (paragraph 3.3.1.2).

These key elements have been studied and modeled in the ways described in the following dedicated paragraphs.

3.3.1.1 Modeling the FPS heat power supply: volumetric heat source approach.

In Figure 44 the various regions of the FPS element are displayed in detail, and its active and inactive portions have also been highlighted:

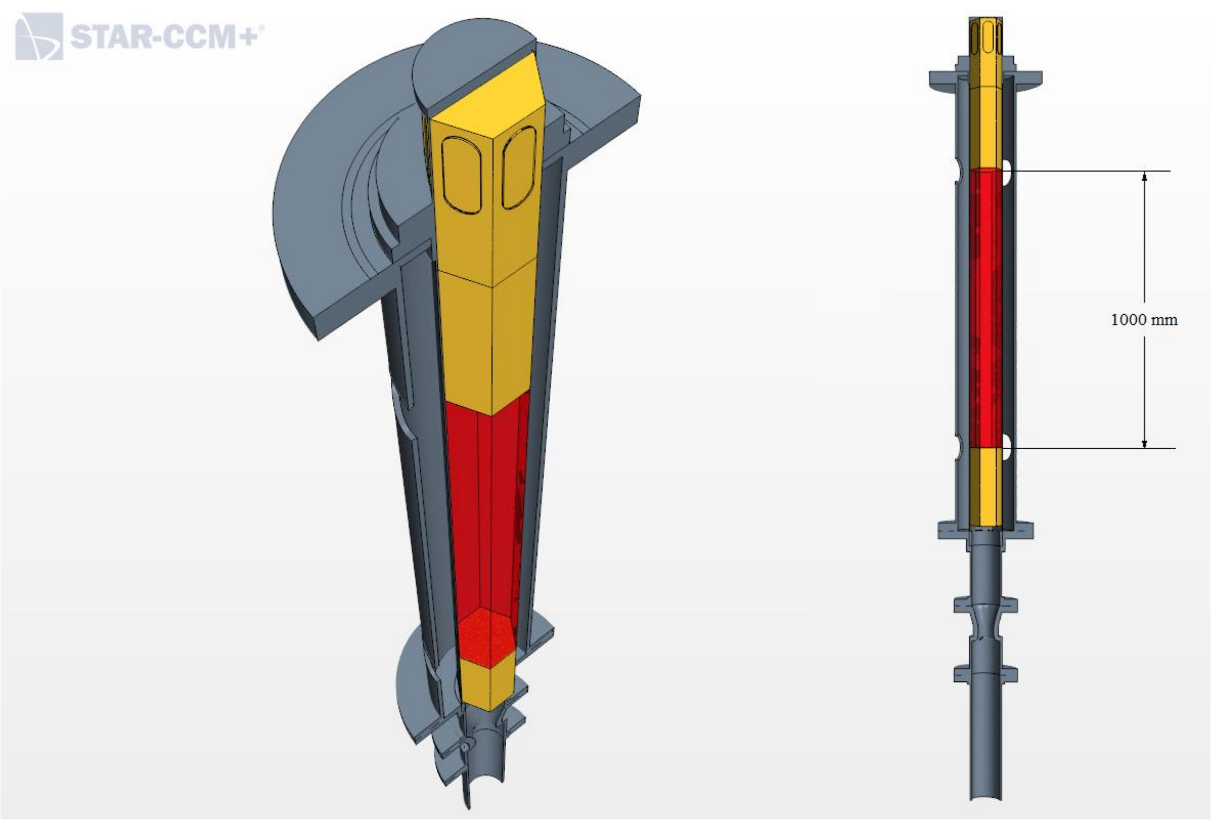

Figure 44. *detailed view of the different portions of the FPS pins region. The "active" region of the FPS (1m length), responsible for the heat power supply to the LBE, is here highlighted in red, while the "inactive regions" are portrayed in yellow.*

In this paragraph the analysis will be focused on the active region of the FPS, displayed in red in the previous Figure 44, which corresponds to the limited region where the actual fuel pins are intended to supply the total heat power of 800 kW; in this model, such effect has been obtained by assigning here a volumetric heat source designed in the attempt to satisfy the following conditions:

1. Matching the total heat power supplied of 800 kW
2. Simulating the LBE temperature field caused by the presence of the actual pins (at least with rough approximation)

In some previous CIRCE models, the volumetric heat source for this FPS active region has been homogeneously assigned only considering the total value of 800 kW, but not keeping into account the real tri-dimensional configuration of the actual temperature field induced by the presence of the pins. In fact, the LBE flowing in the central region of the FPS pin bundle will inevitably reach much higher temperatures than the LBE flowing in the more external region of the same one. This is essentially due to the fact that the LBE in the central region of the pin bundle is affected by the heat flux provided by a larger number of pins, and is conversely not directly affected by the cold LBE outside the hexagonal wrapper (which, on the contrary, tends to cool down the LBE flowing in the external regions of the bundle due to the heat transfer through the hexagonal wrapper). In order to respect this hypothesis on the temperature field, an appropriate FPS cylindrical coordinate system has been defined (with origin at the centre of the FPS active zone and z axis coincident with the FPS vertical symmetry axis), and the volumetric heat source has been designed as a function $S(r, \vartheta, z)$ of the three coordinates of such system (r: radius, ϑ: azimuth, z: height).

$$Volumetric\ heat\ source \quad S(r, \vartheta, z) \quad \left[\frac{W}{m^3}\right] \tag{4}$$

N.B.: The origin of such system and its z axis coincide with the respective ones of the main coordinate system of the model, illustrated in Figure 4.

Furthermore, since there is no need for the volumetric source function to depend from the ϑ and z coordinates, it can be stated that:

$$S(r, \vartheta, z) = S(r) \quad \left[\frac{W}{m^3}\right] \tag{5}$$

The chosen volumetric heat source distribution will thus by axisymmetric and constant with the z heigth (same distribution for each horizontal section of the FPS active region).

It is now important to remember that, globally, the total heat power supplied by the real FPS in the active region ($\dot{Q}_{FPS,r}$, where the “r” stands for “real”) is equal to 800 kW. This obviously implies that the total heat power provided by the volumetric heat source distribution ($\dot{Q}_{FPS,m}$, where the “m” stands for “model”) must be equal to that value. The $\dot{Q}_{FPS,m}$ is calculated as the volume integral of the $S(r)$ over the volume of the FPS active region (FPS_a), namely:

$$\dot{Q}_{FPS,m} = \int_{FPS_a} S(r) dV \quad [W] \tag{6}$$

And, mandatorily:

$$\dot{Q}_{FPS,m} = \dot{Q}_{FPS,r} = 800\ kW \tag{7}$$

In order to determine an appropriate analytic expression that also keeps into account this compulsory constraint, the $S(r)$ has been decomposed into two separate contributions, defined in the following Equation (8) :

$$S(r) = f(r) \cdot \frac{\dot{Q}_{FPS,r}}{F_0} \tag{8}$$

Where:

- $f(r)$ is an adimensional function that "carries" the dependence from the radius (r), and is essentially a "shape function", which can be arbitrarily chosen to define the general profile associated to the $S(r)$.
- $\dot{Q}_{FPS,r}$=800 kW is the total heat power supplied by the real FPS.
- F_0 is the volume integral of the shape function $f(r)$ over the volume of the FPS active region $(FPSa)$, namely:

$$F_0 = \int_{FPS_a} f(r)dV \quad [m^3] \tag{9}$$

It is also important to point out that, once the $f(r)$ has been arbitrarily chosen and fixed, its volume integral F_0 over the volume $FPS_a$is constant. This last property (together with the constancy of the $\dot{Q}_{FPS,r}$) is fundamental in that it allows to state that, for every shape function $f(r)$:

$$\dot{Q}_{FPS,m} = \int_{FPS_a} S(r)dV = \int_{FPS_a} f(r) \cdot \frac{\dot{Q}_{FPS,r}}{F_0} dV = \frac{\dot{Q}_{FPS,r}}{F_0} \cdot \int_{FPS_a} f(r)dV \tag{10}$$

And finally, thanks to Equation (11),

$$\dot{Q}_{FPS,m} = \dot{Q}_{FPS,r} = 800\ kW \tag{11}$$

This means that, by employing the abovementioned subdivision, the constraint fixed in Equation (7) will be satisfied independently from the chosen shape function $f(r)$.

In the present model, a parabolic shape has been chosen for the $f(r)$, the value of the F_0 integral has been internally computed via a dedicated report, and the volumetric heat source distribution could then be computed and associated to the FPS active region. Figure 45 below reports the chosen $f(r)$ profile and also portrays a generic section of the FPS active region together with the final $S(r)$ volumetric heat source profile.

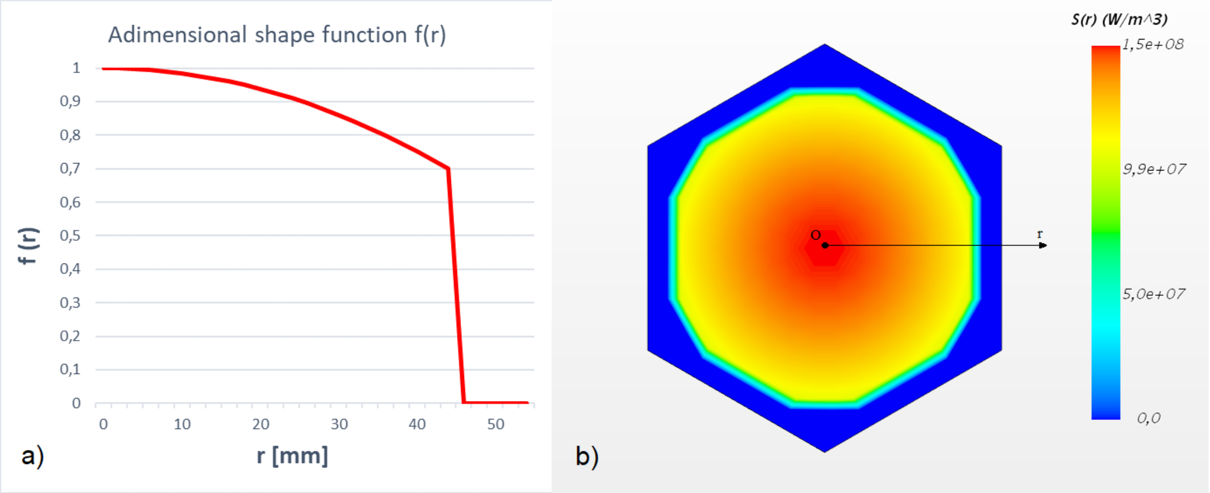

Figure 45. Visualization of the chosen f(r) and S(r) functions. a) chosen profile for the adimensional shape function f(r). The profile is parabolic for 0<r<44mm (representing the distance between the center of the section and the center of the furthest pin of the bundle). b) resulting volumetric heat source function S(r) on a generic section of the FPS active region.

It is important to remember that the $S(r)$ volumetric heat source condition has been only assigned to the active region of the FPS (depicted in red in Figure 44).

3.3.1.2 Porous media approach in the FPS

The fluid dynamic resistances introduced by the FPS pin bundle have been modeled by employing a classic porous media approach. Figure 46 below highlights the porous regions of the FPS.

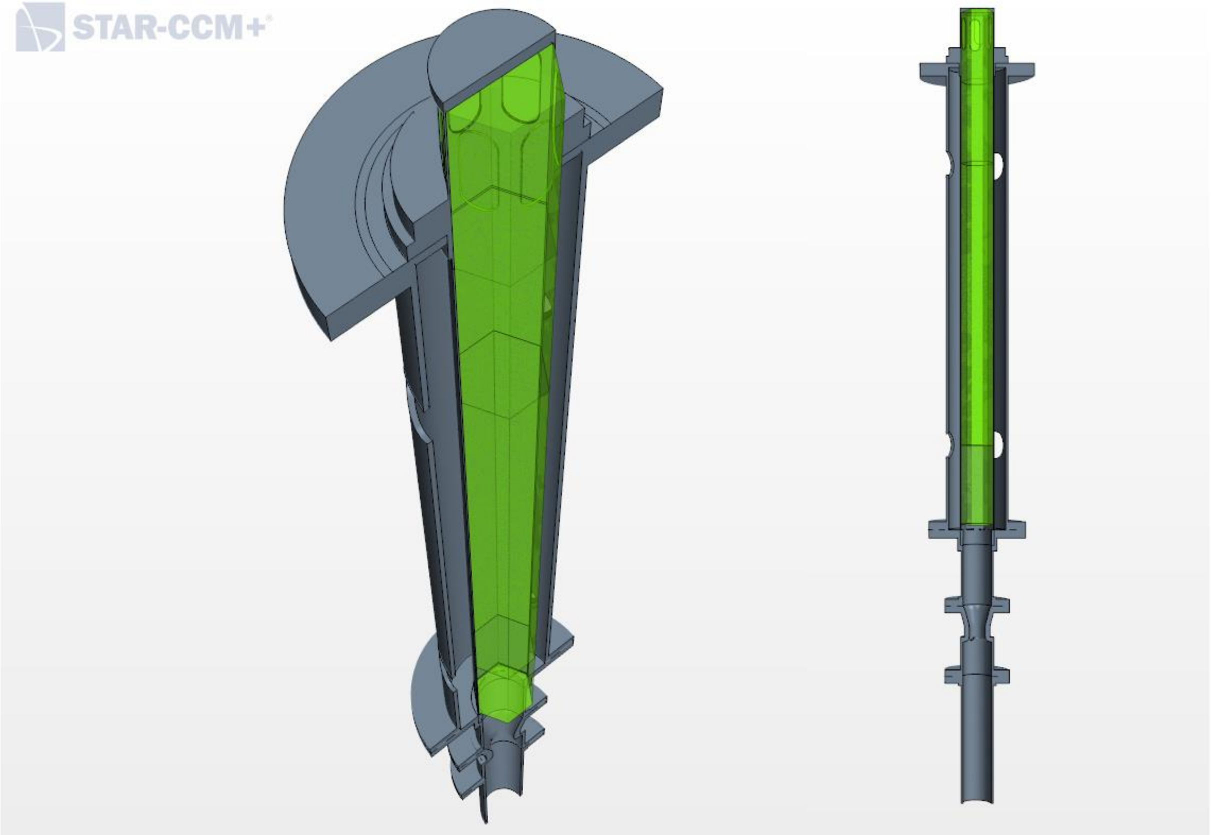

__Figure 46.__ Representation of the porous regions in the FPS element. The region highlighted in green represents the portion of the FPS that hosts the pin bundle (including both the active and inactive zones). The porous conditions discussed in this paragraph will thus be applied to this whole region.

The philosophy behind the porous media approach applied in these regions consists in the addition of a particular source term in each one of the momentum equations (along directions x, y and z). Theoretically, the source term for the i-th coordinate is defined in the general way expressed in the following equation (12) (with reference to [6], p.183):

$$S_i = -\left(\sum_{j=1}^{3} D_{ij}\mu u_j + \sum_{j=1}^{3} C_{ij}\frac{1}{2}\rho|u|u_j\right) \tag{12}$$

The first term in the right hand side of equation (12) refers to the viscous resistance in the porous medium, while the second one takes into account the inertial resistance. Correspondingly, D and C are two matrixes that completely define the resistance of the porous medium from the viscous and inertial point of view respectively, while u, μ and ρ are the velocity, viscosity and density of the fluid flowing through the porous medium.

Furthermore, equation (12) refers to the most generic case possible, with different viscous and inertial resistances along the x, y and z directions.

Porous inertial resistance

The first practical assumption that has been made refers to the fact that the FPS pin bundle presents essentially two main directions characterized by very different porous inertial resistances:

- Cross-stream direction (radial) - high resistance
- Axial direction - low resistance

This is due to the very intuitive reason that a generic flow that approaches the pin bundle perpendicularly (cross stream radial direction) encounters a reasonably higher resistance compared to a flow that proceeds in parallel with the pins (axial direction).

In order to do so, in the STAR-CCM+ software the porous inertial resistance of the FPS regions has been defined by means of an "axisymmetric tensor", which essentially is nothing different than an equivalent formulation of the C matrix of equation (12); the main difference is that the axisymmetric tensor formulation requires the input of only two components in order to completely define the inertial resistance of the porous medium:

- Cross stream component of the tensor
- Axial component of the tensor

The values employed for these parameters are:

- Cross stream component: $354101\ kg/m^4$ (calculated accordingly to [3])
- Axial component of the tensor: $5618\ kg/m^4$ (computed from values reported in [6] (p.185)

Porous viscous resistance

The porous viscous resistance, on the other hand, has been modeled considering an isotropic condition (same viscous resistance along every direction of the flow), and the equivalent of the D matrix of equation (12) has been set as an isotropic tensor, thus specifying only one component.

- Porous viscous isotropic component: $100\,\frac{kg}{m^3 s}$

Porosity

Furthermore, the actual porosity γ of the equivalent media must be set. This parameter is generically defined as:

$$\gamma = \frac{Volume\ occupied\ by\ the\ fluid}{Total\ volume} \tag{13}$$

In the case of the present FPS, considering that the pin bundle and the LBE flowing around it constitute a prismatic geometry with no variations along the axis of the element, the previous expression (13) can be simplified (considering a generic section) as:

$$\gamma = \frac{Area\ of\ the\ section\ occupied\ by\ LBE}{Total\ area} = 0{,}769 \tag{14}$$

FPS spacer grids

The three spacer grids holding together the pin bundle introduce some localized fluid dynamic resistances for the LBE flowing through the FPS. Figure 47 below shows the position of these three grids in the FPS region of the model.

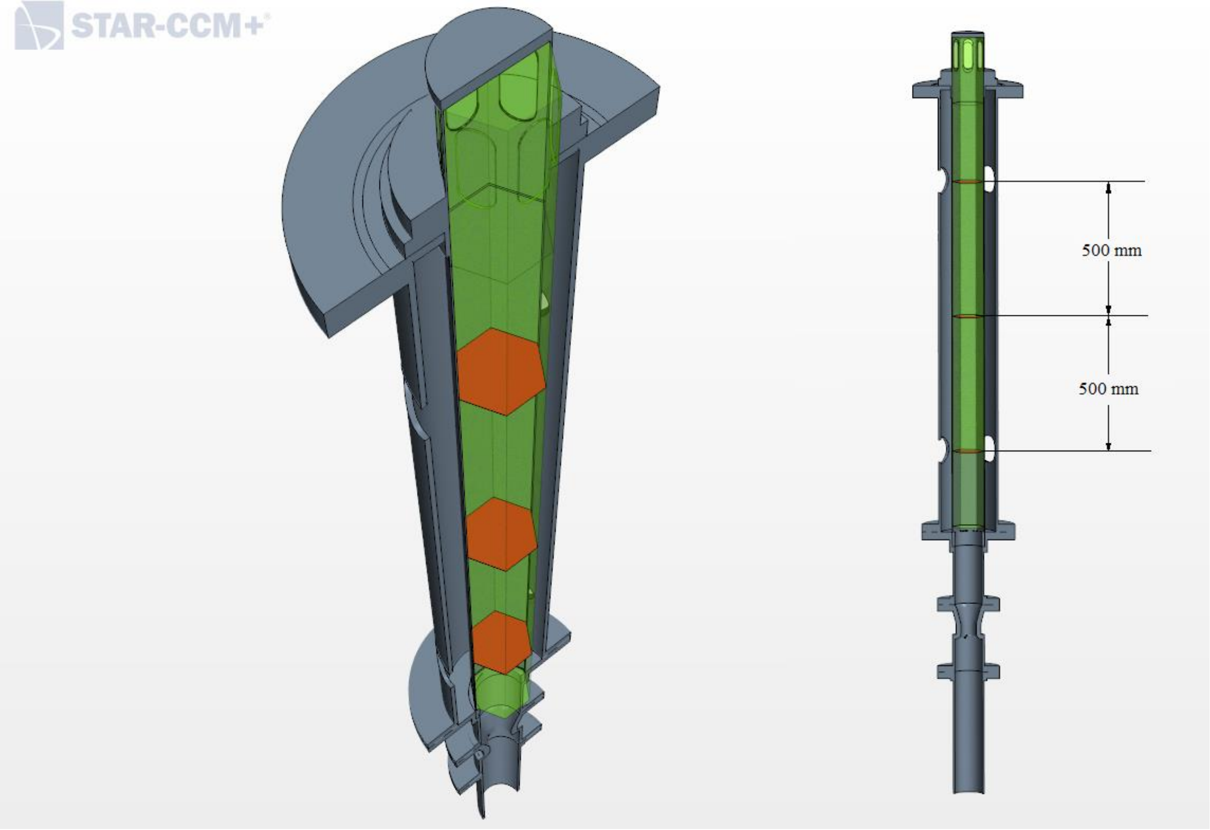

Figure 47. Detailed view on the location of the actual FPS spacer grids. The intermediate grid is located exactly at the centre of the FPS active region.

The local adimensional pressure drop coefficient for the three spacer grids has been considered accordingly to document [6] (p.185) and is equal to 1.431 (all three grids counted together).

In the present model, the pressure drops introduced by these three grids has been concentrated upon the two inlet and outlet sections of the FPS active region, by means of two porous baffle interfaces. The local pressure drop coefficient of each interface has thus been set equal to 0.716 (half of the previous total value for the three grids). Figure 48 shows the position of the two numerical porous baffle interfaces.

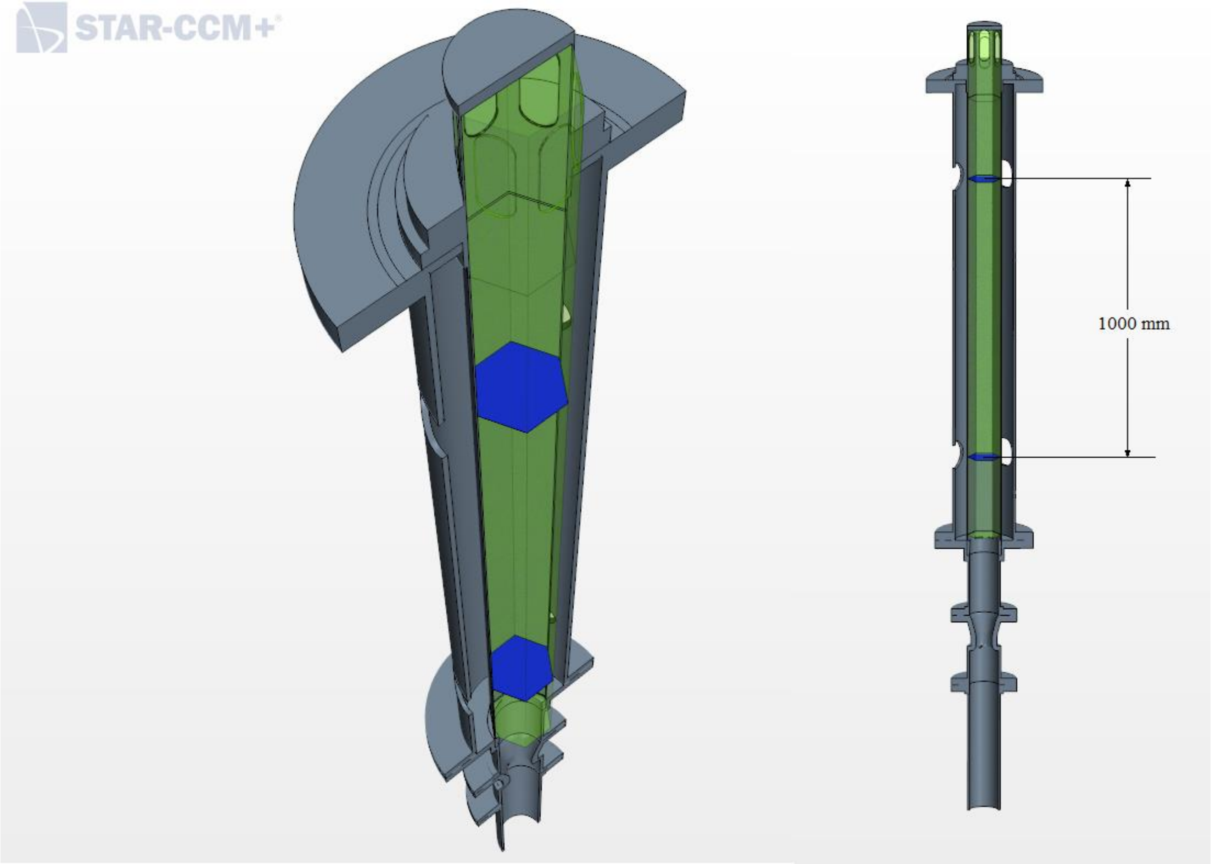

Figure 48. Location of the two modeled "baffle interfaces" meant to simulate the pressure drop effects introduced by the real FPS spacer grids.

FPS "cable caps" modeling

The external pipe surrounding the FPS hexagonal wrapper presents eight holes, meant to host the exiting instrumentation cables for this region. These cables hinder the LBE flow, and have been modeled by means of the porous "cable caps" (previously described in paragraph 1.3.1 and depicted in Figure 9. These elements have been modeled as very simple isotropic porous media, characterized by the following parameters:

- Porous inertial isotropic component: $10000\ kg/m^4$
- Porous viscous isotropic component: $100\,\frac{kg}{m^3 s}$

3.3.2 HX region design

The HX, during the CIRCE ICE regime experiment, works as the heat sink of the circuit, and is designed to subtract a total heat power of 800 kW from the LBE flowing downwards back to the bottom of the facility. In general, the total heat power removed by the HX shows a very irregular and fluctuating behaviour. The plots in Figure 49 below illustrate the measured heat power removed by the HX during two previous CIRCE ICE experiments (different from the "Test 1" studied in the present model, and reported in documents [8] (p.33) and [1] (p.38) respectively.

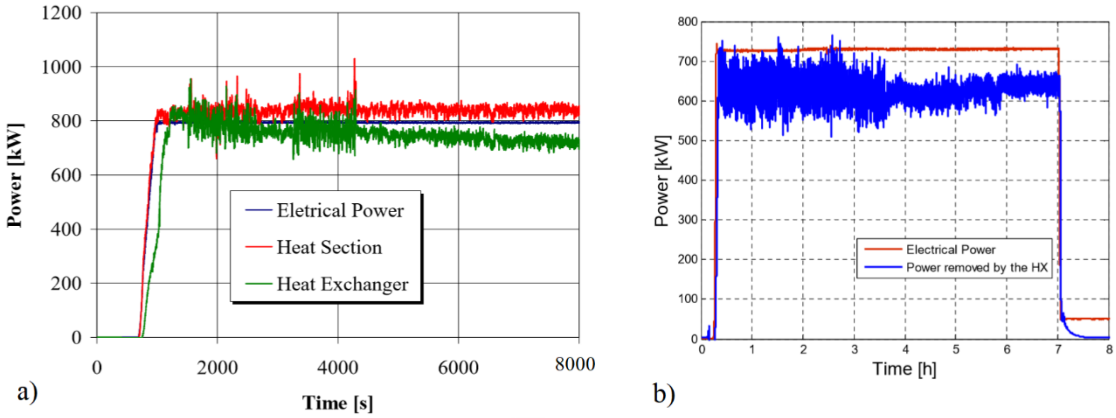

Figure 49. Plots monitoring the total heat power removed by the HX element throughout the duration of two different (older) CIRCE ICE experiments. a) refers to [8] (p.33) and b) to [1] (p.38). Courtesy of ENEA.

These plots clearly describe that, during its years of operation, the ICE HX element has constantly shown clear signs of strongly irregular behaviour, intrinsically ascribable to its constructive design.

Consequently, the accurate steady state modeling of this element in the bigger picture of the whole facility has historically proven to be challenging, and has often been considered one of the main causes of discrepancy between the results of such models and the experimental data.

This is essentially due to the fact that the element is not externally insulated, and the LBE temperature field inside the HX shell has the potential to drastically influence the temperature field in the LBE bulk. It is thus fundamental to determine an appropriate way of simulating the real behaviour of the HX in order to validate the modeling results for the whole facility. Generally, in some previous CIRCE ICE simulations, this element has been modeled via a simple homogeneous porous media approach, coupled to an 800 kW total heat sink condition localized in the cylindrical active zone of the element (double bayonet tubes location). This approach has the advantage of being really simple and straightforward, and allows for a reliable first approach to the modeling of the HX behaviour; on the other hand, it does not take into account some factors involving the geometry of the element, most notably relatively to the hexagonal matrix arrangement of the bayonet tubes. A basic scheme of a generic section of the element is portrayed in Figure 50.

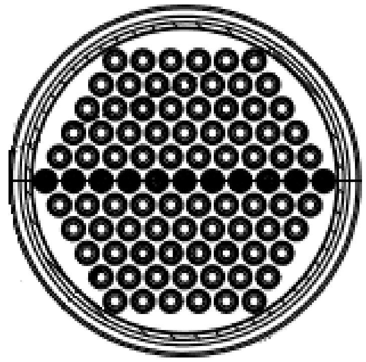

Figure 50. *Generic section of the ICE HX element. The external shell is visible, together with the hexagonal matrix distribution of the double bayonet tubes. Courtesy of ENEA.*

In fact, the physical presence of the double bayonet tubes arranged in such fashion affects the LBE flow in different ways:

- The fluid dynamic resistance encountered by the LBE flowing through the element is definitely not homogeneous: the fraction of the LBE mass flow rate transiting through the interstices between the hexagonal tube matrix and the HX shell encounters much less resistance compared to the one flowing directly through the hexagonal tube bundle (for the same reasons illustrated in paragraph 3.3.1.2 about the FPS pin bundle).

  Moreover, the resistance encountered by the LBE flowing through the double bayonet tube bundle is different in the axial and cross-stream directions.

- The 800 kW heat power removal is concentrated in the central hexagonal region, where the double bayonet tubes are located and exert their influence. Assigning the heat sink condition to the whole cylindrical region inside the shell is a very rough approximation, and badly describes the real temperature gradients of the actual flow.

These effects must be taken into account while choosing an appropriate "equivalent" porous medium meant to simulate the presence of the tubes. In order to do so, a separate dedicated study of the HX has been previously conducted, reported in detail in the next paragraph 3.3.2.1.

3.3.2.1 The HX dedicated model[5]

Essentially, a separate steady state model of the HX has been created, considering a simplified, symmetrized version of the real element. The basic geometry of such model is depicted in Figure 51 below.

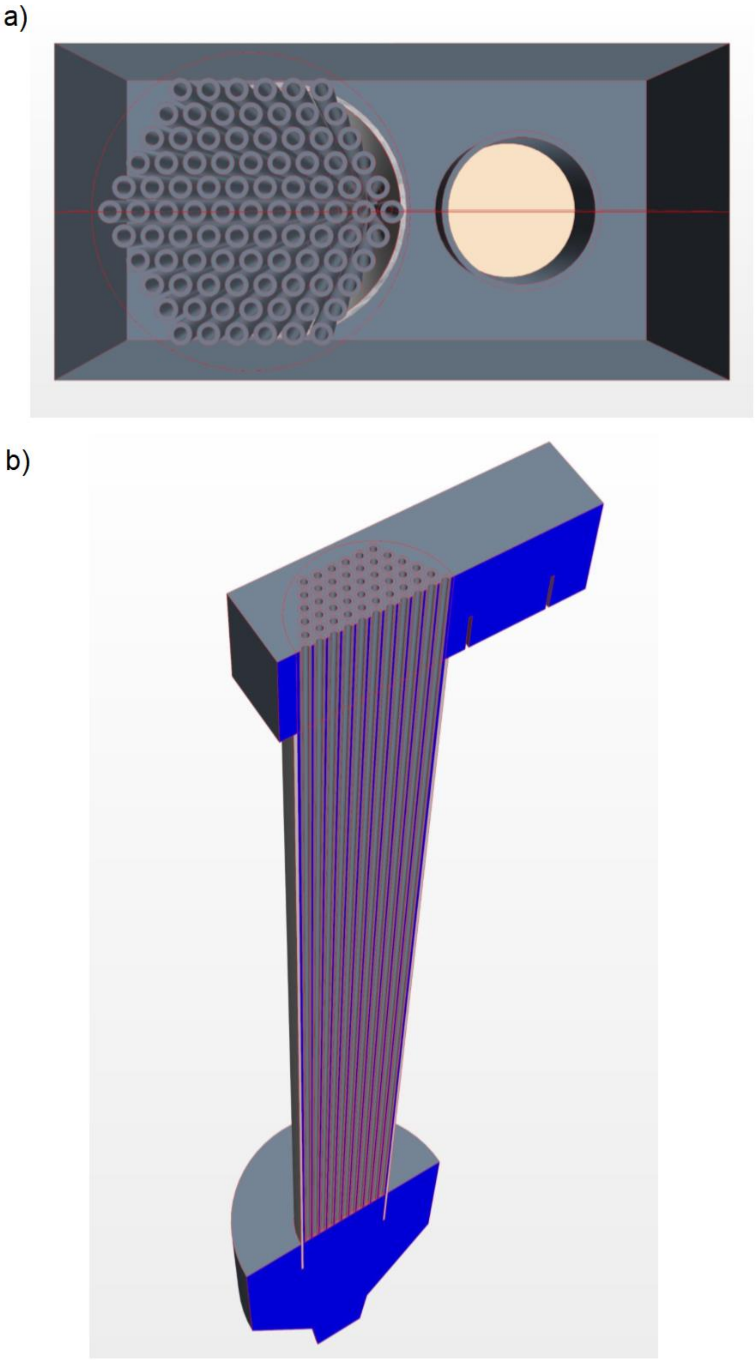

Figure 51. CAD geometry for the HX dedicated model. a) Top symmetrized view (comprehending the riser outlet and the separator). b) global view of the geometry.

As can be noticed, this dedicated HX model does not take advantage of the porous media approach, but simulates the actual physical presence of the solid double bayonet tubes. The separator region has also been simplified (it has a prismatic rectangular shape instead of the real curvilinear one), while the riser outlet is still portrayed, and represents the inlet region of the model (mass flow inlet condition). A pressure outlet boundary condition for the LBE is set at the bottom surface of the geometry, where a dedicated "outlet region" has been created in order to simulate the efflux into the real LBE bulk region of the facility.

The presence of the evaporating water flowing in the double bayonet tubes has been modeled by imposing a fixed temperature boundary condition on their internal surface. Such temperature boundary condition has been defined as a function of the z (height) coordinate, and is thus a $T(z)$ temperature profile that estimates the real temperature field of the evaporating water in the annular section of the double bayonet tubes. The temperature profiles have also been evaluated differently considering the spatial distribution of the tubes. Figure 52 shows the employed $T(z)$ boundary condition profiles:

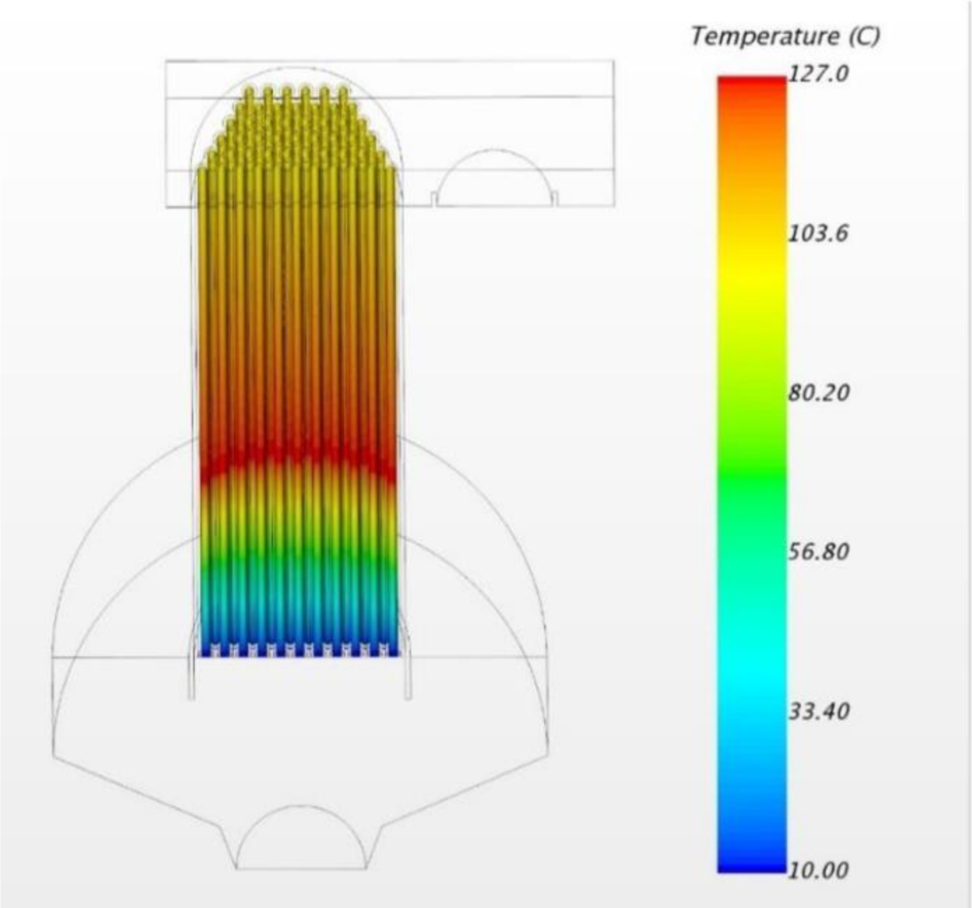

Figure 52. Temperature boundary condition $T(z)$ imposed on the internal surface of the tubes.

Furthermore, the grid at the bottom of the HX has been modeled by means of a porous baffle interface. The value of the essential parameters of this simulation have been set in order to match the official CIRCE experiment reported in document [1]. Some of the results are briefly portrayed in Figure 53 and Figure **54**. Report [5] is available for further details on the construction, results and analysis of this dedicated HX model.

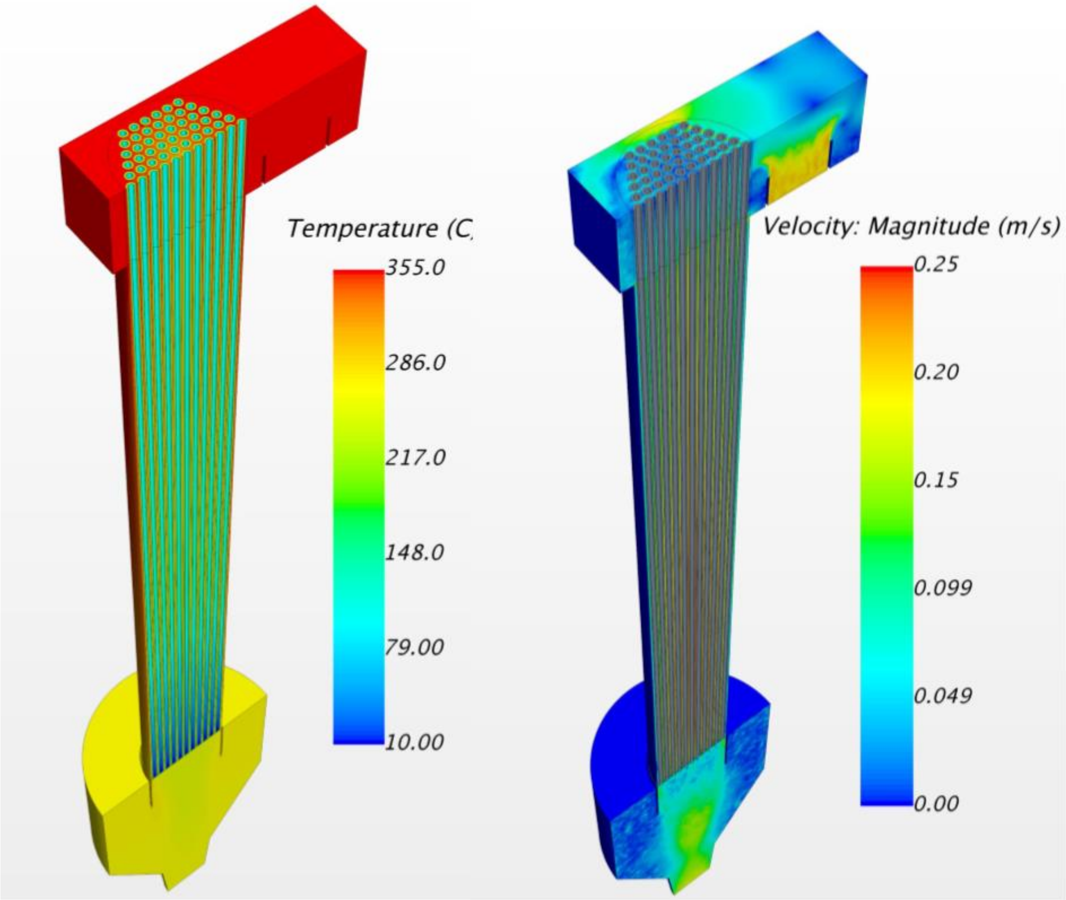

Figure 53.*Resulting temperature (left) and velocity (right) fields for the HX dedicated steady-state model. In this experiment, the HX induces a* $\Delta T \cong 80°C$ *for the LBE. The velocity field is characterized by very low absolute values, and is essentially dominated by the natural convection effects*

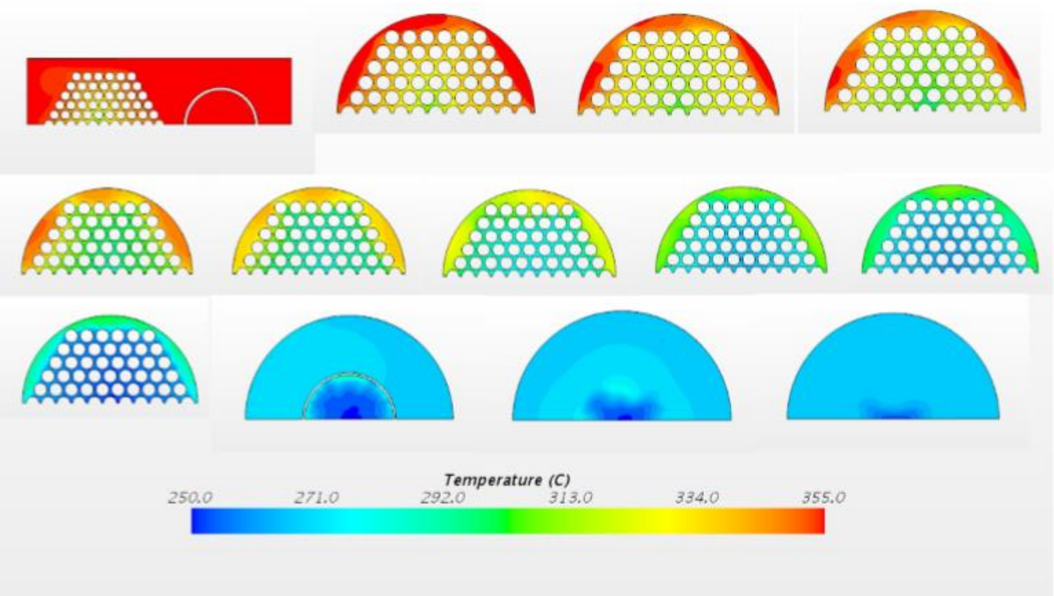

Figure 54. *LBE temperature field on different sections of the HX, from the highest (top left) to the lowest (bottom right). The heat transfer effects towards the water in the double bayonet tubes is heavily concentrated in the central zone of the element and is strongly affected by the hexagonal-shaped matrix of the tubes.*

These results are totally coherent with the assumptions pointed out at the beginning of this paragraph relatively to the influence of the double bayonet tubes on the LBE flow. Most notably, Figure 54 shows how the hexagonal matrix strongly dictates the topology of the temperature field of the LBE, concentrating within itself the heat transfer towards the evaporating water inside the tubes, while leaving some hotter external zones (between the HX shell and the tubes).

The information provided by this study has been used as a basic guideline to correctly simulate the behaviour of the HX within the bigger model of the entire CIRCE facility.

3.3.2.2 HX design – porous media approach

Remembering the considerations on the effects of the presence of the double bayonet tubes explained in paragraph 3.3.2 and taking into account the results of the HX dedicated model discussed in 3.3.2.1, the active regions of the HX have been modeled following a porous media approach based on the following points:

Definition of the zone of influence of the tubes:

Considering a generic section of the real HX, the area of influence of each single tube has been calculated as the area of the "modular hexagon" surrounding the tube, as depicted in the following Figure 55.

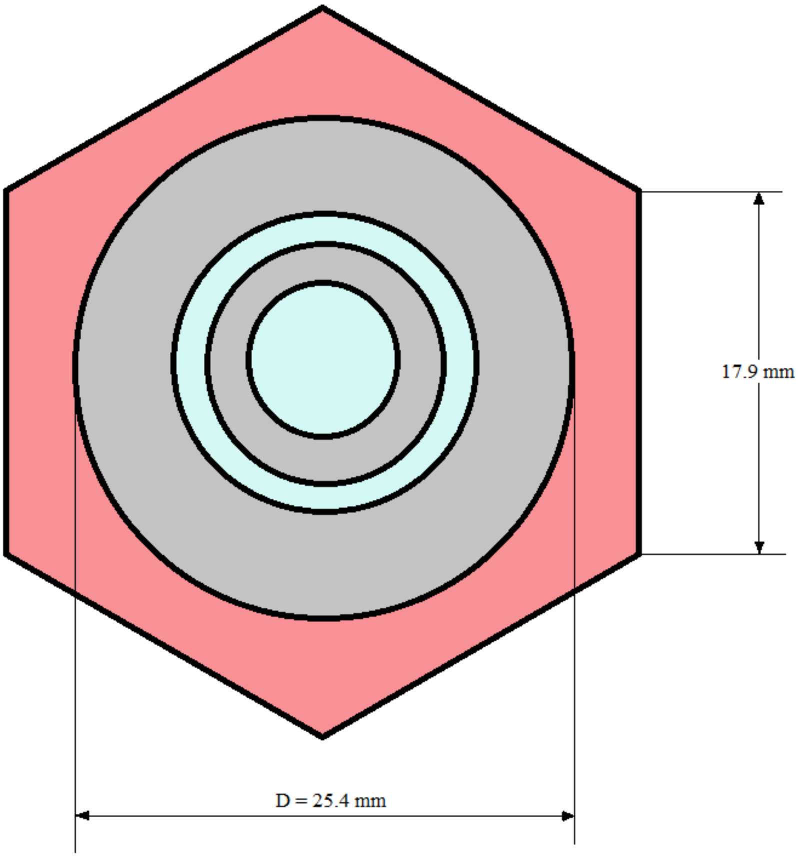

Figure 55. schematic section of a single HX double bayonet tube. The hexagonal "area of influence" of the single tube has been calculated considering the pitch between two adjacent tubes, and is here highlighted in red, together with its dimensions

Such value has then been multiplied for all the 91 tubes assembled in the HX matrix, obtaining the area of influence of all the tubes for any horizontal section of the HX.

This resulting area has been employed to generate a single "equivalent" hexagon (same area) representing the planar zone of influence of the tubes; furthermore, an appropriate field function that isolates such area has been created and defined as the "Characteristic function" of the hexagonal matrix (χ_{hex}). Essentially, this field function is defined as:

$$\chi_{hex} = Hex.char.function = \begin{cases} 1 & inside\ the\ Hex.matrix \\ 0 & outside\ the\ Hex.matrix \end{cases} \qquad (15)$$

Since there is no limitation in the z direction, this field function geometrically identifies a hexagonal prismatic volume. Figure 56 below represents the χ_{hex} characteristic function in some generic sections of the HX active regions.

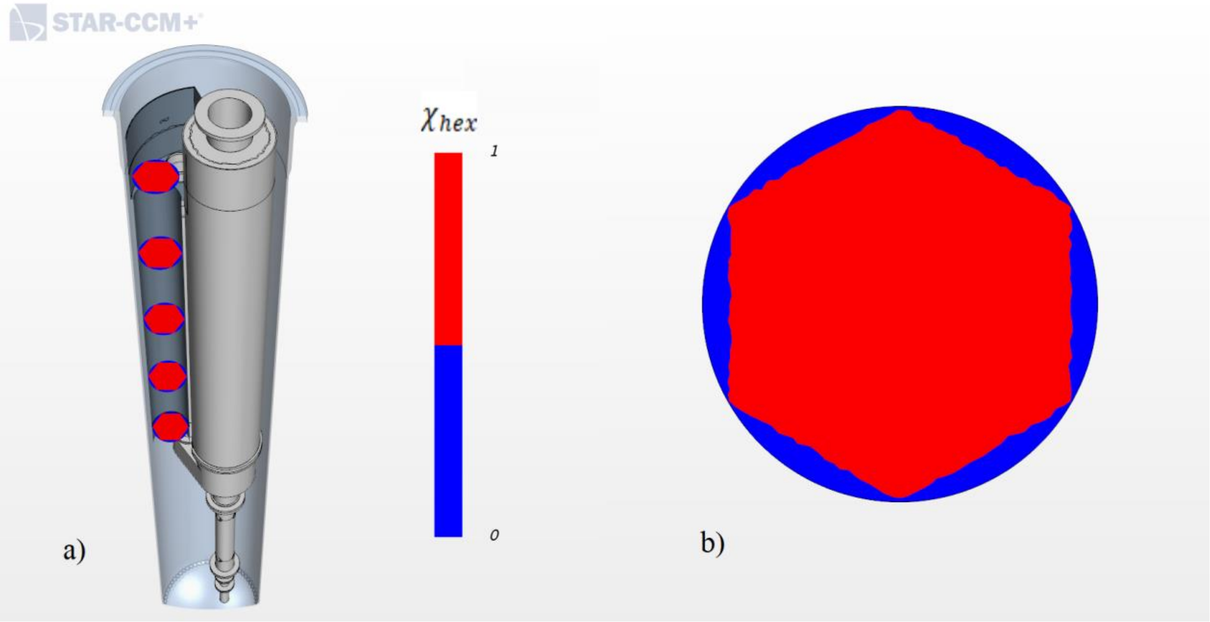

Figure 56. Visualization of the χ_{hex} characteristic function. a) the χ_{hex} function at various sections of the HX active region, meant to represent the hexagonal prismatic volume of influence of the tubes. b) detail.

The χ_{hex} field function will be later employed as a "base" function in order to circumscribe the effects of porosity and of the heat sink condition only to the actual zone of influence of the double bayonet tubes.

Definition of the HX porous medium

The mathematical definition of the porous media approach followed for this element is the same that has been described for the flow through the FPS pin bundle (paragraph 3.3.1.2). In the current HX case, anyway, some modifications were necessary:

- **HX region porosity γ :**

  This parameter has been calculated accordingly to equation (13), which returns:

  $$\gamma = 0.499$$

In order to take into account the fact that this porosity must be applied only to the region of influence of the tubes, the previously defined characteristic function of the hexagon χ_{hex} has been employed to define a new porosity field function for the HX, namely:

$$\gamma_{HX} = \begin{cases} 0.499 & inside\ the\ Hex.matrix \\ 1 & outside\ the\ Hex.matrix \end{cases} \qquad (16)$$

By doing so, the small portions of the LBE flowing between the HX shell and the hexagonal matrix will experience a “free flow” condition (γ=1 implies that the volume occupied by the fluid equals the total volume, while the region inside the matrix will have a porosity equal to 0.499.

- **Porous inertial resistance:**

  The condition for the porous inertial resistance has been specified by means of an axisymmetric tensor, repeating the same considerations explained for the FPS pin bundle (differentiating the resistances along the axial and cross-stream directions). The basic values for the components of such tensor (not yet taking into account the presence of the hexagonal matrix) have been computed as:

  Cross stream component: $1.78 \cdot 10^6\ kg/m^4$

  Axial component: $24.5 \cdot 10^3\ kg/m^4$

  The cross-stream component has been calculated accordingly to [3], while the axial component has been computed considering the values reported in document [6] (p.186). These values have then been filtered by means of the χ_{hex} characteristic function of the hexagon, in order to let the porous inertial resistance act only inside the region of influence of the tubes. The regions between the hexagonal matrix and the HX shell are thus not affected by the porous inertial resistance.

- **Porous viscous resistance**

  The viscous resistance of the medium has been modeled by means of an isotropic tensor (homogeneous viscous resistance). The value of the isotropic tensor component has been set equal to $100 \frac{kg}{m^3 s}$.

  Even this value has been filtered by means of the χ_{hex} characteristic function of the hexagon (equation (15)), letting the porous viscous resistance act only inside the zone of influence of the tubes.

- **HX outlet grid**

  The outlet grid of the HX has been modeled by means of a porous baffle interface, whose local pressure drop has been calculated still considering the presence of the tubes in the internal region of the HX. In fact, the bottom part of each tube is "locked" on the outlet grid of the HX, and thus the orifice/total surface ratio changes considerably from the internal ($\chi_{hex} = 1$) to the external ($\chi_{hex} = 0$) region of the plate.

Accordingly to [4], the local pressure drop coefficient for flow through perforated plates (sharp orifices) can be roughly estimated by means of the following equation (17):

$$\varepsilon = 2.7 \cdot (1-\beta) \cdot (1-\beta^2) \cdot \left(\frac{1}{\beta^2}\right) \tag{17}$$

Where ε is the local pressure drop coefficient of the equivalent porous baffle interface (the value of $\varepsilon/2$ must be actually implemented into STAR-CCM+), and β represents the following ratio:

$$\beta = \frac{Area\ of\ the\ orifices}{Total\ area\ of\ the\ plate} \tag{18}$$

This calculation has been performed for both the internal area of the plate (inside the hexagon of influence of the tubes) and for the external one (between the HX shell and the hexagon). Table 8 below summarizes the results:

	Inside ($\chi_{hex} = 1$)	**Outside ($\chi_{hex} = 0$)**
β	0.369	0.212
ε	10.8	45.4

Table 8. *β and ε values calculated inside (χ_{hex}=1) and outside (χ_{hex} =0) the hexagon of influence of the tubes, in order to determine the porous local pressure drop coefficient of the HX baffle interface.*

The location of this porous baffle interface is highlighted in the following Figure 57.

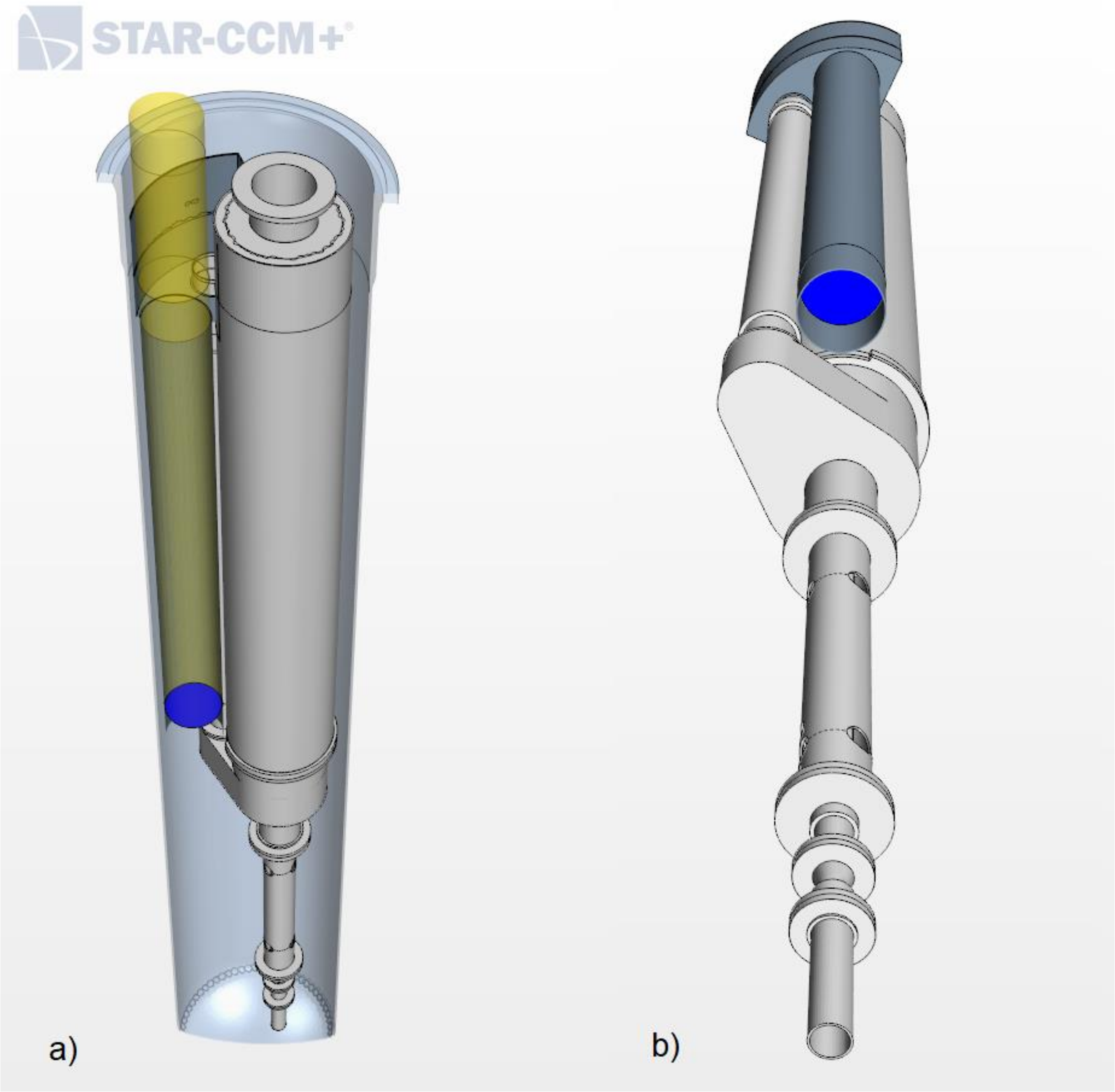

Figure 57. Detailed view of the HX baffle interface (highlighted in blue). a) general position of the interface relatively to the HX region occupied by the double bayonet tubes (yellow). b) bottom detail.

Definition of the HX heat sink

As previously mentioned at the beginning of this paragraph, the actual function of the HX within the CIRCE circuit during the regime experiment is the removal of a total heat power of 800 kW from the LBE flow. To do so, a volumetric heat sink condition needs to be selectively imposed in the hexagonal prismatic volume of the HX described in Figure 56, in order to simulate the concentration of the heat transfer only in the zone of influence of the HX tubes.

The generic formulation of the volumetric heat sink has been chosen accordingly to [6] (p.186), namely:

$$q_{HX} = \frac{\rho c_p}{\tau}(T_0 - T) \quad \left[\frac{W}{m^3}\right] \tag{19}$$

Where:

- q_{HX} represents the volumetric heat source condition that has been implemented in the STAR-CCM+ software.

  N.B.: the value of q_{HX} is **negative** ($T > T_0$, always in the present situation), which means that the even if the software requires an "energy source" option, this will inevitably translate into setting a heat sink (**negative source**) in the desired region.
- ρ is an appropriate reference density of LBE.
- $c_p$is an appropriate specific heat of LBE.
- T_0 is a temperature (or temperature profile) that is significant of the water evaporation process inside the double bayonet tubes.
- T is the LBE temperature.
- τ is a certain "relaxation time" of the HX, that should be comparable to the time of permanence of the LBE inside the HX.

In the present situation, since the heat sink must be concentrated in the zone of influence of the tubes (hexagonal prismatic region), equation (19) has been filtered by employing the χ_{hex} characteristic function of the hexagon, becoming:

$$q_{HX,hex.} = q_{HX} \cdot \chi_{hex} \tag{20}$$

Or, more specifically:

$$q_{HX,hex} = \left[\frac{\rho c_p}{\tau}(T_0 - T)\right] \cdot \chi_{hex} \tag{21}$$

This expression has been employed as the volumetric heat sink of the model in the active region of the HX portrayed in Figure 58.

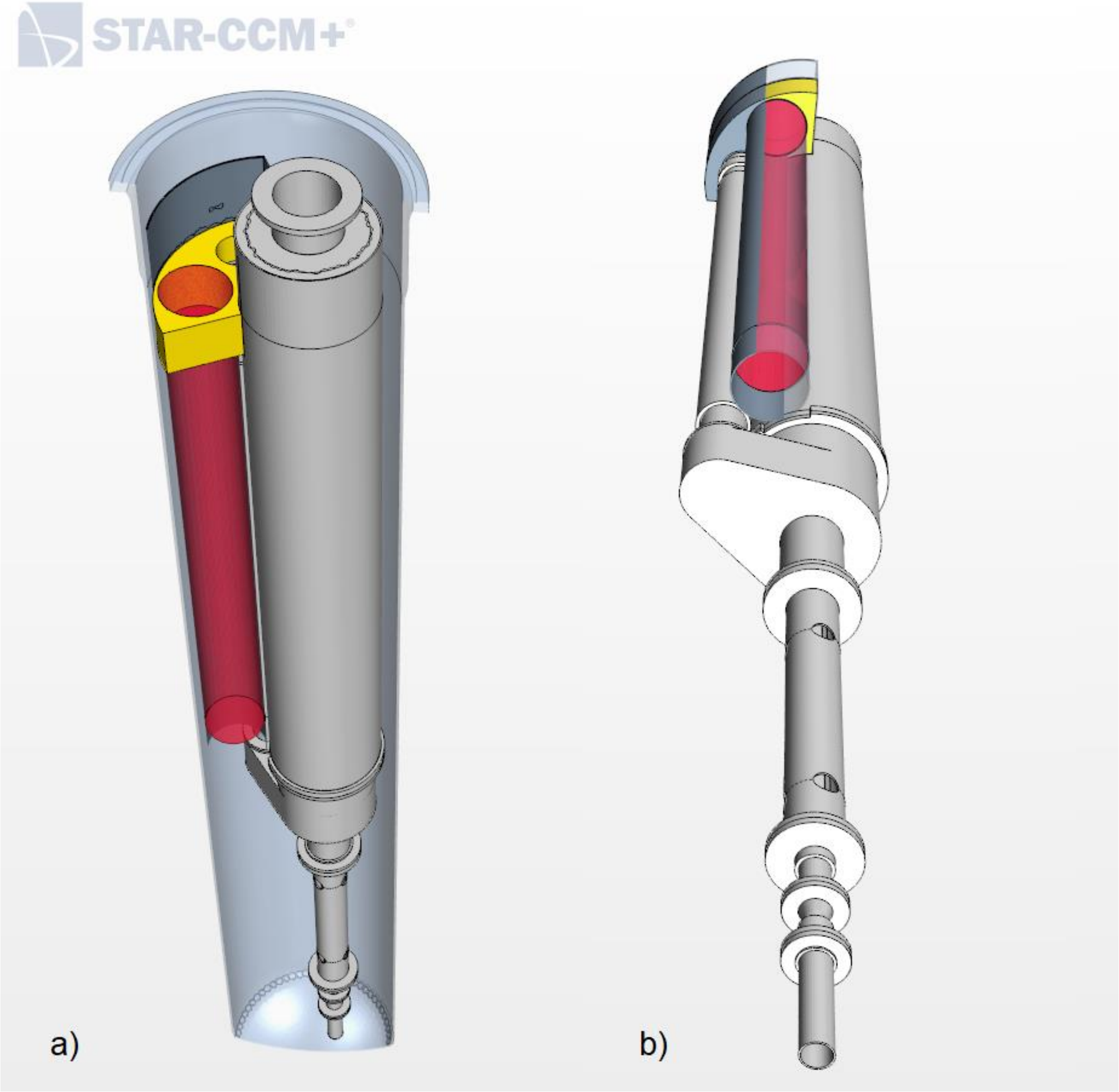

Figure 58. HX active region (red). a) top detail of the HX active region and general location. The LBE contained in the separator is also highlighted (yellow). b) bottom detail.

The values for each of the parameters of the previous equation (21) have been set as follows:

- T_0 has been set as a temperature profile linearly varying along the z coordinate, somehow matching the boundary conditions discussed in paragraph 3.3.2.1. This profile is meant to simulate the varying temperature of water throughout the evaporation process inside the HX tubes (Figure 59):

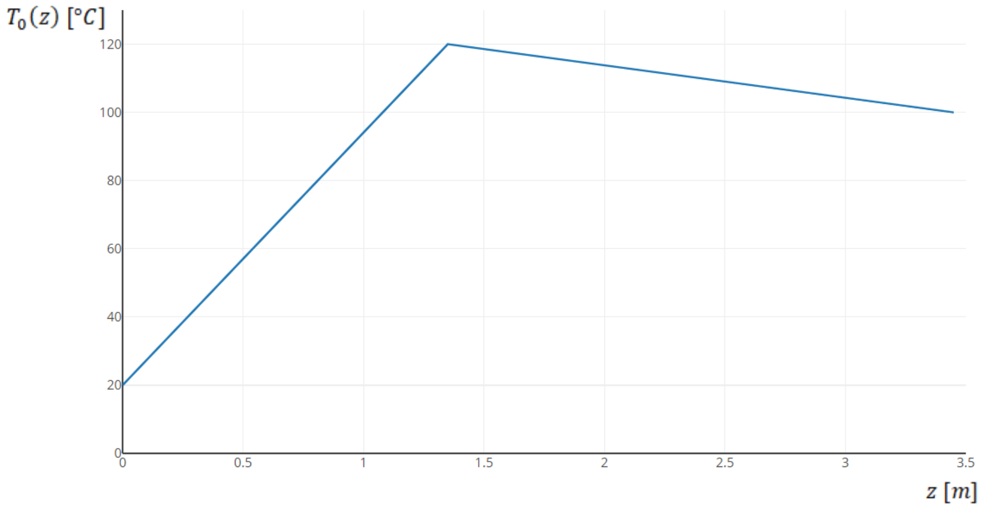

Figure 59. *The chosen $T_0(z)$ profile, meant to simulate the thermal evolution of the pressurized water inside the HX double bayonet tubes.*

- $\rho = 10340\ kg/m^3$
- $c_p = 145\ J/kgK$
- The relaxation time τ has been used as a fitting parameter, and has thus been gradually tuned during the simulation in order to reach the desired value of the total heat power removed by the HX (800 kW). Such total heat power ($\dot{Q}_{HX}$) is calculated as:

$$\dot{Q}_{HX} = \int_{HX_a} q_{HX,hex} dV \qquad [W] \tag{22}$$

Where HX_a in previous equation (22) represents the volume of the active region of the HX. The final appropriate value for the τ parameter has been set to 118 s.

3.3.3 Riser region design

During the regime experiment, an average LBE mass flow rate of approximately 65 kg/s flows through the CIRCE primary loop, as illustrated in Figure 60, accordingly to [7] (p.44). As can be noticed, the LBE mass flow rate shows a strongly fluctuating behaviour, constantly and irregularly oscillating between around 60 kg/s and 70 kg/s.

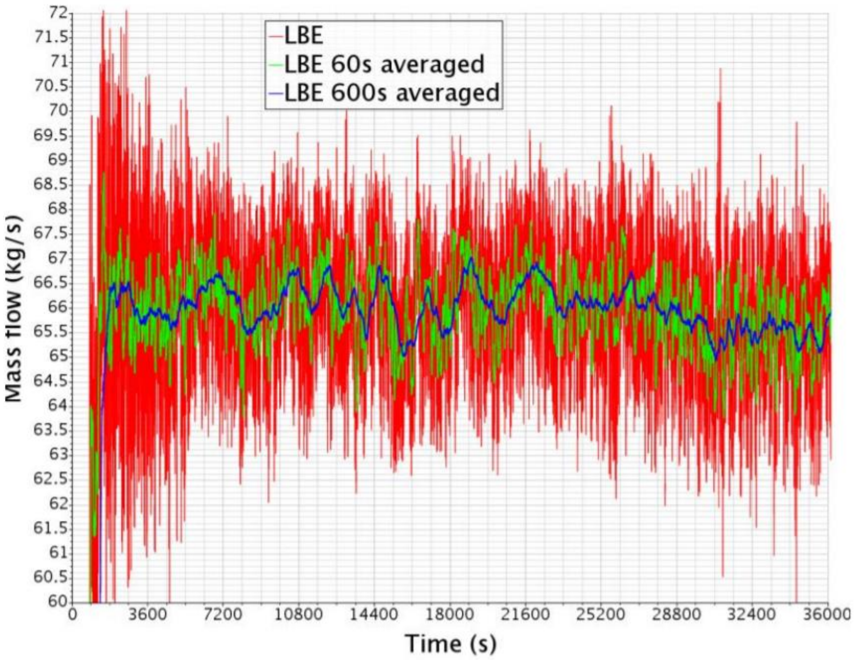

Figure 60. *Monitored mass flow rate in the CIRCE facility during the steady state phase of "Test 1" ICE experiment (from 0h to ~10h). Courtesy of ENEA.*

Such mass flow rate is generated by means of the argon gas lift system illustrated in the introductive chapter. In the present model, the LBE/argon bubbly multiphase flow has not been thoroughly modeled, and the mass flow rate through the circuit has been imposed by setting a homogeneous momentum source term ($\vec{F} = [F_x, F_y, F_z]$) in the region of the LBE flowing through the riser. This allowed for a much less computational demanding approach, since simulating such a complex multiphase flow condition would have required an advanced dedicated VoF model, which lies outside the main focus of this global CIRCE facility model.

Furthermore, considering that the gas lift system is meant to globally generate a **vertical** thrust for the LBE flow, the equivalent momentum source term essentially becomes:

$$\vec{F} = \left[F_x, F_y, F_z\right] = [0,0,F_Z] \quad \left[\frac{N}{m^3}\right] \tag{23}$$

The value for the F_z component imposed in this region has been finely tuned in order to ensure the circulation of the desired LBE mass flow rate through the circuit. At first, a starting value of 8700 N/m^3 (z direction) has been chosen accordingly to a previous CRS4 CIRCE simulation. This value has then been iteratively reduced to the 66% of its original value in order to reach the desired LBE mass flow rate of 65 kg/s. Hence:

$$F_z = 5742 \ \frac{N}{m^3}$$

The difference in the value of the F_z volumetric momentum source is mainly caused by the diverse evaluations of the fluid-dynamic resistances introduced by the FPS and HX porous media between the two models.

Figure 61 below specifies the region of the model where the F_z local momentum source has been imposed:

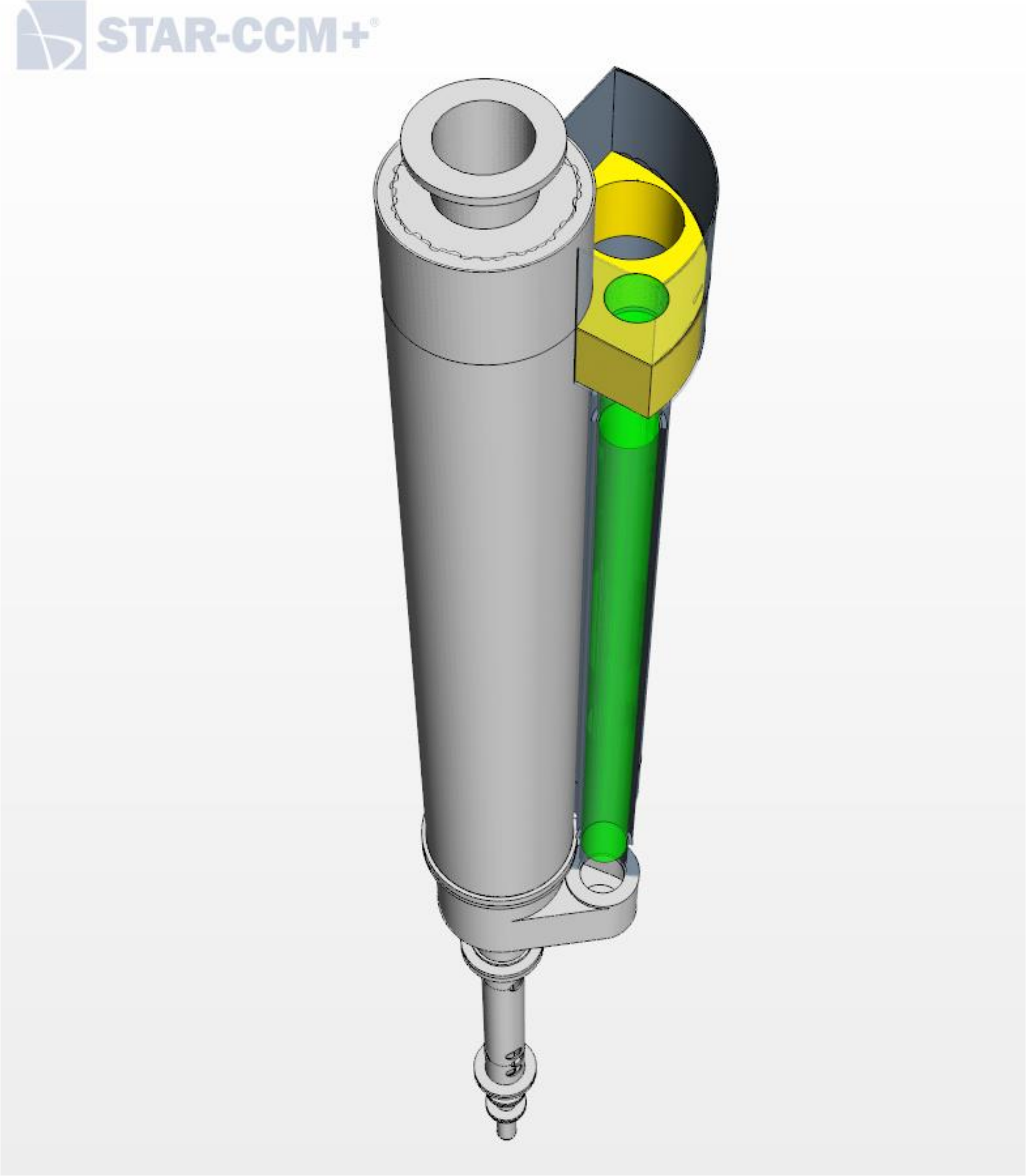

Figure 61. Detailed view of the riser active region, where the $\vec{F}$ momentum source has been imposed.

Another important effect to be noticed is the presence of the “leakage ring” element described in paragraph 1.3.5 and depicted in Figure 14. This element has been modeled as a homogeneous porous medium in the attempt of simulating the supposed direct leakage from the separator to the LBE bulk, with the following characteristics:

- Porous inertial isotropic component: $10^6\ kg/m^4$
- Porous viscous isotropic component: $10^4\ \frac{kg}{m^3 s}$

3.3.4 Dead volume region design (external boundary condition)

The characteristics of the various insulation layers of the dead volume have been discussed in the previous paragraph 3.2.2.2. Here, the main focus is set on the determination of a valid boundary condition for the internal surface of the dead volume, represented in Figure 62.

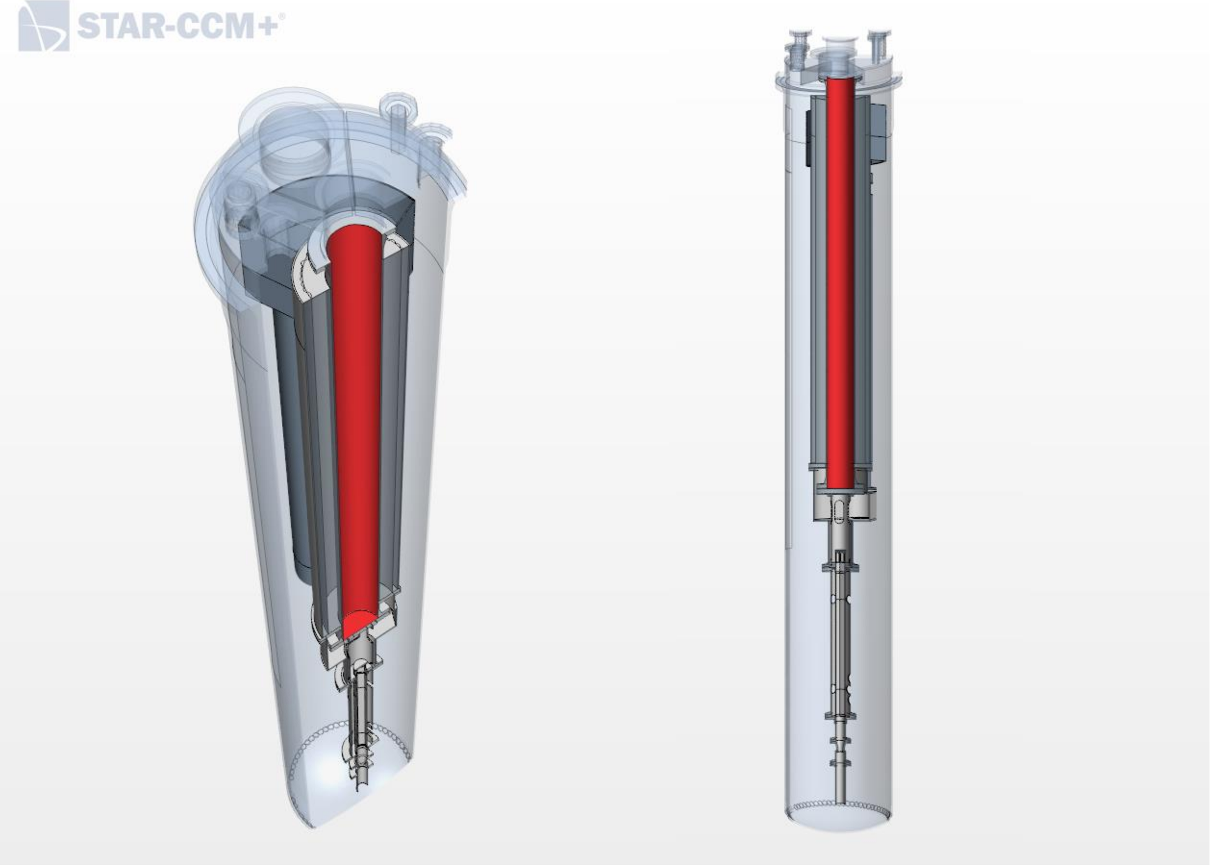

__Figure 62.__ Internal surface of the dead volume element.

The volume circumscribed by this surface hosts the terminating part of the fuel pins that are leaving the facility (and other instrumentation cables), which are refrigerated by a forced air flow, whose main characteristics (air mass flow rate, inlet temperature etc.) are unknown. It is anyway important to take into consideration the convective heat transfer taking place in this region, in order to give at least a qualitative representation of the phenomenon (especially of its effects on the insulation layers of the dead volume). The external boundary condition on this surface has then been assigned hypothesizing the following basic characteristics of the refrigerating air flow:

- Undisturbed flow temperature: $30\ °C$
- Air in forced convection (moderately low velocity)

This translates into imposing convective boundary condition, with the following parameters:

- Environmental temperature (undisturbed): $30\ °C$
- Heat transfer coefficient: $40\,\frac{W}{m^2K}$ (roughly estimated from the values reported in [4])

By doing so, a later (approximated) evaluation of the heat transfer towards the most internal region of the dead volume will be provided (discussed in paragraph 3.4.1).

3.3.5 Notes on the DHR during the regime experiment

Since the DHR is deactivated during the regime experiment (Figure 38), the internal region of this element hosting the refrigerating air flow (inside the DHR double bayonet tube) has been consequently deactivated. This means that the solvers will not perform any calculation relatively to this region while the simulation will be running. The deactivated air region of the DHR element is shown in previous Figure 42.

N.B.: all the other regions of the DHR are still obviously active (the LBE natural flow through its metallic elements is still simulated); this intervention is only meant to selectively deactivate only the air region of the element.

3.3.6 S100 Vessel and Top cover design (external boundary condition)

The external surfaces of the S100 Vessel and top cover of the real facility are insulated towards the external environment, by means of some insulation layers that have not been physically added to the present model geometry. In order to take into account (at least qualitatively) the presence of such layers, an appropriate thermal boundary condition has been imposed on the external surfaces of the abovementioned elements, by specifying the following parameters:

- Total heat transfer coefficient $U = 0.6\frac{W}{m^2K}$, calculated considering a thickness of 10 cm of a standard Cerablanket® insulating layer (thermal conductivity equal to $0.06\frac{W}{mK}$)
- Reference environmental temperature: 40 °C (estimated temperature on the external surface of the insulation layer)

3.4 Results of the steady state simulation.

After having discussed the procedures followed to model the behaviour of each different element of the facility, in this paragraph the results of the whole simulation will be illustrated and analysed. Later, these results will be compared to the official ENEA experimental data relative to the reference CIRCE ICE regime experiment.

3.4.1 Running the simulation and results

Due to the high number of cells in the global volume mesh of the model ($\sim 6{,}58 \cdot 10^6$ cells), the steady state simulation has been run employing 220 CPUs of the CRS4 main clusters. The results will now be portrayed and discussed for each different region of the facility.

FPS region: results

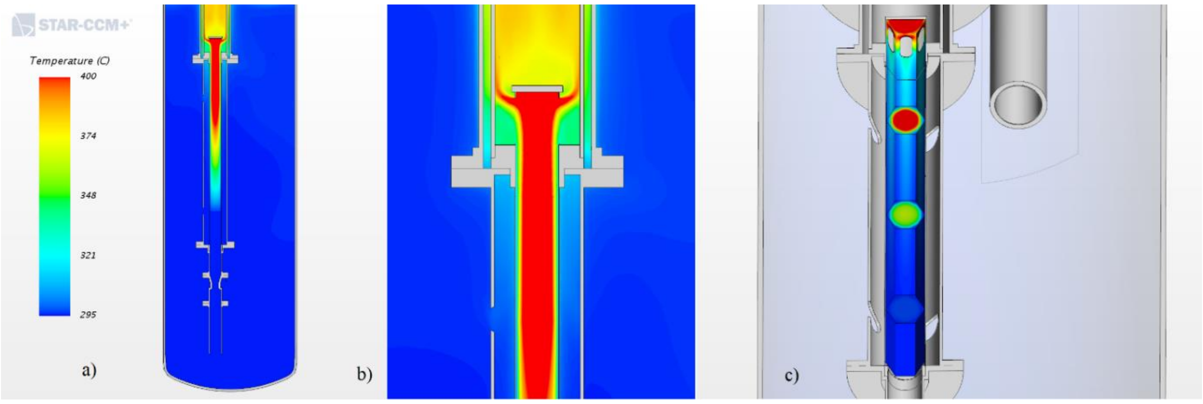

Figure 63. *Steady-state LBE temperature field in the FPS region. a) general configuration of the temperature field. As can be noticed, the effect of the radial volumetric heat source distribution $S(r)$ has had the desired "circumscribing" effect on the LBE temperature field, as discussed in paragraph 3.3.1.1. b) Detail of the LBE temperature field in the outlet region of the FPS, highlighting the turbulent homogenising process happening in the release pipe/conveyor zone. c) highlight of the temperature field on various sections of the FPS and on the internal surface of the hexagonal wrapper.*

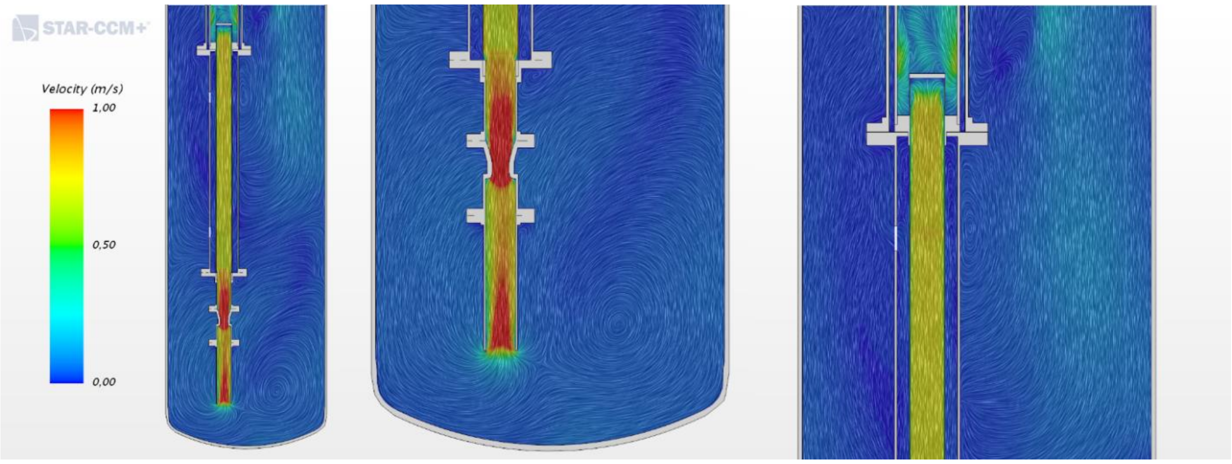

Figure 64. *Steady-state LBE velocity field in the FPS region. a) Global visualization. As can be noticed, the absolute values of the velocities are rather low, reaching their maximum in the throat of the venturi flow meter (detail in b)). Nonetheless, the flow regime through the FPS pin bundle (detail in c)) is still turbulent ($Re \cong 4.6 \cdot 10^4$, hydraulic diameter $D_h \cong 9.5\ mm$), mainly due to the very high density ($\rho \cong 10300\ kg/m^3$) and low dynamic viscosity of LBE ($\mu \cong 1.6 \cdot 10^{-3}\ Pa \cdot s$) in the present temperature conditions.*

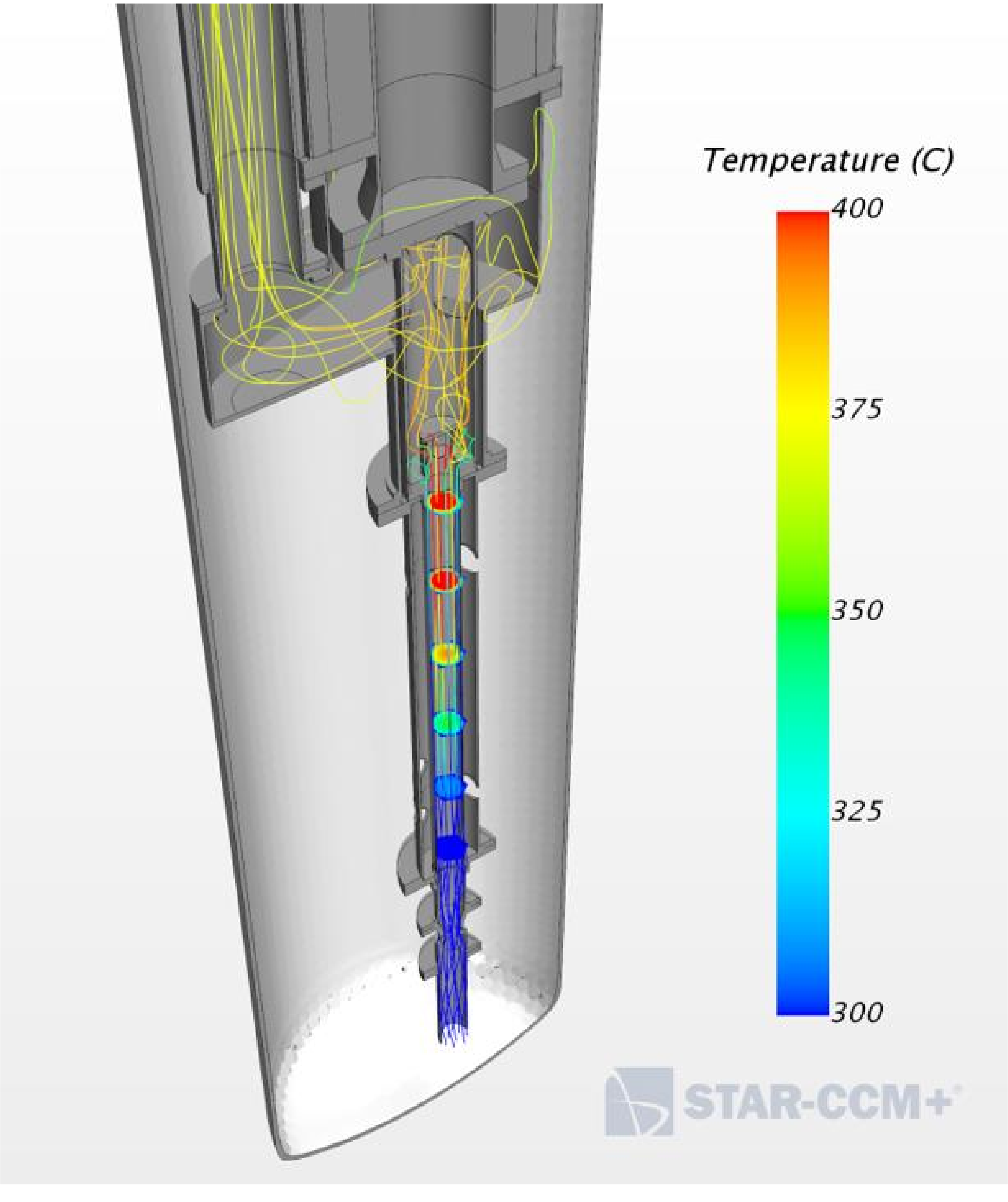

__Figure 65.__ 3D visualization of the LBE flow through the FPS element and into the conveyor region.

Conveyor region: results

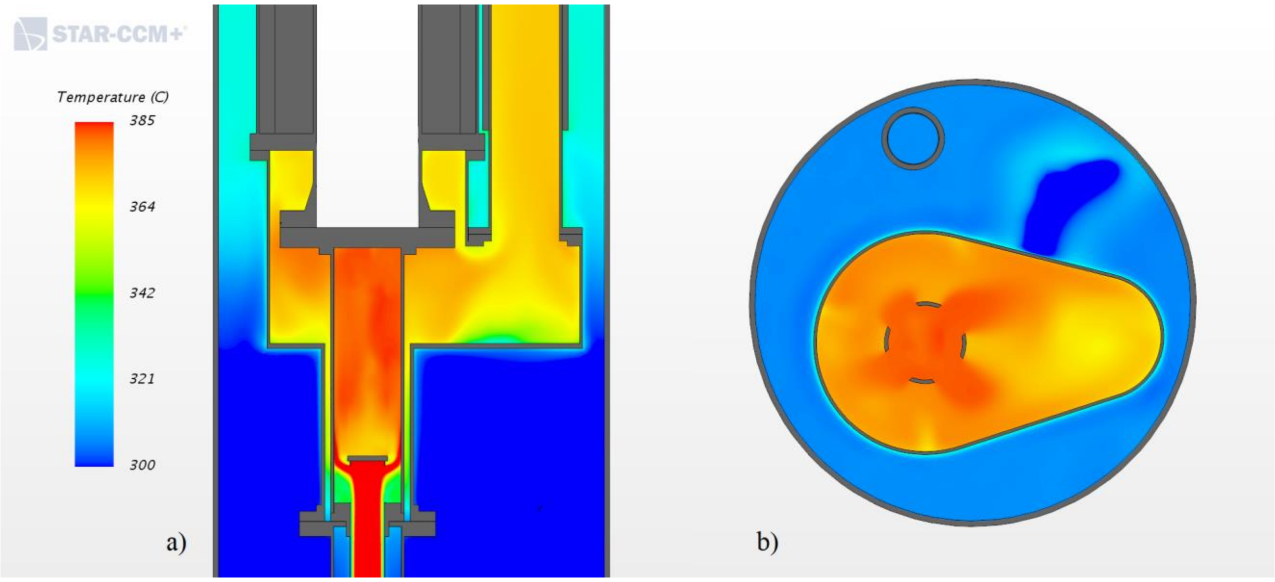

Figure 66. *Steady-state LBE temperature field in the conveyor region. a) Vertical section detail. The LBE flow exits the FPS element with an average temperature of ~385°C and undergoes a first homogenising process in the release pipe element. Later, the LBE flows into the conveyor, where it exchanges heat with the surrounding colder LBE contained in the bulk region, through the conveyor thin steel walls (not insulated). Due to this heat exchange, the average LBE temperature at the riser inlet section is around ~370°C. b) Horizontal section detail. The outflow from the release pipe into the conveyor is highlighted. Furthermore, the colder zone here depicted in the bulk region is related to the LBE exiting the neighbouring HX.*

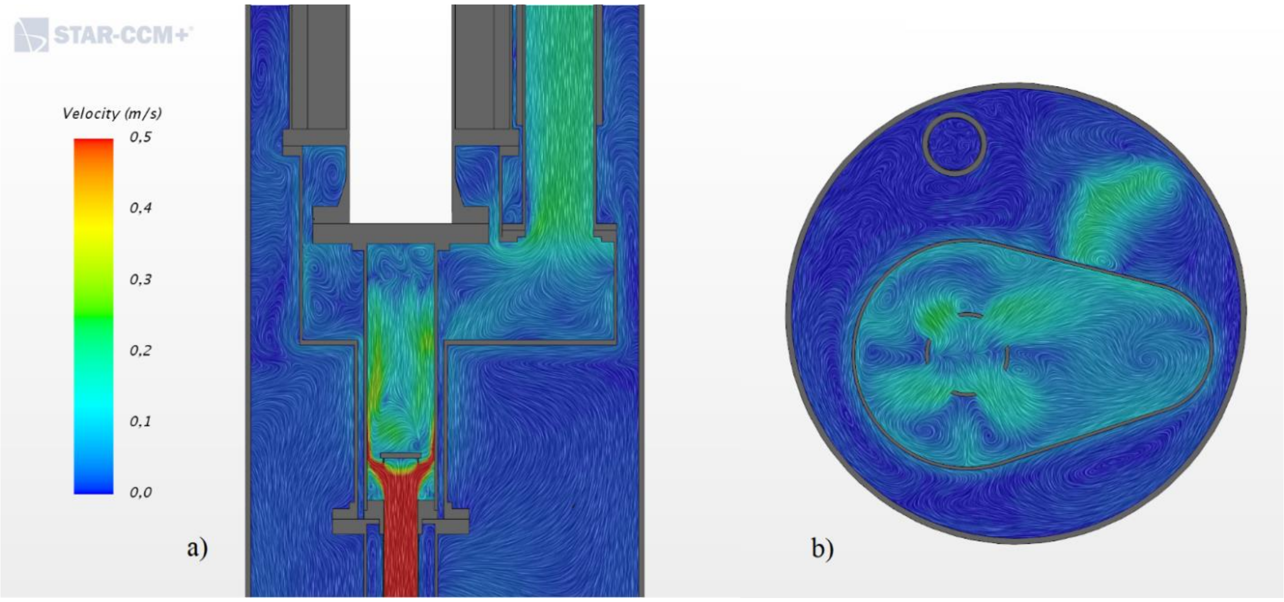

Figure 67. *Steady-state LBE velocity field in the conveyor region. a) Vertical section detail illustrating the outflow from the FPS element into the release pipe and then into the conveyor. As can be noticed, the absolute values of the velocities in the conveyor are even lower than the ones typical of the FPS region; furthermore, the LBE flow regime is completely turbulent. b) Horizontal section detail, also highlighting the higher velocities in the external bulk region due to the LBE outflow from the HX (directed downwards to the bottom of the vessel).*

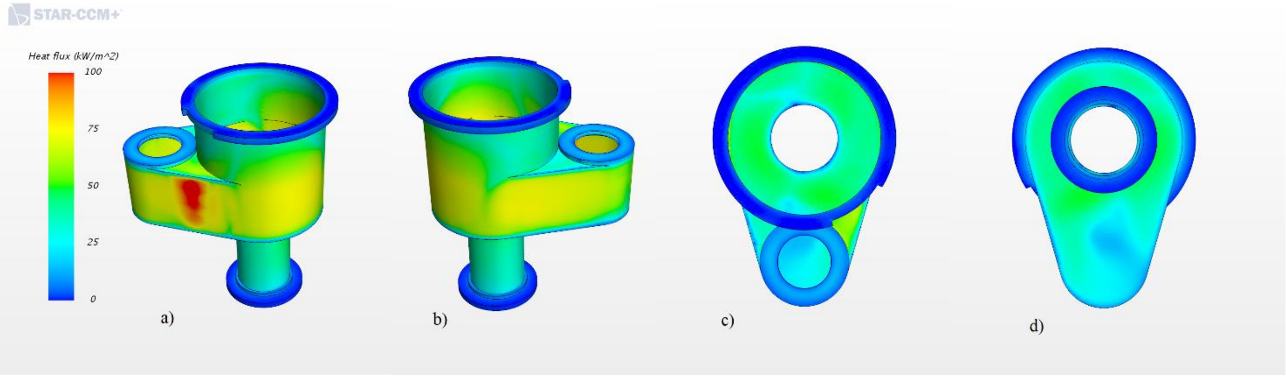

Figure 68. *Heat flux towards the LBE bulk region for the conveyor. As can be noticed, the values are relatively high with a maximum of 110 kW/m^2 concentrated in the lateral surface of the element (details a) and b)). Such high values are essentially due to the fact that the conveyor is not insulated towards the external bulk region. c) detailed view from above. d) detailed view from below. The total heat power supplied by the LBE in the conveyor to the external bulk region is around 100 kW.*

Riser region: results

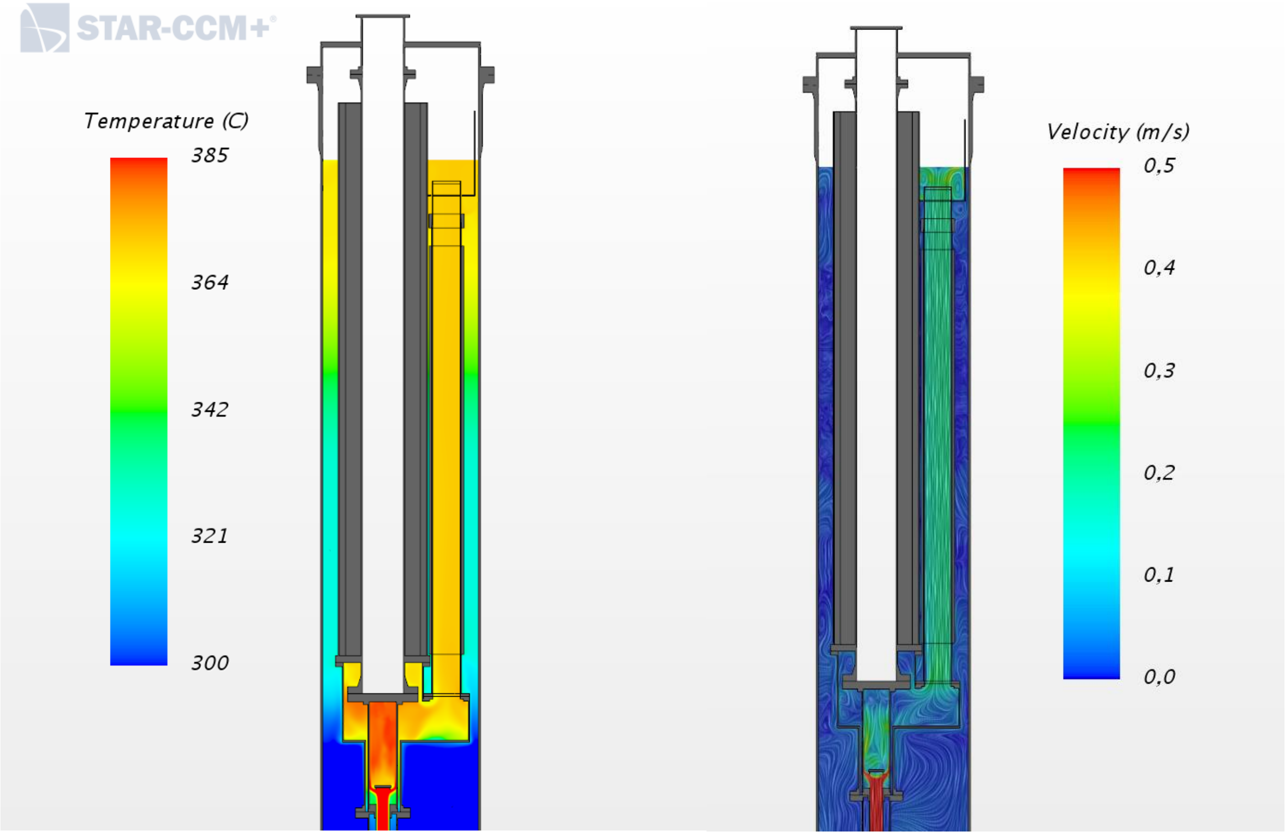

Figure 69. *Steady-state LBE temperature (left) and velocity (right) fields in the riser region. The insulation layer contributes to the almost complete constancy of the LBE temperature (~370°C) along the whole height of the component. Furthermore, the effect of the* $\vec{F}$ *momentum source discussed in paragraph 3.3.3 has an evident influence on the LBE velocity increase throughout the whole riser active region.*

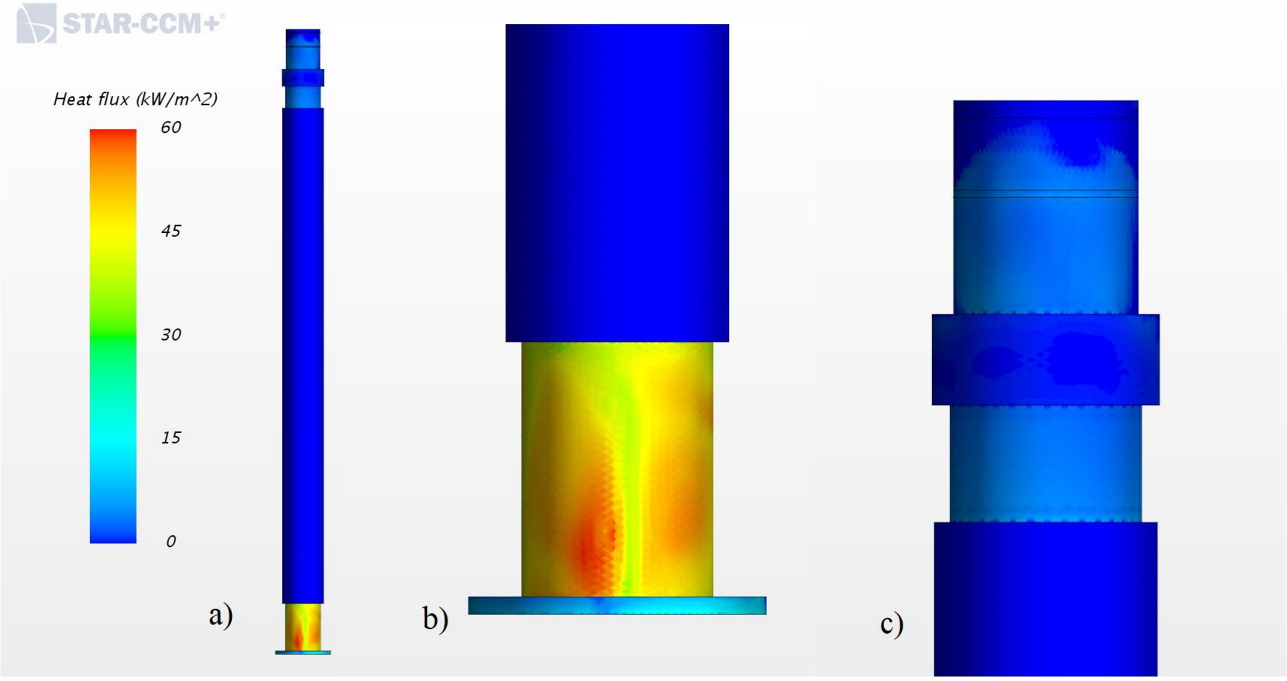

Figure 70. Heat flux towards the LBE bulk region for the riser. a) Global view. The presence of the insulation layer dramatically mitigates the heat flux towards the bulk for the whole intermediate region of the element. On the other hand, as can be observed in b), the bottom region of the riser is characterised by rather high values of the heat flux towards the bulk region. This is due both to the absence of insulation and to the strong temperature difference between the LBE in the bulk and in the riser. The higher portion of the element, highlighted in c), is also not insulated, but the heat flux is considerably weaker compared to the bottom region (b), due to the significantly higher temperatures reached by the neighbouring LBE in the bulk region (thermal stratification of the pool). Globally, the total heat power supplied by the LBE in the riser to the bulk is around 11 kW (10.9 kW of which through non-insulated zones only).

Separator region: results

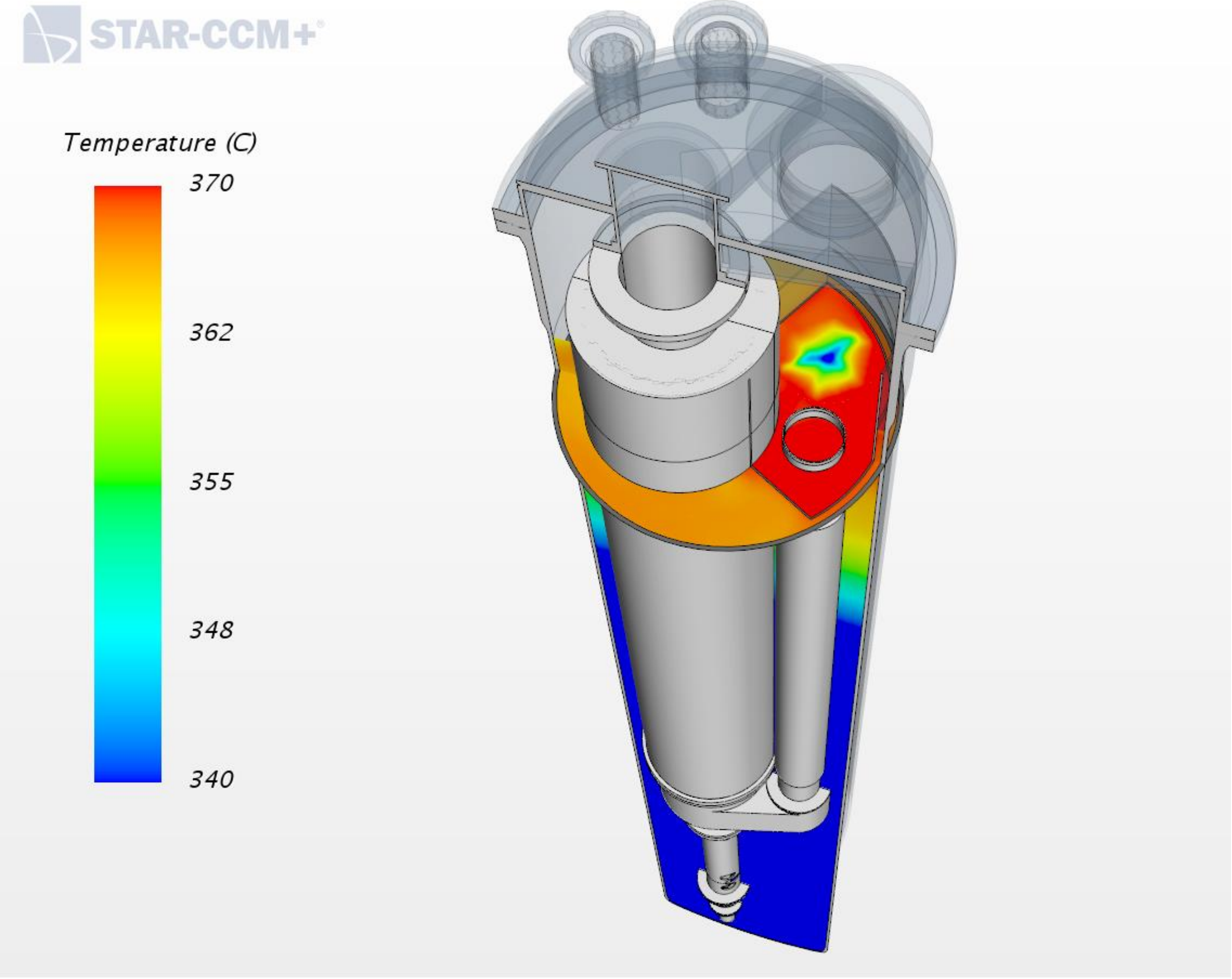

Figure 71. *Global view of the LBE temperature field in the separator region, also partially highlighting the thermal stratification of the underlying LBE bulk.*

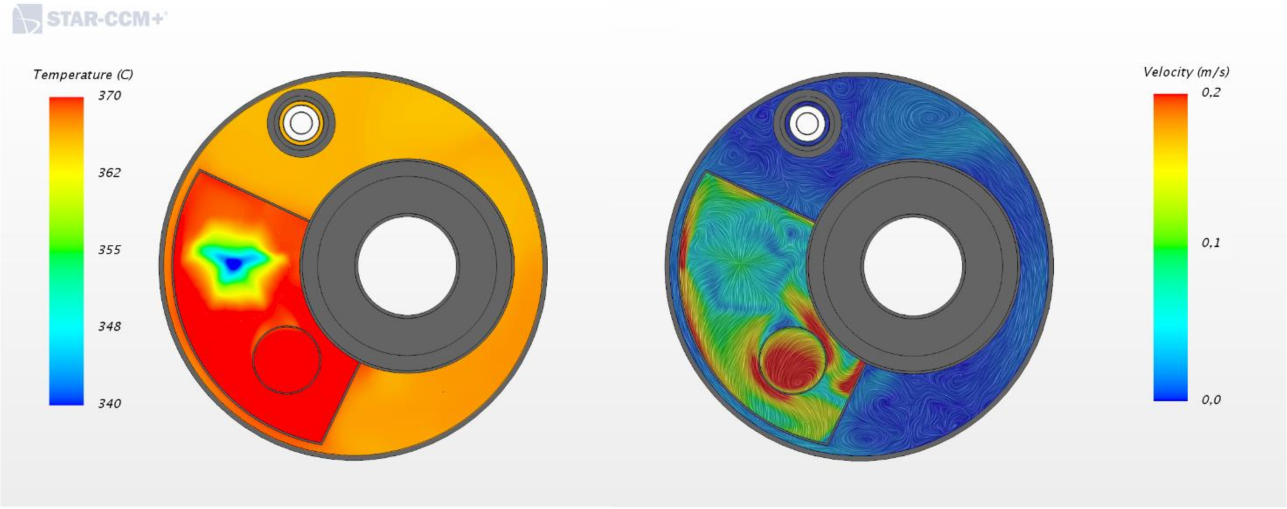

Figure 72. *Detailed horizontal section view of the LBE temperature (left) and velocity (right) fields for the separator region. The effect of the hexagonal zone of influence of the HX tubes is observable in both fields.*

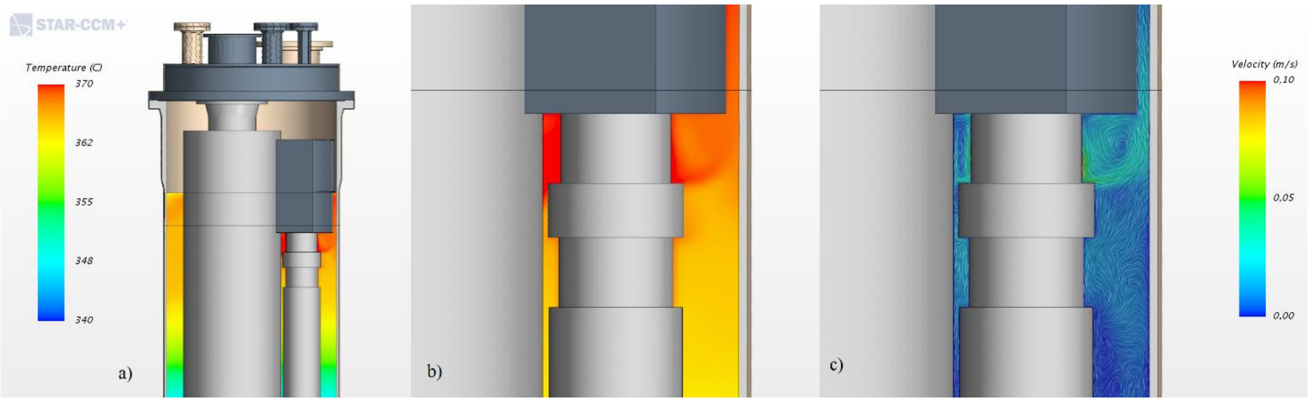

Figure 73. *Detailed view on the modeled LBE leakage phenomenon from the separator into the LBE bulk (previously discussed in paragraphs 1.3.5). a) Global view, also depicting the thermal stratification of the higher zone of the LBE bulk. b) Detail of the influence of the LBE leakage on the bulk thermal field around the riser element. c) Detail of the perturbance of the velocity field associated to the separator LBE leakage.*

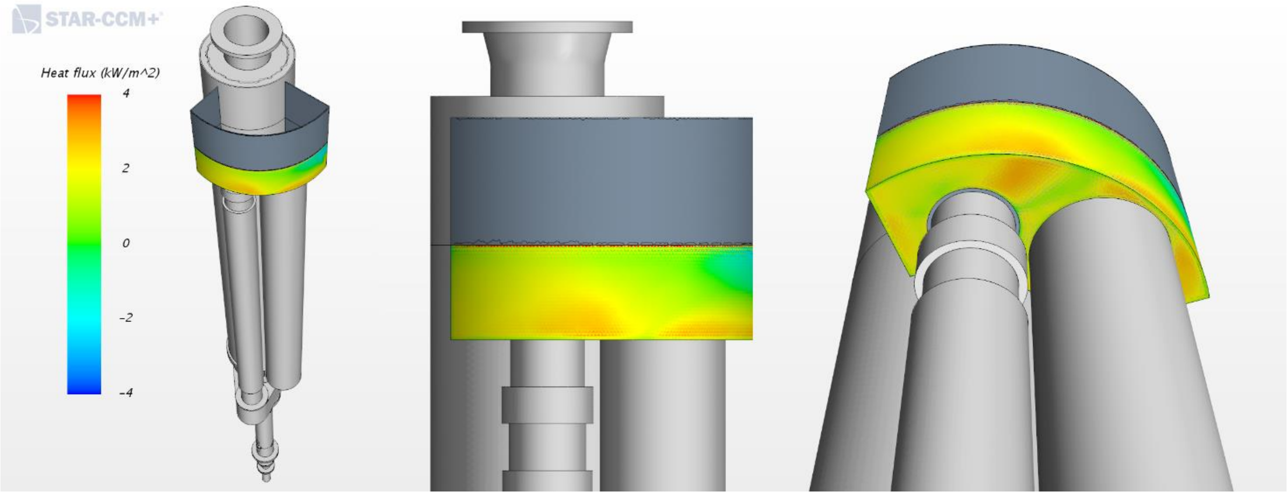

Figure 74. *Heat flux towards the LBE bulk region for the separator element. As can be observed, the behaviour of the separator from this point of view is almost neutral, with very low absolute values of the measured heat flux. This is due to the relatively small temperature difference between the LBE in the separator and the external LBE bulk (Figure 72). Furthermore, the heat flux values range from positive (flux exiting the separator towards the LBE bulk) to negative (flux incoming from the LBE bulk into the separator). Considering the total external surface, the separator elements supplies only ~1 kW of heat power to the LBE bulk..*

HX region: results

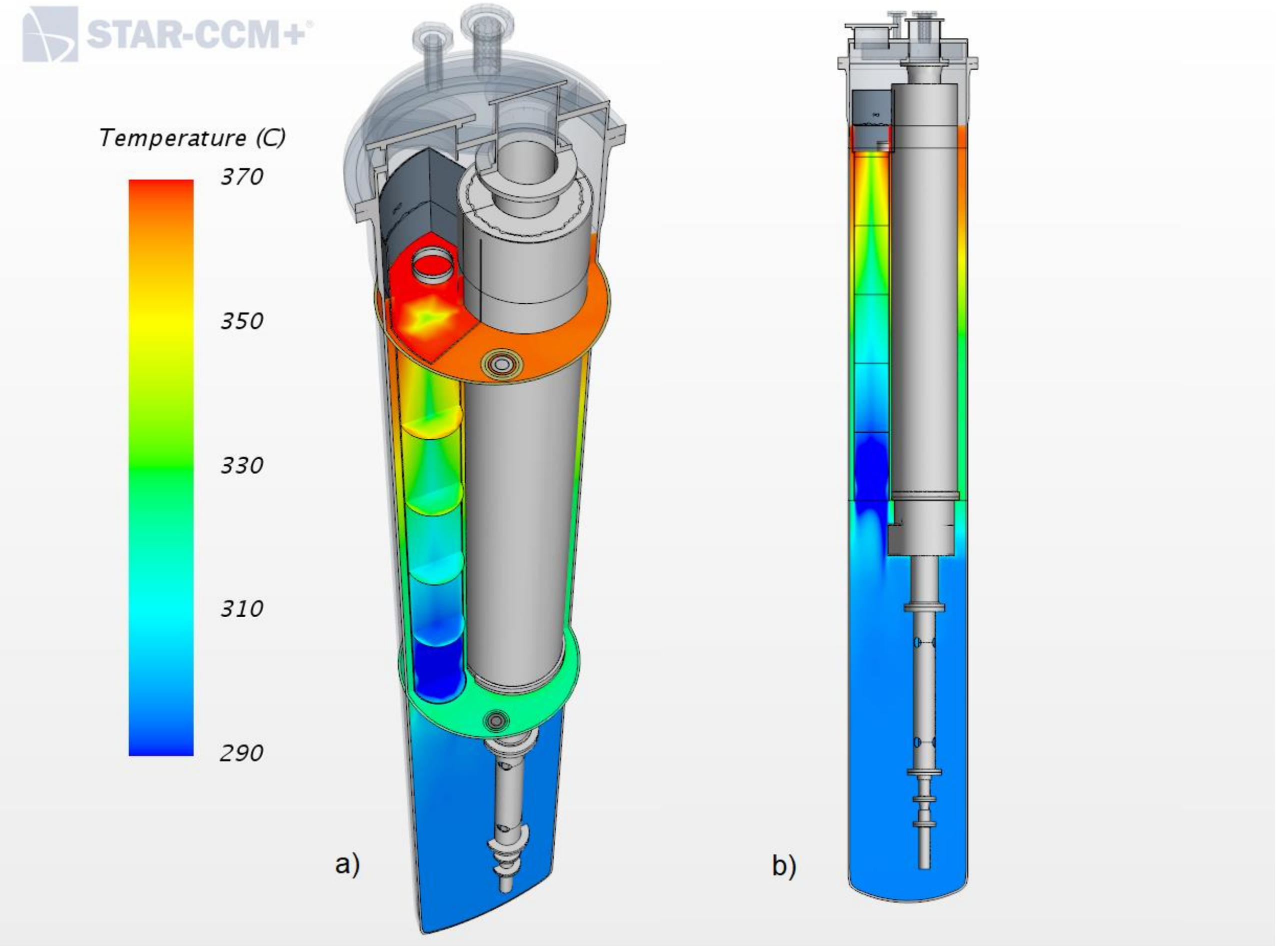

Figure 75. *Representation of the LBE temperature field in the HX region. a) Global view, also depicting the top inlet zone of the HX (inside the separator). Furthermore, some horizontal sections of the LBE in the HX active region are also shown. The effect of the hexagonal region of influence of the tubes is noticeably strong: in fact, the heat sink results concentrated in the most internal zones of the HX active region, due to the reasons previously discussed in paragraphs 3.3.2 and especially 3.3.2.2. b) Vertical section.*

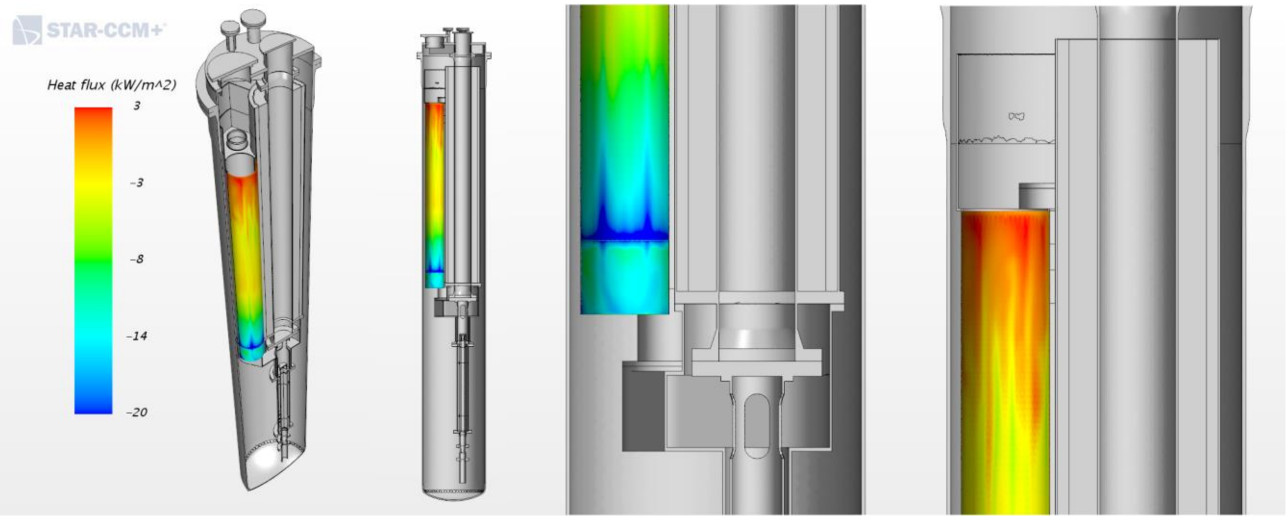

Figure 76. *Heat flux towards the LBE bulk region for the HX element. The higher zones of the HX tend to present small but positive values of the heat flux (flux exiting the HX towards the LBE bulk), while in the bottom regions, where the LBE temperatures inside the HX drop significantly (Figure 75), the heat flux is negative, and is evidently affected by the hexagonal region of influence of the tubes. Therefore, the total heat power* ***absorbed*** *by the LBE in the HX from the LBE bulk is around 18 kW.*

Dead Volume region: results

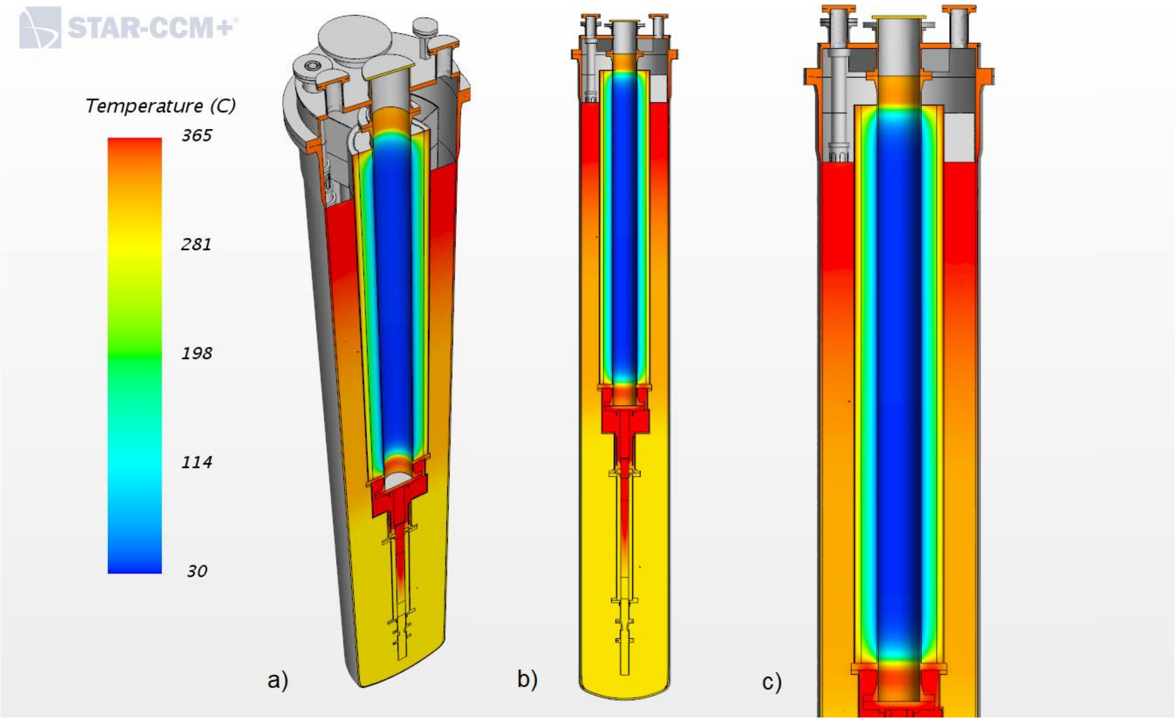

Figure 77. Temperature field of the dead volume region. a) Global view. b) Vertical section. c) Detail of the internal surface of the dead volume, where the convective heat flux boundary condition has been assigned, accordingly to paragraph 3.3.4.

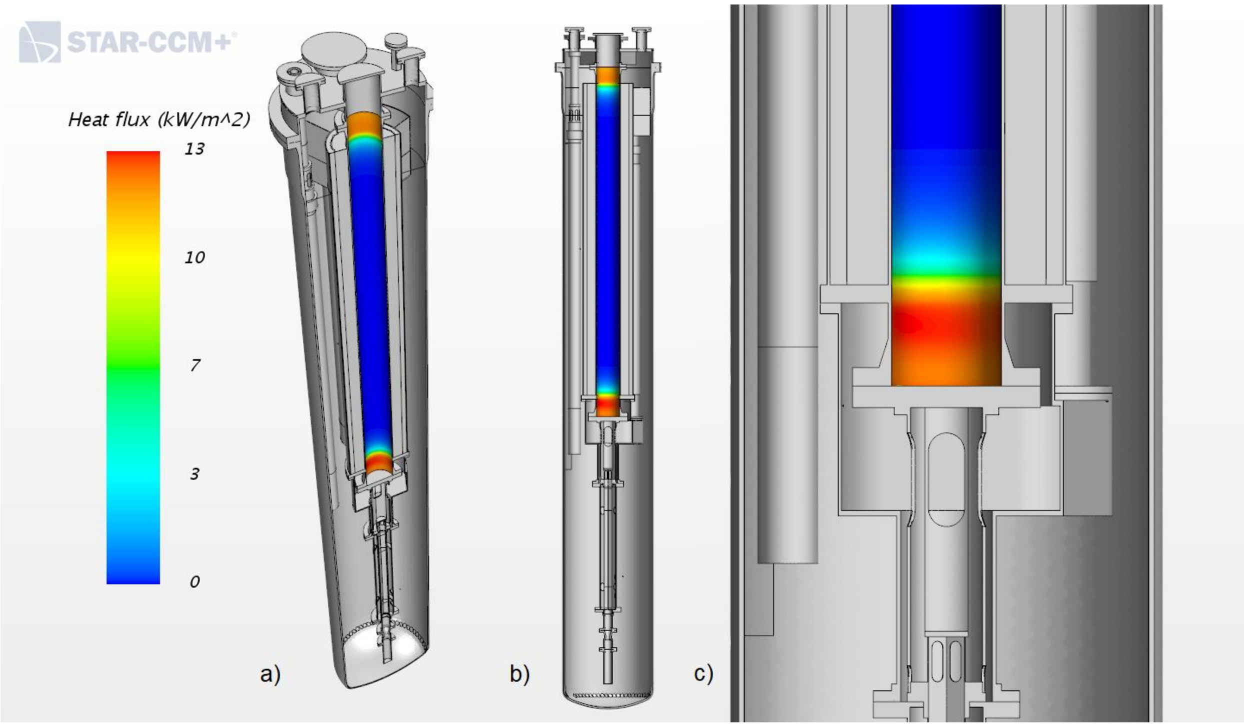

Figure 78. Heat flux towards the internal air region of the dead volume. a) Global view. The dead volume insulation layers (air/Cerablanket®) strongly reduce the heat flux towards the internal air region of the element. On the other hand, such heat flux reaches its maximum values near the top and bottom regions of the dead volume element, due to the complete absence of insulation. b) Vertical section. c) Detail of the bottom region of the internal surface of the dead volume. Here, the high values of the heat flux are also related to the significantly high LBE temperatures in the neighbouring conveyor region. The total heat power transferred to the internal air region is around 7.6 kW.

Bulk region: results

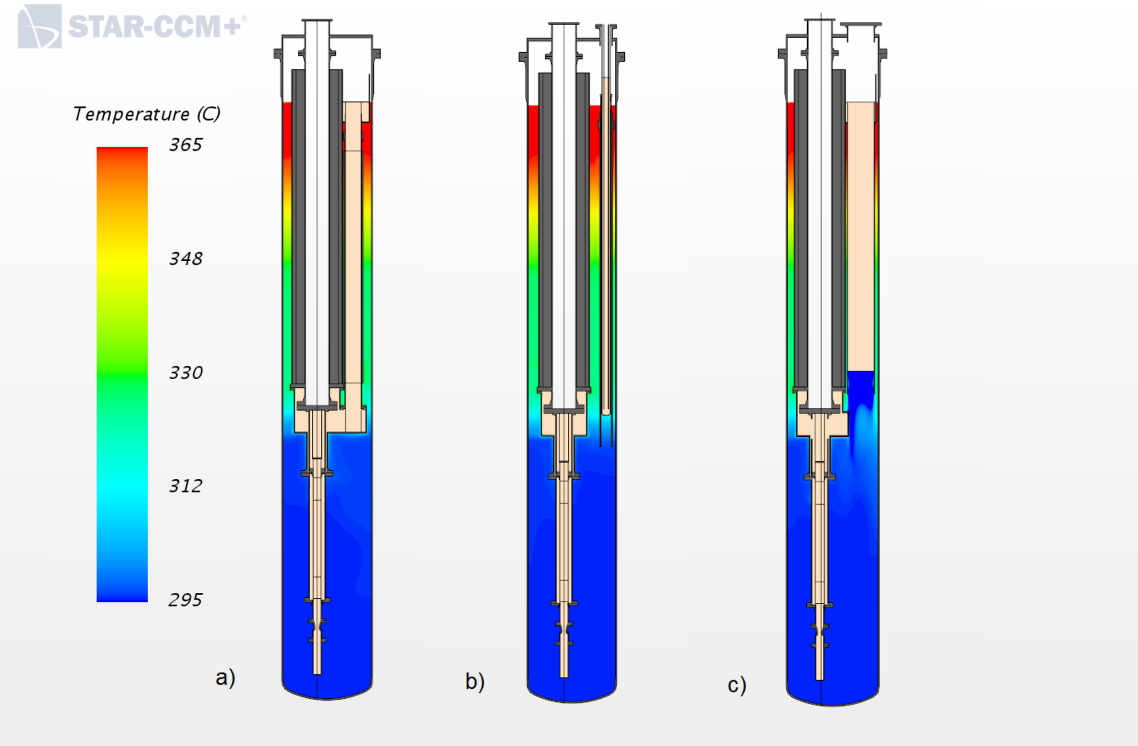

Figure 79. Steady-state LBE temperature field in the LBE bulk, highlighting the pool thermal stratification. a) Conveyor/Riser section. b) DHR section. c) HX section.

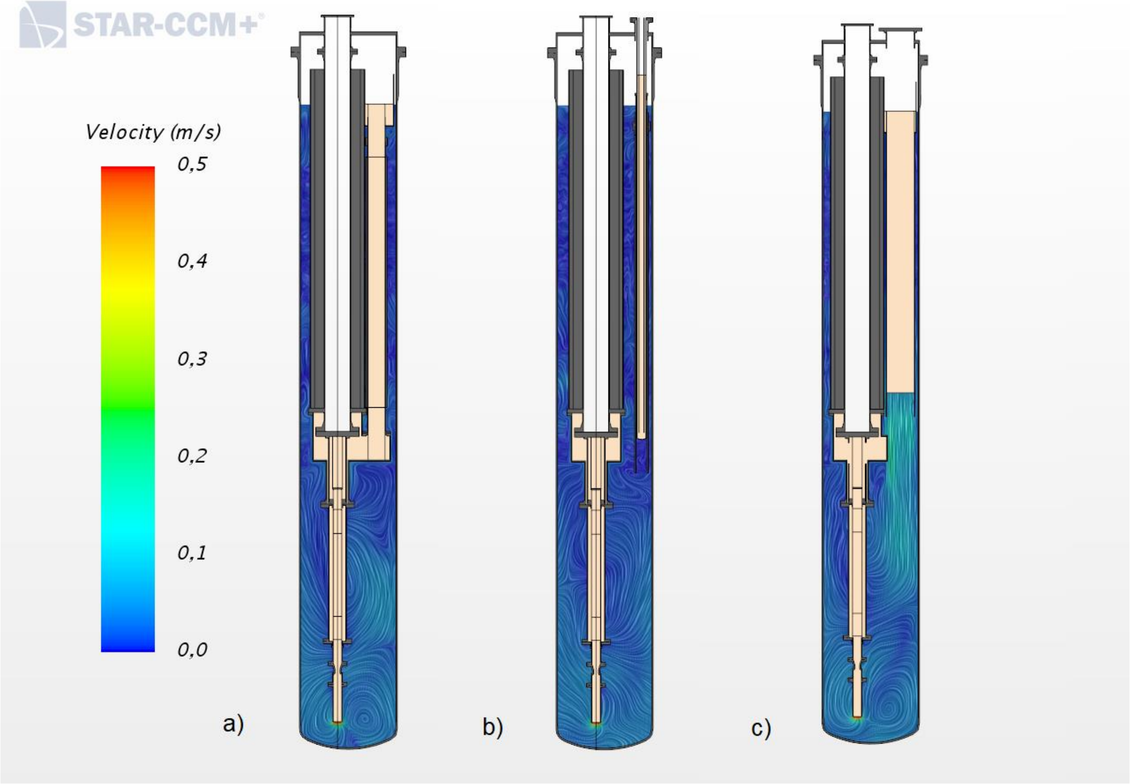

Figure 80. Steady-state LBE velocity field in the LBE bulk. a) Conveyor/Riser section. b) DHR section. c) HX section; the velocity increase at the HX outlet is associated to natural convection effects (low LBE temperatures, with reference to Figure 75b).

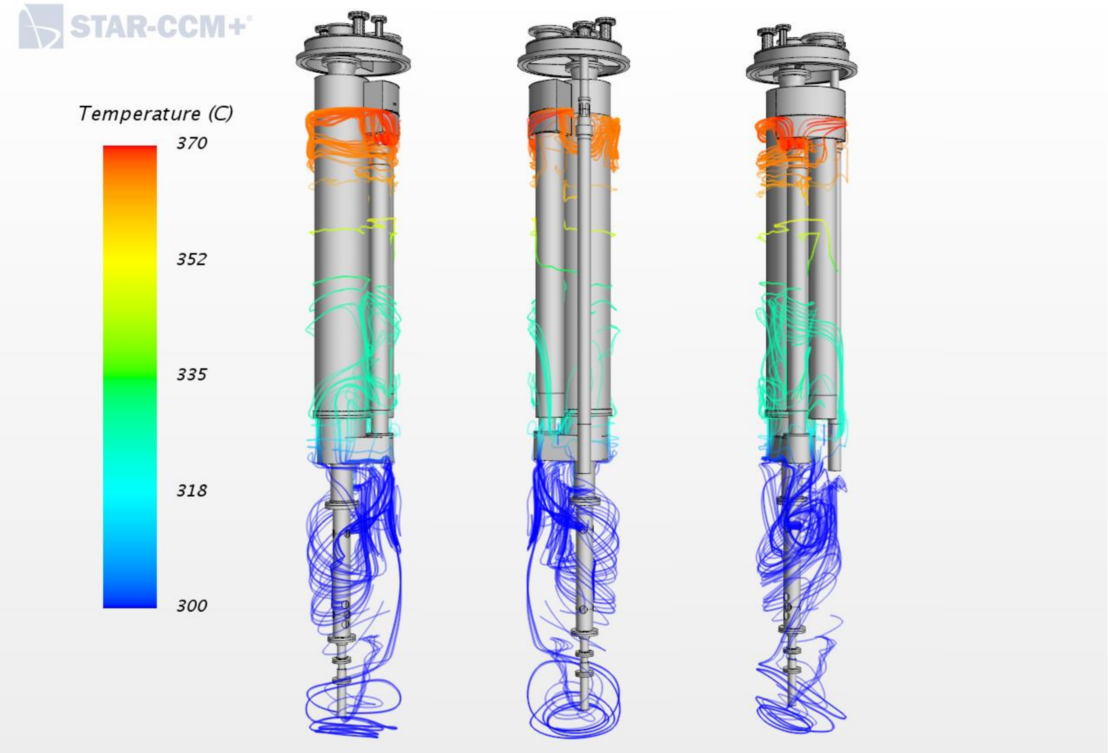

__Figure 81.__ Streamline representation of the characteristics of the LBE flow in the bulk region. The chaotic nature of the flow is evident, especially in proximity of the bottom region of the vessel.

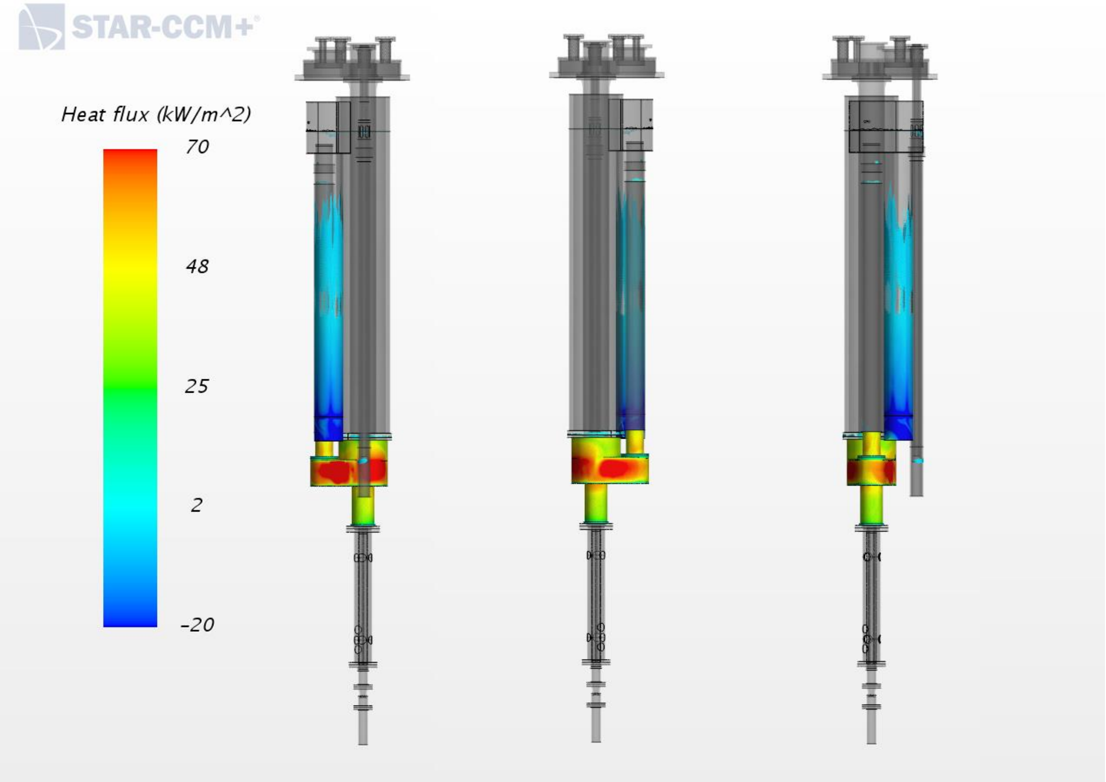

__Figure 82.__ Visualization of the most critical components of the facility from the point of view of the heat flux towards the LBE bulk region. As can be noticed, such elements are the conveyor and the HX, as previously illustrated in Figure 68 and Figure 76.

Furthermore, Table 9 summarizes some crucial heat transfer values regarding the different elements of the facility:

Conveyor: Heat pwr. towards LBE bulk [kW]	100
Riser: Heat pwr. towards LBE bulk [kW]	11
Separator: Heat pwr. towards LBE bulk [kW]	1
HX: Heat pwr. absorbed from LBE bulk [kW]	18
Dead Volume: Heat pwr. towards the internal air region [kW]	7,6
S100 Vessel: Heat pwr. towards the ext. environment [kW]	4,6

Table 9. *Important steady-state heat transfer values.*

3.4.2 Comparing the CFD results to the experimental data

In order to correctly validate the CFD results reported in the previous paragraph 3.4, a satisfying adherence to the experimental data is mandatory. In this same line of thought, it is also fundamental to preliminary analyse which peculiarities of the real experiment are paradigmatic of the functioning of the CIRCE facility, and direct the analysis towards them.

3.4.2.1 Bulk thermocouple lines

The first and foremost experimental observation that is generally considered as strongly representative of the global behaviour of the facility is the analysis of the LBE temperature field in the bulk region. Such field is constantly monitored throughout the duration of the whole experiment (during both the regime and the SCRAM phases) by means of a large number of thermocouples immersed in the LBE bulk region. These thermocouples are organized in nine separate vertical "lines" (from line A to line I), installed as illustrated in the following Figure 83.

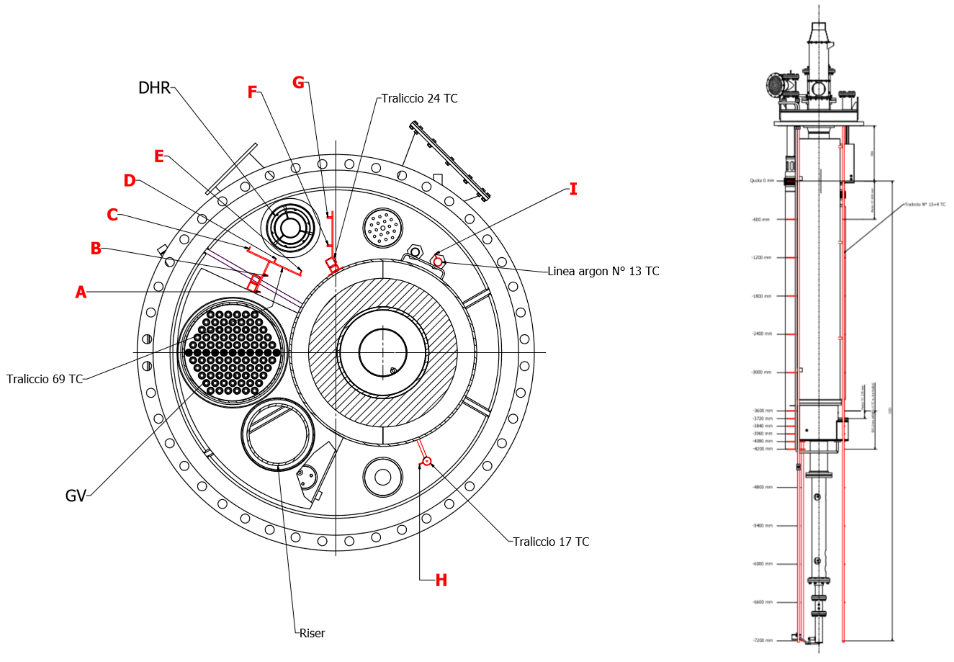

a) b)

Figure 83. Technical drawings illustrating the position of the various thermocouple lines,. a) Bottom horizontal section. b) Vertical global view. Image courtesy of ENEA.

These thermocouple lines are installed in different locations throughout the LBE bulk region, in the attempt to obtain a satisfying portrayal of the temperature field of the whole region. In order to replicate the measurements of these thermocouples, the four most important lines A, B, H and I (shown in previous Figure 83) have been replicated in the present CIRCE steady state model; this has been done by creating a large set of probe points, each one associated to a single thermocouple of the abovementioned lines. The "simulated" lines in the current model are depicted in the following Figure 84.

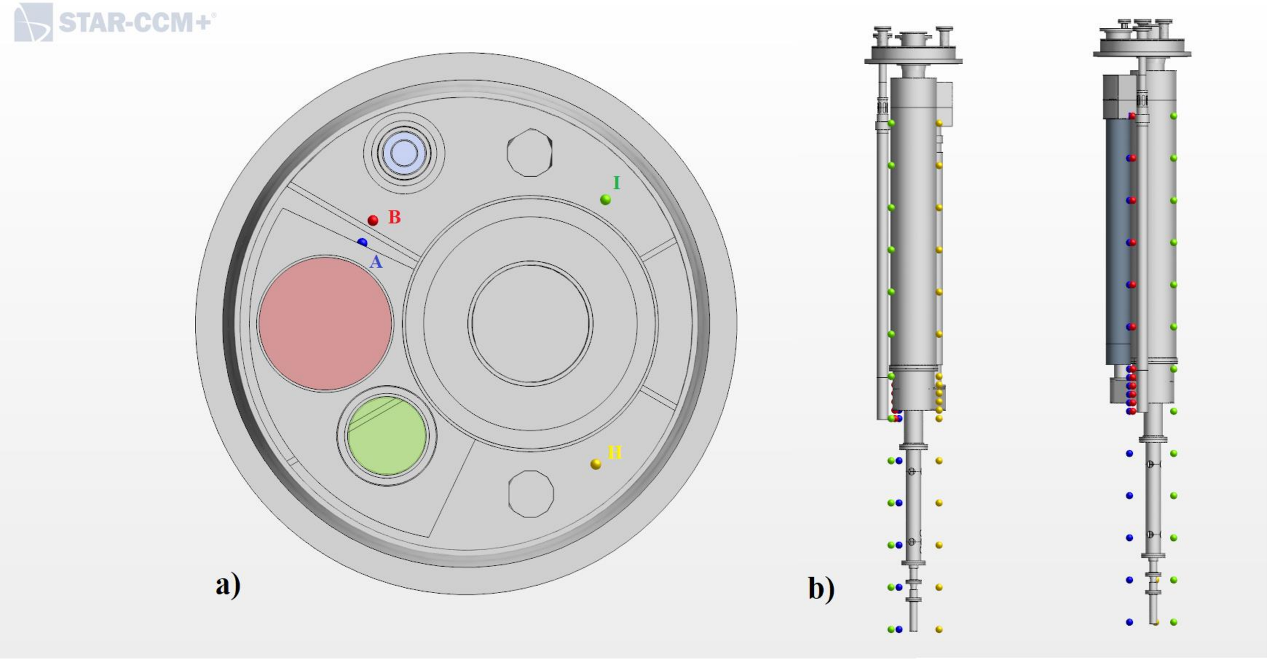

Figure 84. Visualization of the modeled thermocouple lines, matching lines A,B, H and I depicted in Figure 83. a) Bottom horizontal section. b) Vertical global views.

N.B.: thermocouple lines C, D, E, F and G have not been added to the present model since their location is very similar to the location of lines A and B.

In the following plots (from Figure 85 to Figure 88) the temperature measurements of the real thermocouples (relatively to "Test 1" reported in [6]) are compared to the ones acquired via the "simulated" thermocouples of the CFD model; the "position" axis is oriented downwards vertically, with the origin coinciding with the position of the highest thermocouple of each line.

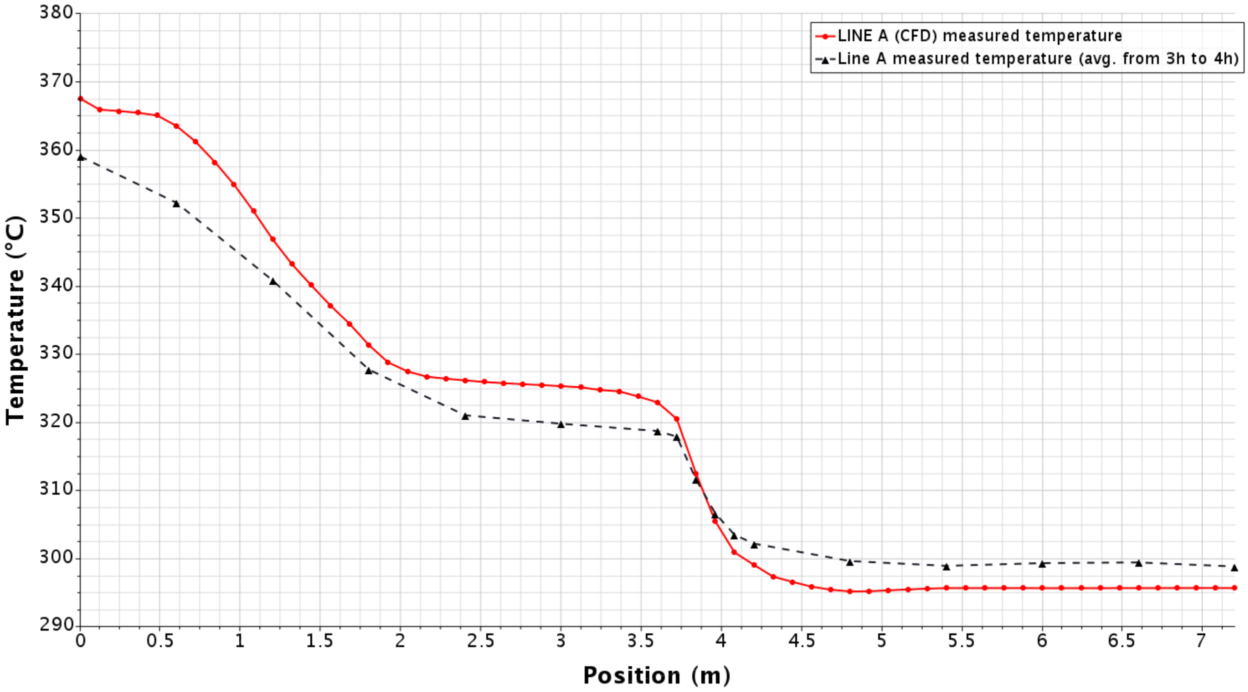

Figure 85. LBE bulk temperature profile measured by thermocouples LINE A. Comparison between the steady-state CFD results and the ENEA experimental data.

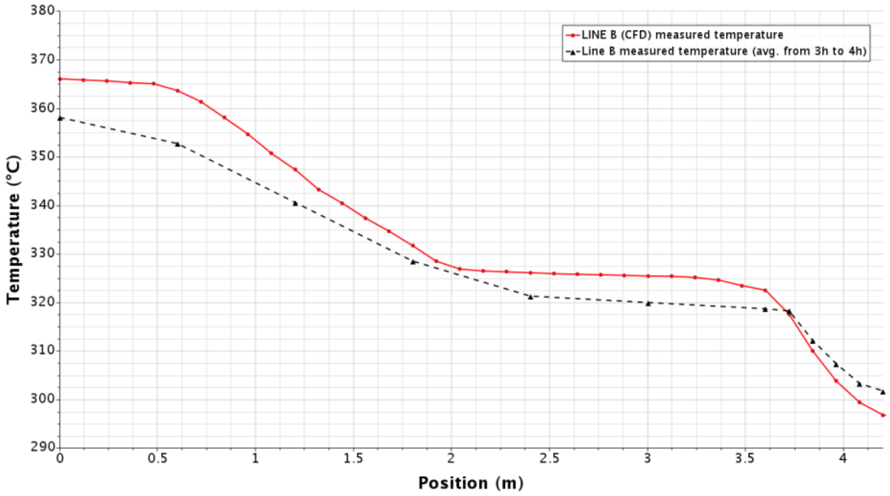

Figure 86. *LBE bulk temperature profile measured by thermocouples LINE B. Comparison between the steady-state CFD results and the ENEA experimental data.*

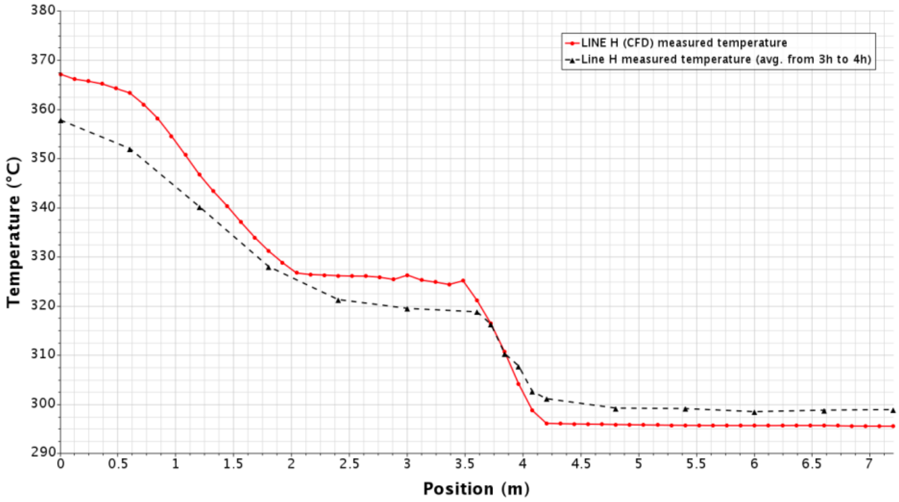

Figure 87. *LBE bulk temperature profile measured by thermocouples LINE H. Comparison between the steady-state CFD results and the ENEA experimental data.*

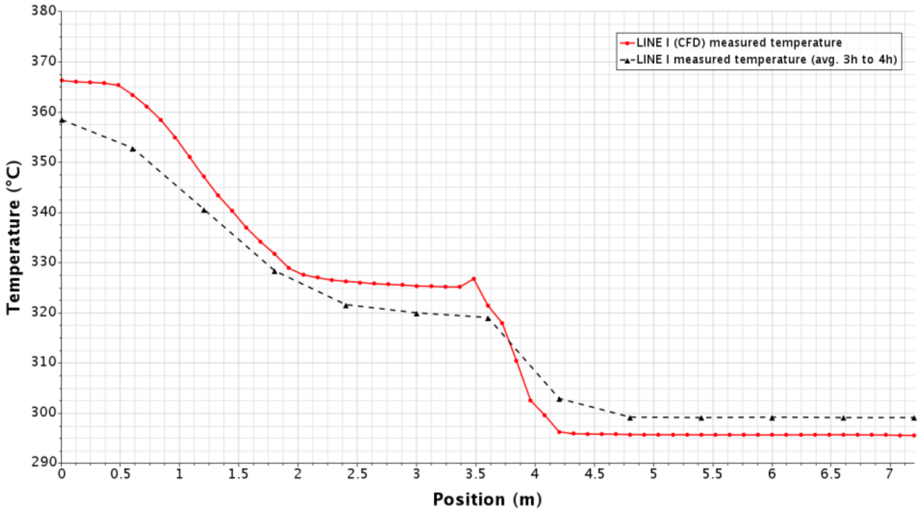

Figure 88. *LBE bulk temperature profile measured by thermocouples LINE I. Comparison between the steady-state CFD results and the ENEA experimental data.*

As can be noticed by the previous comparisons, the bulk temperature profiles measured by the CFD model recall the most important features of the real temperature profile in the bulk region. The modeled and experimental profile shapes are essentially very similar, which suggests that the present CFD model is adequately capable of simulating the general behaviour of the facility (especially in the LBE bulk region) with a good degree of accuracy. At the same time, the model appears to consistently overestimate the absolute value of the LBE temperatures in the higher regions of the bulk (CFD maximum error of +2.5% on the real temperature values), and underestimate the temperatures in the lower regions (CFD maximum error of -1% on the real temperature values). This comparison between the real and simulated thermocouple measurements has historically been at the centre of many previous CIRCE models. Figure 89 below, for instance, shows the same comparison as reported by the previous CRS4 CIRCE ICE model, reported in document [7] (p.56).

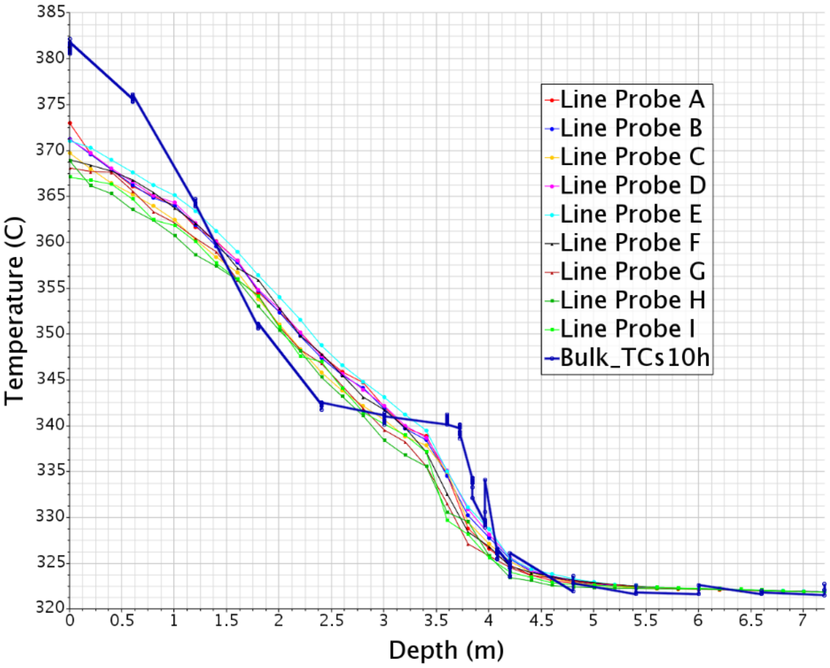

Figure 89. LBE bulk temperature profile measured by thermocouples lines. Comparison between the steady-state CFD results and the experimental data. Older CRS4 CIRCE ICE model, ref. document [7] (p.56). Courtesy of ENEA.

In this case, the CFD-modeled thermocouples generate a bulk temperature profile that retains some characteristics of the real one, but in a more inaccurate way if compared to the result of the present model (from Figure 85 to Figure 88). This is most probably due to the different approach used to simulate the behaviour of the HX element of the facility, which is one of the deepest differences between the two models. In the older simulation, in fact, the HX was modeled as a very simple homogeneous porous medium, not taking into account all the concentrated effects in the hexagonal zone of influence of the HX tubes (which, conversely, has been at the centre of the HX analysis in the present model, as illustrated in paragraph 3.3.2).

Additionally, this furthers the hypothesis that the LBE flow through the HX is capable of strongly affecting the temperature field in the LBE bulk region.

3.4.2.2 HX temperature drop

Figure 90 below reports (accordingly to the reference "Test 1" experiment reported in [6]) the measured average values for the inlet and outlet LBE temperatures in the HX element. As can be noticed, the real values tend to be stable during the initial phase of the regime experiment (condition modeled by the present model), while they later tend to grow before the beginning of the SCRAM experiment.

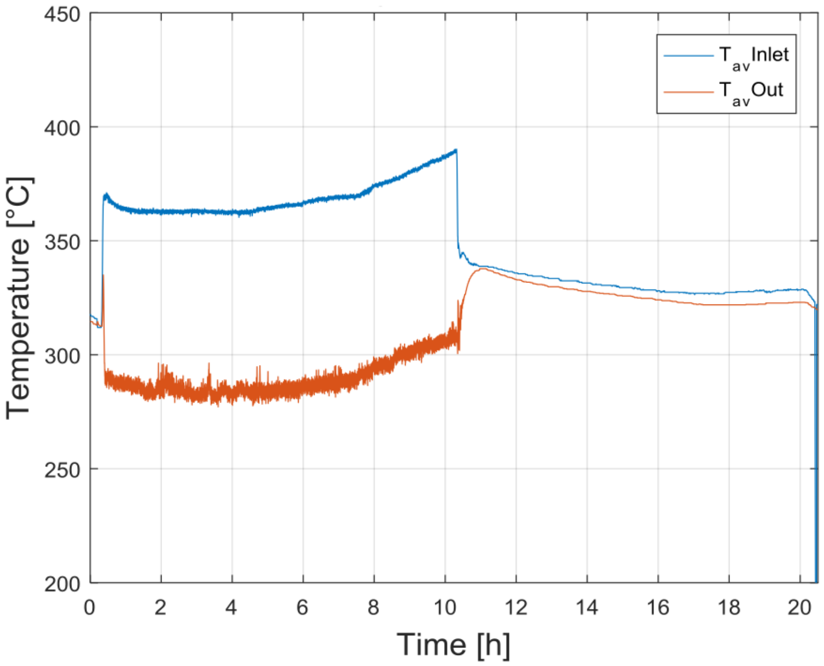

__Figure 90.__ Average temperatures at the inlet and outlet sections of the real ICE HX, during "Test 1", Ref. document [6] (p.37). Courtesy of ENEA.

Accordingly to Figure 90 , during the "proper" regime condition of the real experiment (time between ~1 h and ~5 h), the measured LBE average values in the HX inlet and outlet sections are:

- Average HX inlet temperature $\overline{T}_{IN,HX} \cong 365\ °C$
- Average HX outlet temperature $\overline{T}_{OUT,HX} \cong 285\ °C$
- $\Delta T_{HX} \cong 80\ °C$

The values calculated by means of the CFD model are:

- (CFD) Average HX inlet temperature $\overline{T}_{IN,HX} = 369\ °C$
- (CFD) Average HX outlet temperature$\overline{T}_{OUT,HX} = 284\ °C$
- (CFD) $\Delta T_{HX} = 85\ °C$

Comparing the real and simulated temperature values, the results appear very close. This confirms that the porous media approach followed to model the HX element illustrated in paragraph 3.3.2.2

portrays the behaviour of the element with a good degree of accuracy. Figure 91 below shows a detailed representation of the LBE temperature field in the HX (the effect of the hexagonal zone of influence of the tubes is definitely visible).

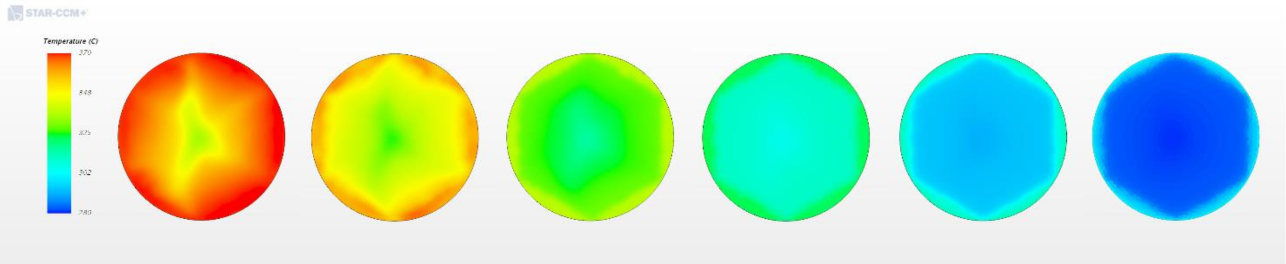

Figure 91. *Visualization of the temperature field on various horizontal sections of the HX active region. These sections are taken at different heights, from the highest one (left, separator zone) to the bottom one (right, outlet baffle interface).*

3.4.2.3 FPS temperature drop

The same analysis has been repeated for the FPS element, considering the reported average LBE inlet and outlet temperatures for the element, and comparing them with the ones calculated by means of the CFD model. The measured values are reported in Figure 92 with reference to "Test 1" documented in [6].

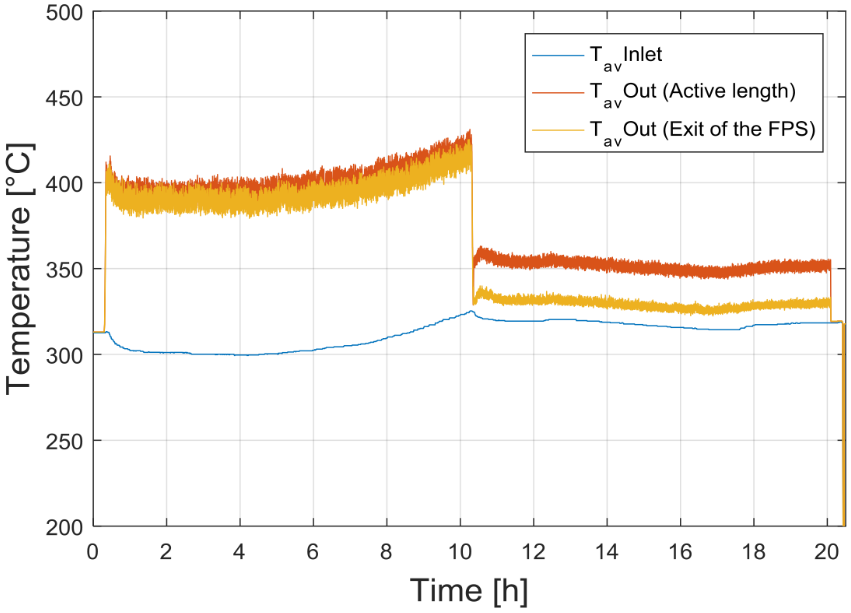

Figure 92. *Average temperatures at the inlet and outlet sections of the real FPS, during "Test 1", Ref. document [6] (p.21). Courtesy of ENEA.*

In this case, the measured LBE average temperatures through the FPS in the real experiment are:

- Average FPS inlet temperature $\bar{T}_{IN,FPS} \cong 300\ °C$°C
- Average FPS outlet temperature $\bar{T}_{OUT,FPS} \cong 390\ °C$

- $\Delta T_{FPS} \cong 90°\mathrm{C}$

The corresponding values obtained in the CFD model are:

- (CFD) Average FPS inlet temperature $\bar{T}_{IN,FPS} = 296\ °C$
- (CFD) Average FPS outlet temperature $\bar{T}_{OUT,FPS} = 385\ °C$
- (CFD) $\Delta T_{FPS} = 89\ °\mathrm{C}$

The CFD results are thus coherent with the experimental data with a good degree of accuracy (error on ΔT_{FPS} around 1%), testifying the validity of the approach used to model the FPS element in the present CFD simulation. Figure 93 below graphically summarizes the results:

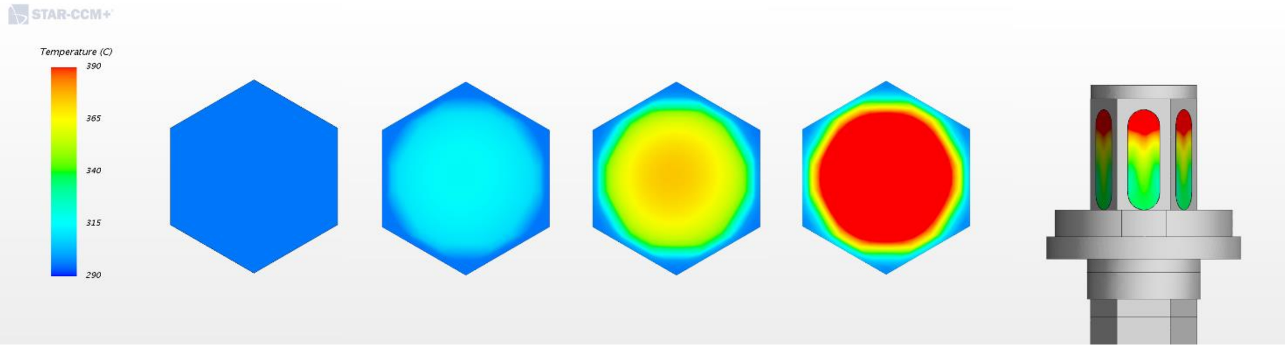

Figure 93. *Visualization of the LBE temperature field on various sections of the FPS LBE region. Each section is taken at a different height, the leftmost one coinciding with the bottom FPS inlet; the rightmost detail, instead, portrays the LBE temperature field at the FPS outlet (top of the hexagonal wrapper).*

3.4.2.4 Riser outlet temperature

In the following Figure 94, the LBE average temperature at the outlet section of the real riser element is reported throughout the whole experiment ("Test 1" reported in [6]).

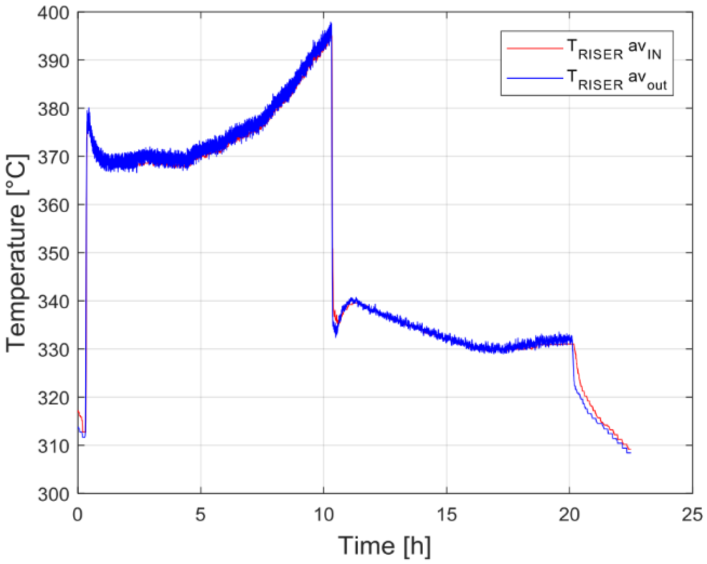

Figure 94. *Average temperatures at the inlet and outlet sections of the real Riser, during "Test 1", Ref. document [6] (p.36). Courtesy of ENEA.*

The average measured value (in the “proper” regime condition time span, i.e. from ~ 1 h to ~ 5 h of the experiment time) for the riser outlet temperature is thus equal to ~370°C. The corresponding average value calculated by the CFD simulation is equal to 370 °C, as illustrated in Figure 95 below.

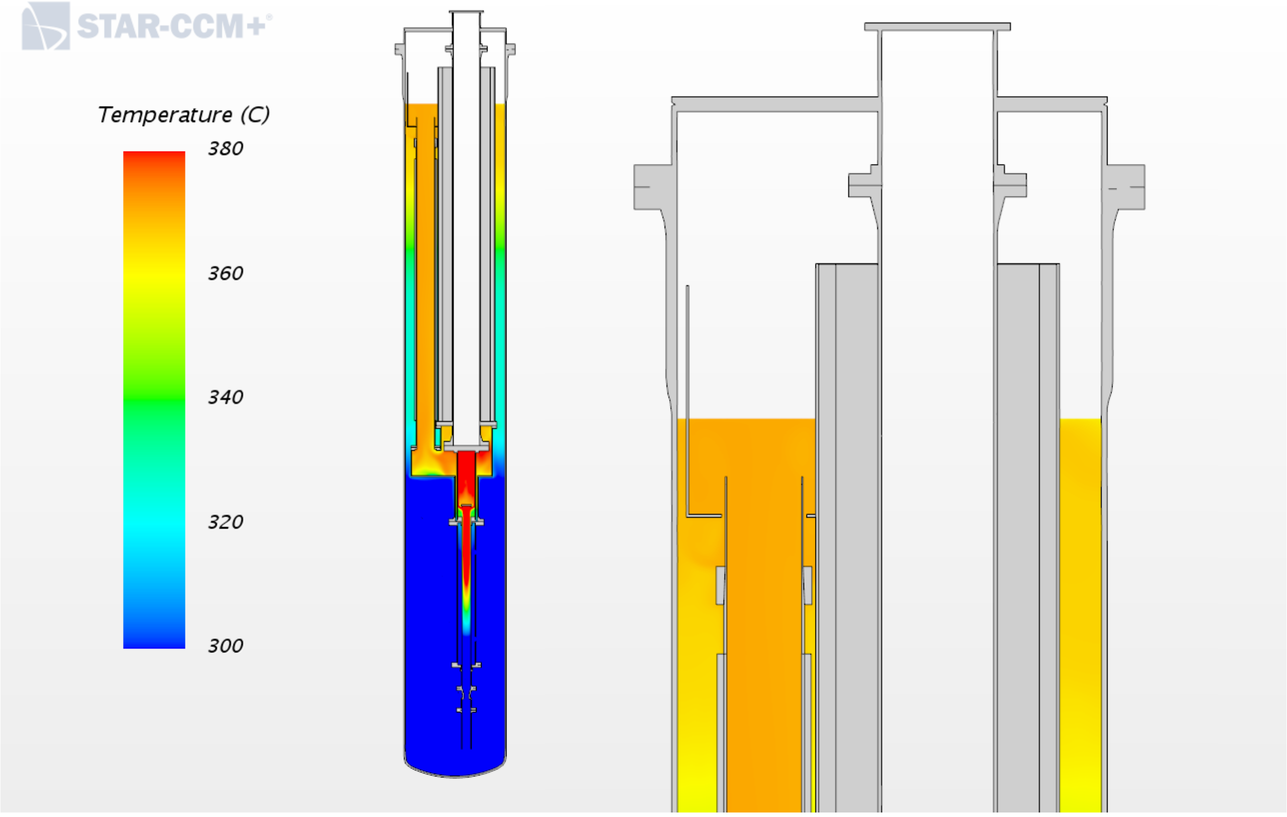

Figure 95. Detail of the LBE temperature field in proximity of the riser outlet region.

The CFD simulation results are in accordance with the real experiment data and provide further validation of the present steady state model.

4. Transient model of the CIRCE ICE experiment

4.1 Aim of the transient model

In previous chapter 3, the stationary CFD model for the CIRCE ICE "regime" experiment has been analysed, paying particular attention to the various approaches followed to model each region of the facility. Its results have then been portrayed, commented and validated by comparison with the official experimental data (paragraph 3.4). This chapter will instead be focused on the modeling of the latter phase of the experiment, which consists of the SCRAM accident simulation (and subsequent decay phase). The peculiarities of this segment of the experiment have been previously described in depth in the introductive paragraph; briefly summarizing, at the beginning of this phase of the experiment the operative parameters of some elements of the facility are changed, namely:

- **FPS**: the heat power supplied by the FPS is reduced from the value of 800 kW to a lower value (different for each single experiment, typically of the order of magnitude of 30 kW).
- **HX**: the HX element is deactivated (the water mass flow rate is suppressed).
- **DHR**: the DHR element is activated (the refrigerating air mass flow rate starts flowing), and takes the place of the HX as the heat sink of the circuit.
- **Riser**: the argon gas lift system is deactivated, and the LBE mass flow rate through the loop becomes a direct consequence of the natural convection effects introduced by the heat exchange in the FPS and DHR elements.

Accordingly to "Test 1" reported in [6] (which also represents the reference experiment for the present simulation), these modifications to the operative parameters of the facility are set to be applied after around 10.5 hours from the beginning of the experiment, as highlighted in the previous Figure 38.

In order to simulate the behaviour of the facility throughout this second part of the experiment, the construction of an appropriate CFD transient model is necessary. Conceptually, the idea behind the development of this model consists in using the stationary one previously described in chapter 3 as the initial condition for the simulation of the SCRAM experiment. Anyway, some preliminary observations about this last point have to be discussed.

In fact, it is fundamental to notice that the CFD steady state model has been created in order to simulate the "proper" stable regime condition of the CIRCE ICE "Test 1", which endures only for the first 5 hours of the experiment (excluding the initial transient); in the time span comprised between the end of such "proper" stable phase of the regime experiment and the beginning of the SCRAM (from ~5 hours to ~10.5 hours of the experiment time), the facility is still operating under the designed regime conditions, but the average LBE temperatures in the whole facility tend to globally increase, for reasons that are not yet completely clear. This semi-stable effect is evident considering previous

Figure 90, Figure 92, Figure 94 and most importantly Figure 96 below, which portrays the temporal evolution of the temperatures measured by the LBE bulk thermocouple lines.

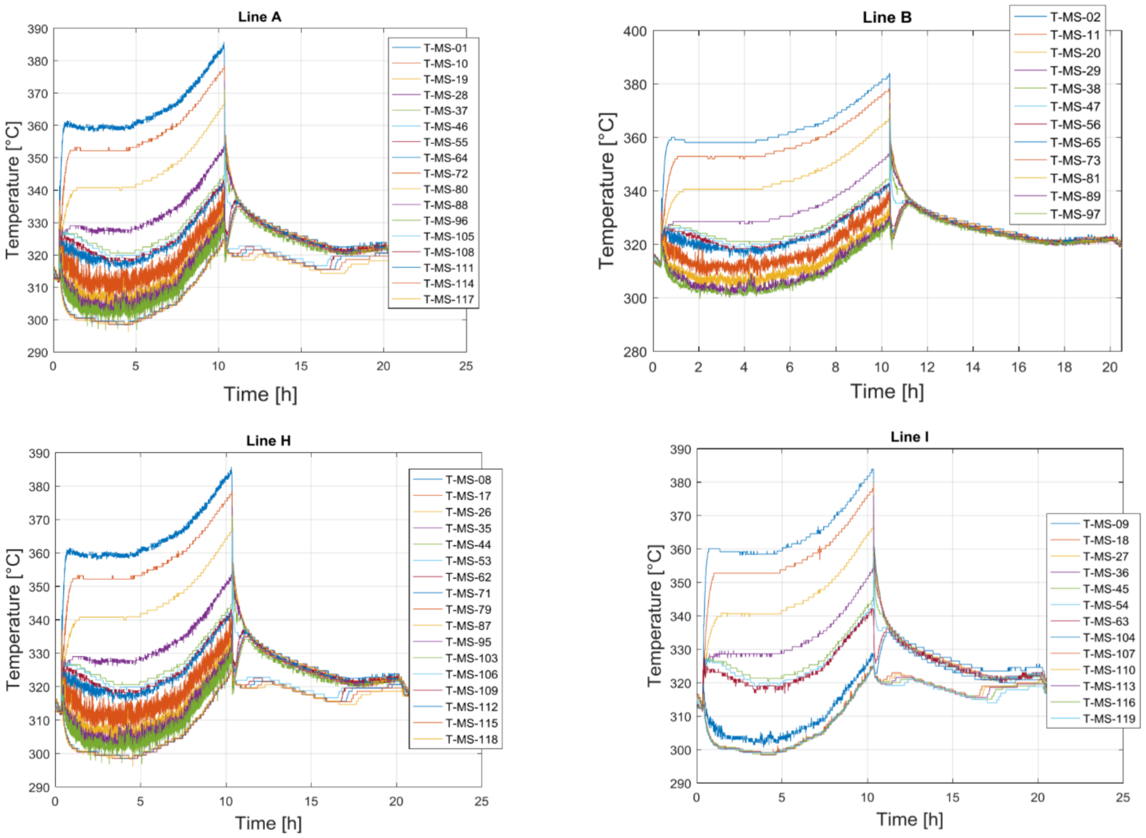

Figure 96. Temperature measured by the real thermocouples of lines A, B, H and I throughout the duration of the whole "Test 1" experiment, Ref. document [6] (pp.42-46). The global increase in the LBE bulk temperature registered from ~5 h to ~10 h is evident, and its main causes are still not completely known (probably related to a malfunctioning of the HX element). Courtesy of ENEA.

This substantially means that, at the end of the regime experiment (around ~10 h), the CIRCE facility has reached a condition that is rather different from the "stable" one portrayed by the CFD steady state model described in chapter 3. Most notably, this implies that using such steady state model as a starting condition for the transient simulation inevitably introduces an important initial error, since the overall LBE temperatures of the real experiment are way higher than the ones portrayed by the stationary model. The only hypothetic way of generating a really accurate transient SCRAM model would thus require the capability of modeling also the abovementioned time-depending "semi-stable" regime condition of the experiment, but such condition cannot be easily simulated, essentially due to the current lack of knowledge about its fundamental causes. Due to this issue, the only solution that allows to generate a transient model for the SCRAM experiment inevitably imposes the use of the "proper" steady state model as the initial condition. Furthermore, since this introduces the abovementioned discrepancies between the model and the experimental data, the main aim of this simulation will be focused on a simple and qualitative analysis of the SCRAM transient; additionally, the real transient experiment is dominated by very intricate and chaotic time-fluctuating phenomena, whose accurate modeling would be extremely complex and not easily feasible. The results of this simulation are thus only meant to approximately capture and visualize a possible scenario of interactions between the elements of the facility during a modified version of the ICE experiment.

In the next paragraphs the strategies used to create this model will be illustrated in detail.

4.2 From the steady state to the transient model

The process of transforming the CFD stationary model discussed in chapter 3 into the initial condition for the transient model is described in the following points:

1. **Activation of the DHR:**

   the air region of the DHR element had been deactivated during the steady state simulation, as illustrated in paragraph 3.3.5. Yet, at the beginning of the real SCRAM experiment the DHR is activated, and the refrigerating air mass flow rate starts flowing through it (0.24 kg/s in the reference “Test 1”). Since the steady state model is meant to represent the initial condition for the transient model (before the start of the SCRAM simulation), it must be updated in order to contemplate the actual presence of the air inside the DHR double bayonet tube. The DHR air region has thus been activated, a mass flow rate inlet condition of 0.001 kg/s has been imposed, and the stationary model has been run again until convergence; such very low value of the mass flow rate has been chosen in order to “initialize” the effective subsistence of the air flow in the DHR element without perturbating the stationary condition of the model. Later, correspondingly to the beginning of the SCRAM simulation, this value will be set to grow up to the prescribed value of 0.24 kg/s, thus modeling the proper activation of the DHR.

2. **Introduction of the “time” dimension and relative models:**

   all the physical continuums presented in paragraph 3.2.2 have been updated by removing the stationary model and substituting it with a “Euler-Implicit” time modeling scheme; by doing so, the “time” dimension has been introduced for all the various regions of the model.

3. **Creation of the “regime condition” start of the transient:**

   the first application of the time models has consisted in the simulation of a short time span (10s) of the “regime condition” of the facility; the modeled operative conditions of the facility were thus still the same ones typical of the stable regime experiment. Additionally, this approach allowed to smoothly introduce the Euler implicit time method into the simulation, by setting extremely short initial time steps (10^{-9} s) and a large number of inner iterations (~15) for the first phase of the calculation, while later gradually proceeding to longer time steps (and fewer inner iterations).

By following these steps, an equivalent “time-depending” version of the stable steady state model has been created. The next paragraph will explain how this “stable” transient model has been employed as a starting condition for the simulation of the SCRAM experiment.

4.3 Modeling the SCRAM experiment

In the reference CIRCE ICE “Test 1”, the SCRAM experiment is set to start at around 10.3 hours of the experiment time. When this phase of the experiment begins, the operative parameters of the DHR, HX, FPS and riser elements are changed following a certain time schedule, reported in the following Table 10.

Component	Event	Experiment time [s]	Experiment time [h]
FPS	FPS 800 kW full power stop	37128	10,31
	FPS heat power reaches 30 kW	37332	10,37
RISER	Deactivation of the gas lift system (initialization)	37265	10,35
HX	Feeding water stop (initialization)	37265	10,35
DHR	Activation	37267	10,35

Table 10. Time schedule for the activation/deactivation of the various components of the real “Test1” experiment, Ref. document [6]. Courtesy of ENEA.

The interaction between the activation and deactivation of these different elements highly affects the general behaviour of the facility, especially during the initial phase of the SCRAM experiment. It is thus necessary to re-define the most important CFD characteristics of the abovementioned elements (actively involved in the transition from the “regime” to the SCRAM experiment), in order to keep into account the time schedule illustrated in Table 10. This translates into defining some time-varying expressions for the various properties of the modeled elements, as will be illustrated in the next paragraphs.

N.B.: the “Physical time” defined in the present model is shifted with respect to the real “Experiment time”; this is due to the fact that the transient SCRAM model is based on a 10s simulation of the previous regime condition phase. Figure 97 below clarifies the employed physical time convention by considering the time-span related to the FPS deactivation process.

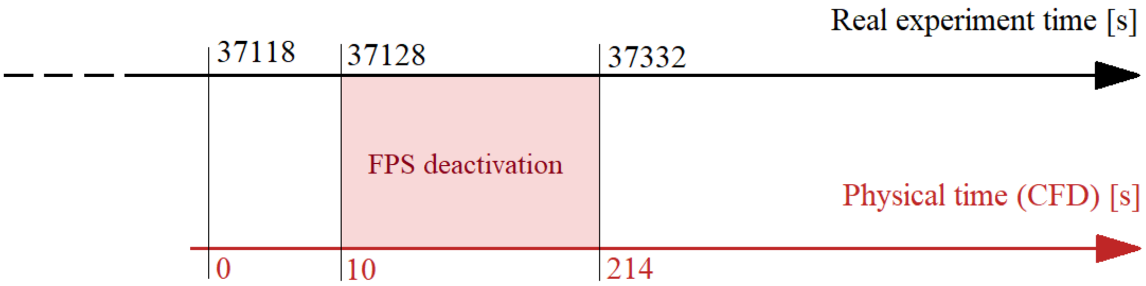

Figure 97. *Real experiment time vs. modeled Physical time reference convention for the present SCRAM transient model.*

4.3.1 FPS transient modeling

At the beginning of the SCRAM experiment, the FPS is set to reduce the supplied heat power from the 800 kW of the regime experiment to the value of 30 kW, upon a time interval of 204 s (with reference to Table 10. From the CFD modeling point of view, this means that the volumetric heat source condition imposed in the active region of the element needs to be modified in order to mimic such time-depending behaviour. As previously illustrated in paragraph 3.3.1.1 in deeper detail, the stationary FPS volumetric heat source condition $S(r)$ has been defined as:

$$S(r) = f(r) \cdot \frac{\dot{Q}_{FPS,r}}{F_0} \quad \left[\frac{W}{m^3}\right] \tag{8}$$

Where $f(r)$ is a "shape function", $\dot{Q}_{FPS,r} = 800\ kW$ represents the regime condition heat power supplied by the real FPS, and F_0 is the volume integral of $f(r)$ over the FPS active regions. The modeled total heat power supplied is hence defined as:

$$\dot{Q}_{FPS,m} = \int_{FPS_a} S(r) dV \quad [W] \tag{6}$$

Where FPS_a is the volume of the FPS active region.

The formulation expressed in equation (8) has been designed in order to later obtain the precise value of $\dot{Q}_{FPS,m} = \dot{Q}_{FPS,r} = 800\ kW$ for the FPS total heat power, independently from the chosen "shape function" $f(r)$. Additionally, such expression is intended to be employed in the stationary model, and is therefore not showing any dependence from the temporal dimension.

In the framework of the transient simulation of the SCRAM experiment, equation (6) needs to be upgraded by considering a multiplicative "time-depending" term:

$$\dot{Q}_{FPS}(t) = \dot{Q}_{FPS,m} \cdot f_{FPS}(t) \tag{24}$$

Where:

- $\dot{Q}_{FPS}(t)$ represents the global, time-dependent expression of the FPS total heat power.
- $\dot{Q}_{FPS,m}$ is the steady state FPS total heat power, as expressed in equation (6); this term is thus constant (independent from time) and equal to 800 kW.
- $f_{FPS}(t)$ is an adimensional "temporal shape function", which is only meant to define the shape of the time profile associated with the $\dot{Q}_{FPS}(t)$.

By employing such formulation, the desired profile for the FPS total heat power supplied could be set, and is displayed in the following Figure 98.

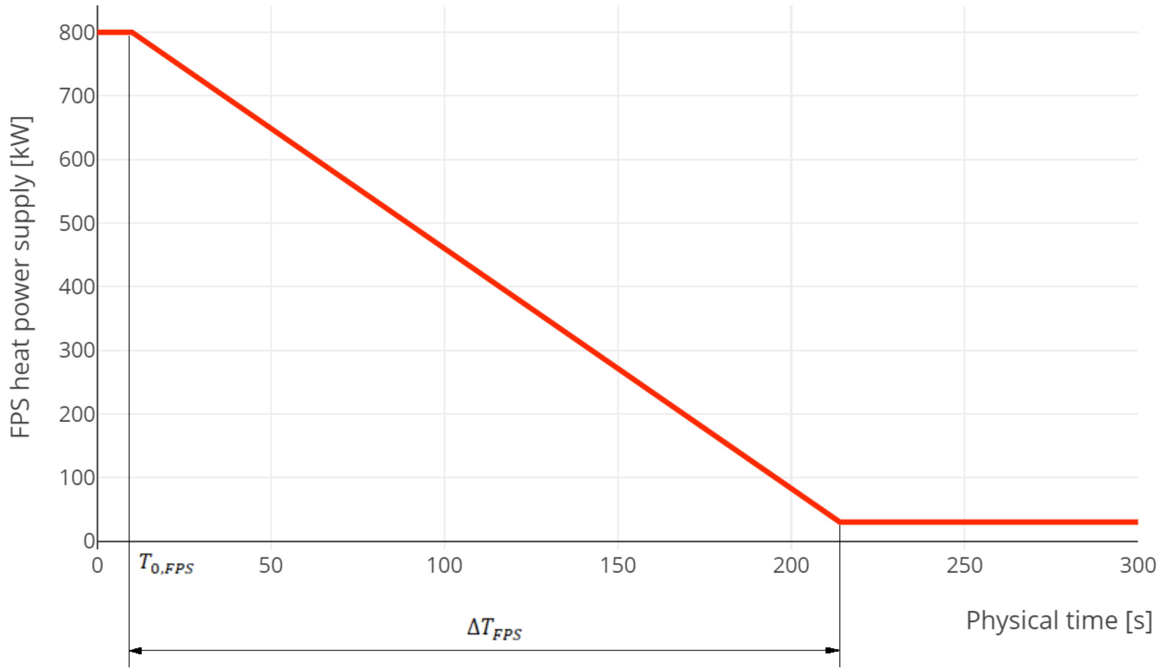

Figure 98. *Modeled temporal profile for the FPS heat power supply during the initial phase of the SCRAM transient. Furthermore,* $\dot{Q}_{FPS}(t)$*=30 kW, constant for 300 s <Phys. Time<4800 s.*

Two important details must be noticed:

- $T_{0,FPS}$ represents the time at which the FPS total heat power starts decreasing; in this simulation it has been set to 10s, which corresponds to the solution time reached by the "stable" transient model (described in the previous paragraph 4.2).
- ΔT_{FPS} is the time interval requested for the total heat power to decrease from its maximum value (800 kW, regime) to its minimum (30 kW). This value has been set to 204 s, accordingly to the official "Test1" data reported in Table 10.

4.3.2 HX transient modeling

The deactivation of the HX is another crucial factor for the simulation of the SCRAM experiment; most importantly, the timing of this process must be analysed and applied to the model in an appropriate way. From the CFD point of view, deactivating the HX element translates into reducing (over time) the heat sink condition imposed there, from its maximum steady state value of 800 kW to zero. Accordingly to paragraph 3.3.2.2, the stationary total heat power removed in the HX region ($\dot{Q}_{HX}$) has been defined as:

$$\dot{Q}_{HX} = \int_{HX_a} q_{HX,hex} dV \quad [W] \tag{22}$$

Where $q_{HX,hex}$ is a volumetric heat sink condition (see reference paragraph for details) and HX_a is the volume of the HX active region (in the steady state model $\dot{Q}_{HX}$ is constant and equal to 800 kW)

The upgraded formulation expressed in equation (2526) has been employed to generate a "time-depending" transient version $\dot{Q}_{HX}(t)$, meant to represent the temporal reduction of the total heat power removed by the HX during the SCRAM simulation, namely:

$$\dot{Q}_{HX}(t) = \dot{Q}_{HX} \cdot f_{HX}(t) \qquad (2526)$$

Where:

- $\dot{Q}_{HX}$ is the steady state total heat power removed by the HX (defined by equation (22), constant and equal to 800 kW)
- $f_{HX}(t)$ is a time depending "temporal shape function" that is only meant to define the temporal profile for the global $\dot{Q}_{HX}(t)$.

The $f_{HX}(t)$ has been generated in order to obtain the final $\dot{Q}_{HX}(t)$ profile depicted in the following Figure 99.

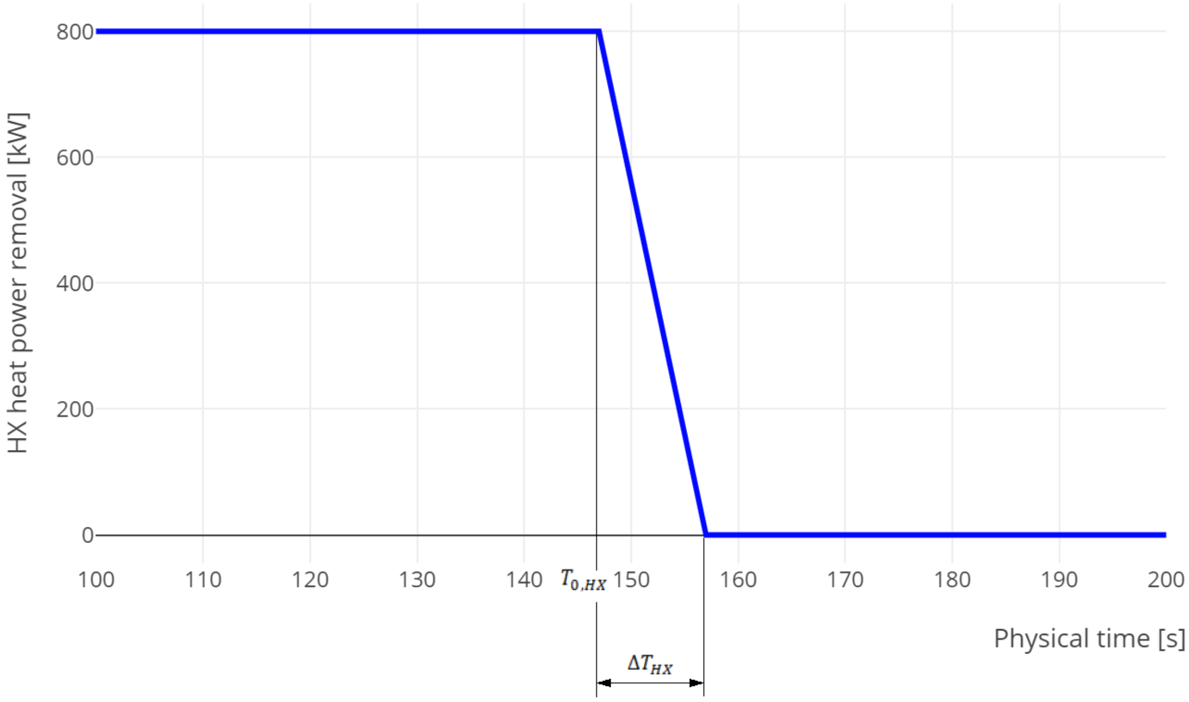

Figure 99. *Modeled temporal profile for the HX heat power removal, simulating the HX deactivation during the SCRAM transient.* $\dot{Q}_{HX}(t)$*=800 kW for 0 s<Phys. Time<100 s and* $\dot{Q}_{HX}(t)$*=0 kW for 200 s<Phys. Time< 4800s.*

As can be noticed considering Table 10, the only information available about the deactivation was its starting time, while no data could be found about the duration of the process itself, in fact:

- Considering that for the present simulation the $T_{0,FPS}$ time has been set to 10 s, the $T_{0,HX}$ (which represents the simulation time at which the HX starts deactivating) has been set to 147 s, in order to respect the scheduled time intervals of the real experiment.
- The ΔT_{HX} value (duration of the HX deactivation process) has been hypothesized due to lack of data and set equal to 10 s.

4.3.3 Riser transient modeling

During the regime condition experiment, the Riser argon gas lift system is activated, and generates a LBE mass flow rate of approximately 65 kg/s through the CIRCE primary loop. Later, at the beginning of the SCRAM phase of the experiment, the gas lift system is disabled, and the LBE mass flow rate is induced by natural convection effects only.

In order to model the deactivation of the argon gas lift system, the steady state volumetric momentum source in the riser region (paragraph 3.3.3) needs to be transformed into an expression that appropriately defines its decrease over time. In the steady state model, the F_z momentum source in the LBE riser region (along the z direction) was set as constant and equal to:

$$F_z = 5742 \frac{N}{m^3}$$

The "time depending" volumetric momentum source $F_z(t)$ meant to simulate the behaviour of the region during the SCRAM experiment has then been defined as:

$$F_z(t) = F_z \cdot f_{riser}(t) \tag{27}$$

Where:

- F_z is the steady state value for the vertical volumetric momentum source in the riser region.
- $f_{riser}(t)$ is an adimensional "temporal shape function" that has the only purpose of establishing the temporal profile for the $F_z(t)$ function.

The final $F_z(t)$ function is illustrated in the plot in Figure 100 below:

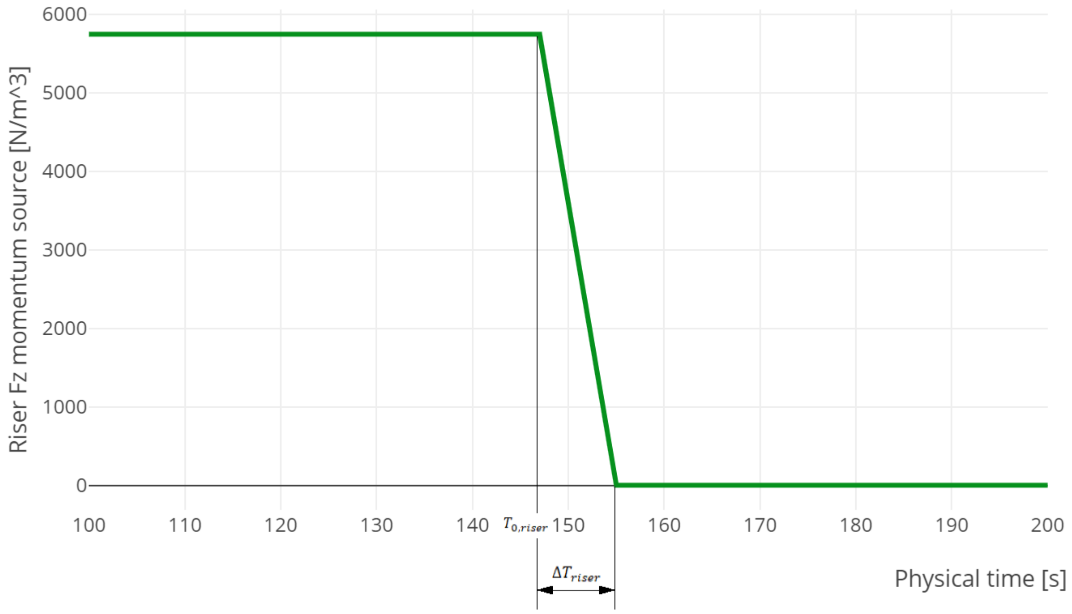

Figure 100. Modeled temporal profile for the Riser momentum source, simulating the deactivation of the gas lift system during the SCRAM transient. $F_z(t)$=5742 N/m^3 for 0 s<Phys. Time<100 s and $F_z(t)$=0 N/m^3 for 200 s<Phys. Time< 4800s.

Important details:

- $T_{0,riser}$ represents the time at which the gas lift system starts deactivating, and has been set equal to 147 s (contemporary to the HX deactivation, $T_{0,riser} = T_{0,HX}$)
- ΔT_{riser} has been hypothesized and set equal to 8 s (no official data found for "Test 1" in Table 10).

4.3.4 DHR transient modeling

In the last phase of the steady state modeling ("stable" pre-SCRAM transient described in paragraph 4.2), the air mass flow rate through the DHR double bayonet tube has been set equal to 0.001 kg/s; this value has been chosen only to initialize the air mass flow rate in the transient model. In the analysed "Test 1", at the beginning of the SCRAM experiment the DHR element is activated, and such air mass flow rate increases up to a nominal value of 0.24 kg/s. From the modeling point of view, this translates into reformulating the mass flow inlet condition for the air region in the DHR, considering an appropriate temporal profile. The procedure employed to determine the time depending expression for the DHR air mass flow rate ($\dot{m}_{air}(t)$) is comparable to the ones illustrated in the previous paragraphs (from 4.3.1 to 4.3.3) and the final result is illustrated in the following Figure 101.

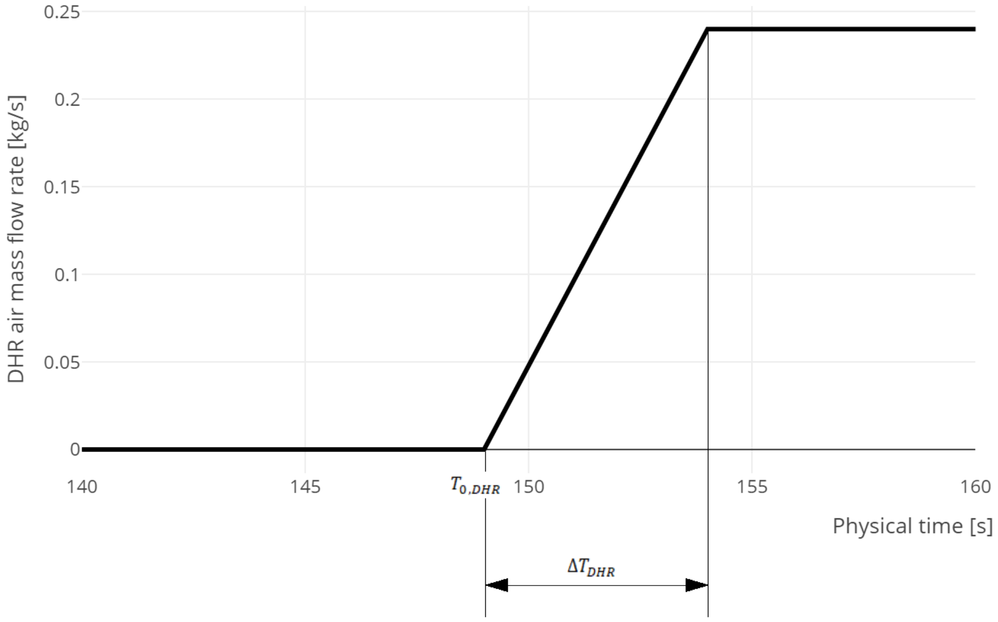

Figure 101. Modeled temporal profile for the DHR air mass flow rate, simulating the activation of the element during the SCRAM transient. $\dot{m}_{air}(t)$*=0.001 kg/s for 0 s<Phys. Time<140 s and* $\dot{m}_{air}(t)$*=0.24 kg/s for 160 s<Phys. Time< 4800s.*

Important details:

- The time at which the DHR starts activating ($T_{0,DHR}$) has been set equal to 149 s (in order to respect the time intervals of the real experiment, as described in Table 10).
- The ΔT_{DHR} (duration of the activation process) has been hypothesized due to lack of official data, and set equal to 5 s.

4.4 Results of the transient model

After having defined and set the time-depending expressions for the properties of the various elements of the facility, the transient CFD simulation of the SCRAM experiment has been run. During the early phase of the calculation, the chosen time step has been kept relatively low (~10^{-1}s), in order to ensure a stable behaviour of the solvers. This value has then been progressively increased in order to be able to simulate 4800s of physical time (1 hour and 20 minutes of the real SCRAM experiment) in a reasonable span of calculation time. Due to the large number of cells in the volume mesh, the calculation has been carried out employing 220 CPUs of the CRS4 main clusters. The behaviour of the different elements of the model during the simulated transient experiment is illustrated in the following paragraphs:

Activation of the DHR

The activation of the DHR element is set to start at 149 s of physical time ($T_{0,DHR}$), in accordance with the profile illustrated in Figure 101, and is set to be completed in a time interval (ΔT_{DHR}) of 5 s. The next Figure 102 illustrates this activation process showing the velocity field in the DHR air region and in the surrounding LBE bulk at different values of physical time.

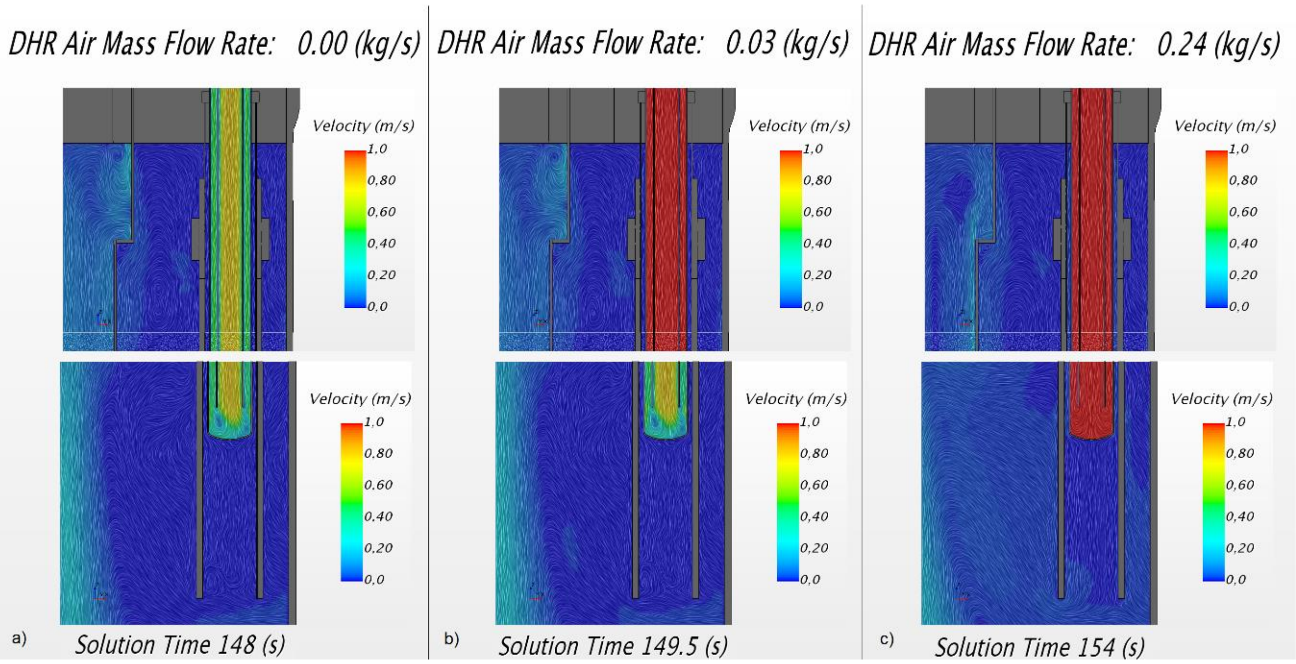

Figure 102. *Velocity fields for the DHR air region and LBE bulk during the DHR activation process, focusing on the top and bottom regions of the element. a) velocity fields 1 s before the start of the activation process. b) velocity fields 0.5 s after the start of the activation process. As can be noticed, the DHR air mass flow rate is starting to increase, influencing the velocity field in the top portion of the DHR air region. c)velocity fields exactly at the end of the activation process (154 s). The mass flow rate has reached the desired value of 0.24 kg/s.*

Furthermore, during the decay phase of the experiment following the "core SCRAM" (here simulated by the gradual reduction of the heat power supplied by the FPS), the LBE mass flow rate circulation in the CIRCE loop becomes a direct effect of the natural convection effects established in proximity of the DHR and FPS elements. Figure 103 illustrates the influence of such effects on the LBE bulk velocity field, highlighting three essential moments of the transient model.

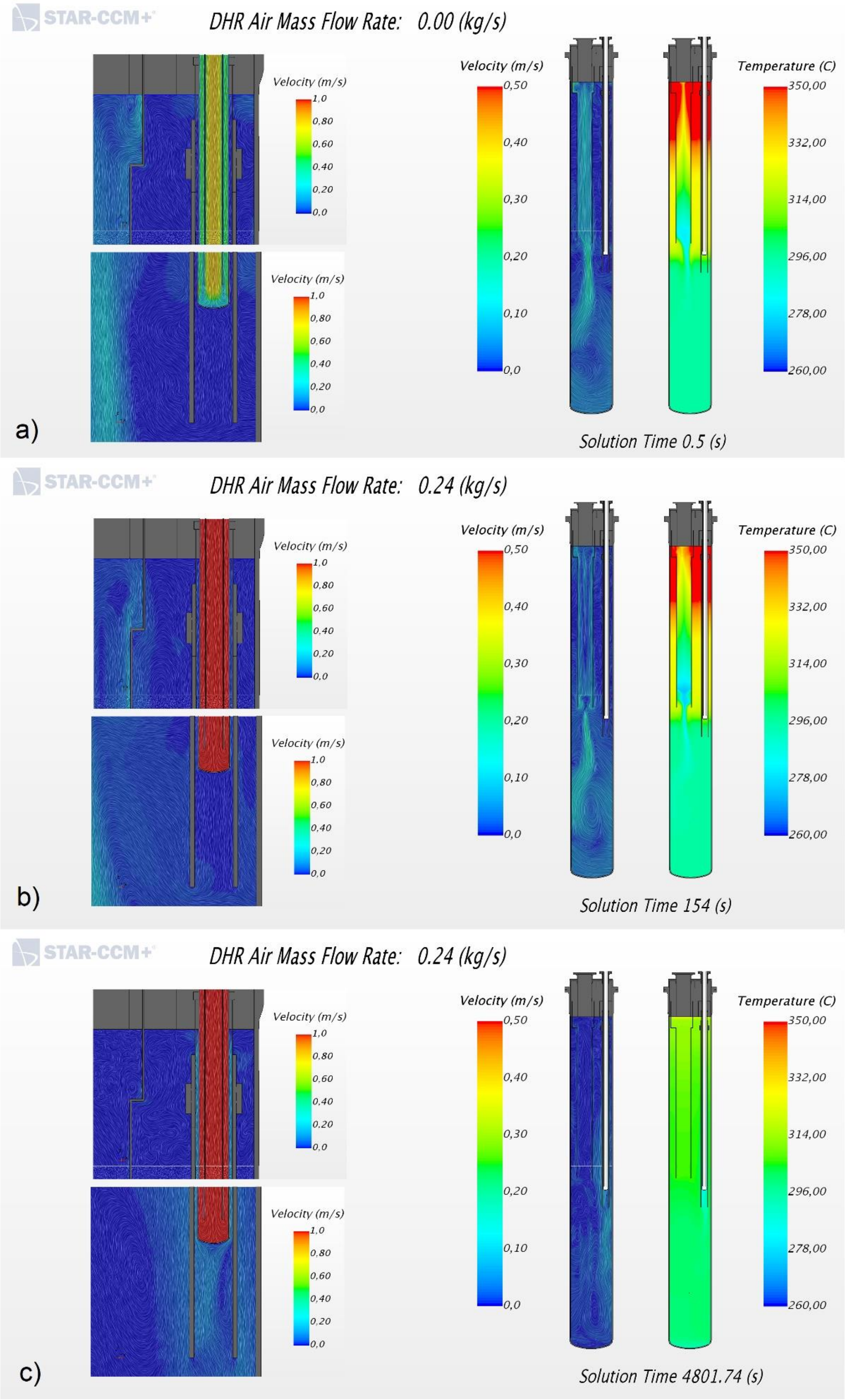

Figure 103. *LBE bulk velocity and temperature fields. a) Steady state condition (FPS core scram at 10 s). The influence of the HX element on the velocity field (natural convection, due to colder LBE) is particularly noticeable. b) Visualization of the LBE bulk velocity field exactly after the complete activation of the DHR element. c) LBE bulk velocity field at the end of the present transient simulation (~4800s). The natural convection effects that once were produced by the HX element are now completely established and visible at the bottom of the DHR.*

In the next figures some other important parameters relative to the DHR element are illustrated.

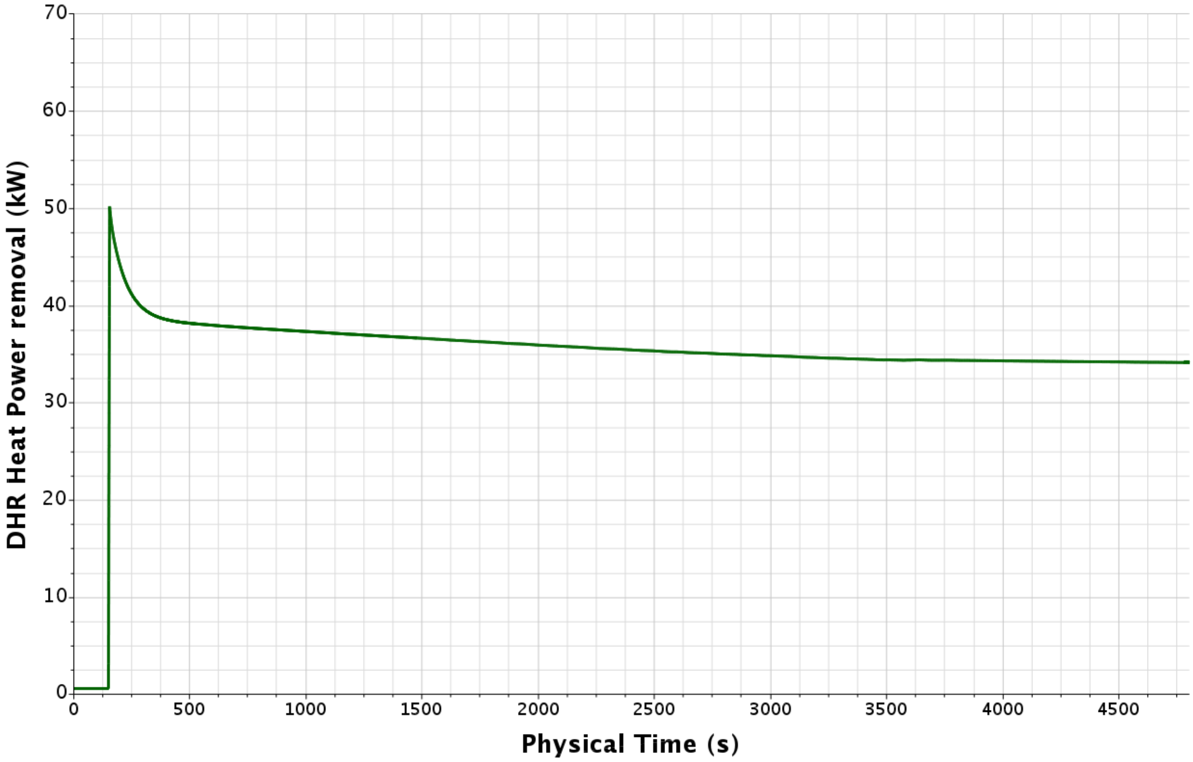

Figure 104. *Heat power removed by the DHR element during the transient SCRAM simulation.*

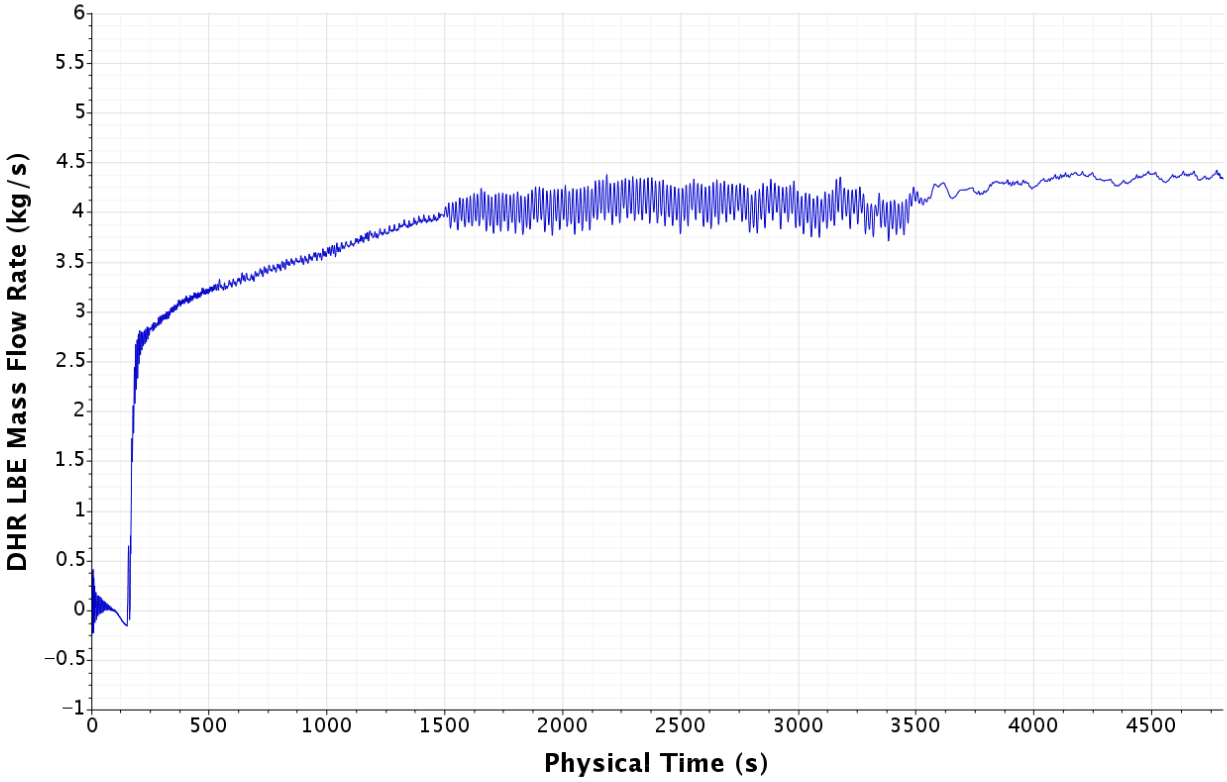

Figure 105. *LBE mass flow rate measured at the outlet section of the DHR element during the transient SCRAM simulation. The insurgence of the LBE natural convection effects coincides with the activation of the DHR, and become progressively more pronounced over time.*

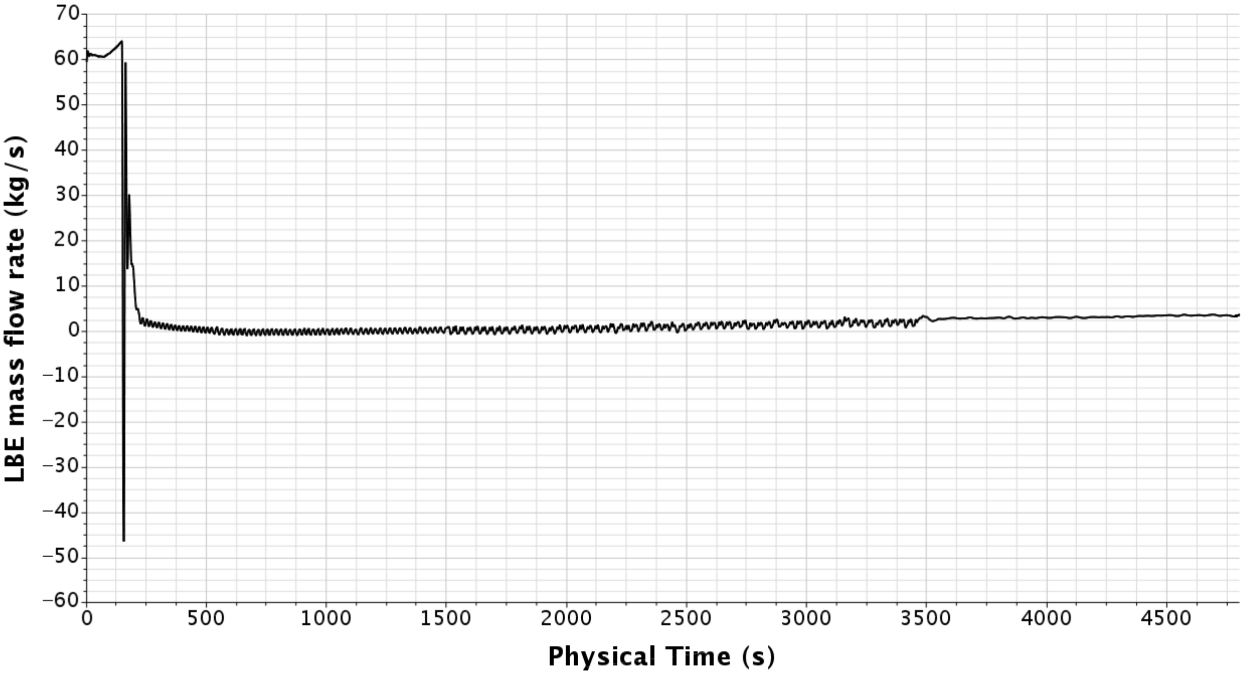

Figure 106. *Total mass flow rate in the CIRCE loop measured at the FPS bottom inlet. As can be noticed, the mass flow rate value passes from around ~62 kg/s (steady "regime" condition) to the value of ~4.5 kg/s at the end of the transient simulation. Considering the previous Figure 105, this furtherly testifies that the global LBE mass flow rate circulating in the loop during the decay phase is a direct consequence of the natural convection phenomena induced by the FPS and the DHR.*

FPS, HX and Riser transient behaviour

The next Figure 107 illustrates the behaviour of the temperature field of the FPS, Riser and HX elements throughout the whole duration of the SCRAM transient simulation, portraying how the interaction between their deactivation processes influences the thermal stratification in the LBE bulk region.

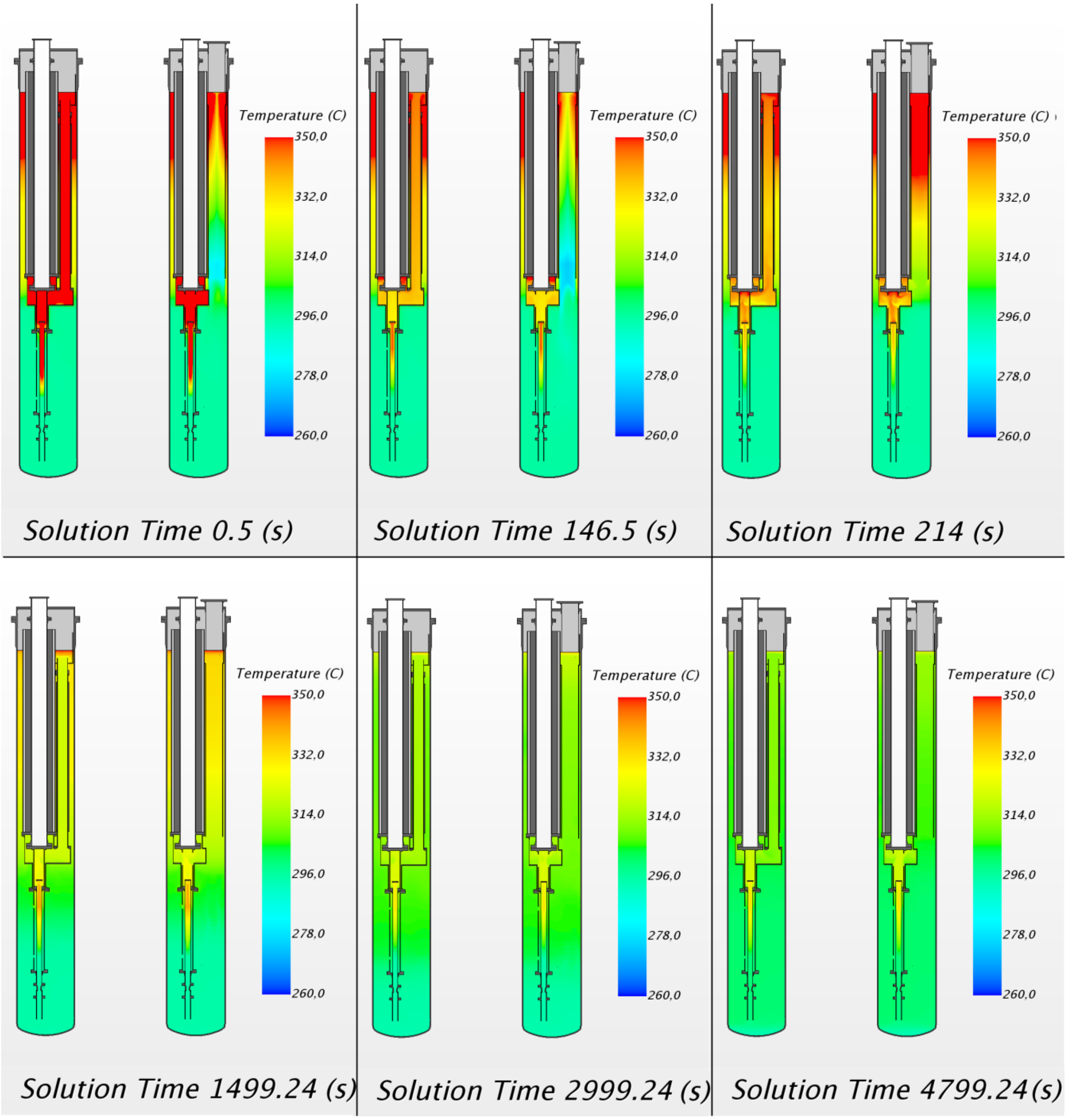

Figure 107. *Visualization of the LBE temperature field in the FPS, Riser, HX and bulk regions at different values of the physical time, during the SCRAM transient simulation. At 0.5 s the experiment is still under the steady "regime condition" phase (FPS SCRAM starts at 10s). At 146.5 s the deactivation of the gas lift system, the HX and the activation of the DHR are imminent. At 214 s the FPS heat power supply has reached its nominal 30 kW value, and the activation/deactivation of the other elements has been completed. As can be noticed, in fact, the LBE temperatures in the FPS, conveyor and riser elements have decreased significantly, while they have dramatically increased in the HX active region. The bottom images visualize the gradual homogenization of the LBE temperature fields at 25 min, 50 min and 1h 20min of the transient simulation.*

Other important data regarding the transient behaviour of the abovementioned elements is reported in the next figures:

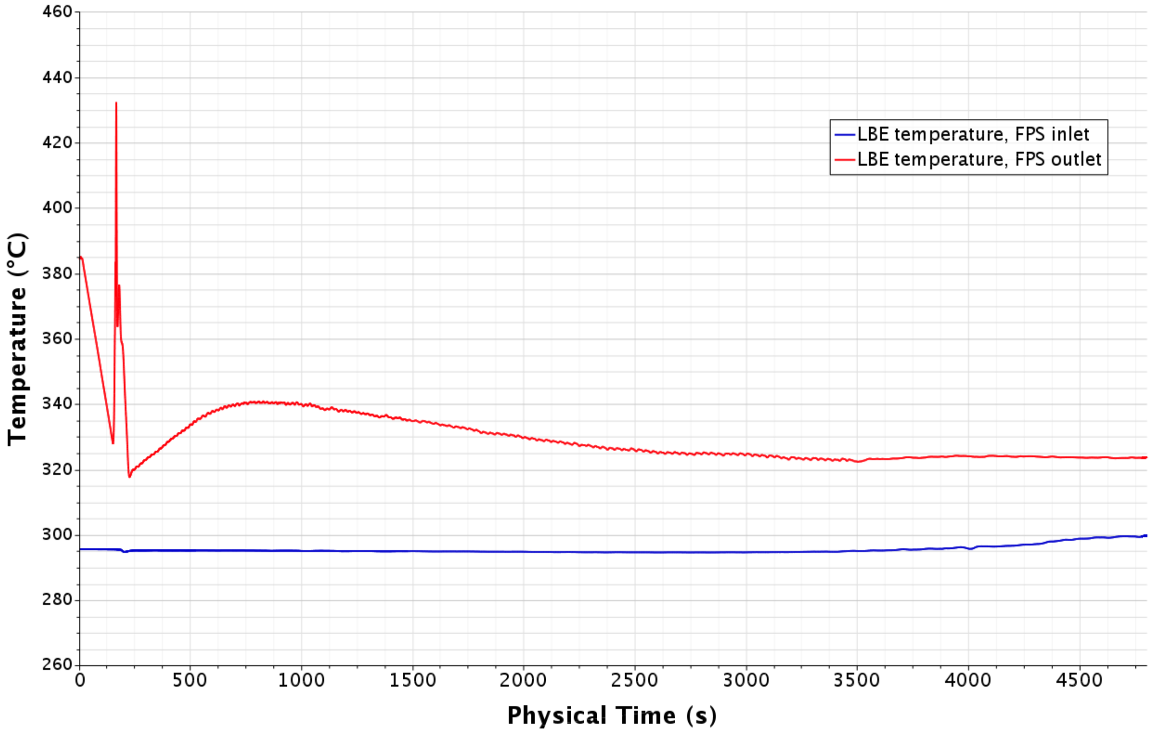

Figure 108. *LBE temperatures at the inlet and outlet sections of the FPS during the transient simulation. The peak temperature reached at the outlet section at ~150 s is essentially due to the deactivation of the riser gas lift system: at that precise moment, in fact, the LBE mass flow rate in the loop drops immediately (Figure 106), causing a sudden decrease of the LBE velocities in the FPS active region. This allows the LBE to stay in contact with the FPS volumetric heat source for a considerably longer time, explaining the temperature peak.*

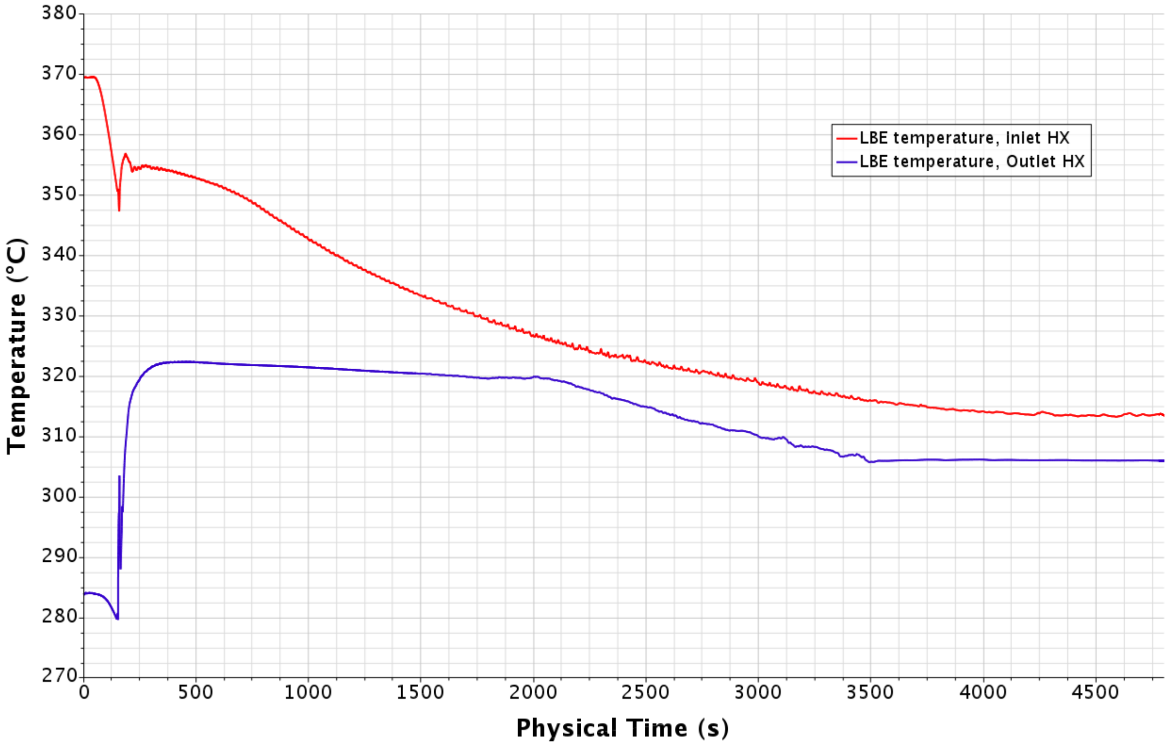

Figure 109. *LBE temperatures at the inlet and outlet sections of the HX element during the transient simulation.*

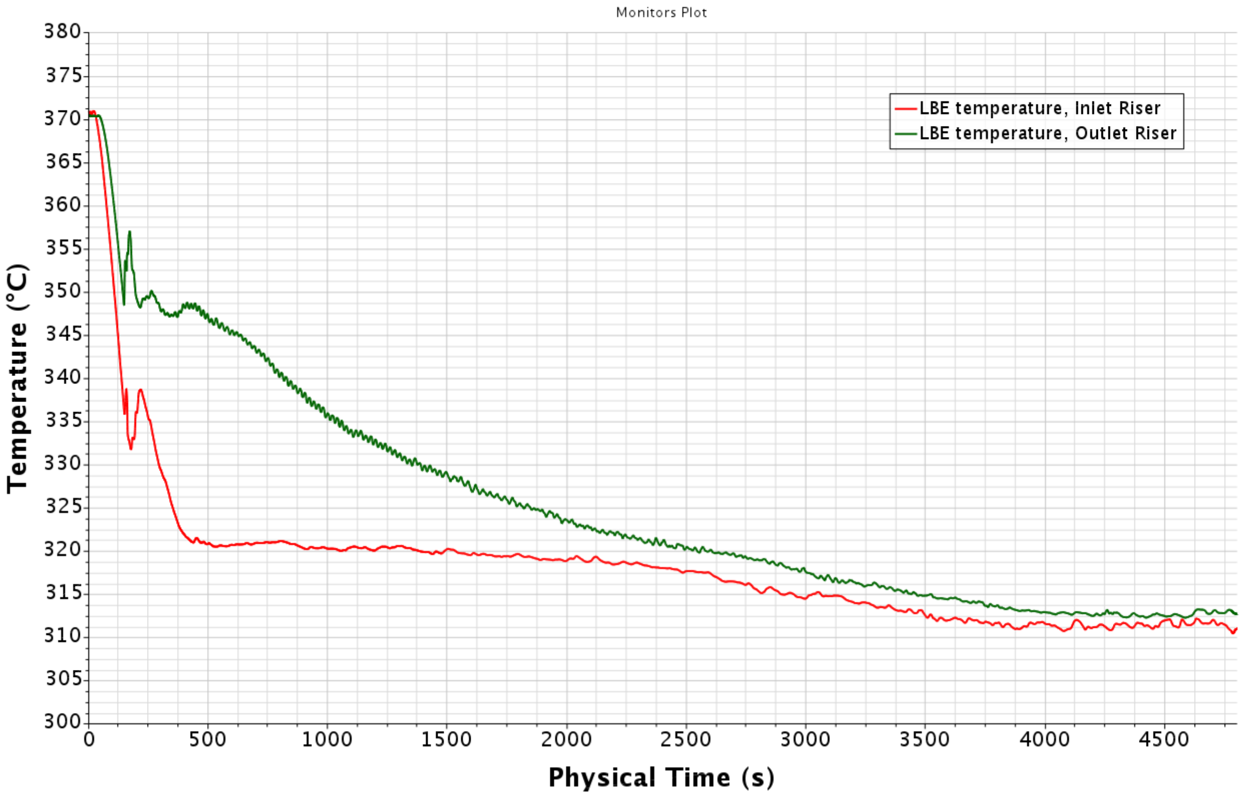

Figure 110. *LBE temperatures at the inlet and outlet sections of the riser element during the transient simulation. Initially (0s <Phys. Time> ~150s), the outlet and inlet temperatures tend to decrease in a similar fashion, due to the gradual reduction of the heat power supplied by the FPS. Later, once the riser gas lift system is deactivated, the outlet temperature decreases much slower than the inlet temperature. This can be ascribed to the fact that the LBE contained in the separator at that moment is still at a very high temperature, and tends to be stationary (gas lift system deactivated), thus explaining the temperature difference between the riser inlet and outlet.*

Bulk thermocouple lines

In analogy with what has been previously mentioned in paragraph 3.4.2.1 , one of the most important parameters that very well portrays the behaviour of the facility during the experiment is the bulk temperature profile measured by the thermocouple "lines". Figure 111 below illustrates how such profile varies over the physical time due to the effects introduced by the activation/deactivation of the different elements.

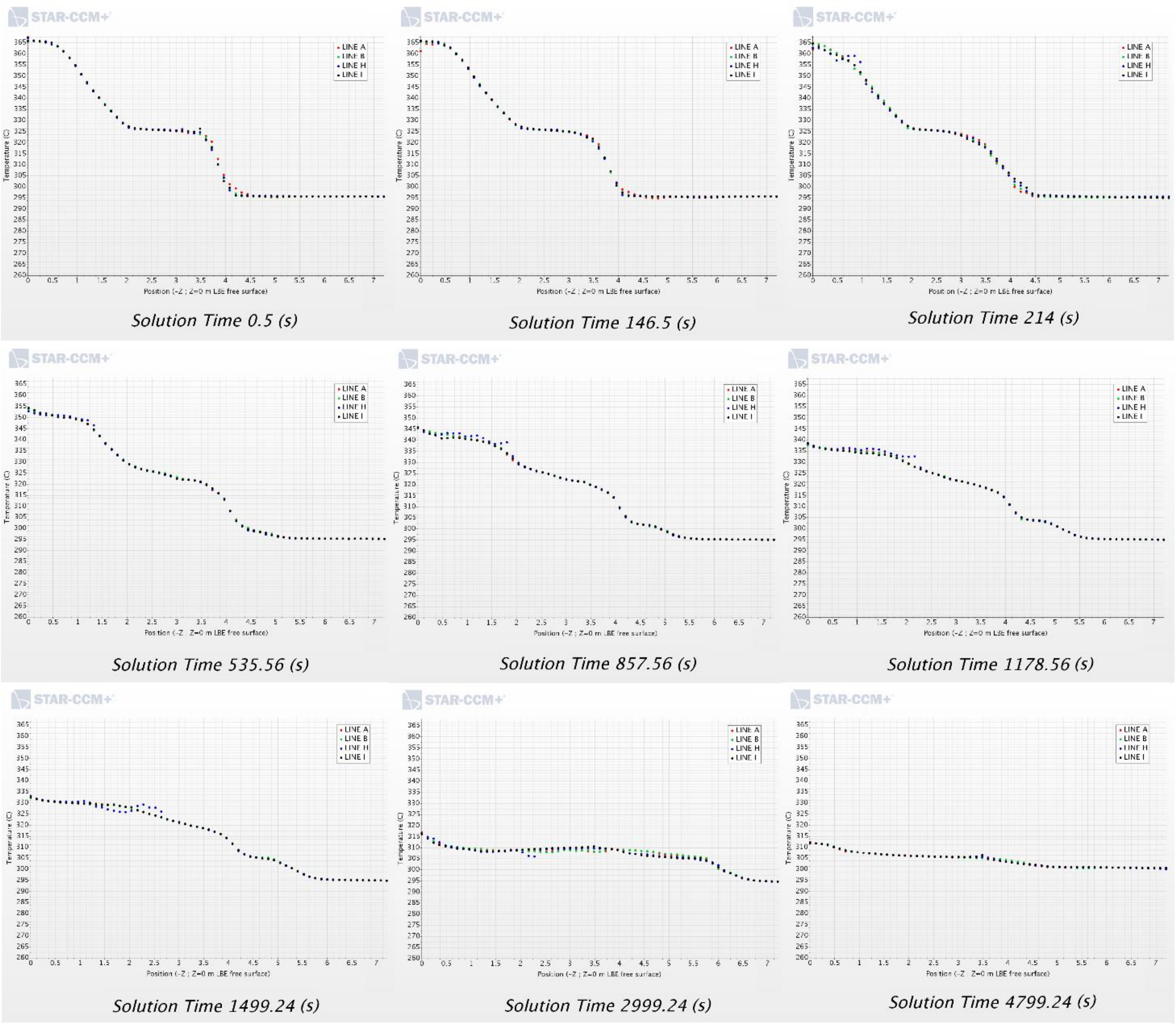

Solution Time 0.5 (s)

Solution Time 146.5 (s)

Solution Time 214 (s)

Solution Time 535.56 (s)

Solution Time 857.56 (s)

Solution Time 1178.56 (s)

Solution Time 1499.24 (s)

Solution Time 2999.24 (s)

Solution Time 4799.24 (s)

Figure 111. Visualization of the temperature profiles in the LBE bulk region as captured by the modeled thermocouple lines A,B,H and I during the transient SCRAM simulation (different values of the physical time).

The initial bulk temperature profile is the same one measured during the steady state simulation (physical time < 10s, right before the start of the SCRAM experiment). Later, after the start of the SCRAM phase (physical time > 10s) such profile tends to gradually become flatter over time, and the bulk temperature field shows a furtherly decreasing degree of thermal stratification (decreasing magnitude of vertical thermal gradients), reaching a condition of almost complete homogeneity (Figure 107, ~4800s). In conclusion, still keeping into account all the factors discussed in paragraph 4.1, the results hereby illustrated offer an approximated and mostly qualitative representation of the behaviour of the facility during the initial phase of the SCRAM experiment.

Conclusions

The research work illustrated in the present thesis has been strictly focused on the analysis and numerical modeling of the fluid-dynamic phenomena involving lead bismuth eutectic (LBE) in the primary loop of the CIRCE facility during the ICE experiment. The achievement of a satisfying degree of confidence in understanding and, most importantly, correctly predicting the behaviour of LBE under the circumstances imposed by the CIRCE ICE experiment is of vital importance in the bigger picture of the design process of the next LFR 4th generation nuclear reactors. More precisely, the consistent validation of the numerical models represents an essential step for this particular purpose.

The CIRCE ICE CFD model described in the previous chapters has thus been created from its very roots keeping this crucial objective in mind. Furthermore, such model has also been designed in order to be versatile enough to be employed for future development of the research in this environment. In the pursuit to reach this goal, the structure of the model has been based on a simple modular approach, described in detail in paragraph 1.3.6.

The most interesting results of the present study are related to the steady state modeling of the "regime condition" phase of the CIRCE ICE experiment, described in chapter 3. In fact, as highlighted in paragraph 3.4.2, the stationary model is characterized by an unprecedented adherence to the official experimental data, testifying the validity of the simulation. Most notably, the accurate numerical modeling of the components of the facility and of their operative behaviour has allowed for a satisfying portrayal of the thermal stratification in the CIRCE LBE pool (bulk) region, which represents one of the key objects of study relatively to the future LFR reactors.

Furthermore, considering the data reported in paragraph 3.4.1, and especially in Figure 82, it can be stated that the two elements that basically dictate the shape of the thermal stratification profile in the LBE bulk region are the heat exchanger (HX) and the conveyor, due to the magnitude of the heat transfer phenomena involved. One of the main reasons behind the improvement in the adherence to the experimental data comparatively to the CIRCE older models is thus ascribed to the more accurate numerical modeling of the HX element (described in paragraph 3.3.2), based on the results of a separate dedicated HX model briefly illustrated in paragraph 3.3.2.1.

Due to its proven reliability, the present CFD stationary model has been upgraded to the current CIRCE HERO experiment configuration (taking advantage of the modular structure), and is presently being adopted by the CRS4 research center to simulate the behaviour of the CIRCE facility under these new experimental conditions. This application furtherly testifies the versatility of the modular approach adopted in this model, which will become a valuable basic tool not only for the analysis of the current HERO experiment, but most importantly for the design and study of the next CIRCE experiments that will be conducted in the future.

Additionally, this steady state model has been employed as the initial condition for a transient CFD model, meant to portray the SCRAM/decay phase of the ICE experiment, as described in chapter 4. Due to the strong but necessary approximations that had to be introduced in order to complete the calculation (paragraph 4.1), and to the inherently fluctuating nature of the phenomena involved, the results of this model are only intended to provide a qualitative overview on the transient SCRAM phase of the experiment, and will thus be the central object of study of further, more specific researches.

Bibliography

[1] Agostini P., Martelli D., Tarantino M. (2015) *CIRCE reference document*, ENEA report CI-I-R-162.

[2] Badillo A., Niceno B. (2016) *Summary for the recommended physical properties for the main fluid and liquid materials used for the MELILOO-stand and TALL-3D freezing experiments*. Paul Scherrer Institute.

[3] Beale S. (2011) *Crossflow over tube banks*. Retrieved from:

https://dx.doi.org/10.1615/AtoZ.t.tube_banks_crossflow_over

[4] Bird R.B., Stewart W.E., Lightfoot E.N. (1960) *Transport Phenomena* (1st ed.), John Wiley & Sons.

[5] Lampis S., Moreau V. (2017) Study and CFD modeling of the behaviour of liquid-state Lead-Bismuth eutectic, with particular reference to the main heat exchanger of the CIRCE experimental facility, located at ENEA, Brasimone (Italy)., CRS4 internship report.

[6] Martelli D., Moreau V., Zwijsen K. (2017) *CIRCE experiments: pre-Test, dataset and analysis*, Deliverable D. 3.2, ENEA Report CI-T-R-292.

[7] Moreau V., Zwijsen K., Lampis S. (2018) *CIRCE experiment: CFD model validation*, Deliverable D. 3.4, SESAME project report, ENEA.

[8] Tarantino M., Di Piazza I., Gaggini P., Bandini G., Cinotti L. (2011) *Innovative Heat Exchanger and Steam Generator Designs for Fast Reactors*, Issued by ENEA.